Title
Applications of MRI in Tissue Engineering: Environmental Control and Noninvasive Culture Surveillance

Author
Archer, Brian

Publication Date
2021

Peer reviewed|Thesis/dissertation

UNIVERSITY OF CALIFORNIA

Los Angeles

Applications of MRI in Tissue Engineering: Environmental Control and Noninvasive Culture Surveillance

A dissertation submitted in partial satisfaction
of the requirements for the degree
Doctor of Philosophy in Bioengineering

by

Brian John Archer

2021

ABSTRACT OF THE DISSERTATION

Applications of MRI in Tissue Engineering:
Environmental Control and Noninvasive Culture Surveillance

by

Brian John Archer
Doctor of Philosophy in Bioengineering
University of California, Los Angeles, 2021
Professor Song Li, Co-Chair
Professor Louis-Serge Bouchard, Co-Chair

Growth of engineered tissue constructs is dependent on spatiotemporally regulated signals. The optical opacity and dynamic physical properties of developing tissue present a challenge for controlling flow-induced shear distribution in thick, perfused constructs. Tools capable of applying controlled mechanical stimuli throughout engineered tissue constructs and simultaneously obtaining readouts of construct growth have not been developed. The features of magnetic resonance imaging (MRI) that make it clinically suitable; primarily its noninvasiveness, large penetration depth, number of available contrast weightings, and use of non-ionizing radiation; make it worth investigating as a tool for monitoring thick and increasingly complex tissue cultures.

This work presents an MRI compatible, multi-inlet perfusion bioreactor capable of delivering arbitrary flow and, by extension, flow-induced shear patterns throughout 3D tissue constructs by varying flowrates between twelve inlets. Multiple scaffolds were evaluated for mechanical compatibility with the perfusion bioreactor and biocompatibility with endothelial and parenchymal cell lines. Cell population distribution was compared in identical scaffolds cultured under static and patterned perfusion conditions. Diffusion, T_2, and magnetization transfer (MT) MRI weightings were investigated as a means to generate quantitative maps of cell density and viability.

It was found that flow induced shear maps could be calculated in multiple environments from a combination of MRI velocimetry maps, culture chamber geometry, and substrate properties. Several biopolymer hydrogels and macroporous sponges were shown to be mechanically compatible with long term perfusion while promoting sufficient endothelial and parenchymal cell growth. Flow-induced shear patterns within a tissue engineering construct were shown to influence cell distribution. Viable cell density was quantifiable within physiological ranges using diffusion-, T_2-, and MT-weighted MRI. Viability was independently quantified from cell density using a combination of MT- and diffusion-weighted MRI with a multivariate surface calibration.

This work demonstrates the components necessary to achieve the long-term goal of closed loop, flow and shear controlled tissue development. The tools described here can be immediately applied toward determining the relationship between cell population distribution and shear pattern in the centimeter scale, which is a critical piece of information necessary to create a tissue growth control algorithm.

The dissertation of Brian John Archer is approved.

Jacob J. Schmidt

Andrea M. Kasko

Louis-Serge Bouchard, Committee Co-Chair

Song Li, Committee Co-Chair

University of California, Los Angeles

2021

To Amalia who encouraged me to persevere.

TABLE OF CONTENTS

LIST OF FIGURES

LIST OF TABLES

ACKNOWLEDGMENTS

Copyrighted Materials: Chapters 3 and 4 were reprinted from [31, 32] in accordance with IEEE guidelines for reprinting a copyrighted paper in a thesis or dissertation. The IEEE does not endorse any of The University of California, Los Angeles's products or services. Internal or personal use of this material is permitted. If interested in reprinting /republishing IEEE copyrighted material for advertising or promotional purposes or for creating new collective works for resale or redistribution, please go to `http://www.ieee.org/publications\_standards/publications/rights/rights\_link.html` to learn how to obtain a License from RightsLink.

Funding: This work was supported in part by the National Science Foundation during the final year, in part by the National Heart, Lung, and Blood Institute (NHLBI) at the National Institutes of Health (NIH) under Grant 1-R01-HL114086, in part by the NIH award 5 R01 HL114086-03, in part by Ruth L. Kirschstein National Research Service Award T32HL69766, in part by the National Science Foundation OISE through "IRES: Training Next Generation Researchers in Advanced Magnetic Resonance at Chemistry Interfaces" (#1658652), and in part by the German Academic Exchange Service (DAAD) through its Thematic Network "ACalNet" funded by the German Federal Ministry of Education and Research (BMBF).

Additional Acknowledgements: Gratitude is acknowledged to current dissertation committee members: Professors Song Li, Louis-Serge Bouchard, Andrea M. Kasko, and Jacob J. Schmidt; to previous committee members Luisa M. Iruela-Arispe and Linda L. Demer; to colleagues from the Bouchard Lab: Dr. Khalid Youssef, Dr. Jennifer Prado, Till Überrück, Deniz Rall, Denis Wypysek, Robin Möller-Gulland, Martin Kolen, Mathias Clemens Held, Dr. Negin Majedi, Dr. Jeff McCormick, Dr. Nanette Jarenwattananon, Greg Schuette, Thomas Chang, and Dr. Michael Lake; to our collaborator Julia J. Mack; to colleagues from abroad: Martin Wiese, Prof. Dr. Bernhard Blümich, Matthias Wessling, Dr. Meike Emondts, and Prof. Dr. Jürgen Klankermayer; and to undergraduate volunteers:

Amichai Goldsman, Fadi Dahoud, Sara Acosta, Abraham Goldstein, and Russell Nakasone.

VITA

2011–2013	Biology Laboratory Assistant Mellon Lab University of California, San Diego (UCSD)
2012	Analytical Quality Control (QC) Process Development Intern Shire Regenerative Medicine La Jolla, California.
2013	B.S. (Bioengineering (Biotechnology)) UCSD
2014	M.S. (Bioengineering) University of California, Los Angeles (UCLA)
2014–2017	Vascular Biology Training Grant Ruth L. Kirschstein National Research Service Award T32HL69766
2015–2020	Teaching Assistant, Department of Chemistry and Biochemistry, UCLA Taught section of Chem 14BL (General and Organic Chemistry Laboratory I) under direction of Dr. Kristina Wilson, sections of Chem 153A (Biochemistry: Introduction to Structure, Enzymes, and Metabolism) under direction of Dr. Heather Tienson and Dr. Awad Agape, and sections of Chem 153B (Biochemistry: DNA, RNA, and Protein Synthesis) under direction of Professor Guillaume Chanfreau, Professor Albert Courey, and Dr. Heather Tienson
2018	International Research Experience for Students (IRES) summer fellows program, Collaborative research project at RWTH Aachen University

PUBLICATIONS AND PRESENTATIONS

B. J. Archer, J. J. Mack, S. Acosta, R. Nakasone, F. Dahoud, K. Youssef, A. Goldstein, A. Goldsman, M. C. Held, M. Wiese, B. Blümich, M. Wessling, M. Emondts, J. Klankermayer, M. L. Iruela-Arispe, and L.-S. Bouchard. "Mapping Cell Viability Quantitatively and Independently from Cell Density in 3D Gels Noninvasively." *IEEE Transactions on Biomedical Engineering* (2021).

B. J. Archer, T. Überrück, J. J. Mack, K. Youssef, N. N. Jarenwattananon, D. Rall, D. Wypysek, M. Wiese, B. Blümich, M. Wessling, M. L. Iruela-Arispe, and L.-S. Bouchard. "Noninvasive Quantification of Cell Density in Three-Dimensional Gels by MRI." *IEEE Transactions on Biomedical Engineering* 66(3), 821-830 (2018).

K. Youssef, N. N. Jarenwattananon, B. J. Archer, J. Mack, M. L. Iruela-Arispe, and L.-S. Bouchard. "4-d flow control in porous scaffolds: Toward a next generation of bioreactors." *IEEE Transactions on Biomedical Engineering* 64(1), 61-69 (2016).

J. J. Mack, T. S. Mosqueiro, B. J. Archer, W. M. Jones, H. Sunshine, G. C. Faas, A. Briot, R. L. Aragón, T. Su, M. C. Romay, A. I. McDonald, C.-H. Kuo, C. O. Lizama, T. F. Lane, A. C. Zovein, Y. Fang, E. J. Tarling, T. Q. de Aguiar Vallim, M. Vavab, A. M. Fogelman, L.-S. Bouchard, and M. L. Iruela-Arispe. "NOTCH1 is a mechanosensor in adult arteries." *Nature communications* 8(1) 1620 (2017).

Rall, D., Archer, B. Optimized flow control of a multi-channel 3D bioreactor. *ACalNet Workshop*, University of California, Berkeley, April 25, 2015

Abada, E., Archer, B., Fu, M., Gardner, A. An Extracorporeal Artificial Pancreas Design for Insulin-Dependent Diabetics. *59th ASAIO Conference*, June 15, 2013

CHAPTER 1

Introduction

1.1 Tissue Engineering

Severe injury or disease, including end-stage autoimmune disorders, may cause permanent loss of function of whole organs or regions of tissue that ultimately requires treatment consisting of replacement tissue [33–40]. The availability of autograftable tissue is limited, and using it can lead to donor site morbidity [41–43]. Allograft donor tissue is accompanied by the risk of rejection and infectious disease transmission [44–46], and there has been a donor organ shortage that shows no sign of waning [47–49]. Despite the shortcomings, donor tissue continues to remain the "gold standard" of care for patients requiring extensive tissue replacement, and in many cases it is the only treatment option available [33]. Larger quantities of replacement tissue have been sought from multiple sources including interspecies chimeric hosts [50] and *in vitro* engineered tissue constructs. Tissue engineering (TE) is the design of therapies composed of a combination of cells, structural biomaterials, and biochemical factors [51] for the purpose of restoring the natural tissue's lost function [52], thereby reducing the need for donor tissue. Additionally, the development of engineered tissue constructs is incentivized by their potential to serve as model *in vitro* systems applicable to pharmaceutical development and biological research [1].

The specific combination of cells, materials, and factors used to engineer a tissue depends on the application, and not all components are necessarily required to achieve fully restored function. Whereas a cellularized construct is necessary to restore function of a whole organ [53], an acellular scaffold may be sufficient to restore the function of a damaged peripheral nerve [54]. When applicable, acellular scaffolds are ideal because they reduce

the need for donor tissue and the possibility of transplant rejection simultaneously, which was shown to be the case for recombinant human collagen corneal implants [55]. When cells are required, considerations include their source, availability, proliferative capacity, and potency [56].

Some considerations for engineering an *in vitro* tissue model are diagrammed in Fig. 1.1. The TE construct is comprised of cells and a three-dimensional (3D) scaffold structure to which cells attach [52]. Cells can be cultured to synthesize their own scaffold [57–60], seeded on a scaffold prior to implantation [61, 62], or encouraged to migrate into a scaffold from a patient's surrounding tissue post implantation — a process that can be enhanced by impregnating the scaffold with a chemoattractant [63–65]. Cells at multiple stages of differentiation have been seeded on scaffolds prior to implantation, including stem cells, progenitors, and fully differentiated phenotypes [62, 66–68]. Lastly, appropriate environmental conditions and signals are required to cultivate the TE construct to the stage at which it is capable of performing its desired function following implantation. The device that provides the environment, referred to as a bioreactor, can range in complexity from a tissue culture dish to an *in vivo* implantation site [69–73].

1.1.1 Cell Considerations

For a TE construct to function properly, the construct needs to be populated with a sufficient quantity of cells of the correct phenotype.

1.1.1.1 Cell Selection

Multiple cell sources have been investigated for tissue engineering. Autologous cells are preferred for their immunocompatibility with the recipient, but are limited in supply [74]. Allogenic cells have been successfully used in engineered dermal substitutes where they promote wound healing prior to experiencing immune rejection [3]. Progenitors, adult unipotent or multipotent stem cells, and induced pluripotent stem cells (iPSCs) are being investigated in TE applications [3]. Embryonic stem (ES) cells are capable of indefinite self-renewal

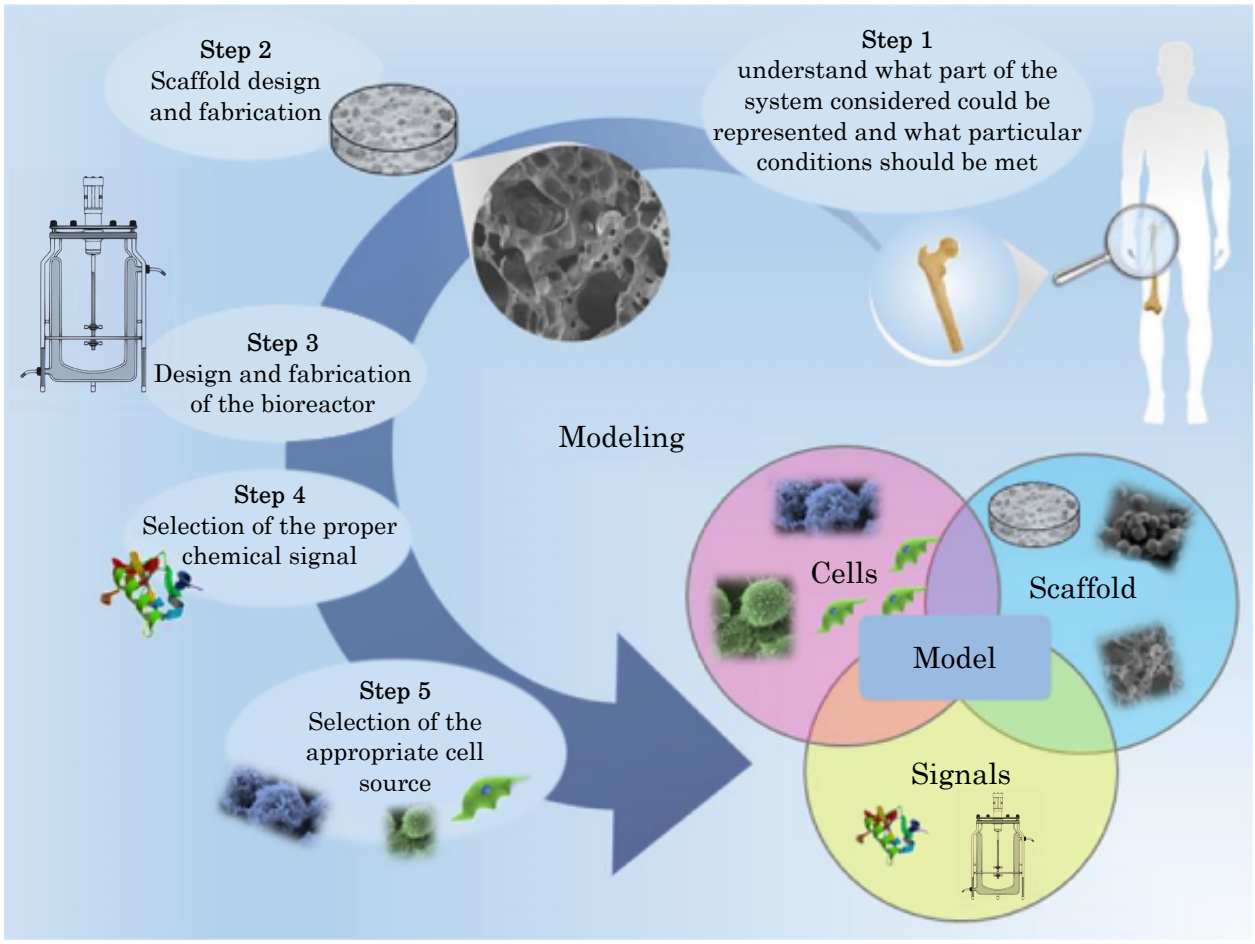

Figure 1.1: **Tissue Engineering Overview.** Diagram highlights the primary considerations for engineering a functional *in vitro* tissue model including the cells, scaffold, and growth environment. © 2017 Caddeo, Boffito and Sartori. Adapted from [1, 2]; originally distributed under the Creative Commons Attribution License. © Jessica Montero Zamora, 2018. Adapted from [2]; originally disbributed under Attribution-NonCommercial-ShareAlike 4.0 International (CC BY-NC-SA 4.0).

and differentiation into nearly every lineage (pluripotency) [3]. These properties make ES cells candidates for *in vitro* expansion followed by differentiation into a desired phenotype once a sufficient quantity has been obtained — a strategy that is currently being clinically tested [3]. One challenge with ES cells is that their potency and self-renewal capacity make them potentially tumorigenic [4]. Adult stem cells are found in every organ system [75], have a limited number of divisions during which they are usable [4], and can differentiate into

a few lineages or a single lineage (multipotent and unipotent, respectively) [3]. Progenitor cells are further differentiated towards a specific lineage and cannot renew themselves indefinitely [75]. The harvesting and expansion of autologous stem or progenitor cell populations has been successfully implemented in a few dermal and cartilage TE products [3]. Most research on stem cell harvest, isolation, culture, and differentiation has been done on adult stem cells and progenitors due to ethical concerns and reduced tumorigenic risk, but recent advances in ES cell culture technology suggests their future use in TE products is likely [3].

Fully differentiated adult somatic cells, which are typically only capable of a limited number of divisions and incapable of further differentiation, have been genetically reprogrammed into iPSCs [76,77]. This potentially circumvents the limited supply of other stem cells, given the abundance of fully differentiated adult cells. Research is being done to reduce the T cell-mediated immune response observed when transplanting autologous iPSCs [4]. Additionally, research is being done to induce multipotent or unipotent cell lines from fully differentiated cells to circumvent the need for early stage differentiation that is required when cells are dedifferentiated to the pluripotent state [3].

1.1.1.2 Cell Behavior

When assessing tissue growth and developing analytical methods to probe it, cell proliferation, migration and differentiation are cell behaviors of interest, which, if measured, could provide useful biological insights into the final cellular content and functional capacity [52,78]. Environmental parameters which influence these behaviors are summarized in Table 1.1.

Table 1.1 demonstrates that individual environmental cues have been shown to influence multiple cell behaviors. For example, substrate stiffness influences all behaviors listed in the table [89]. Additionally, multiple types of stimuli have been shown to influence a single type of behavior. For example, differentiation is influenced by scaffold composition [79, 97, 98], soluble factors [96, 99], substrate stiffness [89], surface roughness [88, 96], electrical stimulation [95], substrate topography [88], surface chemistry [86], hydrostatic pressure [94], and shear stress [91, 92]. Scaffold composition refers to the materials comprising the scaf-

Table 1.1: Cell Behaviors.

Behavior	Behavior Measurement	Environmental Cues
Proliferation	time course cell counts [79], MTT Assay [80], XTT Assay [81]	Soluble factors [82–85], substrate topography [86–88], substrate stiffness [89], Shear Stress [90–93], surface chemistry [86], surface roughness [88], hydrostatic pressure [94], electrical stimulation [95]
Differentiation	Cell lineage marker expression [79, 96]	Scaffold composition [79, 97, 98], soluble factors [96, 99], substrate stiffness [89], surface roughness [88, 96], electrical stimulation [95], substrate topography [88], surface chemistry [86], hydrostatic pressure [94], shear stress [91, 92]
Migration	Individual cell tracking [100], scratch wound healing assay [101]	Electrical stimulation [95], stiffness gradient [89], hydrostatic pressure [94], soluble gradient [102, 103], shear stress [90]
Adhesion	Integrin expression [79], centrifugation assay [79, 104], optically evaluated morphology [79, 96]	Scaffold composition [79], surface chemistry [86, 96, 103], surface roughness [88, 96], substrate stiffness [89], shear stress [105]
Cell alignment	Optical microscopy and image analysis software [106–108]	Electrical stimulation [95, 106], surface topography [87, 109], shear stress [93, 109, 110], substrate stiffness [89]

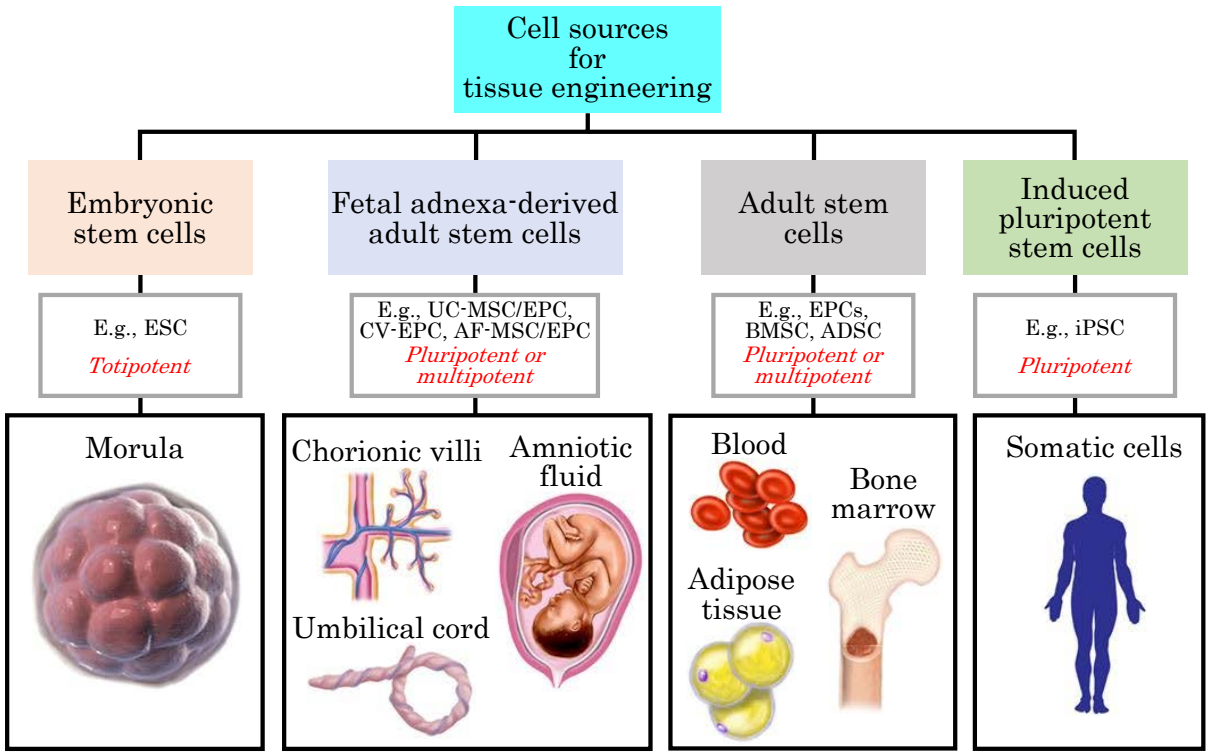

Figure 1.2: **Cell Sources for Tissue Engineering.** Reprinted from [3], Copyright (2020), with permission from Elsevier. Adapted from [4]; originally distributed under the Creative Commons Attribution License (CC BY).

.

fold. Soluble factors are dissolved molecules including growth factors, small molecules, and cytokines [111]. Roughness is a measurement of micro-irregularities formed by peaks and valleys on a material's surface [112]. Electrical stimulation refers to the flow of electric current through a material [95].

The stimuli listed in Table 1.1 have been applied in a variety of ways to induce different behavioral responses. Topography refers to the patterned placement of surface features such as chemical modifications, grooves, and holes. Surface chemistry refers to molecular modification including integrin adhesion molecules, ion implantation, self-assembled monolayers, polymer brushes, functional groups, etc. The geometrical parameters of the topographic features (width, depth, spacing, etc.) are known to contribute to cell behavior [86, 87]. Scaffold topography has been used to influence chondrocytes, endothelia, epitena, epithe-

lia, fibroblasts, leucocytes, lymphocytes, macrophages, mesenchyme, neurons, osteocytes, oligodendrocytes, smooth muscle cells, and tumor cells [87]. Electrical stimulation has been applied to cells by direct coupling, capacitive coupling, and inductive coupling; in monophasic and biphasic patterns; and as sinusoidal, square, triangular, and saw tooth waveforms to induce varying cell responses [95]. Surface roughness is modulated by blasting, electro polishing, nanofiber formation, chemical treatment, photolithography, electron beam lithography, dip-pen nanolithography, imprint lithography, and colloidal lithography [88]. Surface roughness has been shown to influence behaviors such as adhesion, cytokine release, and gene expression [88].

Migration cues shown in Table 1.1 applied homogenously throughout a cell culture have been used to alter cell motility, or the rate at which a cell moves randomly along its substrate [102]. An example is matrix density. Cell motility is known to peak at an optimal matrix density. Increasing the density of matrix fibers and, consequently, adhesion points in a homogenous matrix beyond the optimal amount reduces cell motility due excessive adhesion forces a cell must overcome. Decreasing the matrix density below optimal levels can also reduce cell motility by preventing cells from gaining traction [113]. Directed migration has been induced through asymmetric environmental cues, or gradients, and is defined by the type of cue inducing the directional migration: chemotaxis for soluble signals, haptotaxis for surface chemistry, galvanotaxis (electrotaxis) for electrical potential, and durotaxis for mechanical signals [102, 103]. Multiple simultaneous environmental gradients may be present, and their combined influence on cell migration is not always simply additive. Instead, complicated, cell-type dependent signal hierarchies and interdependencies factor into cell migration behavior [102]. Behaviors are also dependent on cell type. For example, smooth muscle cells align perpendicular to the direction of applied shear stress compared to endothelial cells, which align themselves parallel [114].

Multiple classes of stimuli applied simultaneously have been shown to have cooperative influences on cell behavior. A combination of inductive coupling with a high sulfated hyaluronan derivative substrate was used to synergistically stimulate mesenchymal stem cells (MSCs) toward osteogenic differentiation [95]. There is evidence that soluble factors and

integrin adhesion receptors cooperatively regulate cell cycle, influencing the rate of proliferation [115]. Shear stress and matrix stiffness cooperatively influence endothelial elongation and intercellular junction tightness [116].

Beyond simply populating the scaffold, additional cell behaviors indicative of a functional engineered tissue include proper cell morphology, patterns of gene and protein expression, and metabolic function [117–122]. Combinations of multiple types of cell behavior are required for proper morphogenesis, or the formation of larger, multicellular structures such as tissue functional units [52].

The type of behavior a cell demonstrates is dependent on the cell's intrinsic biology (cell type) as well as environmental conditions, the latter featuring more prominently within the scope of tissue engineering [78, 117–119]. Environmental conditions include the chemical constituents and mechanical stresses present in a cell's microenvironment, both of which can be presented to cells in a controlled manner through scaffold and bioreactor design [123–126]. The following sections will discuss some ways by which a cell's 3D environment can be influenced and controlled through the bioreactor's inputs and the scaffold properties.

1.1.1.3 Flow and Shear Promote Vascular Morphogenesis

Flow induced shear is a shear stress generated at a boundary, such as the surface of a solid, by a fluid moving in relation to that boundary. It can be generated by flow past protein fibers inside a biopolymer hydrogel matrix or by flow over the surface of a hydrogel. Both flow and shear have been shown to impact endothelial cell behavior, and the specific effects of shear can depend on parameters such as flow direction, quantity of shear, and chemical signals [127–129]. This section will briefly describe examples of ways in which shear or flow can impact vascular morphogenesis. One example is that interstitial flow — or flow through extracellular matrix — at a velocity of 10 μm $\cdot$s^{-1} has been shown to promote the formation of multicellular networks of branched, lumen-containing structures in a process resembling neovascularization *in vitro* compared to static culture [130]. Another example is that the quantity of wall shear stress over a monolayer of endothelial cells has been shown to promote angiogenic sprouting

in terms of the total number of sprouts formed and the depth to which they penetrate the underlying matrix [127]. Also, there is an optimal quantity of shear for promoting angiogenic sprouting, above or below which the behavior is less pronounced [127]. Interstitial flow has been shown to work in conjunction with VEGF to promote formation of larger (higher numbers of cells/structure) and more densely packed branched, lumen containing structures [128]. When two prefabricated, endothelial-seeded channels are adjacent to each other, angiogenic sprouting into the space between channels has been shown to be dependent on the direction of interstitial flow between the channels, the quantity of wall shear in either channel, and the distribution of VEGF (concentration gradient or uniform) between channels [129]. It has also been shown that the spatial distribution of transmural shear corresponds to spatially distinct patterns of endothelial vascular morphogenesis [19]. Finally, it has been demonstrated that the timing, or temporal pattern, of applied shear stress can modulate the intracellular Ca^{2+} response in endothelial cells, a response which is known to influence cell behaviors that promote vascular morphogenesis [131, 132].

1.1.2 Scaffold Design

When engineering tissues, it is common practice to seed cells in a scaffold [52]. Scaffolds provide a high surface area matrix that is mechanically sound, enabling dispersion of cells in 3D space at a given cell concentration (high enough to promote cell-cell interactions, but low enough to avoid overcrowding), while supporting the growth of cells under quasi-immobilized conditions [133,134]. The growth of cells requires continuous exchange of soluble factors (O_2, growth factors, nutrients, metabolic byproducts, etc.) [135]. Hence, placing cells in a scaffold of the right porosity and mechanical strength is necessary to ensure delivery and removal these vital supplies and wastes via transport [134]. Without a 3D scaffold, cells are typically unable to grow over extended periods, since they eventually crowd their substrate as a monolayer and begin to experience contact inhibition, making it impossible to generate thick tissue. [136].

Scaffolds provide an engineered tissue with its initial support and influence cell behav-

ior [52]. Cell behavior has been shown to depend on mechanical, chemical, and architectural scaffold properties such as stiffness, density and type of attachment points, crosslink density/mesh size, and macropore size [124, 137–142]. Some scaffold properties (attachment points, stiffness, and topography) and cell behaviors which are influenced by these properties (proliferation, differentiation, spreading and migration) are diagrammed in Fig. 1.3. Matrix stiffness refers to the material's resistance to deformation, which is characterized by the elastic modulus. An example of the influence of stiffness on cell behavior is the dependence of fibroblast motility and focal adhesion organization on polyacrylamide gel stiffness [143]. The elastic modulus of natural tissue spans from a few hundred pascal (brain, liver) to over ten gigapascal (bone) [89, 144]. Cells respond to mechanical stimuli in the environment, including matrix stiffness, shear force, or tension or compression applied directly to a scaffold by a mechanism called mechanotransduction [145]. Mechanical stimuli are transduced into biochemical pathways through a mechanically sensitive structure, such as the cytoskeleton or a mechanically sensitive ion channel, that undergoes a conformational change in response to the stimulus [145]. Mechanical stimuli present in the scaffold are transmitted to the F-actin cytoskeleton by heterodimeric transmembrane receptor proteins called integrins [146]. Following ligand binding, integrins spaced within 70 nm of each other recruit additional proteins which cluster into a larger structure called a focal adhesion [146]. This clustering improves mechanotransduction robustness, and it is dependent on ligand density since multiple, closely-spaced integrins must bind to their ligand for clustering to occur [146].

Scaffolds can be made from a variety of uniform or hybrid materials ranging from biopolymers such as proteins and glycosaminoglycans (GAGs) to completely synthetic polymers to bioceramics [52, 147, 148]. A list of TE scaffold materials is shown in 1.2 with some of their advantages and disadvantages.

Scaffold materials listed in Table 1.2 need to have appropriate structural and chemical features in order to successfully perform as a TE scaffold. For example, a titanium orthopedic implant with a porous surface promotes bone ingrowth into the metal scaffold, and the amount of ingrowth depends on pore size [164]. A polished titanium surface does not allow any ingrowth, and hence does not function as a TE scaffold [165]. Another example of

Table 1.2: Summery of materials and techniques used to fabricate tissue engineering scaffolds. Adapted from [29]; originally distributed under the Creative Commons License (CC BY). HAp: Hydroxyapatite; β-TCP: beta-Tricalcium Phosphate; PLGA: poly(D,L-lactic-glycolic acid); PCL: polycaprolactone; PEO: poly(ethylene oxide); PPF: poly(propylene fumarate)

Material Category	Example Materials	Fabrication Methods	Advantages (+) and limitations (–)	References
Metals	NiTi, titanium alloy, magnesium alloy, porous tantalum	3D Printing, casting, powder sintering	+ High young's modulus + High compressive strength – Not degradable – Ion release	[149–152]
Ceramics	TiO_2, HAp, β-TCP, Bioglass	3D Printing, sol-gel, selective laser sintering	+ Chemically biocompatible + Can be biodegradable – Brittle – Prone to fracture and fatigue	[153–157]
Natural polymers	Collagen, chitosan, hyaluronic acid, silk fibroin	Hydrogel crosslinking, electrospinning, freeze drying, solvent displacement	+ Biocompatible + Biodegradable + Osteogenic – Low mechanical strength	[158–160]
Synthetic polymers	PLGA, PCL, PEO, PPF	Electrospinning, crosslinking	+ Tunable properties – Acidic degradation byproducts – Rapid strength degradation *in vivo*	[161–163]

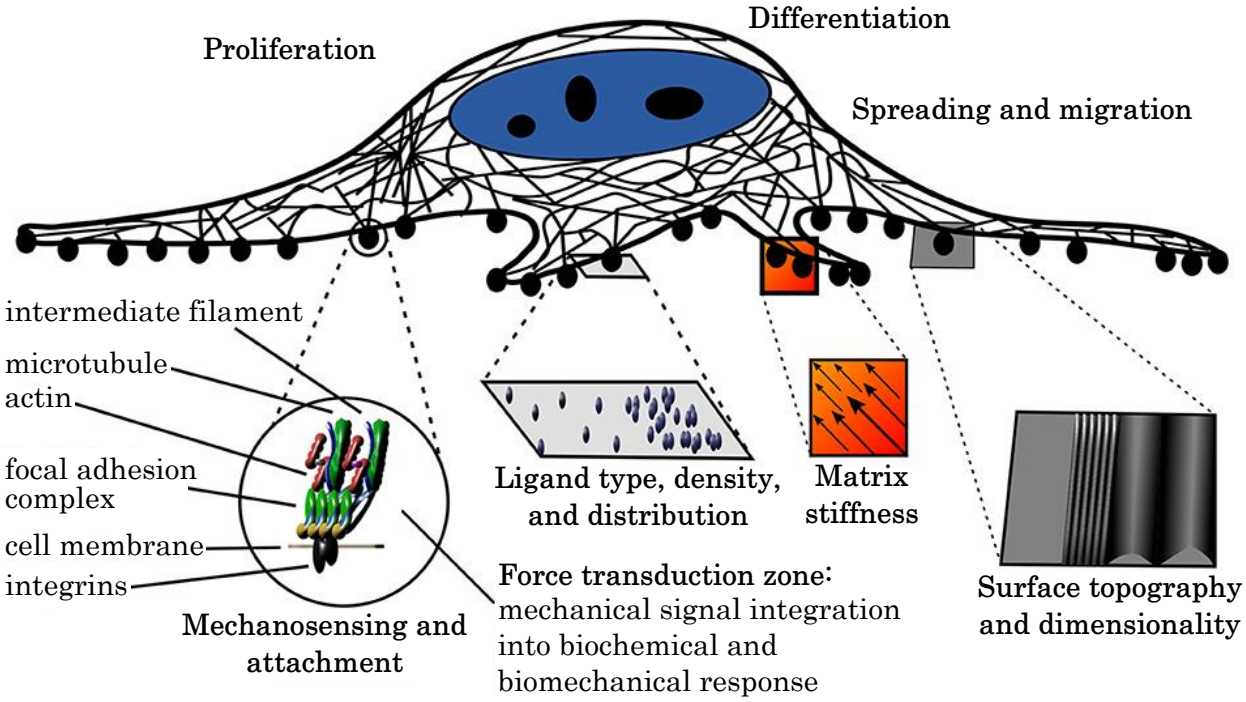

Figure 1.3: **Scaffold Properties that Influence Cell Behavior.** Properties include the arrangement of cell attachment points, the scaffold stiffness, and the surface topography. © 2019 Hickey and Pelling. Adapted from [5]; originally distributed under the Creative Commons Attribution License.

.

a scaffold material requiring modifications is a poly(ethylene glycol) diacrylate (PEGDA) hydrogel. Alone this material does not promote human umbilical venous endothelial cell (HUVEC) attachment or spreading, but when it is chemically modified to include Arg-Gly-Asp (RGD) peptides, HUVECs adhere and spread [148]. Fig. 1.4 (a) shows an example RGD modification.

Structural features of TE scaffolds, such as, molecular chains, pore size, and macroscopic geometry have been engineered over a range of size scales [147, 166–170]. A selection of scaffold modifications spanning this scale is shown in Fig. 1.4. Molecular level scaffold modifications include polymer chain, cell adhesion point, and crosslinker design [167, 171, 172]. A controllable, cell behavior-influencing scaffold structural property is hydrogel mesh size, loosely defined as the distance between chain crosslinks, range from a few to hundreds of

nanometers [173, 174]. Mesh size has been controlled by crosslink structure and chain size, examples of which are shown in Fig. 1.4 (c). The following is an example of mesh size influencing cell behavior: smooth muscle cell RhoA signaling and metabolic activity were shown to correlate with PEGDA mesh size ranging from ∼3.2 nm to 13 nm [175]. Hydrogel stiffness, another cell influencing hydrogel property, is known to depend on hydrogel mesh size [176]. Pore size, shown in Fig. 1.4 (d-f) influences cell behavior. Example: osteoblast detachment from collagen-GAG scaffolds was shown to be inversely proportional to pore size under perfusion [177]. Porogenation techniques are used to introduce macroporous structures (defined as pore sizes larger than 50 nm) up to hundreds of micrometers in diameter [178, 179]. Note: the terms pore size and mesh size are sometimes interchangeably used in the literature to refer to the spacing between polymer backbones, especially in the cases of biopolymer hydrogels, which naturally form larger meshes with physical crosslinking [171, 180–182]. Another type of scaffold property controlled in tissue engineering is macroscopic scaffold geometry, examples of which are shown in Fig. 1.4 (g) and (h). An example of a macroscopic geometric modification is channel patterning, or the direct placement of open channels throughout a scaffold. Channels are introduced as a template for cellular organization and to promote oxygen and nutrient transport by mimicking a vascular network [183]. Channel patterning and other topographical modifications can range in size from a few microns up to the centimeter scale in order to promote cell organization and nutrient delivery over large tissue volumes [183–185]. One example of why macroscopic topographical modifications are of interest is because they were shown to influence flow and shear patterns when subjected to perfusion [168]. Macroscopic control over scaffold geometry and environmental stimuli is important to properly culture cell populations filling large tissue volumes, which are needed to address large volumes of tissue loss due to injury or illness.

The final scaffold parameter that will be discussed in this introduction is degradation. Scaffolds provide an initial support for cell growth, but gradually they are broken down and replaced by new tissue growth, preventing a long-term foreign body response and eliminating the need for surgical removal of a foreign material post implantation [134]. The rate of degradation and the byproducts of degradation — whose concentrations are dependent on

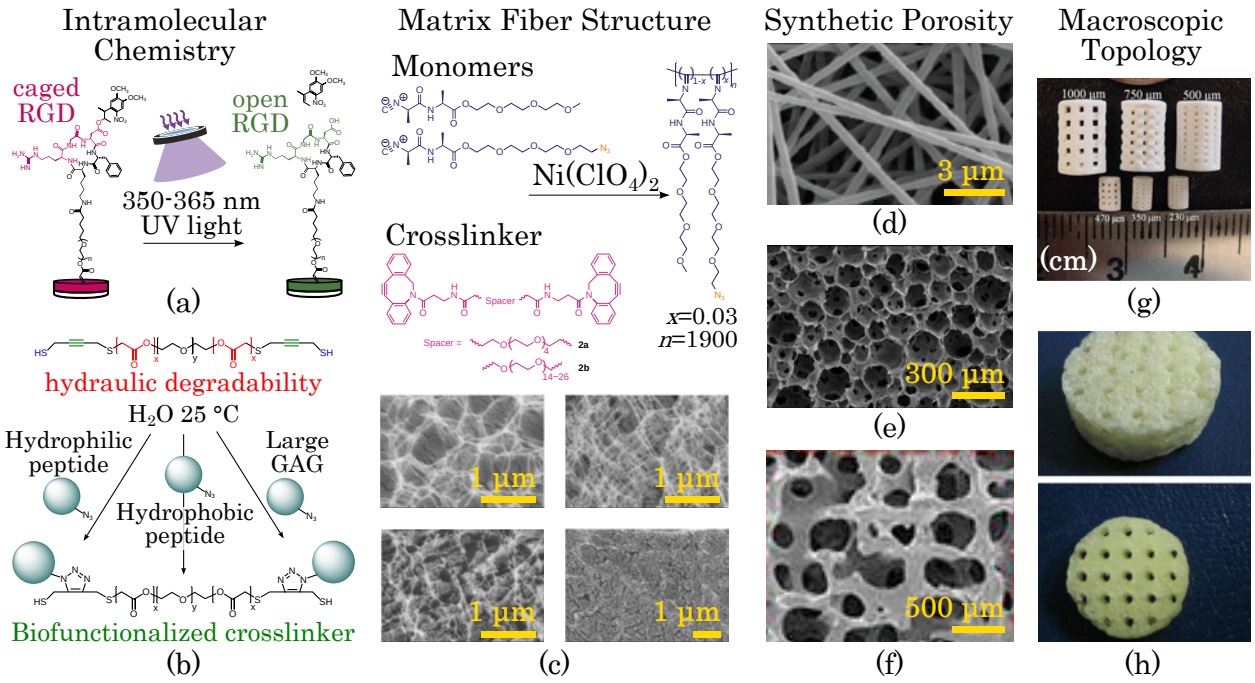

Figure 1.4: **Scaffold Engineering.** Examples of scaffold engineering over several size scales from intramolecular modifications (including the addition of cell attachment points and crosslinker design) to macroscopic topology. (a) Reprinted by permission from Springer Nature Customer Service Centre GmbH: Springer Nature, Nature Materials [6], © 2015. (b) © 2019 Guo et al. Adapted from [7]; originally distributed under the Creative Commons Attribution Non Commercial License 4.0 (CC BY-NC). (c) © 2018 Schoenmakers et al. Adapted from [8]; originally distributed under the Creative Commons Attribution 4.0 International License. (d) © 2016 Zagho et al. Adapted from [9]; originally published under the Creative Commons Attribution 3.0 Unported License. (e) and (h) Adapted from [10] with permission from Taylor and Francis, © 2010 Taylor and Francis (`www.tandfonline.com`). (f) © 2013 Korean Academy of Periodontology. Adapted from [11]; originally distributed under the Creative Commons Attribution Non-Commercial License 3.0.

degradation rate — have been shown to influence cell growth and viability [186]. It is desired for the rate of degradation (rate of material loss) to match the rate of new tissue growth [187]. Scaffolds have been engineered to degrade by multiple mechanisms — including hydrolysis, oxidation, and photochemistry — which depend on scaffold material design elements such

as functional groups, water uptake, and copolymer composition [187]. In addition, scaffold degradation depends on environmental conditions such as pH and the presence of hydrolytic enzymes that catalyze hydrolysis of polymers [187]. An example enzyme involved in degradation is collagenase, a matrix metalloproteinase (MMP) that catalyzes the hydrolysis of collagen, a natural biopolymer that has been used in TE scaffolds [148].

1.1.3 Justification for Perfusion Bioreactor Design

Bioreactors are designed to provide cells or tissue with environmental controls and signals that help maintain homeostasis and regulate cell behaviors (examples of which are covered in previous sections) [188, 189]. In the context of tissue engineering, the minimum requirement of the bioreactor is to control a culture's temperature and pH, provide the cells with sufficient nutrients, and prevent the buildup of metabolic waste products [69, 190]. Nutrient delivery and waste management are challenges in 3D tissue culture both pre and post implantation due to the 100-200 μm diffusion limit of molecular transport within the interstitial space of a scaffold. This can limit the maximum achievable cell density and viability at further distances from the scaffold surface (see Fig. 1.5) [12, 191]. Figure. 1.5 shows scaffolds cultured under static conditions. One scaffold was suspended in media on a needle and four repeated scaffolds were allowed to settle on the bottom surface of the culture dish. Figure. 1.5 (a) shows oxygen concentration measured throughout the scaffold starting from the top surface using a dissolved oxygen probe. Figure. 1.5 (b) is a live/dead stain of cell viability throughout a scaffold. The red cells are nonviable and the green cells are viable. Figure. 1.5 (c) shows cell viability quantified at certain distances from the top surface of the scaffold cultured on the bottom of the dish. Figure. 1.5 (d) shows cell density quantified at certain distances from the top of the same scaffold. In addition to the basic requirements for cell survival and maintenance, bioreactors may be configured to provide and control environmental signals that are unique to the cell or tissue being cultured [70]. Environmental signals may include chemical, mechanical, electrical, or photo stimuli [70, 192]. Chemical stimuli can include dissolved molecules that influence cell behavior, such as cytokines, growth factors, hormones, and small molecules [111, 193, 194]. Specific examples of chemical stimuli include insulin,

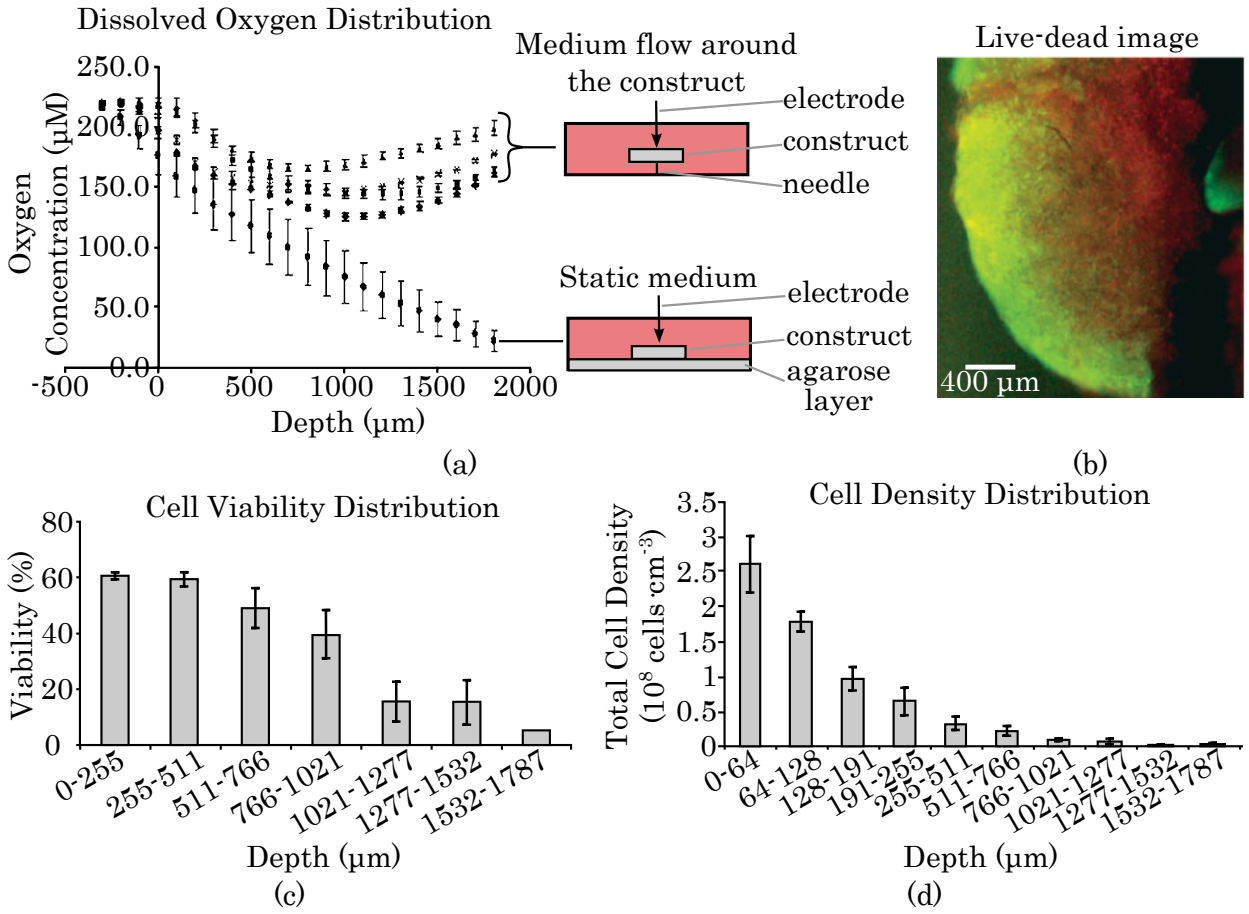

Figure 1.5: **Cell Dependence on Nutrient Diffusion Limit.** Cellular metabolism depletes oxygen throughout a construct surrounded by nutrient rich media. Diffusion of oxygen into the scaffold from the surroundings is only capable of sustain large numbers of viable cells near the scaffold surface. At steady state, oxygen concentration, cell density, and cell viability are functions of distance from the scaffold surface. Adapted from [12] with permission, © 2005 Wiley Periodicals, Inc.

transferrin, prolactin, triiodothyronine, bone morphogenetic protein-2 (BMP-2), vascular endothelial growth factor, fibroblast growth factors (FGF-2, FGF-4, FGF-6), hepatocyte growth factor (HGF), hepatic stimulatory substance (HSS), and heparin-binding epidermal growth factor-like growth factor (HB-EGF) [111, 194]. These molecules have roles in many different biological processes including cell differentiation, angiogenesis, wound healing, and tumor growth [195–198]. Mechanical stimuli provided by bioreactors include fluid flow in-

duced shear, hydrostatic pressure loading, and compressive and tensile forces externally applied to a tissue [69, 70, 190, 199, 200]. The response of cells to mechanical stimuli was covered in previous sections.

Some examples of mechanical bioreactors are shown in Fig. 1.6 (a). Spinner flask bioreactors are vessels in which cell culture media is continuously mixed with a submerged impeller, and scaffolds are suspended in the media by skewering them on a submerged metal rod [201]. In this environment, mass transport is driven by convection, and shear stress is relatively high compared to the other bioreactor designs shown. The shear forces are heterogeneously distributed throughout the scaffold, which can cause nonuniform tissue development [201]. One application particularly suited to spinner flask bioreactors is dynamic cell seeding, or the constant agitation of a cell suspension in which a scaffold is mounted. This type of seeding facilitates a high percentage cell attachment [202]. A rotating wall bioreactor is a chamber between two concentric cylindrical walls in which the outer wall is continuously rotated about its axis, generating laminar flow and lower levels of shear than a stirred tank bioreactor. During culture, the sedimentation velocity of the TE construct becomes equal in magnitude and opposite in direction to velocity of the fluid — a state referred to in literature as "free fall" [13]. This environment generates more uniform cell proliferation and protein expression throughout a construct than in stirred tank bioreactors because the shear distribution is more uniform, but in thicker constructs nutrient transport to the core can be limited [201]. This type of bioreactor has been explored as an option for culturing engineered cartilage and skin as well as 3D cell aggregates [201, 203]. A perfusion bioreactor is a device that forces cell culture media through the pores of a scaffold. This mechanism facilitates the transport of nutrients and wastes throughout the core and periphery of a cell-seeded TE construct. A potential drawback of perfusion bioreactors is that the pores may form a few paths with low resistance to fluid flow, especially when using scaffolds with a wide pore size distribution. This can cause the majority of fluid to pass through a reduced fraction of the total volume, leading to inhomogenous nutrient and shear distribution within a construct [201]. In this environment, nutrient and waste exchange can be driven by both convection and diffusion. Shear forces generated in a perfused scaffold are intermediate compared to stirred tank and

rotating wall bioreactors. Perfusion bioreactors have been used for generating environments physicochemically similar to many tissue types including intestinal, bone, cartilage, and arterial [201]. In a perfusion bioreactor, cell culture media provided to cells can be contained in a reservoir separately from the culture chamber and continuously circulated through the culture chamber until nutrients become depleted and metabolic byproducts concentrate to toxic levels [204–207]. The volume of the media reservoir can be ~ 100 times greater than the volume of a static culture dish, enabling continuous circulation for multiple weeks when compared to static dish culture, which requires media replacement every 2–3 days [204]. Since metabolic byproducts are acidic, a colored pH indicator is commonly used to determine when to replace cell culture media [207]. In compression bioreactors, a motorized piston applies a static or dynamic compressive load directly to a construct housed in a chamber. This bioreactor is designed to condition engineered tissue that experiences compressive loading *in vivo*, such as bone [13].

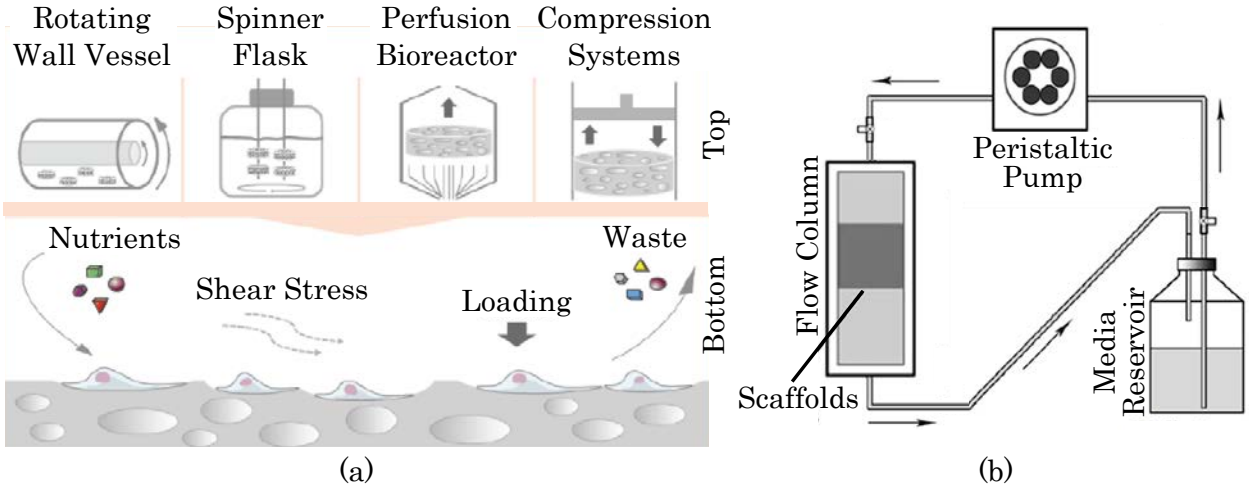

Figure 1.6: **Mechanical Stimuli Bioreactors.** (a) Top: Examples of bioreactors designed to apply mechanical stimuli to TE constructs. Bottom: Types of homeostatic maintenance and mechanical forces that are governed by bioreactor design. © 2014 Sladkova et al. Adapted from [13]; originally published under the Creative Commons Attribution 3.0 license. (b) Schematic of simple perfusion system. © 2014 Wang et al. Adapted from [14]; originally published under the Creative Commons Attribution license.

In 3D biological environments, the maximum distance across which sufficient O_2 can diffuse to sustain a population of cells, referred to as the diffusion limit, is approximately 100–200 μm, which is also the maximum distance between capillaries *in vivo* [208]. Cell density and viability drop beyond this distance, limiting the thickness of statically cultured, avascular TE constructs [12]. To overcome the diffusion limit *in vitro*, fluid flow is employed to efficiently deliver nutrients and remove wastes from 3D cell and tissue cultures via convection [52, 69, 70, 190]. A comparison of the oxygen concentration profile within a construct limited to diffusive transport and a construct subjected to interstitial perfusion is displayed in Fig. 1.7. In addition to increasing nutrient exchange, fluid flow introduces shear forces. Therefore, both the chemical and mechanical stimuli in a cell's microenvironment are dependent on fluid flow [15, 69, 209]. Some of the effects of introducing fluid flow are indicated in Fig. 1.6 (a). Convective transport can be generated by spinning impellers or bubbling gas within bioreactors or by continuously shaking, rocking, or rotating them [69, 70, 190]. It can also be generated with pump driven flow through a scaffold in a fluid flow path, a process analogous to perfusion [69, 70, 190, 200], which will be the primary type of convective transport examined in this work. Figure 1.6 (b) diagrams a bioreactor perfusion circuit. In this diagram a peristaltic pump circulates cell culture media from a reservoir through a flow column in which the construct is mounted.

The *in vivo* environment post implantation must be considered when engineering a tissue. In some situations, it may be desired to engineer a tissue to replace a naturally vascularized tissue. Vascularized tissue is supplied with nutrients from the body's circulatory system [208]. Because engineering vascular networks *in vitro* has been a challenge, attempts have been made to engineer thin, avascular tissue constructs to replace portions of naturally vascularized tissue [210]. In this work, avascular engineered tissue refers to an engineered tissue without a vascular network. An avascular engineered tissue may be designed to replace a naturally vascularized tissue type or avascular tissue such as cartilage. When designed to replace naturally vascularized tissue, an avascular engineered tissue can potentially be vascularized *in vivo*, post-implantation by ingrowth of host vessels [191]. For an avascular engineered tissue to take advantage of the body's circulatory system, it must promote rapid

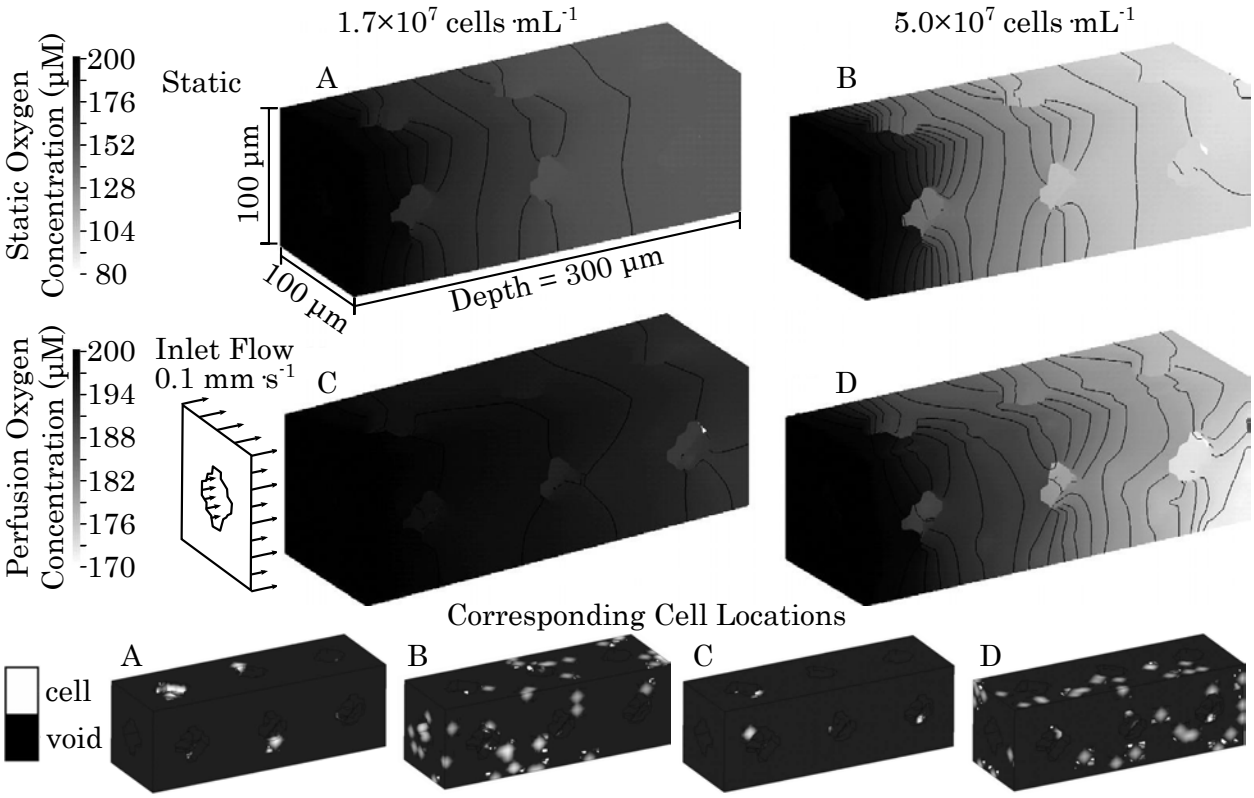

Figure 1.7: **Model of Diffusive Versus Convective Oxygen Transport into TE Construct.** The four large volumes labelled A-D are contour maps of dissolved oxygen concentration modelled in liquid phase cell culture media filling the void space of solid, macroporous, cell-seeded scaffolds that were cultured statically (top) and under perfusion (bottom). Cell growth was modelled over time, and O_2 concentration contour maps were taken at time points when cells reached densities of 1.7 (left) and 5.0 (right)$\times 10^7$ cells$\cdot$mL^{-1} (50 and 150 total cells per volume shown, respectively). Cells were modeled as discreet points with maximum consumption rates of 4×10^{-7} nmol$\cdot$cell$^{-1}\cdot$s^{-1}. The smaller volumes below show exact cell locations corresponding to each contour map A-D. Flow into the construct maintains higher higher oxygen concentrations further from the surface. Adapted from [15] with permission from Taylor and Francis, © 2007 Taylor and Francis.

angiogenesis into the construct, minimizing the time during which the core of the construct experiences hypoxia. If the construct is too thick for angiogenic sprouting to reach the construct core quick enough, the construct must be prevascularized with its own robust vascular

network that can reliably connect to the patient's vasculature in the vicinity surrounding the implantation site [183, 191, 211, 212]. Two example methods for growing vascularized TE constructs are synthetically constructed scaffold structural elements and cell mediated vascular morphogenesis.

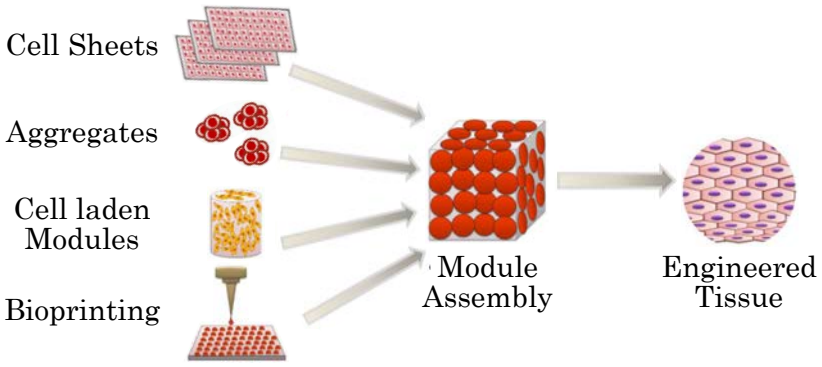

Figure 1.8: **Modular Assembly.** Diagram showing TE subunits that can be combined in the process of modular assembly. Cell sheets are single or multiple layers of cells adhered to each other via cell-cell junctions [16]. Cell aggregates are clumps of cells adhered to each other via cell-cell junctions [17]. Cell laden modules can be cells encapsulated in a hydrogel [18]. Adapted from [18]; originally distributed under the Creative Commons License (CC BY).

Channel patterning, porogenation, and assembly of modular scaffold units are methods by which synthetic scaffold structure and geometry are constructed to generate perfusable vasculature [183,185,191,211,212]. Channels can be formed using techniques such as bioprinting—layer by layer deposition of cells and biopolymer gel; photolithography; soft lithography; or templates made from microneedles, fibers, or polyvinyl alcohol [183–185, 211, 212]. Specific methods of porogenation, or the process of introducing pores, include particle leaching, lyophilization, gas foaming, liquid-liquid immiscibility, or electrospinning [185, 191]. Modular assembly is the construction of a scaffold from smaller, prefabricated building units. An example of a modular scaffold unit is a hydrogel bead containing parenchymal cells encapsulated in the matrix, evenly distributed throughout the bead. A bioreactor culture chamber can be filled with these units in a packed bed fashion which leaves spaces between the beads open as void space to allow fluid flow [18]. In addition to encapsulating parenchymal cells throughout the 3D volume of the beads, endothelial cells can be seeded on the bead surfaces

after the beads have gelled. A perfusion bioreactor densely packed with these units generates a situation in which the void space between the beads resembles endothelial lined flow paths [183, 185, 213]. Examples of modular units used to assemble larger engineered tissue are shown in Fig. 1.8.

Types of biologically induced blood vessel formation, or cell mediated vascular morphogenesis, relevant to this work include endothelial mediated angiogenic sprouting and neovascularization (also referred to as postnatal vasculogenesis in some literature [212]). Angiogenesis is the process by which new vasculature forms from existing vascular structures [191, 211, 212]. A process resembling angiogenic sprouting is observed *in vitro* when endothelial cells in a monolayer covering the surface of a matrix — whether it be a flat surface normal to gravity or a round channel — begin to migrate into the scaffold and form an endothelial lined lumen [19, 127, 129, 214, 215]. Neovascularization is the formation of new vascular structures without the presence of preexisting structures [191,211,212]. Processes resembling neovascularization have been observed *in vitro* when endothelial cells encapsulated within the bulk of a biopolymer gel spontaneously rearrange to form endothelial lined lumen [128,130]. When a prevascularized construct is implanted, its vascular network connects with the host vasculature at the interface of the implant site in a process called anastomosis, which takes about 14 to 48 days [216].

In order to promote vascular morphogenesis, the effect of soluble chemical signals [191, 211] and mechanical stimuli on cell behavior must be understood and properly utilized. This includes combined effects of multiple stimuli and the effects of spatiotemporal inhomogeneity [185, 212]. Specifically, spatiotemporal control over vascular endothelial growth factor (VEGF) is known to be able to promote angiogenesis [217]. Important to this work is the impact of fluid flow induced shear on vascular morphogenesis. Flow induced shear is a shear stress generated at a boundary, such as the surface of a solid, by a fluid moving in relation to that boundary. A shear stress is a stress generated by force applied parallel to a material's cross-sectional area. Higher flow rates, which generate wall shear stresses of 2-20 dyn·cm^{-2} in vascular lumen, have been shown to influence endothelial cell morphology and angiogenic sprouting [19, 127, 129, 214, 215]. The shear caused by interstitial and transmu-

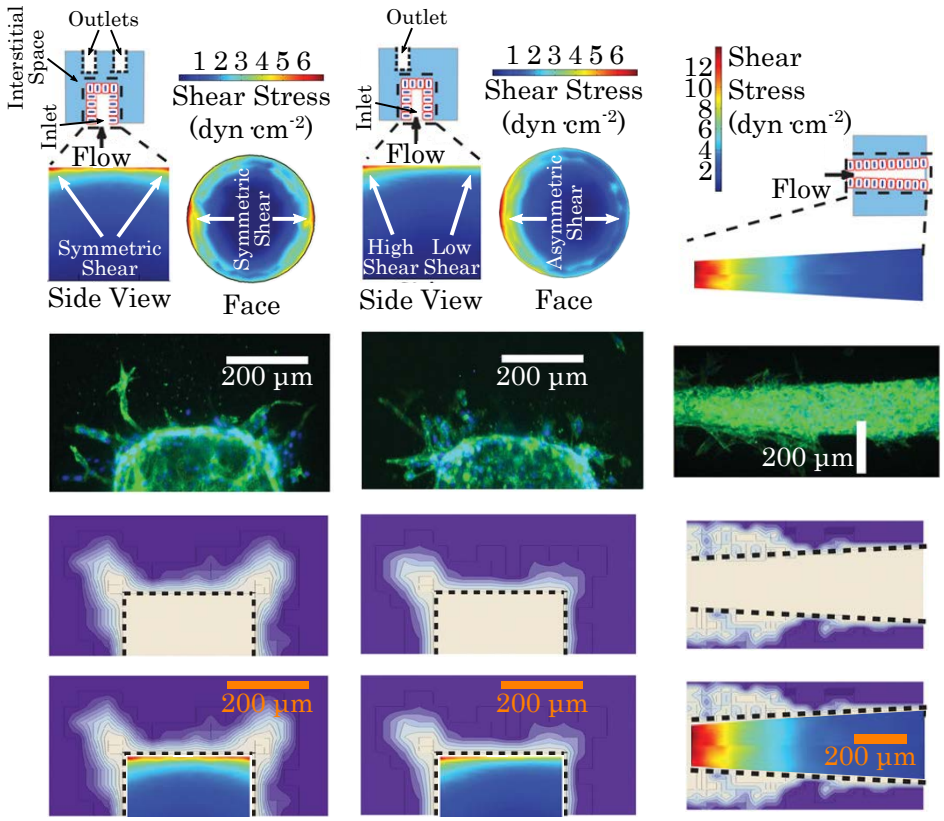

Figure 1.9: **Shear Directed Angiogenesis.** Angiogenic sprouting is observed in response to transmural (left and center columns) and luminal (right column) shear gradients. The top row shows the shear pattern being applied within the boundary of the channel, the second row shows representative confocal micrographs of angiogenic sprouting out from a channel, the third row shows frequency plot of average sprouting density with the channel wall outlined, and the fourth row shows the shear map overlaid on the average sprouting density map. In both types of flow there is a shear stress threshold above which sprouting is induced. Graphic was adapted from [19]; © 2014 Galie et al., originally published under the under the exclusive PNAS License to Publish.

ral flow velocities on the order of 2.5–35 μm·s^{-1} impacts neovascularization and angiogenic sprouting [19,128–130,212]. Transmural flow velocity is the velocity of fluid passing through a wall, such as flow moving from a vascular lumen across the endothelial lining into the interstitial space. Sprouting is the first step of angiogenesis in which endothelial cells in an established vessel begin to protrude into the interstitial space, eventually leading to tube

formation [218]. The mechanical shear stress introduced by flow promotes morphogenesis by acting directly on endothelial cells. This force causes endothelial cells to demonstrate certain behaviors such as migration, morphology changes, and proliferation. Many endothelial cells experiencing these cues will go through vascular network morphogenesis [219]. Flow speed and direction work in conjunction with chemical signal gradients, such as VEGF, to promote the formation of an organized vascular network [128, 129].

The spatial pattern influence sprouting [19]. Figure 1.9 shows how spatial variations in fluid shear, or shear patterns, impact angiogenic sprouting in the cases of transmural and luminal flow. In Fig. 1.9, two unique transmural flow patterns were generated by creating a pressure difference between an endothelial seeded inlet channel and either one or two outlet channels. In between the inlet and outlet channels was a 2 mg/mL collagen gel through which liquid passed. In the case with two symmetrically placed outlets, shown on the left, a symmetric shear pattern was generated at the wall of the inlet channel. A density plot of angiogenic sprouting showed a corresponding symmetric pattern of sprouting. In the case with one outlet channel, shown in the middle, an asymmetric shear stress pattern was generated, which corresponded to an asymmetric pattern of angiogenic sprouting. Lastly, on the right, a gradient of wall shear was generated by flowing liquid through a tapered, endothelial seeded channel. The corresponding sprouting density map showed a shear cutoff, above which sprouting did not occur. The bottom row of Fig. 1.9 shows the shear pattern generated within each channel overlaid on the angiogenic sprouting density map.

An apparent limitation of cell mediated vascular morphogenesis is that angiogenic sprouts only penetrate about 100-300 μm into the matrix [19, 127, 129, 215], limiting the scalability to thicker tissue volumes.

The reproducibility, scalability (in terms of both physical size and production quantity), and cost of each technique must be considered when engineering a vascularized engineered tissue. In general, cellular independent, synthetic construction strategies are better understood and more controllable and scalable than cell mediated vascular morphogenesis [185]. However, each technique has limitations listed in Table 1.3

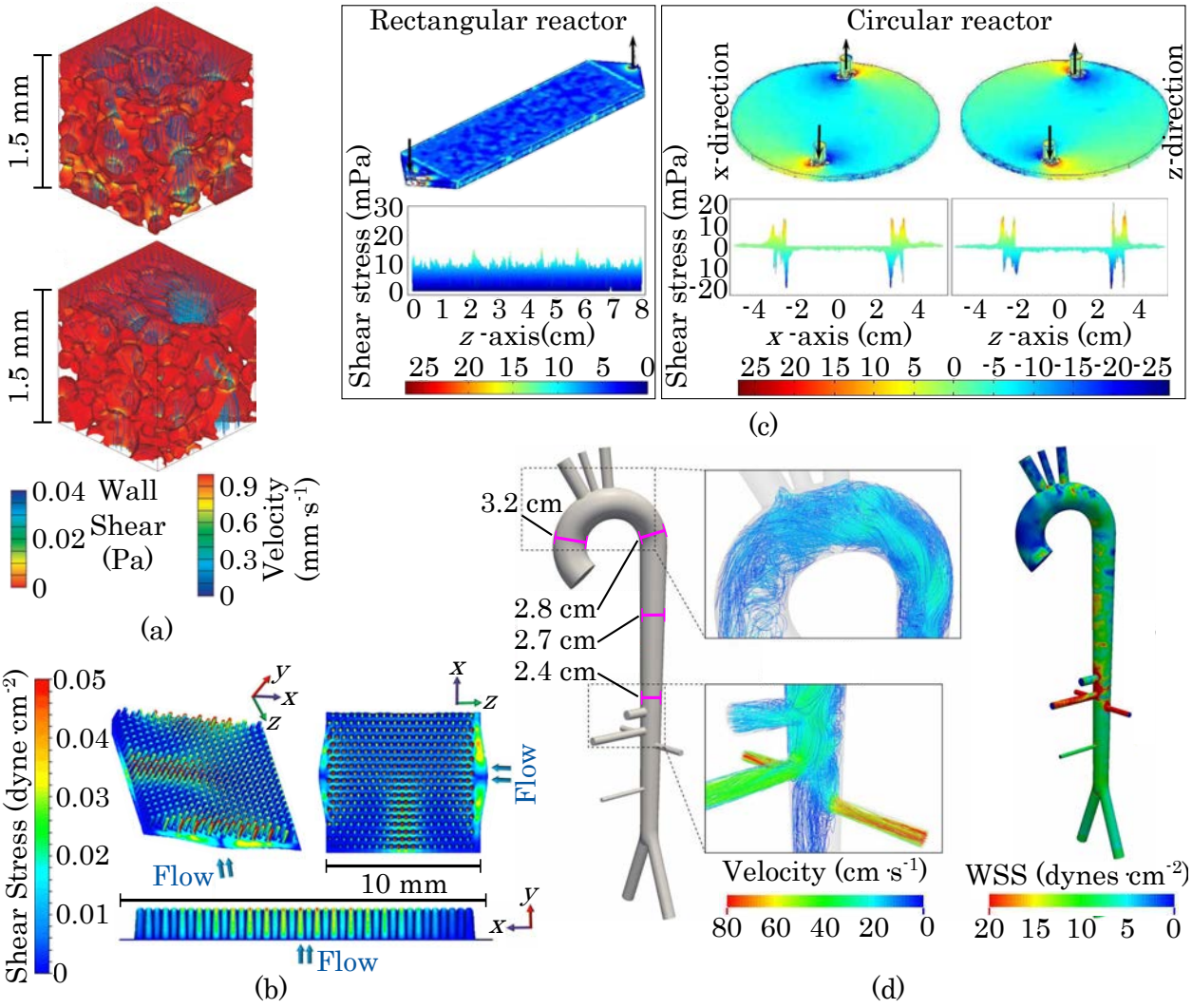

Figure 1.10: **Impact of Scaffold and Bioreactor Geometry on Shear Patterns.** (a) Flow induced shear modeled in scaffold pores. Reprinted from [20], © 2009 Wiley Periodicals, Inc. (b) Wall shear modelled in bioreactor with intestinal topography. © 2017 Costello et al. Adapted from [21]; originally published under the Creative Commons Attribution 4.0 International license. (c) Shear map models comparing bioreactor flow chamber geometries. Adapted from [22] with permission, © 2008 Wiley Periodicals, Inc. (d) Wall shear stress and flow modelled in the human aorta. Used with permission of The Company of Biologists Ltd, from [23], © 2013; permission conveyed through Copyright Clearance Center, Inc.

Modular assembly and porogenation produce much more variation in the exact scaffold geometry than channeling, but certain parameters such as total void fraction and pore size

Table 1.3: Vascularized TE Strategies.

Strategy	Limitations
Bioprinting	requires specialized equipment
Photolithography	limited number of available materials
Soft Lithography	limited channel geometry in the third spatial dimension
Needle Template	requires manual handling
Modular assembly and porogenation	inexact pore geometry

distribution can be controlled with well-defined process parameters [185, 191, 220, 221]. Since the construction of synthetic scaffold elements is reproducible and well understood, these strategies are often used to augment cell mediated techniques. Ideally techniques are paired to compensate for each other's limitations [183, 211]. The potential to generate a scalable TE construct fully permeated with a robust network of endothelial lined microcapillaries ranging down to 5 μm in diameter makes a synthetic and biologically mediated, combinatorial approach one of the most promising paths worth further investigation [185, 212]. A perfusion bioreactor that can enable the control flow and shear distributions throughout a large scaffold volume has the potential to direct vascular morphogenesis on a size scale relevant for tissue engineering. It also has the potential to influence and direct parenchymal cell distribution by controlling nutrient access and the distribution of soluble signaling molecules.

1.1.4 Controlling Flow and Shear Patterns

Shear distribution, or spatial patterns, directly impact the pattern of endothelial sprouting as shown in Fig. 1.9. It has also been shown that shear stress stimuli presented to endothelial cells with specific spatiotemporal patterns can modulate the intracellular Ca^{2+} response in endothelial cells [222]. The type of Ca^{2+} response endothelial cells experience influences cell behaviors including migration, proliferation, and tube formation, which play a role in angiogenesis and vasculogenesis [131, 132]. Despite having the knowledge that these stimuli influence cell behaviors that lead to the formation of vascular networks, generating functional

vascular networks within thick, engineered tissue constructs remains a challenge [223]. This is in part due to a lack of full understanding of the exact spatiotemporal signal patterns required to induce proper vascular morphogenesis throughout a large volume and the limited technology available that can apply these specific signal patterns to endothelial cells. Given the importance of flow and shear distribution in vascular morphogenesis, accurate characterization and control over these distributions, or spatial patterns, is of high importance for promoting vascular network formation. Spatial distribution of shear is known to influence cell growth [19], and perfusion chambers can be configured to generate controlled shear distributions within a porous environment [224], but the influence of shear distribution on cell populations in thick scaffolds has not been investigated. Therefore, this work will focus on flow of cell culture media through benchtop-scale perfusion bioreactors containing thick TE constructs in order to evaluate the extent to which spatiotemporal control over flow can promote individual cell behaviors like proliferation and migration which contribute to more complex behavior such as vascular morphogenesis *in vitro*.

To evaluate the influence of a shear pattern on vascular morphogenesis in thick TE constructs, a device is needed which can apply specific shear patterns throughout such constructs. Shear is generated by gradients in fluid velocity, so the distribution of fluid velocity, or the velocity map, must be controlled to generate a specific shear pattern. In order to control a velocity map, a measurement or readout of a recently acquired velocity map is required along with an adjustable input that can be used to change the pattern [24]. Since vascular morphogenesis involves remodeling and lumen formation, it is a type of biological process which may influence the fluid permeability of a developing TE construct. Changes in fluid permeability can result in changes to the velocity map. The growth rate of new vessels can range from 6 to 12 mm per day (250 μm to 500 μm per hour) [225]. Given the rate of scaffold remodeling, a velocity map to be used for control of shear distribution can safely have been acquired within an hour.

One potential way to predict a specific shear pattern without acquiring velocity maps is to model the fluid flow through a scaffold using computational fluid dynamics (CFD) simulations [226–231]. Perfusion has been modelled in TE scaffolds using CFD simulations,

and some models include dynamic processes related to tissue engineering such as extracellular matrix (ECM) deposition and cell growth [226–231]. The reason that groups have modelled such situations is because models of shear stress within TE constructs can be used to predict whether the shear stress will promote tissue growth or cause cell detachment or death [226, 227]. Models of fluid flow from the macroscopic scale to the scale of individual pores can be seen in Fig. 1.10. Figure 1.10 (a) shows a shear map within individual pores based on real titanium and hydroxyapatite scaffold pore geometry measured by micro-computed tomography (μCT). Figure 1.10 (b) shows shear modelled over a polymeric scaffold 3D printed with the topography of the intestine. Figure 1.10 (c) shows shear modelled through an effective porous medium with defined pore size and density in multiple bioreactor chamber geometries. Figure 1.10 (d) shows shear modelled in an idealized human aorta. Velocity maps have been measured over cells and in scaffolds by methods such as particle image velocimetry (PIV), dye tracing, and flow weighted magnetic resonance imaging (MRI) [27, 228, 232, 233]. PIV achieves better resolution, but it only works with thin, optically transparent media flowing over a glass cover slip, whereas MRIs can be acquired on volumes within thick, optically opaque media that are more akin to the environment found in tissue [234].

Flow induced shear patterns and, by extension, cell behaviors that are impacted by shear, depend on the geometry of the perfusion chamber, the total flow rate, the fluid permeability and geometry of the scaffold, and the interface between the scaffold and the bioreactor [125, 200, 230, 231, 235, 236]. In addition, the fluid permeability and architecture of a scaffold can change over time due to shear-induced erosion, cell proliferation, and scaffold remodeling [227, 229, 237]. One method was developed to actuate shear distributions throughout a scaffold by flowing liquid into the scaffold through multiple inlets [24]. When these inlets were arranged around the scaffold, the shear pattern formed was shown to be dependent on the combination of flowrates in all the inlets [24]. It was shown that, in order to generate a target shear map using a multi-inlet flow chamber as an actuator, an adaptive control algorithm was required to determine which inlet flowrates should be used as inputs [24]. Figure 1.11 shows the progress of an adaptive control algorithm and multi-inlet perfusion bioreactor at generating and maintaining a controlled shear rate map throughout

a porous environment despite inhomogeneous changes to the environment's fluid permeability properties. Shear rate refers the rate at which layers of fluid slide past adjacent layers. Shear rate can be converted to shear stress by multiplying it by the dynamic viscosity of the fluid. The algorithm compared the shear rate map in the flow chamber to the targeted shear rate map and made iterative adjustments to the inlet flowrates in order to minimize the difference between the two shear rate maps. After each iteration, the recently adjusted inlet velocities generated a new shear map, which was then compared to the target shear map again. After several adjustments, the shear map in the flow chamber approached the target shear map. The difference between the target shear rate map and the shear rate map in the flow chamber was quantified by a cost function value, such that the reduction in the cost function value corresponded to a reduction in the difference between the shear rate map in the flow chamber and the target shear rate map. In Fig. 1.11, the images labelled (a-e) are shear rate maps generated at the indicated iterations of adaptive control algorithm. At the iterations immediately following those listed in (a-e) (101, 126, 151, 176, and 201), solid obstacles were added or increased in size as shown in (f-j), changing the flow permeability properties of the environment. A plot of the cost function value versus algorithm iteration corresponding to this situation is shown on the right side of Fig. 1.11. The sudden changes in environmental obstacles caused the shear map to differ from the target shear map immediately after the changes occurred, but the adaptive control algorithm continued to converge on a solution (approach the target shear map).

1.1.5 Sterility

In addition to environmental controls and stimuli, another consideration in bioreactor design is the need to generate a sterile environment [238]. Sterility refers to the absence of any organisms, including bacteria, viruses, fungi, and other cell lines being cultured in the same facility. Bioreactors provide a favorable growth environment for many potential microbial contaminants from the bacterial and fungal kingdoms as well as other mammalian cell types [239]. The most common biological contaminants in labs are mycoplasma, bacteria, viruses, and yeast [240]. Mycoplasma are a type of prokaryote without a cell wall that are only

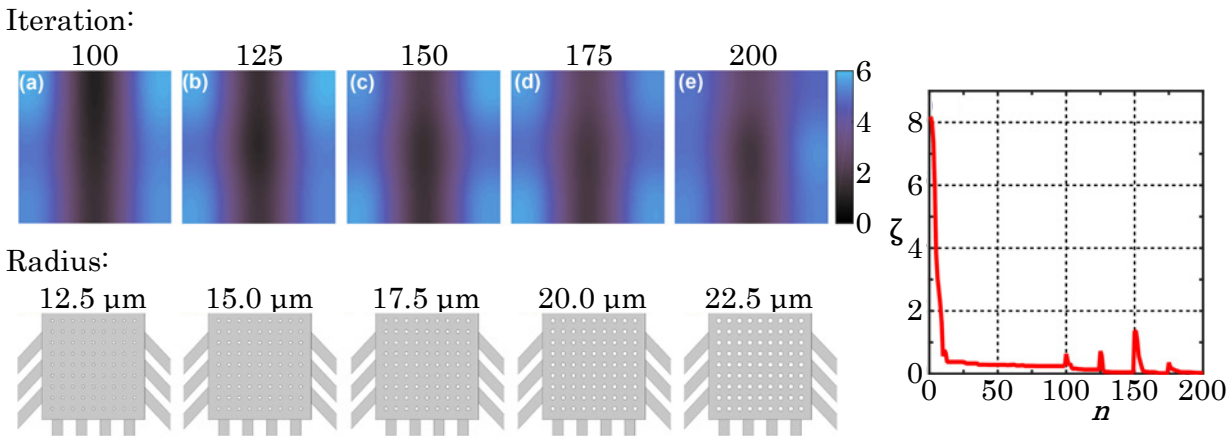

Figure 1.11: **Controlling Shear Patterns.** Model of an adaptive control algorithm maintaining a desired shear pattern throughout a TE construct in spite of discreet changes in the internal environment. Top: shear patterns at the indicated algorithm iteration. Bottom: display of flow obstructions changed at the indicated iteration. Right: convergence plot with y-axis corresponding to the cost function and x-axis corresponding to the iteration number. Figure was adapted from [24] with permission from IEEE, © 2016 IEEE.

0.2 μm in diameter [241]. The most common species of mycoplasma contaminants include *M. fermentans* (human), *M. orale* (human), *M. arginine* (bovine), and *A. laidlawii* [242]. Viral contaminants detected in bovine serum include bovine viral diarrhea virus (BVDV), bovine herpes virus (BHV), bovine parainfluenza-3, and epizootic hemorrhagic disease [243]. Some commercially available cell lines are known to be infected with Epstein-Barr virus, human T cell leukemia virus, and hepatitis virus [239]. Common bacterial contaminants include *Pseudomonas*, *Micrococci*, *Escherichia coli*, *Staphylococcus*, *Bacillus*, *Enterococcus*, and *Staphylococcus* species [244, 245]. Common fungal contaminants include *Candida sp.*, *Penicillium sp.*, *Aspergillus niger*, *Aspergillus flavus*, *Botrytis sp.*, and *Paecilomyces sp.* [245]. Biological contaminants can potentially outcompete the cells being studied, form a parasitic relationship with them, or otherwise alter experimental outcomes by producing exotic proteins or metabolic byproducts [239, 246]. Specific impacts of contamination on cells include reduction of cell proliferation (resulting from nutrient depletion); morphological changes; cytopathic effects; alterations in DNA, RNA, and protein synthesis; chromosomal aberra-

tions; and alterations to the cell membrane and membrane receptors [244, 245]. To prevent contamination, all surfaces of a bioreactor that are wetted with cell culture contacting fluids must be sterilized prior to culture, and the bioreactor must maintain a barrier that prevents the entry of biological contaminants from the surroundings [238]. The term sterilization refers to a process which causes a 6 $\log_{10}$ reduction in the number of viable contaminant organisms, or a kill rate of 99.9999% [247]. Additionally, aseptic technique must be used when handling cells. Aseptic processes refer to procedures which prevent the introduction of contaminants into an environment. Once an environment is sterilized, aseptic technique must be used to keep it sterilized. In general, a clean space must be maintained. Surfaces should be cleaned with 70% alcohol prior to handling cells every time they will be exposed, and talking, coughing, and sneezing should be avoided during handling. Lab coats should be cleaned. Cell culture containers should be opened in a HEPA filtered, laminar flow environment. Windows and doors to the laboratory space should be sealed [245]. A closed system is one in which matter exchange does not occur between the system and the surroundings, but energy can be exchanged. By this definition a closed system will prevent biological contaminants from entering. Cells require nutrients such as dissolved O_2, glucose, amino acids, etc. In a closed system, cells will deplete available nutrients and eventually die. Since gas and cell culture media exchange are required for mammalian cell culture, a bioreactor cannot be a closed system. In perfusion bioreactor systems, gas is flowed in and out of a cell culture media reservoir through a membrane filter with pore sizes smaller than any living organism [69, 248]. Typically, static cell cultures are kept in an environment which is 5% CO_2 and 95% air. A loose fitting lid behaves as a microbial barrier that protects the culture from airborne spores, which may otherwise settle in the media due to gravitational force on the spores. The lid is loose fitting to allow gas exchange with the 5% CO_2 atmosphere. By keeping the cell culture media in equilibrium with this gas mixture, CO_2 reacts with water to form carbonic acid. The carbonic acid interacts with its conjugate base, the bicarbonate ion, to form a pH buffering system. Sparging (bubbling gas into cell culture media) a bioreactor media reservoir with this gas mixture achieves a similar equilibrium. The purpose of filtering the sparged gas mixture through a 0.22 μm pore size filter is to remove any biological

contaminants from the gas mixture (sterilize it) before it enters the sterile environment.

There are several available sterilization methods approved by the United States (US) Food and Drug Administration (FDA) including thermal inactivation (pressurized steam or dry heat), chemical (ethylene oxide gas and solutions of ixatives, including formaldehyde and glutaraldehyde), low temperature H_2O_2 plasma, and ionizing radiation (γ irradiation and electron beam (e-beam)) [30, 249, 250]. Given all these options, the method selected must be compatible with the materials, components, and configuration of the bioreactor system. Table 1.4 provides a general overview of some common sterilization methods, their microbicidal (microbe deactivation) mechanism, and advantages and disadvantages of each process. During bioreactor design, the available methods of sterilization must be taken into account when selecting materials to be used in construction and when determining device geometry. For example, some materials, such as polyvinyl chloride (PVC), nylon, and acrylic will melt or deform under conditions present during dry heat or steam sterilization. Another example is that H_2O_2 plasma sterilizers may be limited in their ability to fully penetrate the lumen of tubing with a high length to inner diameter ratio [251].

1.2 Nuclear Magnetic Resonance

Nuclear magnetic resonance (NMR) is a phenomenon in which atomic nuclei of matter placed in a static magnetic field and excited with the proper radiofrequency (RF) generate a precessing net magnetization with a component perpendicular to the static field that is detected by current induced through a proximal coil of wire.

1.2.1 Nuclear Spins in a Magnetic Field

In the context of this work it is sufficient to describe the NMR phenomenon with the traditional analogy to classical mechanics. In this analogy, atomic nuclei with a nuclear spin quantum number $I = 1/2$ behave like small bar magnets with nuclear magnetic moments that precess, with a slightly offset tilt angle, around an axis that is parallel or antiparallel to the static magnetic field in which the nuclei reside (depicted in Fig. 1.12 (a)). In

Table 1.4: Sterilization Methods [30]

Method Name	Microbicidal Mechanism	Advantages	Disadvantages
Dry Heat	denatures proteins	Non-toxic, environmentally safe, no residues	Limited material compatibility
Steam	denatures proteins	Low cost, short duration, non-toxic, environmentally safe, no residues	Limited material compatibility
ethylene oxide	alkylation of proteins, DNA, and RNA	moderate temperature, compatible with many materials, high penetrability	long processing time (exposure + aeration time), environmental hazardous
Fixatives	indiscriminate crosslinking of proteins	room temperature, no aeration	difficult residue removal, no liquid sterilization
H_2O_2 Plasma	hydroxyl and hydroperoxyl free radicals break DNA	environmentally safe, no aeration time, moderate temperature	no liquid sterilization, low penetrability, H_2O_2 residue
γ Irradiation	·OH free radicals formed by ionizing radiation break DNA	room temperature, higher penetrability than e-beam	radiolytic byproducts, uncontrollable dose rate
E-beam	·OH free radicals formed by ionizing radiation break DNA	room temperature, no residues, less radiolytic byproducts, controllable beam strength	specialized equipment, lower penetrability than γ irradiation

the absence of a magnetic field, the precession axes of a population of nuclei are randomly oriented. [252, 253].

The parallel and antiparallel configurations correspond to low and high energy states, respectively, which can be observed only when the nuclei are placed in a magnetic field [252, 254]. This is an example of the Zeeman Effect. In thermal equilibrium, the nuclei have a slight preference for the lower energy state (parallel orientation) as shown in Fig. 1.12 (b) [255]. The detectable NMR signal is proportional to the difference in the number of spins between the low and high energy states, this difference being referred to as polarization [252]. The ratio of the number of spins in the upper energy state (N_β) to the number of spins in the lower energy state (N_α) is determined from the Boltzmann equation:

$$\frac{N_\beta}{N_\alpha} = e^{-\frac{\Delta E}{kT}} \tag{1.1}$$

where ΔE is the energy difference between the two orientations, k is the Boltzmann constant, and T is the absolute temperature of the sample [252, 254]. The difference in energy between the two states is:

$$\Delta E = \frac{\gamma h B_0}{2\pi} \tag{1.2}$$

where γ is the gyromagnetic ratio of the nucleus of interest in rad·s^{-1}·T^{-1}, h is Planck's constant, and B_0 is the strength of the magnetic field in T [252,254]. The only two experimentally controllable parameters are the temperature and magnetic field strength. Mammalian tissue culture, however, is restricted to physiological temperature (310 K) to maintain proper metabolic activity [256, 257]. Most high-field NMR is performed in a static magnetic field that is instrument dependent and invariant over the course of an experiment. According to Eq. 1.2, in the 9.4 T microimaging system used throughout this work, for every 1,000,000 nuclei in the low energy state there were 1,000,062 nuclei in the high energy state, meaning the technique possesses inherently low sensitivity, which is consistent with most NMR [252].

Conventionally, the direction of the static magnetic field is defined as the positive z direction in a Cartesian coordinate system. Considering the analogy of atomic nuclei as bar magnets with nuclear magnetic moments precessing around the positive or negative z-axis (referred to as spins in NMR texts [252, 254]), the sum of these individual nuclear magnetic

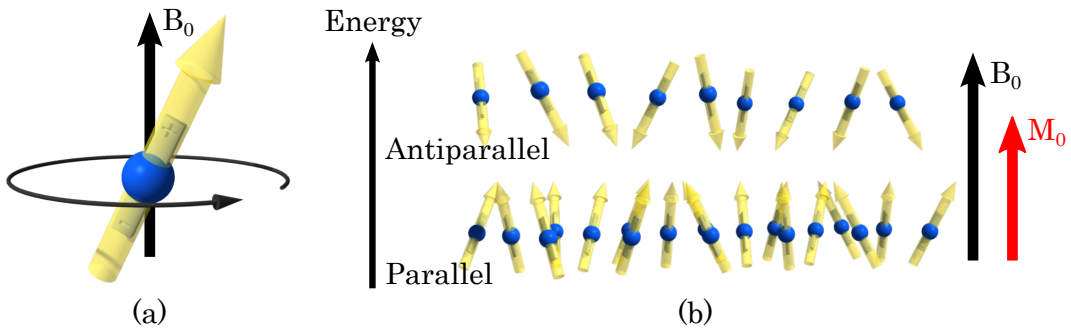

Figure 1.12: **Nuclear Spin.** (a) Depiction of a single nuclear spin in a magnetic field analogized to a bar magnet. The yellow arrow indicates the orientation of the magnetic dipole. The circular arrow indicates the precession direction. (b) Depiction of a population of nuclear spins in a magnetic field at thermal equilibrium. The difference between the number of spins in the high and low energy states is exaggerated for visual clarity. There is no phase coherence. The difference between energy states generates net magnetization vector, M_0 (shown in red) in the same direction as B_0.

moments generates a net magnetization vector, M_0, for the sample along the positive z-axis at thermal equilibrium due to the slight preference for the parallel orientation [252–255, 258].

1.2.2 RF Excitation

In order to excite the spins, the RF wave applied to the sample must have the same frequency as the precession of the nuclei, known as the Larmor frequency. The Larmor frequency expressed as an angular frequency, ω, is:

$$\omega = -\gamma B. \tag{1.3}$$

where B is the local magnetic field around a nucleus [252–255]. When expressed in Hz, the frequency is $v = \frac{-\gamma B}{2\pi}$. If all nuclei of a particular atom in a sample experienced a perfectly homogenous magnetic field of strength B_0, then their precession frequency would be identical. However, field inhomogeneities lead to a broad distribution of precession frequencies throughout a sample centered roughly around $\omega_0 = -\gamma B_0$ [252, 255]. Additionally, electron shielding variations throughout a molecular structure result in particular nuclei within

that structure experiencing local magnetic field variations dependent on the chemical structure [252, 254]. The RF pulse applied to excite a particular type of nucleus has a broad enough frequency range to ensure signal is detected from all nuclei regardless of slight variations in local magnetic field strength [255]. Note that the energy of an electromagnetic wave at the Larmor frequency is equal to the energy difference of the nuclei's parallel and antiparallel energy states according to Eq. 1.2 [253].

As the nuclei of a sample are excited with RF, the net magnetization initially tilts away from the z-axis into the xy or transverse plane [252, 254, 258]. The degree to which M_0 tilts away from z, called the flip angle, α, is determined from the relationship:

$$\alpha = \gamma B_1 t_p \tag{1.4}$$

where B_1 is the oscillating magnetic field of the RF pulse and t_p is the time over which RF is applied [252]. Once M_0 tilts out of thermal equilibrium, it is composed of a longitudinal (z direction) and transverse (xy plane) component. The longitudinal component, M_z, is determined by the difference in the number of spins between the parallel and antiparallel orientations, or the polarization [254,255]. The polarization is maxed at thermal equilibrium. When RF is applied the polarization is initially reduced until there are an identical number of spins in both states when α=90°. At this angle the longitudinal magnetization component is completely eliminated [252]. The transverse component, M_{xy}, is determined by the amount of phase coherence of the population. At thermal equilibrium, the angular positions or phases are random. Applying RF initially increases phase coherence as polarization is lost. A 90° pulse generates the maximum amount of phase coherence, converting the net magnetization entirely from longitudinal to transverse magnetization as shown in Fig. 1.13 (a) [252].

RF can be applied for a longer periods, further rotating the magnetization vector. Pulses between 90° and 270° result in an excess of spins in the antiparallel orientation. A 180° pulse completely inverts M_0 as shown in Fig. 1.13 (b). A 270° will place M_0 completely in the transverse plane with a precession that is phase shifted from the 90° pulse by 180°. A 360° returns M_0 to its thermal equilibrium position.

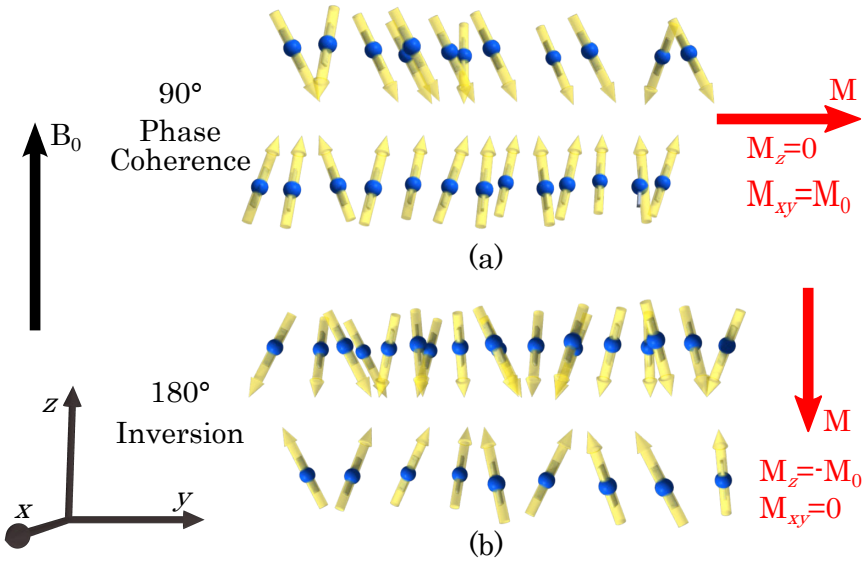

Figure 1.13: **90° and 180° Pulses.** (a) Depiction of a population of nuclear spins immediately after exposure to a 90° pulse from thermal equilibrium. The amount of phase coherence is exaggerated for visual clarity. (b) Depiction of a population of nuclear spins immediately after exposure to a 180° pulse from thermal equilibrium.

1.2.3 M_0 Detection

When M_0 is tilted such that it has a component in the transverse plane, this component is detectable by the same coil that was used to initially excite the sample. As M_{xy} precesses around the z axis, electromagnetic induction generates an alternating current in the coil as shown in Fig. 1.14 [253]. The signal is the summation of multiple sinusoidal waves generated by nuclei experiencing slightly different magnetic field strengths due to factors such as B_0 inhomogeneity or chemical shielding. When the signal is Fourier transformed, the frequencies and their respective quantities are revealed as peaks in the frequency domain. The center of the peak indicates the frequency of precession, and the magnitude of the peak (determined from integration) indicates the relative quantity of nuclei with that frequency [252–254]. As B_0 becomes more homogenous, the peaks become narrower, improving spectral resolution. In this work, the only nucleus observed is the ^{1}H in H_2O, which is highly abundant and easily detected in physiological environments.

1.2.4 Relaxation

Following excitation, M_0 will gradually return to thermal equilibrium along a path like the one shown in Fig. 1.14. There are two types of relaxation processes: transverse and longitudinal relaxation [258]. The return of spins to their original polarization in the z direction is longitudinal relaxation, which is characterized by the time constant T_1. T_1 is the time it takes for the longitudinal polarization to return to approximately 63% of its thermal equilibrium value. Transverse relaxation refers to dephasing of spins, which is characterized by the time constant T_2. T_2 is the time it takes for the phase coherence to decay to about 37% of its initial value following excitation [252]. These two forms of relaxation often occur at different rates, with $T_1 \geq T_2$ [259]. T_1 and T_2 measurements provide information relevant to the physiological environment. Parameters such as temperature, viscosity, structure, and molecular size influence T_1, whereas the presence of paramagnetic materials and macromolecules influence T_2 [258].

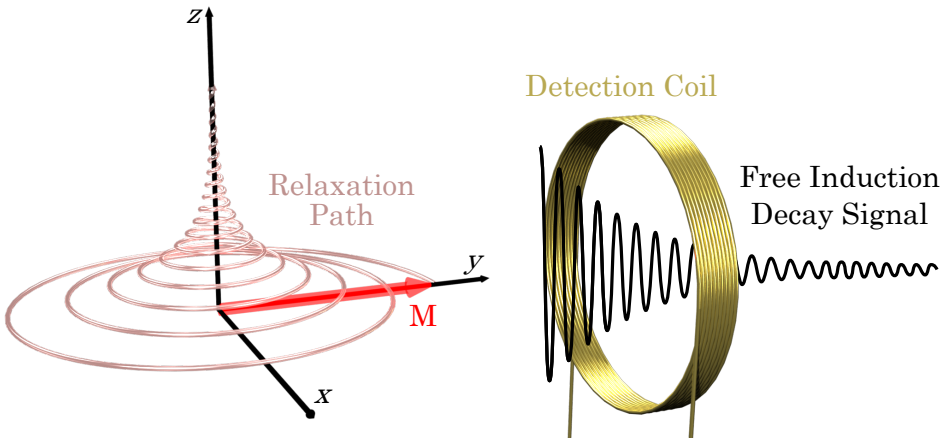

Figure 1.14: **Free Induction Decay Detection.** Diagram of relaxation and detection of net magnetization following a 90° pulse. Transverse relaxation occurs in the xy plane and longitudinal relaxation occurs in the z direction. A coil detects magnetization in one dimension of the transverse plane (in this diagram the y component of magnetization is detected). The sinusoidal decay along this dimension forms the FID.

After an initial excitation pulse, dephasing is caused by both transverse relaxation and magnetic field inhomogeneity. This dephasing results in the NMR signal taking on

the appearance of an exponentially decaying sinusoidal wave called a free induction decay (FID) [252]. In this work transverse relaxation rates were measured with a Carr-Purcell-Meiboom-Gill (CPMG) pulse sequence seen in Fig. 3.1 (a) [260]. To decouple transverse relaxation from signal loss on account of field inhomogeneity, a 180° pulse is applied following the initial excitation and a time delay. After another identical time delay, dephasing due to magnetic field inhomogeneity is momentarily corrected as spins with higher precession frequencies briefly re-phase with lower frequency spins. The signal, which becomes detectable as a result of this momentary re-phasing, is referred to as a spin echo. A series of repeated 180° pulses are applied to the sample to generate a corresponding series of spin echoes. Over time the intensity of the spin echoes decays due to transverse relaxation [260]. The echo intensities are plotted versus time to determine the rate of transverse relaxation according to $M_{xy}(t) = M_{xy,max}e^{-t/T_2}$ [259].

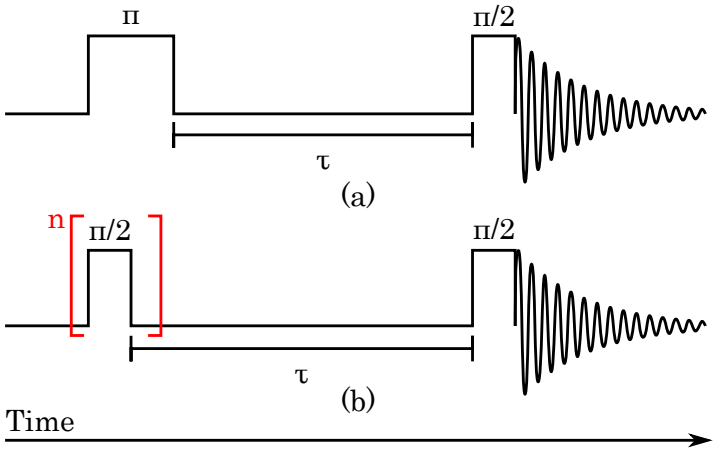

Figure 1.15: T_1 **Pulse Sequences.** (a) Inversion Recovery (b) Saturation Recovery.

Two common pulse sequences for measuring T_1 include saturation recovery and inversion recovery, shown in Fig. 1.15 (a-b). Both pulse sequences initially move M_0 into a non-equilibrium position that has no transverse component. This is done by tilting the magnetization vector 180° (inversion recovery), or by saturating the spins with a continuous RF wave or a large number of short pulses in rapid succession. Following the initial pulse, M_0 is allowed to partially return to thermal equilibrium in the time delay, τ. Following the delay, the partially recovered longitudinal component is excited with a 90° pulse, converting it to

a detectable signal in the transverse plane [252]. The recovered signal is plotted against τ to determine the rate of longitudinal relaxation according to $M(\tau) = M_0\left(1 - e^{-\tau/T_1}\right)$ [259].

1.2.5 Diffusion

The diffusion coefficient of a substance reveals important biological information and can be measured by NMR. In this work the self-diffusion coefficient of water was measured with a Pulsed Field-Gradient STimulated-Echo (PFG-STE) pulse sequence, which is diagramed in Fig. 3.1 (c). The principle behind diffusion measurements is the application of two bipolar magnetic field gradients of equal magnitude and duration following excitation. Gradients are generated by applying current through coils of wire on either side of the sample; an example configuration is shown in Fig. 1.16 [261]. The first gradient introduces a phase shift that is dependent on the nucleus's position along the gradient direction. The second gradient refocuses, or undoes the phase shift introduced by the first gradient. A delay time in between gradients, known as the diffusion time, nuclear position to change via molecular motion. Molecular diffusion along the direction of the applied gradient reduces the degree of refocus completion [262].

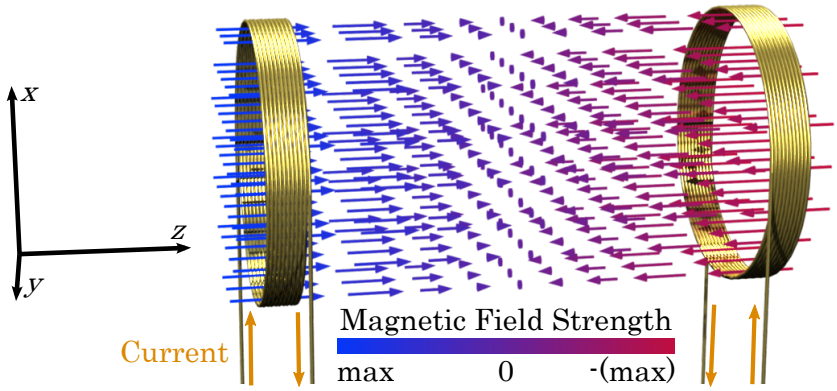

Figure 1.16: **Magnetic Field Gradient.** Diagram of coils used to generate a linear magnetic field gradient along the Z direction. The gradient shown here will be added to the static field, B_0. Only the Z component of the field is shown. Transverse components are not shown.

The PFG-STE sequence introduces the concept of a stimulated echo. A stimulated echo occurs after a 90° pulse initially excites spins, dephasing occurs, a second 90° pulse places the dephased spins into the xz-plane, and a third 90° pulse places the spins back into the transverse plane in reverse orientation, allowing an echo to occur [263]. Unlike spin echoes, which are limited by the timescale of transverse relaxation, the magnitude of the stimulated echo is dependent on the timescale of longitudinal relaxation [263], which was much greater than that of transverse relaxation in all experiments performed in this work. Hence, the second 90° pulse is said to store the initial excitation and dephasing information in the longitudinal direction. This is useful in diffusion weighted NMR since longer diffusion times may be desired when examining systems with barriers [264], such as the diffusion of water inside cells.

1.2.6 Magnetization Transfer

Magnetization transfer (MT) is a magnetic resonance technique that measures macromolecular content. The pulse sequence used to detect macromolecular content is shown in Fig. 3.1 (b). It relies on the principle that nuclear spins associated with macromolecules have a broader absorption spectra than unbound spins as shown in Fig. 1.17 (a). It also relies on the exchange, or transfer, of magnetization between nuclei associated with macromolecules and unbound nuclei via dipolar coupling or direct chemical exchange [25, 26]. A diagram of the two-pool model used to describe these two populations and the exchange between them is shown in Fig. 1.17 (b). In the MT pulse sequence, a saturation pulse is first applied with a frequency that is shifted away, or off-resonance, from the Larmor frequency. A resonant 90° excitation pulse is then applied before acquisition. When a saturation pulse is applied on resonance, it removes all longitudinal magnetization prior to excitation, causing no observable signal. A saturation pulse far off resonance has no influence on the observed signal. In between, there is a degree of signal suppression that depends on saturation pulse frequency. In addition, there is a range of frequencies over which the degree of signal loss depends on macromolecular content, which is due to its broader excitation spectrum. Nuclei associated with macromolecules are saturated by off-resonance pulses, and their saturated magneti-

zation is transferred to unbound water molecules prior to excitation, thereby reducing the measured signal.

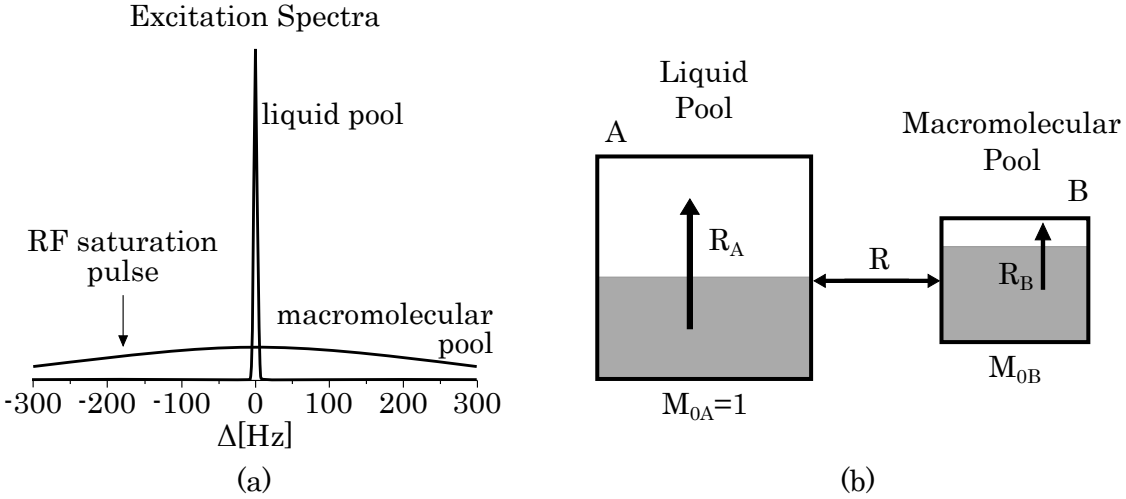

Figure 1.17: **Principles of MT.** (a) Absorption spectra comparison of macromolecular and unbound liquid nuclei. Adapted from [25] with permission, Copyright © 2001 John Wiley & Sons, Ltd. (b) Two-pool model of MT. A is the free liquid pool, B is the macromolecular pool, R is the exchange rate between pools, R_A/R_B are longitudinal relaxation rates for each pool, M_{0A} is the number of free spins (normalized to 1), and M_{0b} is the relative fraction of macromolecular spins. Adapted from [26] with permission, Copyright © 1993 by Williams & Wilkins.

1.2.7 Spatially Resolved Magnetic Resonance

To obtain spatially resolved NMR signal intensity data, or MRIs, magnetic field gradients are applied at specific time intervals during a pulse sequence. The information required to construct an MRI can be obtained with a spin or stimulated echo and three types of orthogonal magnetic field gradients. A slice select gradient is applied during the excitation pulses so that only spins in a single plane perpendicular to the direction of the slice select gradient are in resonance with the RF pulse. A frequency encoding gradient is applied during acquisition in a direction orthogonal to the slice select gradient. Application of this gradient causes the nuclei to have precession frequencies corresponding to their position along the

frequency encoding direction. When the signal is Fourier transformed, the frequency of the signal is used to determine its position along the frequency encoding direction. Lastly, the pulse sequence is repeated a number of times equal to the desired resolution in the third spatial dimension. A phase encoding gradient with an array of strengths is applied between excitation and acquisition for a brief period to cause a degree of dephasing. The difference in the amount of phase change at a point caused by different gradient strengths corresponds to the position in the third dimension. In order to generate an image, a 2D plot of frequency encoding and phase encoding data, which is referred to as k-space, is processed using a 2D Fourier transform [259].

Additional weightings are often applied when acquiring images of nuclear density including relaxations, MT, diffusion, and velocimetry [259, 265–267]. A STimulated Echo Multi-Slice (STEMS) pulse sequence diagram is shown in Fig. 3.3 with options for including an off resonance saturation pulse (for MT weighting) or bipolar gradients (for diffusion weighting). T_2 weighted images can be acquired by adjusting the delay time between the initial excitation and the signal peak, known as the echo time, t_{E}. A flow weighted spin echo multi-slice (SEMS) sequence is shown in Fig. 1.18. In this sequence, bipolar gradients are applied in the directions of fluid velocity measurements.

1.3 MRI Applied to Biological Systems

Magnetic resonance is frequently used to obtain information about biological systems. Its most widely known biological application is clinical imaging. Diffusion, MT, T_2, and flow weighted MRIs are acquired in clinical settings [234, 268–270]. Some clinical research has investigated the use of MRI for purposes that hold value in tissue engineering, such as obtaining cell density information in tumors or brain abscess [271–284].

1.3.1 Magnetic Resonance *In Vitro*

In addition to being applied to clinical imaging, magnetic resonance has been used to obtain metabolic information and image cell and tissue cultures. Multiple configurations for housing

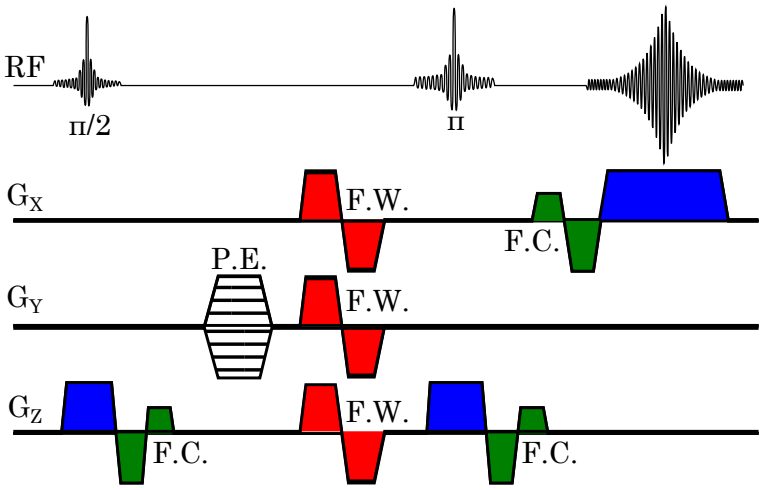

Figure 1.18: **MRI pulse sequence.** Modified spin-echo multi-slice (SEMS) pulse sequence for phase-contrast velocity measurements in three-dimensions. Flow compensation (F.C.) gradients are shown as green lobes and flow weighting (F.W.) bipolar gradients are shown as red lobes. Reprinted from [27], Copyright 2012, with permission from Elsevier.

viable cells in a high magnetic field have been developed for this purpose. Some groups have constructed NMR compatible flow chambers in which cells are seeded on microcarrier beads, hollow fibers, or fabrics; or cells are encapsulated in gel threads or spheroids [285, 286]. Others have developed MRI compatible incubation systems [287–289], which have been used to investigate the cytotoxicity of magnetic fields and RF electromagnetic radiation [290, 291].

NMR has been used to monitor metabolites in cell populations that have been pelleted [292, 293] and encapsulated in gels [294, 295]. NMR based metabolic studies have been used to distinguish cell types [293], monitor differentiation of stem cells [292, 296], or observe metabolic profiles over extended periods of culture [294]. Although NMR can provide metabolic information about a cell population, metabolites are not present in high enough concentrations to generate enough signal for metabolic imaging without metabolite specific contrast enhancement such as ^{13}C pyruvate [297]. Therefore, most metabolic data obtained from cell cultures are averages of entire cultures within the NMR probe's RF region.

The quantity of cells in a tissue culture presents a signal challenge for MRI of whole cells, especially when cells are seeded and cultured at much lower densities than physiologically

observed. For example, the average physiologic hepatocellularity is 1.12×10^8 cells·mL^{-1} (based on a reported average hepatocellularity of 1.07×10^8 cells·g^{-1} [298] and an average hepatic density of 1.051 g·mL^{-1} [299]) whereas engineered hepatic seeding densities have been reported with an upper range that is an order of magnitude less [300]. To enhance cellular visibility, cells are often labelled with contrast agents [295, 301–306]. MRIs have been acquired of cells in suspension [302–304, 307], encapsulated in gels [295, 305, 308], seeded in porous scaffolds [287, 289, 309], and cultured on bead surfaces within hollow fiber devices [306, 310, 311]. These MRIs have been used map cell location [310, 311] and measure their contrast agent uptake [306]. A few studies have acquired MRIs of cells without contrast agent labelling [232, 287, 289, 308, 309], which would be preferred for long term tissue culture, since cell division and turnover may lead to inaccurate labelling.

Given the ability of MRI to map cells and fluid velocity, and given the influence of fluid flow on cell behavior, the application of MRI to examine the influence of flow on engineered tissue construct development is expected to yield results that will contribute to the long term goal of controlling large tissue growth. The goal of this work was to establish the tools needed to culture thick, optically opaque TE constructs in a flow controlled environment and methods by which noninvasive readouts of tissue development and health could be quantitatively mapped and correlated to maps of shear.

CHAPTER 2

Design and Operation of Twelve Channel Bioreactor

2.1 Introduction

Injury and disease can cause loss of biological tissue, which is a condition that can be treated with replacement tissue [33–40]. Donor tissue has been used as a replacement for lost tissue, but limited availability [47–49] and rejection and disease transmission risks [44–46] have motivated the search for alternative tissue replacements, such as engineered tissue [52]. In order to grow and condition engineered tissue constructs to the point at which they are capable of performing the function of natural tissue, appropriate environmental conditions and signals must be provided. A bioreactor is a device that has been developed to provide such an environment [69]. Over time, new insights into the complex environmental requirements for culturing engineered tissue have driven the development of bioreactors with novel functionalities in an attempt to meet these requirements [189]. One aspect of the environment that has been shown to be critical to the developmental outcomes of multiple tissue types is the spatiotemporal heterogeneity of physiological signals. Both biomechanical and biochemical spatiotemporal signal distributions have been observed in the development of dermal, vascular, cardiac, neural, and craniofacial tissue [312–318], and timed micromechanical signaling has been used to control intercellular interactions [319].

Behaviors of an individual change in response to mechanical stimuli in the environment by a mechanism called mechanotransduction [145]. Mechanotranstruction is the process by which mechanical stimuli activate or suppress biochemical pathways through a mechanically sensitive structure, such as the cytoskeleton or an ion channel, that undergoes a conformational change in response to the stimulus [145].

Cell-cell signaling networks govern more complex processes such as tissue remodeling and the self-organization of a population of cells into large, multicellular structures [320, 321]. In these networks, genetic programs control behavioral responses to stimuli throughout a cell population. Delays in transcription and translation, or delayed positive and negative feedback loops may result in signal oscillations, or distinct temporal patterns within signaling networks that influence network behavior [322]. Similarly, the temporal presentation of a signal with a bioreactor may promote certain cellular responses, such as the intracellular Ca^{2+} response in endothelial cells to sinusoidal flow and ATP concentration patterns [222]. This specific Ca^{2+} response has been linked to behaviors that play a role in vascular morphogenesis [131, 132]. The spatial distribution of a signal influences where multicellular structures localize and to what degree they form at spatially varied locations, guiding the overall process of tissue formation [19].

Because biomechanical spatiotemporal signal patterns have been shown to play a role in the development of tissues and organs, efforts have been made to map extracellular matrix (ECM) stiffness and flow at the cellular and tissue scales [27, 318, 323, 324]. The impact of spatiotemporal heterogeneity of physiological signals on engineered tissue development must be understood in order to determine the proper signal presentation to guide engineered tissues through multistage development processes. In order to promote tissue development, an appropriate signal pattern may need to be determined. A signal pattern refers to a specific spatiotemporal distribution of the signal magnitude throughout the volume a TE construct. For example, a shear pattern refers to the organization (in time and space) of the quantity of shear stress. A dissolved nutrient pattern refers to the spatiotemporal distribution of the concentration of that nutrient. One strategy to investigate signal patterns has been to replicate patterns observed *in vivo* inside bioreactors [325, 326], but practical limitations of current tissue culture (TC) technology currently make it impossible to replicate all aspects of the *in vivo* environment. Fluid velocity distributions generated in bioreactors have been shown to promote vascular morphogenesis [129, 225]. To investigate the effects of a range of shear patterns on three dimensional (3D) cell culture and engineered tissue development, recent bioreactors have been designed with the ability to generate arbitrary velocity maps through

perfusion tissue cultures [224]. Biomechanical signal patterns produced *in vitro* have been shown to promote biological outcomes such as tendon homeostasis, cartilage development, bone development, and vascular morphogeneis [19, 327–329]. The ability to monitor and control fluid-induced shear forces noninvasively in thick, optically opaque media make this bioreactor design suitable for studying the influence of varied spatiotemporal biomechanical signaling on engineered tissue development.

A TE construct can be composed of a scaffold and cells seeded on the scaffold [52]. This scaffold is required to support a 3D volume of cells, and it should allow sufficient nutrient delivery and waste removal [52]. One method to ensure sufficient exchange of nutrients and wastes is to perfuse a scaffold with cell culture media [206]. Perfusion introduces mechanical signals to the TE construct [206]. Generally, a TE scaffold must be biocompatible and promote cell growth. A scaffold for perfusion should possess sufficient permeability to allow flow (while minimizing compression) and mechanical resistance to resist erosion [330, 331]. TE scaffolds are sometimes made from biopolymers, such as those found in the natural ECM including collagen, fibronectin, laminin, and elastin [332]. The biopolymer hydrogels studied here are water swollen matrices composed of a mixture of several types of randomly oriented, physically crosslinked ECM protein fibers [333].

Scaffolds composed of biopolymers are used because these molecules are known to possess desirable biological properties (biocompatible, biodegradable, etc.) *in vivo* [332]. Many biopolymer hydrogels are unable to support pressure-driven interstitial flow at velocities greater than $\sim$100 μm/s due to low fluid permeability and low mechanical strength. *In vivo*, interstitial flow is movement of a fluid through ECM outside of blood vessels. *In vitro* the term is used to refer to flow through scaffold material, such as the biopolymer strands making up a hydrogel. Subjecting biopolymer hydrogels to perfusion results in scaffold deformation and degradation on time scales much shorter than what is required for tissue development [27]. Fluid permeability depends on several interdependent properties of the scaffold including porosity (total void fraction) and pore interconnectivity, tortuosity, and size distribution [334–339]. Fluid permeability is a measure of flow conductance — the pressure drop across a material through which liquid is flowed is inversely proportional to the fluid

permeability of the material. This pressure difference exerts a compressive force on the material. A material's resistance to compression is a function of material stiffness [340,341]. The allowable quantity of compressive force before the material fractures or irreversibly deforms depends on the compressive strength of the material. Irreversible deformation or fracturing are generally undesirable outcomes since they alter the structure of the engineered tissue. Therefore, a material requires sufficient permeability for perfusion. The exact permeability considered sufficient for perfusion depends on the compressive strength of the material, the material geometry, and the desired flow rate.

Another impact flow can have on a material is shear-induced erosion, or the removal of material at the scaffold surface due to shear forces exerted by fluid flow. In some scaffolds, noticeable erosion at the channel wall can occur within hours, leading to undesirable loss of engineered tissue [27]. One mechanism of shear-induced erosion is polymer chain scission [342]. A scaffold's resistance to shear-induced erosion depends on the uniformity of wall shear, which can be promoted by optimizing scaffold microarchitecture [330].

In order to address scaffold compression, open channels have been included in scaffolds to provide low resistance flow paths, increasing the scaffold's permeability. Alternatively, hydrogel scaffolds have been lyophilized to form more permeable macroporous sponges. Macroporous sponges refer to materials containing large (>10 μm) pores separated by thin walls of insoluble material, which can be synthesized by lyophilizing collagen and gelatin hydrogels [343, 344]. Without channels or large, interconnected pores to accommodate flow, the low fluid permeability of the gel causes a pressure differential to form across the gel that may result in gel compression. The insertion of channels into a scaffold is an example of a topological modification. Topological modifications refer to the insertion of architectural features that are preserved despite deformations to the material structure containing these features. Topological modifications have been shown to influence velocity maps within porous scaffolds [168].

In addition to the physical properties of a scaffold, biological properties such as impact on cell behavior should be considered. Cell behaviors that could contribute to the final cellular content and function of an engineered tissue include proliferation, migration and differentia-

tion [52, 78]. Proliferation refers to the division of cells into daughter cells. Proliferation can be promoted to reach a target cell density after initially seeding a scaffold with a smaller number of cells. Migration refers to the movement of cells. It plays a role in the formation of organized multicellular structures, such as vascular networks. Differentiation is a series of changes in gene expression which result in a cell performing specialized functions. After seeding a scaffold with stem cells or progenitor cells, signals can be provided to promote differentiation into cell types with specialized functions. Cell behaviors depend on the same scaffold structural properties that influence scaffold permeability and mechanical durability, such as matrix stiffness, pore size, biopolymer composition [89, 179, 180, 345–347].

Magnetic resonance imaging (MRI) is capable of mapping cell distribution [232, 287, 289, 308, 309] and mapping fluid velocity in thick, optically opaque environments [348]. Given the influence of fluid flow on cell behavior, the application of MRI to examine the influence of flow on engineered tissue construct development is may yield results that will contribute to the long term goal of controlling large tissue growth.

In this study we propose an MRI compatible, 12-channel inlet bioreactor capable of generating arbitrary velocity maps. The design features a removable tissue culture (TC) chamber to accommodate multiple scaffold types. The removable culture chamber enables the user to prepare the scaffold outside the bioreactor, which facilitates the inclusion of any desired topology, and then insert it for use.

The new bioreactor design was evaluated for its ability to maintain several types of biopolymer scaffolds under perfusion for up to two weeks, a length of time sufficient to observe the formation of vessels ∼8-16 cm in length based on a vessel growth rate of 6 to 12 mm per day [225]. In addition, these scaffolds were evaluated for their ability to promote endothelial migration and proliferation. Scaffolds used include commercially available porous collagen and gelatin sponges and several unique biopolymer hydrogel mixtures. A biopolymer mixture known to promote vascular morphogenesis, referred to as the magic mixture, which is known to succumb to erosion and compression [27], was modified to be suitable for withstanding mechanical forces of perfusion. The new composition was selected to balance mechanical durability and stiffness with relevant levels of vascular morphogenesis. Mechanical durability

was evaluated by the resistance of the scaffold to wear under perfusion for up to two weeks. Stiffness was evaluated by the scaffold's ability to supported channel architecture without collapsing.

Finally, the bioreactor was used to culture cells in a macroporous gelatin sponge under a heterogeneous flow velocity distribution. During culture, MRI was used to measure the velocity map and the corresponding maps of cell density and viability.

2.2 Materials and methods

2.2.1 Bioreactor Setup

2.2.1.1 Bioreactor Body and Water Jacket Assembly

The twelve-inlet bioreactor body was fabricated from a United States Pharmacopeia (USP) Class VI biocompatible stereolithographic resin (Formlabs, Dental SG Resin). Additive manufacturing, or the computer controlled layer-by-layer deposition of material based on a computer-aided design (CAD) file, was chosen for its ability to create intricate internal flow path geometries. Stereolithography was chosen because it produces non-porous, high-resolution parts. The resin used was both biocompatible and autoclavable, making it suitable for applications that required cell culture contact. It was found to be compatible with prolonged contact with ethanol, isopropanol, and glutaraldehyde-based sterilization solutions.

Renderings of the bioreactor body from multiple angles are shown in Fig. 2.1 (a). The ends of the bioreactor were cylindrical, allowing the bioreactor to be vertically aligned within the 40 mm inner diameter (ID) MRI probe. The middle of the bioreactor was a 0.3 inch thick flat plate centered on the cylindrical axis of the MRI probe. A tapered square hole in which the TC chamber was inlayed passed through the center of the flat plate. Grooves for o-rings surrounded the hole on both faces of the plate. Removable polycarbonate windows were sealed against the o-rings on both faces of the bioreactor to contain the internal flow path. The windows were mounted with polyether ether ketone (PEEK) screws and nuts that threaded into holes built directly in the body of the bioreactor. The windows provided high

sample visibility and a potential path for optical imaging.

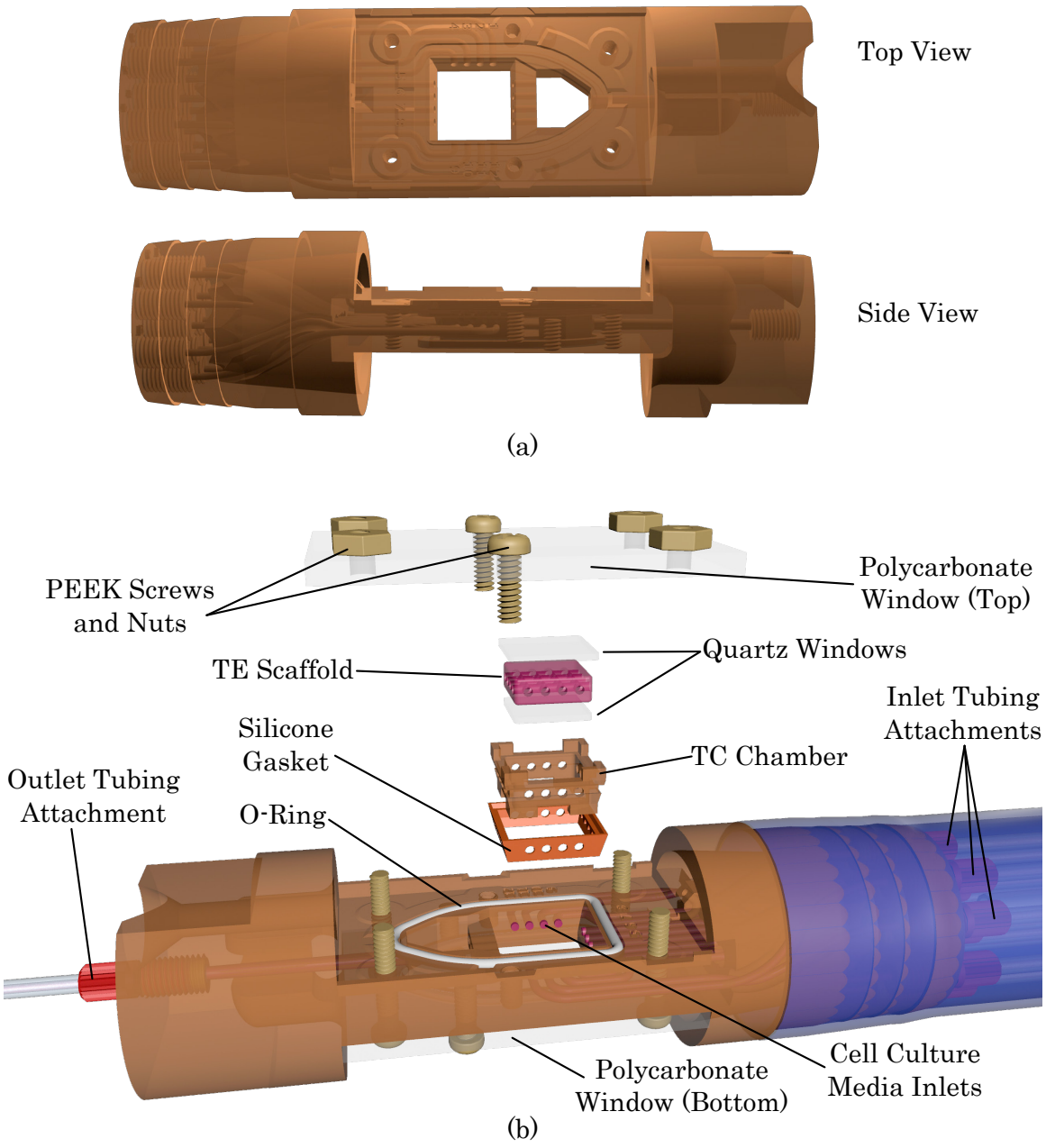

Figure 2.1: **Bioreactor Diagram.** (a) 3D schematic of bioreactor body only from top and side perspective. (b) Expanded view of all components in fully assembled bioreactor including TC chamber.

Rather than place a sponge or cast a gel directly in the bioreactor, a separate insert known as the TC chamber was developed to give more control over the scaffold preparation

process. Made with Dental SG Resin, the TC chamber was a 4 mm tall retaining wall surrounding an empty 1.2 cm × 1.2 cm square-shaped region in which the tissue engineering scaffold was contained. Four holes passed through each side of the chamber aligning with the bioreactor inlets. The outside of the chamber was angled to sit within the tapered hole in the center of the bioreactor. Four hooked prongs extended below the corners of the TC chamber to seat a quartz window that served as a flat base to support the bottom of the scaffold. Four corner prongs extended above the TC chamber around a small ledge on which a slightly larger quartz window was placed. The windows created well-defined geometric boundaries for the TC chamber and provided extra mechanical support for gels cast in the chamber by serving as an additional rigid surface to which the gel attached. An expanded diagram of the assembled bioreactor components is shown in Fig. 2.1 (b).

In early tests of the TC chamber concept, the chamber was inserted into the bioreactor without a gasket. In these tests, fluid preferentially passed between the walls of the bioreactor and TC chamber rather than the scaffold. In order to prevent liquid from circumventing the desired flow path through the scaffold, the silicone gasket was developed to make a seal between the walls of the TC chamber and bioreactor. It was cast from a food grade liquid silicone (Make Your Own Molds, CopyFlex®) in a mold made from stereolithographic resin (Formlabs, Clear Resin). Stainless Steel tubes were positioned during casting to create channels in the silicone gasket that aligned with the bioreactor inlets. A syringe and needle were used to inject the liquid silicone into the mold (see Fig. 2.2). Silicone gaskets were cured for eight hours. The cured gaskets were removed from the mold and soaked in deionized water for five days at 50°C to leach out residual toxins that were found to disrupt cell culture. Following the leaching step silicone molds were placed in static six well plate cell cultures and verified to have no influence on cell morphology, growth rate, or viability.

Twelve 0.125 inch outer diameter (OD) fluorinated ethylene propylene (FEP) tubes containing cell culture media were attached to the bioreactor via flat bottom, nut and ferrule fittings screwed into 1/4-28 threaded holes manufactured directly in the bioreactor's cylindrical base. These holes fed into the twelve inlet channels that directed flow from the cylindrical end of the bioreactor into three sides of the TC chamber. Cell culture media passed through

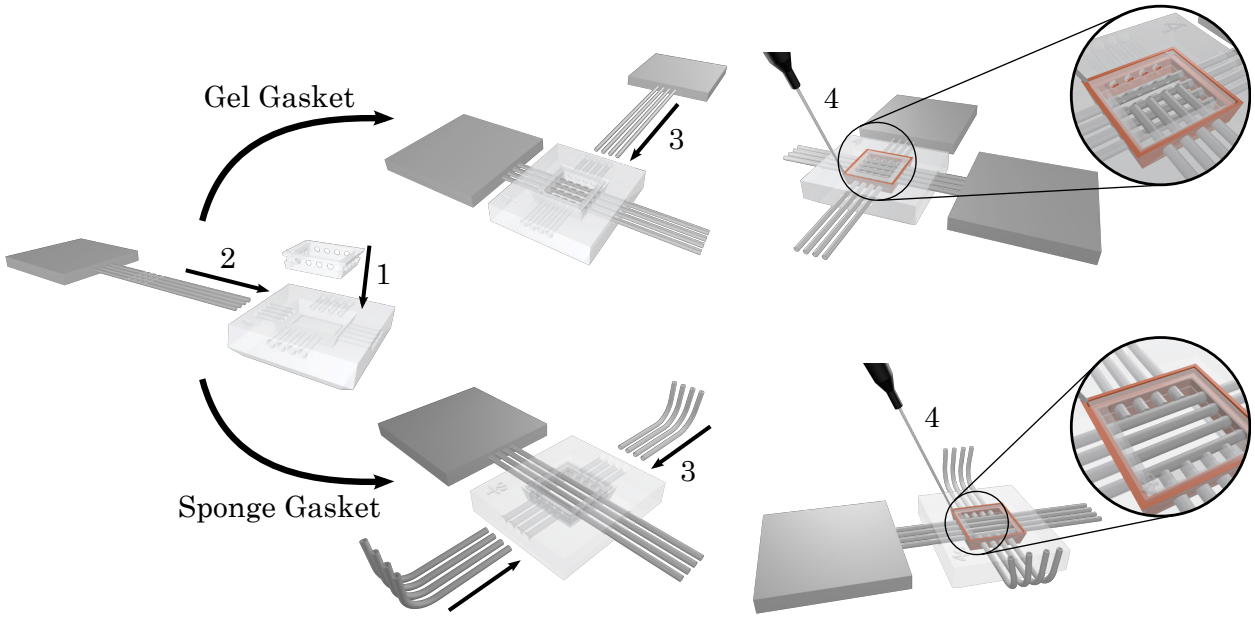

Figure 2.2: **Silicone Gasket Casting.** Workflow diagram of the silicone mold assembly and casting for sponges and biopolymer gels. The open channels in the gasket made for gels are offset from each other in order to accommodate stainless steel tubing alignment required when casting gels (see Fig. 2.5), whereas the channels in the sponge gasket are all in the same plane. A magnified view of the last step highlights how metal tubing was aligned during the making of the gaskets.

the scaffold and exited the bioreactor through a single channel at the opposite end of the bioreactor inlets. Around the cluster of threaded holes in the base of the bioreactor was a barbed fitting over which a silicone tube fit. The silicone tube jacketed the FEP tubes containing cell culture media, and it contained water maintained at 37°C by a circulating bath. A diagram of the fully assembled water jacket is shown in Fig. 2.3 (a)-(b). The purpose of the water jacket was to warm cell culture media to body temperature immediately prior to entering the bioreactor. Water baths are also a potential source of cell culture contamination [239]. Due to the risk of biologically contaminated water coming into close contact with the bioreactor, the circulated water was eventually replaced with heated airflow. Pressurized air was passed through a high-efficiency particulate air (HEPA) filter and heating element (Belilove Company-Engineers, Mini Clean Flow Heater) at 5 standard cubic feet per minute

(scfm). A thermocouple located in the base of the heat exchange jacket and the heating element and were connected to a PID controller (Belilove Company-Engineers, BCE10390). Heated air passed through insulated tubing into the jacket. From the jacket it was discharged to the atmosphere. The heated air flow path is diagrammed in A.10.

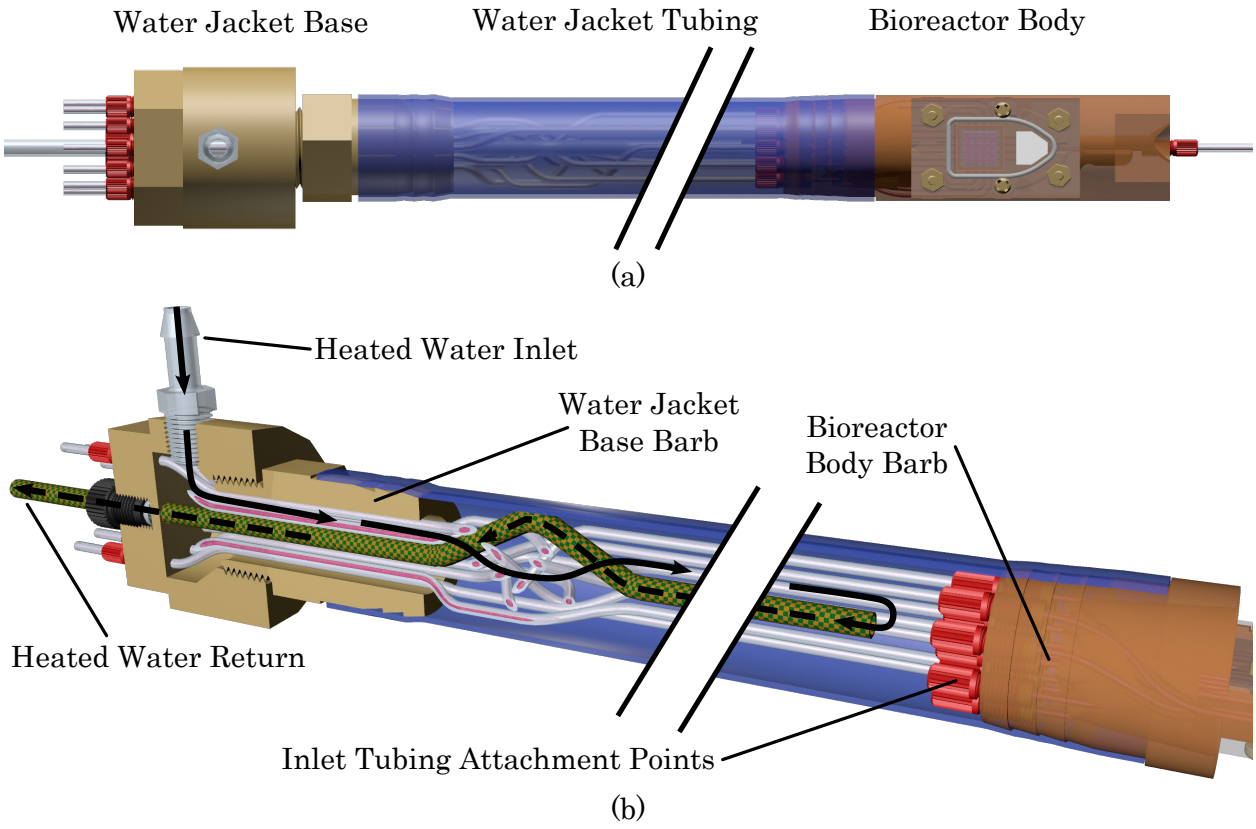

Figure 2.3: **Water Jacket Diagram.** (a) Top view of bioreactor with fully assembled water jacket. (b) Cross section view of water jacket showing flow path of heated water. Solid black arrows indicate heated water flow from the entrance of the water jacket to the base of the bioreactor. Dotted arrows indicate heated water flow out of the water jacket through an exit tube, which is highlighted by a checkered pattern.

2.2.1.2 Bioreactor Flow Process

A process flow diagram (PFD) detailing the bioreactor flow setup is presented in Fig. 2.4.

Primary Flow Path: The primary flow path is a closed circuit in which a peristaltic pump

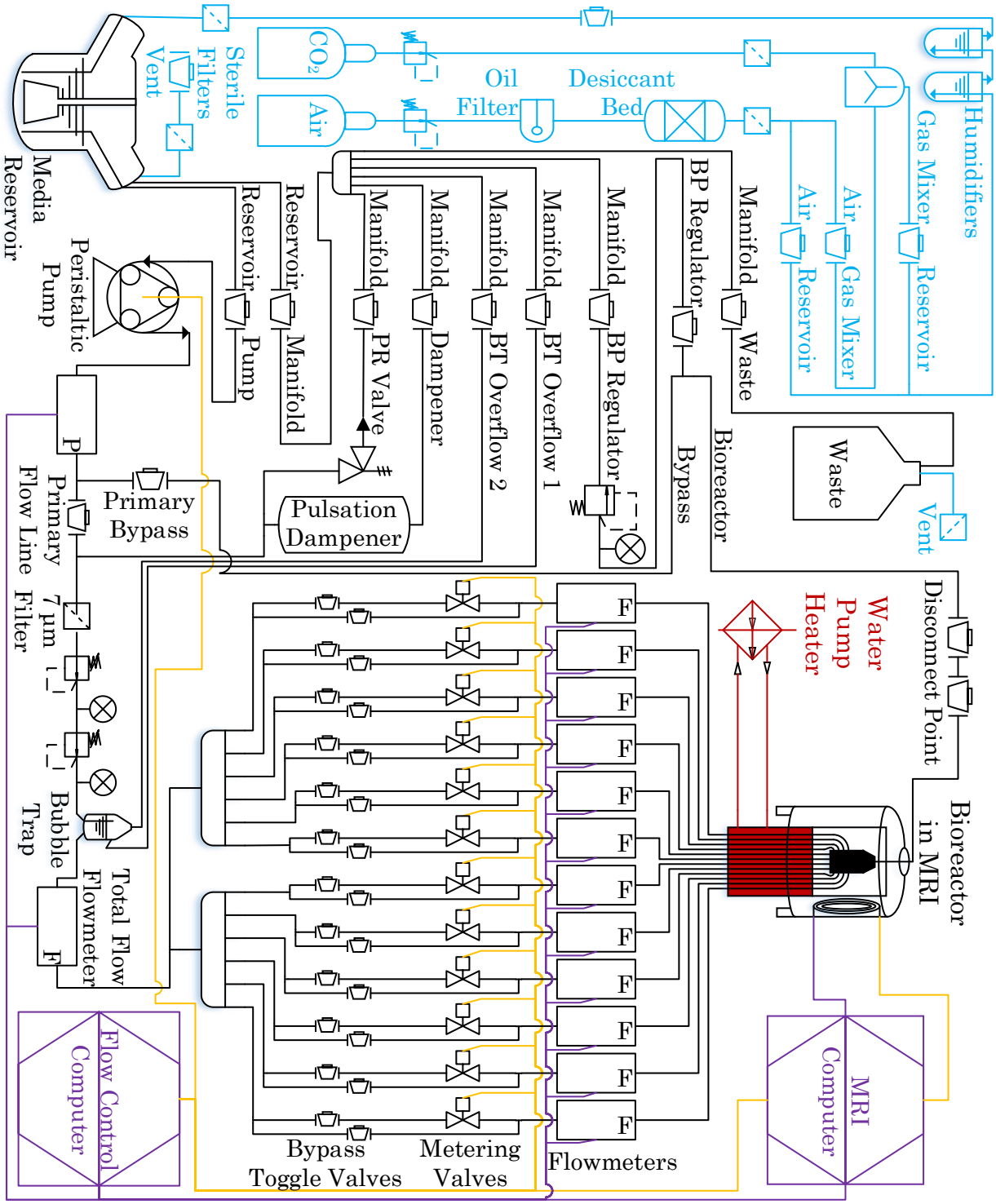

Figure 2.4: **Process Flow Diagram.** Color Legend: Black - cell culture media, blue - gas flow, yellow/purple lines - digital signals generated and received by computer, red - 37°C water. Abbreviations: BT - Bubble Trap, PR - Pressure Relief, BP - Back Pressure

circulates cell culture media through the twelve channel bioreactor. The pump draws media from a reservoir and sends it through two pressure reducing pressure regulators in series that dampen pressure spikes generated by peristaltic motion. A digital pressure gauge monitors output from the pump. From there the media passes through a bubble trap and then a digital flowmeter measuring the total volumetric flow rate passing through the bioreactor. The path separates into twelve parallel channels. Each of these channels includes a computer actuated metering valve and digital flowmeter to independently control all bioreactor inlet flow rates. Cell culture media passes through about 25 feet of tubing before entering the bioreactor. The six feet of tubing immediately upstream of the bioreactor are contained in a jacket maintained at 37°C to bring cell culture media to body temperature prior to entering the TC chamber. Downstream of the bioreactor the media passes through a back pressure regulator before entering a manifold and then returning to the reservoir. The primary flow path is highlighted in Fig. A.11.

Secondary Flow Paths: The manifold through which cell culture media passes prior to returning to the reservoir serves as a convergence point for several secondary flow paths configured in parallel to the primary flow path. In conjunction with a series of stopcocks the manifold is used to redirect and manage flow through these paths. In order to prolong the life of the tubing in the peristaltic pump (GORE® STA-PURE®), the pressure downstream of the pump head is prevented from exceeding 40 PSI with a pressure relief valve installed in a secondary flow path parallel to the primary bioreactor flow circuit. During normal operation, any cell culture media that passed through the pressure relief valve was returned directly to the reservoir through the manifold. Another secondary flow path in parallel to the bioreactor circuit includes a segment of large inner diameter (ID) tubing. The stopcock used to toggle flow through this path was kept closed during normal operation in order to trap a volume of air. The trapped air experiences cyclical compression and dampens peristaltic induced pressure spikes. Dampening the pressure spikes reduces pulsatile flow rates, hence this component was named the pulsation dampener. Lastly, the bubble trap used in the primary flow path (Radnoti) is constructed with two overflow ports. These ports are both connected to the manifold and normally remain closed, but they could be opened briefly to

remove any buildup of trapped air during daily operating inspections. The secondary flow paths are highlighted in Fig. A.12.

Other Flow Paths: The final flow path connected to the manifold leads to a waste collection vessel. A flow line called the primary bypass connects the output of the peristaltic pump to the flow line immediately downstream of the bioreactor. Each computer controlled metering valve includes a small bypass that was used for rinsing the system quicker than it could be rinsed with the metering valve alone. These flow paths are highlighted in Fig. A.13.

2.2.2 Scaffold Preparation

Two classes of scaffold were prepared for use in the bioreactor: macroporous sponges and hydrogels. In both cases scaffolds were comprised of natural extracellular matrix (ECM) proteins. Multiple types of scaffolds were investigated to demonstrate that this bioreactor is a tool that can be applied to several different TE environments. It was also done to show the impact of different scaffolds on velocity maps and to show the steps necessary to adapt scaffolds with different properties for use in the proposed multi-inlet design.

2.2.2.1 ECM Hydrogel Mixtures

Hydrogels were cast with a mixture of fibrin, Matrigel® (Corning®), and rat tail derived type I collagen (Corning®). Matrigel® is approximately 33% laminin, 60% collagen IV, and 5.4% heparan sulfate [341]. Several hydrogels made from different combinations of ECM proteins were evaluated for their mechanical stability under flow and ability to promote endothelial cell organization. Endothelial cells were used because of their well-established response to flow and shear stress [19, 127–130, 214, 215] and because 3D *in vitro* models of endothelial vessel linings have immediate practical applications in current research due to their ability to better represent *in vivo* conditions [349]. The complete composition of each gel mixture is seen in Table 2.1. Final concentrations of the structural ECM components are seen in Table 2.2. Prior to casting the gel, fibrinogen and thrombin powders were dissolved and sterile filtered through a 0.22 μm pore size membrane. Fibrinogen was dissolved in

Table 2.1: ECM Hydrogel Compositions.

All Components	Gel 1	Gel 2	Gel 3	Gel 4
	Volumes (μL)			
Collagen (9.66 mg·mL^{-1})	96.34	306	235	241
NaOH (1 M)	4.82	15.31	11.75	11.84
10X DMEM	28.9	28.3	28.5	22.2
FBS	3.85	3.77	3.80	2.96
Thrombin (100 units·mL^{-1})	28.9	28.3	40.0	44.4
Matrigel®	48.2	47.2	47.5	37.0
Fibrinogen (mg·mL^{-1})	289 (10)	70.7 (25)	133.5 (25)	141.1 (25)

Table 2.2: Final ECM Concentration

ECM Components	Gel 1	Gel 2	Gel 3	Gel 4
Collagen (mg·mL^{-1})	1.9	5.9	4.5	4.7
Fibrinogen (mg·mL^{-1})	5.8	3.5	6.7	7.0
Matrigel® (%)	9.6	9.4	9.5	7.4

Dulbecco's Modified Eagle Medium (DMEM) and kept in a warm bath at 37°C prior to use. Thrombin was dissolved at 100 units·mL^{-1} in 0.1% (w/v) bovine serum albumin (BSA) solution and kept at 4°C.

When preparing gels, collagen solution and NaOH were combined first to neutralize pH and kept on ice to preventing premature gelation. The 10X DMEM, fetal bovine serum (FBS), Thrombin, and Matrigel® were added to the neutralized collagen solution and mixed on ice carefully with a positive displacement pipette to prevent bubbles from entering the solution. While the chilled solution was kept on ice, human aortic endothelial cells (HAECs) were trypsinized and counted. 9×10^5 cells were placed into a separate tube and pelleted in a centrifuge. After aspirating the neutralized trypsin, the pellets were suspended in fibrinogen solution. Fibrinogen cell suspension containing 7.5×10^5 cells was added to the

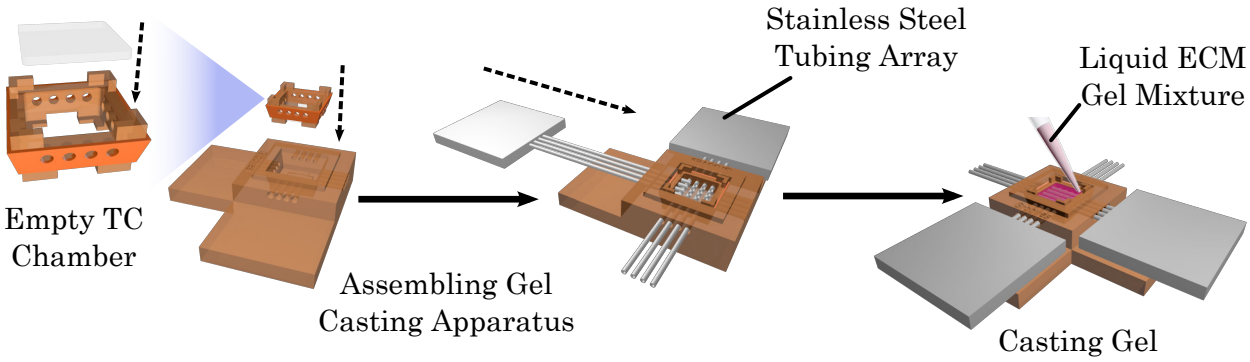

Figure 2.5: **Diagram of the components and assembly of the gel casting apparatus.** All components except for the top quartz window were assembled during steam sterilization. The top quartz window was placed with sterile forceps immediately after the chamber was filled with liquid gel in order to flatten the convex meniscus that formed at the surface of the gel.

chilled solution and mixed quickly and thoroughly to generate a final cell concentration of 1.5×10^6 cells·mL^{-1}. Care was taken not to introduce air bubbles during mixing. Within thirty seconds after combining the fibrinogen and thrombin the mixture was transferred to either a gel casting chamber for perfusion experiments or a 96 well plate for static culture experiments. The mixture was placed in an incubator at 37°C for 30 minutes to anneal. Following gelation the wells were filled with cell culture media, or the TC chamber was loaded in the bioreactor.

Due to low hydraulic conductivity and mechanical strength of natural ECM based hydrogels, open channels in the gel were created to accommodate fluid velocities corresponding to physiologically relevant wall shear stresses (5-20 dyn·cm^{-2}) for endothelial cells [28]. In order to form a gel with channels, the gel was cast over a grid of stainless steel tube segments that could be removed following annealing. A gel casting chamber was designed to align tubes with the inlets of the TC chamber. The gel casting chamber was assembled and steam sterilized in a stainless steel catheter instrument tray. A diagram of the gel casting chamber is seen in Fig. 2.5. In order to generate a grid of overlapping channels in the gel using two perpendicular tubing arrays, notches were machined into one tubing array to allow the other

tubing array to pass through it. This design resulted in the two perpendicular tubing arrays being offset from each other by 50% of the tubing diameter and offset from the bioreactor inlets and outlets by 25% of the tubing diameter. Despite the offset, a continuous plane of connected channels was established in the middle of the gel. Compared to a macroporous sponge in which all channels were cut in the same plane, the degree of channel offset in a biopolymer hydrogel is highlighted in a cross section view of the gel in Fig. 2.6.

The specific protocol for gel preparation follows. Matrigel®, which is delivered as a frozen solution, was thawed overnight in an ice bucket in a 4°C refrigerator. Fibrinogen powder was dissolved in DMEM to form a solution with a fibrinogen concentration of 25 mg·mL^{-1}. Fibrinogen solution was filtered through a 0.22μm pore size syringe filter to sterilize. Thrombin powder was dissolved in 0.1% (w/v) BSA solution to form a solution of 100 units·mL^{-1} and sterile filtered before use. Each lot of thrombin specifies the activity of the enzyme powder in units·g^{-1}, allowing a solution to be prepared according to enzymatic activity based on a mass measurement. Collagen is shipped as a sterile liquid solution with the concentration specified on the vial. If it is too concentrated, it can be diluted with sterile deionized water. Sodium hydroxide solution can be prepared by dissolving solid pellets or purchased as a premade solution. Sodium hydroxide solution was sterile filtered before use. All other components (FBS and DMEM) are commercially available as sterile solutions.

All components of the casting chamber except for the top quartz window were assembled and steam sterilized inside a metal catheter tray. The top quarts window and a pair of forceps were sterilized in the tray as well. During gel preparation, cold positive displacement pipette tips were used to measure viscous solutions containing collagen or Matrigel®. Solutions of collagen, NaOH, 10X DMEM, FBS, thrombin, and Matrigel® were kept on ice immediately prior to use. After the addition of each component, the mixture was pipetted up and down repeatedly to mix. Care was taken no to introduce bubbles when pipetting.

Once all components were in solution form, the collagen, NaOH, 10X DMEM, FBS, thrombin, and Matrigel® were combined with micropipettes and mixed well in a tube sitting in ice. Cells cultured in a 5% CO_2 atmosphere at 37°C were trypsinized, counted, and pelleted in a separate tube that was kept warm in a 37°C bath. Cells were suspended in the

fibrinogen/DMEM solution. The cell suspension was combined with the cold ingredients, mixed quickly, and then cast into the tissue culture chamber or the well of a 96 well plate within $\sim$ 15 seconds. The top quartz window was positioned with the sterile forceps. The catheter tray was then closed and placed in the 37°C incubator for 1.5 hour to allow gel annealing. Gel annealing occurs by three mechanisms: the cleavage of fibrinogen into fibrin, the warming of collagen, and the warming of Matrigel®. Once the gel had annealed, the needles were removed, leaving behind open channels.

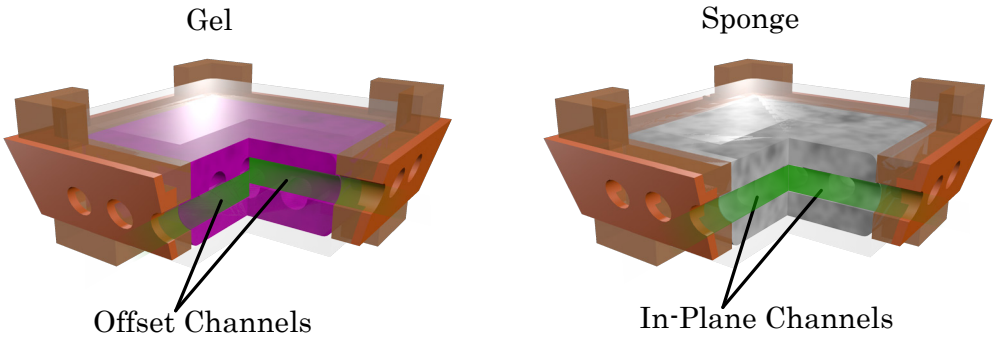

Figure 2.6: **Channel Alignment Comparison.** Diagram of channel alignment in cross sectional view of completed scaffolds. The channel paths are highlighted in green.

2.2.2.2 Porous Sponges

Macroporous sponges evaluated in this study were either collagen- (Ultrafoam™, Avitene™) or gelatin- (Gelfoam®, Pfizer) based. Sponges were cut into blocks with a scalpel blade and discs with a circular biopsy punch. To cut sponges consistently with appropriate dimensions for the TC chamber, scalpel blades were aligned with slits in parts made from Dental SG resin. Dry sponge blocks were attached to the inner walls of the TC chamber with a nitrocellulose-based adhesive film (New-Skin® liquid bandage) to prevent the sponge edges from retracting from the walls of the TC chamber following wetting. Scaffolds not properly anchored to the bioreactor chamber wall (due to initial placement or erosion) may result in edge flows in which cell culture media preferentially flows around the scaffold rather than through it, and erosion can occur [27, 200, 231]. Edge flows increase nutrient delivery to

cells in the peripheral regions and reduce transport to the interior of a scaffold [231]. They also introduce flow behavior that may be unaccounted in predictive fluid simulations. After allowing the adhesive to dry for four hours, channels were cut through sponges by focusing a 1500 mW laser (Genesis CX, Coherent) tuned to 532 nm through the holes in the sides of the TC chamber. In order to prevent damage to the TC chamber during laser cutting, a slightly smaller channel diameter of 1.4 mm was used to keep the beam a safe distance from the chamber walls. Prior to laser cutting, the TC chamber containing the adhered sponge was sealed in a steam sterilized laser cutting box made from Dental SG. Microscopy coverslips adhered to the sides of the box with a high temperature resistant epoxy allowed light to enter the sponge while preventing microbial contamination during cutting. The box was secured on a stepper motor with a grub screw. The motor was used to rotate the box in 90° increments to allow cutting through all sides of the box. The motor was mounted on a three directional micrometer stage used to position the box beneath the focused laser beam. Sterile filtered (0.22 μm pore size) airflow was directed through the space between the sponge and coverslip to remove smoke particles from the chamber that were generated during the cutting process. A diagram of the laser cutting assembly can be seen in Fig. 2.7.

Following laser cutting sponges were seeded by soaking them in cell suspension containing 1.5×10^6 cells·mL^{-1} for 2 hours. After seeding the remaining cell suspension was removed and sponges were placed in either a six well plate for static culture or into the bioreactor for perfusion culture.

2.2.2.3 Biological Evaluation of Scaffolds with Endothelial Cells

Scaffold materials were evaluated for their ability to promote endothelial cell attachment and branching morphology using thin test scaffolds. Thin scaffolds were used so that diffusion limits would not reduce cell growth in the scaffold interior. The objective of this test was to determine if these scaffold materials promote attachment, migration, and branching morphology. Cells were seeded on test scaffolds and cultured statically for five days at 37°C in 5% CO_2. At the end of that period, constructs were fixed by submersion in 2% formaldehyde so-

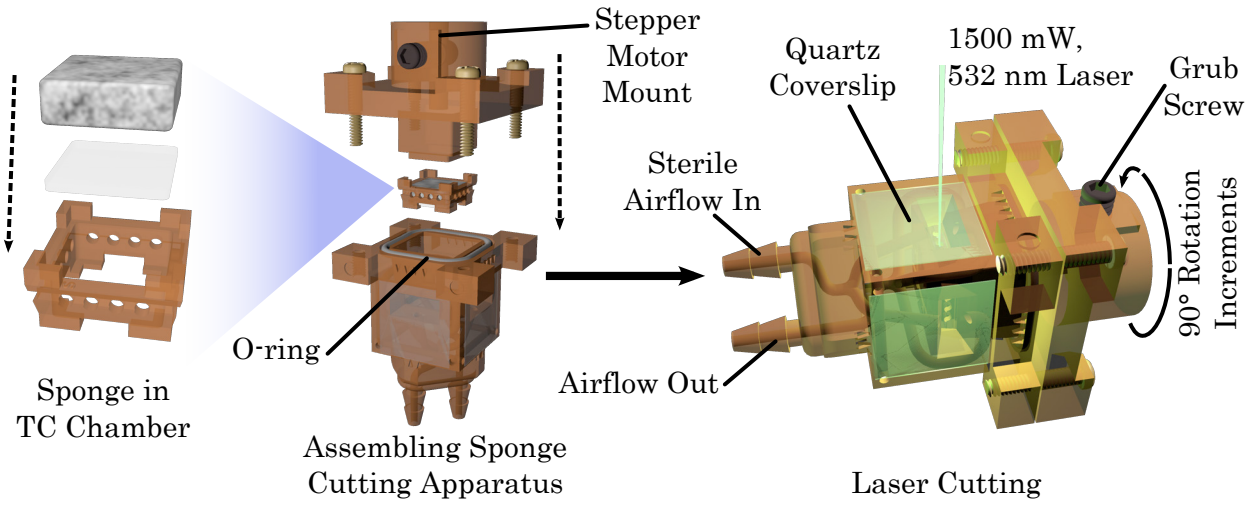

Figure 2.7: **Sponge Laser Cutting Apparatus.** Diagram includes the components and assembly steps of the apparatus used to contain and position the sponge during laser cutting. All components were steam sterilized prior to assembly. Before placing the sponge in the TC chamber, nitrocellulose based adhesive film was applied to the inner walls of the TC chamber with a brush.

lution for one hour. The 2% formaldehyde solution was prepared by diluting a commercially available 16% formaldehyde solution with phosphate buffered saline (PBS). After fixation, constructs were rinsed with PBS and permeabilized. A permeabilization solution was prepared by combining 25 mL Hank's Balanced Salt Solution, 75 μL Triton-X, and 12.5 μL Tween-20. Scaffolds were submerged in permeabilization solution for one hour. After permeabilization, test constructs were stained with 4',6-diamidino-2-phenylindole (DAPI) and Texas Red™-X Phalloidin and imaged with a confocal microscope (Leica SP2). DAPI stains cell nuclei and Texas Red™-X Phalloidin stains the actin cytoskeleton. A 0.14 mm^2 field of view was acquired to demonstrate attachment and spreading.

2.2.2.4 Confocal Imaging of Full-Size Scaffold

B16-F10 cell distribution was mapped in full-size (0.4 cm × 1.2 cm × 1.2 cm) constructs cultured statically and under flow. The distribution of B16-F10 cells cultured statically was mapped across the entire scaffold area using confocal tile stitching. Following culture,

samples were fixed and permeabilized as described in the previous section. Next, since the samples were thick, they were embedded in paraffin, sectioned into 20 μm thin sections, deparaffinized, blocked, stained with primary and secondary antibodies for Ki67 (a proliferation marker) using Opal 650 (Akoya), and stained with Hoechst 33258. Hoechst 33258 is an alternate nuclear stain, which was used because it distinguished cell nuclei more clearly.

2.2.3 Bioreactor Operation

2.2.3.1 Glutaraldehyde Sterilization

Prior to using the bioreactor for perfusion experiments, the entire system was sterilized with glutaraldehyde based sterilant (Cetylcide-G, Cetylite®). First the system was drained of existing liquid such as cell culture media from a previous experiment using a liquid removal cycle (see Supplemental Sec. A.1). Next the system was primed with deionized water using a liquid priming cycle (see Supplemental Sec. A.2) to rinse out any residual cell culture media (proteins in FBS can potentially precipitate out of solution and clog filters and valves if not removed prior to sterilization). A liquid removal cycle was used to drain the system of the rinse water. Once emptied, the waste reservoir was emptied and the media reservoir was filled with sterilant. The system was then primed with sterilant. During priming, care was taken to remove all air bubbles and ensure all interior surfaces were wetted with sterilant. Any sterilant discharged into the waste reservoir during priming was recycled into the media reservoir as needed. Once the system was primed with sterilant, it was incubated for a time period of greater than or equal to 10 hours according to the manufacturer's (Cetylite®) instructions to ensure complete sterilization.

In addition to priming the internal volume of the system with sterilant, two external regions of the system outside of the sealed flow path were flushed with sterilant due to the potential for them to experience brief contact with cell culture media at specific points of operation. These two regions include the space in between the top bioreactor window and the bioreactor body and the Luer lock connection between the stopcocks at the disconnect point (see Fig. 2.8). Both were soaked with sterilant for the required time.

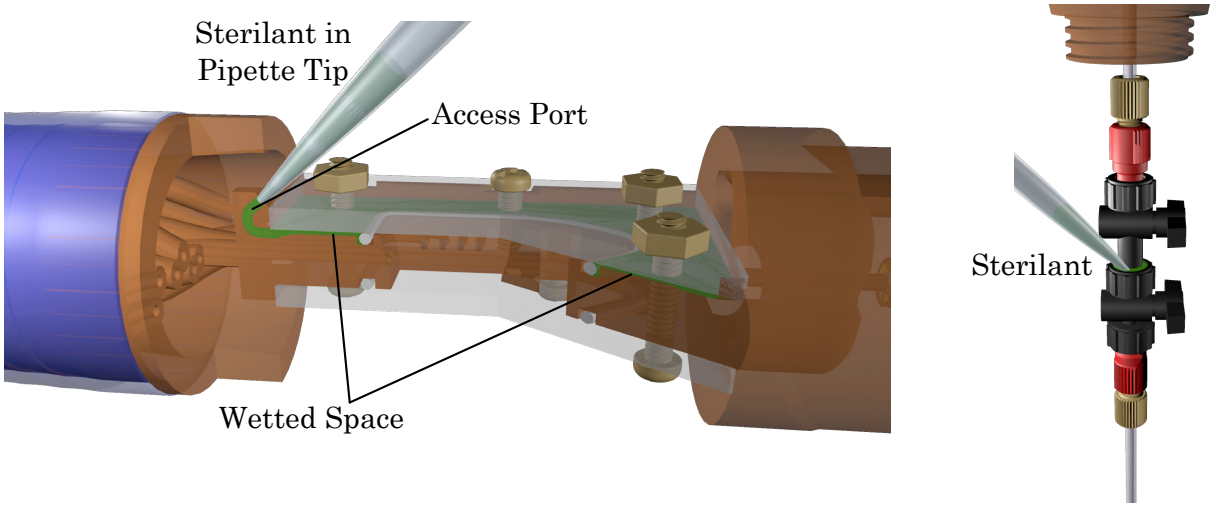

Figure 2.8: **External Sterilization.** Diagram showing sterilization of bioreactor components outside of the closed circuit flow path. The left side shows a cross section view in which the thin space between the bioreactor body and the top polycarbonate window is injected with sterilant. The right side shows sterilant being injected into the threads surrounding the Luer lock connection at the disconnect point.

During the incubation period, the media reservoir was disconnected from the rest of the system, washed, and steam sterilized. In order to disconnect the reservoir aseptically, the stopcocks at the ends of the two flow paths connecting to the media reservoir containing sterilant were closed prior to removal. The ends of these stopcocks were submerged in a sterilant bath while the reservoir was autoclaved. The two flow paths connected to the media reservoir used for gas phase flow were capped with 0.22 μm pore size filters that were compatible with steam sterilization (Whatman™ Polyvent). These filters were kept on the media reservoir during the steam sterilization cycle.

After the incubation time the media reservoir was reconnected to the rest of the system. The sterilant was drained from the system using a liquid removal cycle. Residual sterilant was rinsed from the system using deionized water that had been steam sterilized. In order to thoroughly remove residual sterilant, the system was first primed with sterile deionized water. Next, each component of the system was flushed with volumes of sterile deionized

Table 2.3: Rinse Volumes for each Flow Path

Flow Path	Rinse Quantity (L)	Valve Configuration
Manifold to Media Reservoir	0.5	1
Primary Bypass	1	2
Dampener to Manifold	1	3
Pressure Relief to Manifold	1	4
Bubble Trap Overflow 2 to Manifold	1	5
Bubble Trap Overflow 1 to Manifold	0.5	6
Flow Control Valve Bypasses (Initial Rinse)	0.5	7
Flow Control Valves	-	8
Flow Control Valve Bypasses (Final Rinse)	1	7

water in the order and quantity specified in Table 2.3. The media reservoir was pressurized to 20 PSI with compressed air to drive rinse flow throughout the system to the waste reservoir. Every time the rinse water was depleted, the reservoir was depressurized by closing the stopcock that allowed compressed air into the reservoir and opening the reservoir vent so that fresh water could be added. Sterile deionized water was added to the system aseptically by transferring it to the media reservoir in a HEPA filtered environment. When rinsing the digitally controlled metering valves, a program was run that opened all channels sequentially for four minutes each. Following all rinsing, the system was drained of deionized water.

Prior to running the bioreactor, the surfaces inside the HEPA filtered environment and the surrounding lab benches were wiped down with 70% ethanol solution. Floors in the lab were mopped with dilute acetic acid solution. Exterior surfaces of the bioreactor were wiped down with 70% ethanol solution.

2.2.3.2 Ethylene Oxide Gas Sterilization

Due to the large quantities of sterile water and time required for flushing glutaraldehyde residues from the system, a second sterilization method was used involving ethylene oxide

(EtO) gas. In order to ensure the bioreactor system could physically fit into the available gas chamber (interior dimensions: 29 cm × 29 cm × 70 cm), the bioreactor system was separated into discrete modules which could be disassembled at luer lock connections. Separating the bioreactor into modules also ensured that the ratio of tubing lumen length to inner diameter was small enough to allow complete gas sterilization. All interior surfaces were rinsed with deionized water and dried prior to sterilization to remove residual salts and protein, which is required for proper sterilization [350]. The Luer lock ends were capped with 0.22 μm syringe filters prior to sterilization to allow gas penetration during sterilization and prevent microbial entry following the sterilization cycle. The separate modules that were sterilized are shown in Fig. 2.17 (c) and highlighted in Fig. A.10. These modules include the media reservoir (red), the bioreactor body and temperature controlled jacket (green), the flow controllers (yellow), and a centralized hub with manually operated stopcocks (blue). The ∼20 feet of tubing in between the flowmeters and temperature controlled jacket as well as the ∼20 foot long return line between the bioreactor outlet and disconnect point (magenta) were steam sterilized after wrapping the ends with foil. Following sterilization of the modules, all tubing ends were reassembled aseptically in a laminar flow HEPA filtered workspace.

2.2.3.3 Bioreactor Experiment Initialization

Tissue Culture Preparation: Following glutaraldehyde sterilization, the bioreactor system was fully primed and drained of PBS to remove any deionized water residue that could lower the osmotic concentration when priming with cell culture media. The system was primed with 500 mL of cell culture media using a modified liquid priming cycle that differed from the one described in Sec. A.2 in three ways. First, rather than using pressurized air to prime the entire system, pressurized air was only used to prime the line from the reservoir to the peristaltic pump tubing using the flow path configuration shown in Fig. A.4. Once the peristaltic pump tubing was primed, the pump head was engaged and activated to circulate cell culture media back to the media reservoir rather than discharge to the waste reservoir. The primary and secondary flow circuits, with the exception of the pulsation dampener (see Figs. A.11 and A.12), were primed using the pump. Second, the bioreactor was oriented with

its outlet below its inlets in Earth's gravity to trap air in the space for the TC chamber. Third, the pulsation dampener path was not primed with any cell culture media in order to leave a large pocket of trapped air in the dampener.

Sample Loading: After preparing the bioreactor system for tissue culture and seeding a scaffold, the bioreactor was clamped horizontally in a HEPA filtered environment so that the inlets and outlets were at a level height. In order to prevent any spillage from occurring when opening the bioreactor, the valves in the system were set to flow configuration 8 (diagramed in Fig. A.9), and the peristaltic pump was activated in reverse at a low speed to generate a slightly negative gauge pressure in the bioreactor. The top window on the bioreactor was removed with sterile tools, and the TC chamber was inserted into the empty bioreactor chamber. The top polycarbonate window was put back in place and tightened with nuts and screws. Tightening the window caused it to push down on the upper prongs of the TC chamber forcing the chamber to seal against the tapered walls of the bioreactor chamber.

Bubble Removal: Once the TC chamber was in place, the bioreactor was oriented vertically with the outlet above the inlets. All inlet flow rates were set to 0.3 $\text{mL}\cdot\text{min}^{-1}$ to push air out of the bioreactor chamber. Light transmitted through the TC chamber was used to identify trapped bubbles, which were dislodged by mechanically agitating the bioreactor. Persistent bubbles were removed by increasing the hydrostatic pressure in the bioreactor to 25 PSI with the BP regulator. The pressure increase reduced the size of the trapped bubbles and allowed them to be dislodged with mechanical agitation and flow. Once all bubbles were removed the inlet flow rates were set to desired values for the experiment.

Aseptic Placement of Bioreactor in MRI: To insert the sterile, closed circuit bioreactor in the MRI, the two stopcocks at the disconnect point were closed and disconnected from each other in a HEPA filtered environment. The end to be inserted through the MRI was closed off from its surroundings with a part made from stereolithographic resin that had been pre sterilized (see Fig. 2.9), allowing it to be handled outside of a HEPA filtered environment without experiencing microbial contamination. The protected stopcock was pulled up through the MRI probe and magnet with a string attached to a hook built into the stopcock cover. Once it passed through the magnet it was reattached to the other

stopcock of the disconnect point. The bioreactor could then be positioned in the magnet.

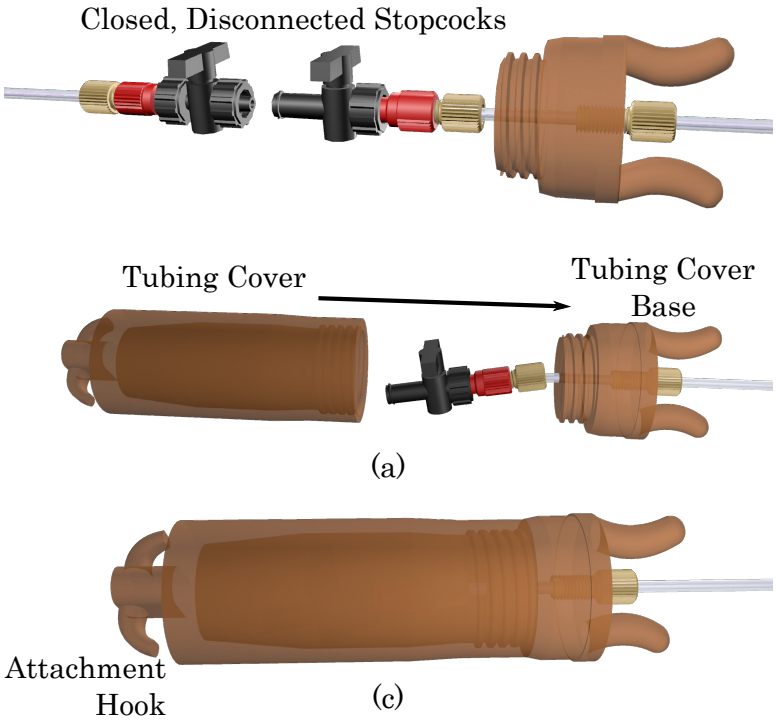

Figure 2.9: **Disconnect Point Cover.** (a) Assembly of the cover for the disconnect point. The assembly is done aseptically in a HEPA filtered environment. The tubing cover is sterilized before assembly. (b) Fully assembled tubing cover.

2.2.3.4 Flow Controller

Individual flow rates were controlled automatically by a MATLAB program that measured each channel's volumetric flow, determined the difference between the measured flow rates and the set points, and adjusted the degree to which the metering valves were opened based on the difference. The following is a brief description of the algorithm. Once the program is initiated, MATLAB is connected to an Arduino MEGA 2560 and two Fluigent Flow Rate Platforms connected to twelve flowmeters (Fluigent XL) using libraries provided by Fluigent. Digital pulse width modulation (PWM) voltage outputs from the Arduino are used to set the position of the metering valve actuators (VA21, ETI Systems). In MATLAB, the valve position corresponds to a PWM integer value from 0 to 255 where 0 corresponds to the valve's

fully closed position, 255 corresponds to fully open, and all numbers in between correspond to linearly spaced degrees of openness. All valve PWM values are initially set to 0.

Once the connections to the flowmeters and Arduino have been established, flow rates in all twelve channels are read into MATLAB every 2.3 seconds. This delay was chosen to prevent the software from frequently crashing while maintaining an adequate temporal response. All twelve set points are read into MATLAB from a text file at the same time interval. The differences between the set points and measured flow rates is calculated. Initially, the program quickly searches for the PWM value at which the set point is reached. During this initial search, if the setpoint is greater than the measured flowrate in a channel by less than 0.3 mL·min^{-1}, the PWM value is increased by 5. If the difference is greater than 0.3 mL·min^{-1} but less than 0.9 mL·min^{-1}, the PWM value is increased by 10. If the difference is larger than 0.9 mL·min^{-1}, the PWM value is increased by 18. Once the set point has been passed, adjustments are made in PWM increments of 1. If the flow rate is greater than the set point, the PWM value is decreased by 1, and if the flow rate is less than the PWM value, it is increased by 1. This method allowed all channels to reach their set points within two minutes (See Fig. 2.16).

2.2.3.5 Flow and Shear Maps

A flow-weighted spin echo multi-slice (SEMS) pulse sequence was used to acquire fluid velocity maps within the bioreactor. The pulse sequence for flow imaging can be seen in Fig. 1.18. One image was acquired during perfusion, and another image was acquired while flow was turned off. Each no-flow velocity map was subtracted from its corresponding flow velocity map to account for artifacts from gradient nonidealities including eddy currents and nonlinearities. A map of the magnitude of flow speed was generated from the velocity maps using the equation:

$$\bar{s} = \sqrt{\bar{v}_x^2 + \bar{v}_y^2 + \bar{v}_z^2} \tag{2.1}$$

where $\bar{s}$ is the flow speed magnitude and $\bar{v}_x$, $\bar{v}_y$, and $\bar{v}_z$ are the orthogonal components of the velocity measured with MRI. They are represented with overhead horizontal bars since they

are measurements of the average velocity throughout the entire slice thickness, Z_{th}. Shear maps were calculated using:

$$\bar{\dot{\gamma}} = \left(\partial_x \bar{v}_y + \partial_y \bar{v}_x\right)/2 \tag{2.2}$$

where $\bar{\dot{\gamma}}$ is the shear rate of a voxel (measured in s^{-1}) and $\partial_x \bar{v}_y$ and $\partial_y \bar{v}_x$ are determined using finite differences. Briefly: given an $m \times n$ matrix, $\bar{v}_y$, of y direction velocity measurements, the matrix, $\partial_x \bar{v}_y$, of size $m \times (n-1)$ is approximated by taking the differences between all y velocity measurements adjacent to each other along the x direction and dividing them by the width of the voxels in the x direction, Δx. This can be expressed as:

$$\partial_x \bar{v}_y|_{i,j} \approx \left(\bar{v}_y|_{i,j+1} - \bar{v}_y|_{i,j}\right)/\Delta x \tag{2.3}$$

where i is an integer from 1 to m representing each row index and j is an integer from 1 to $n-1$ representing each column index. Similarly, $\partial_y \bar{v}_x$ can be approximated as:

$$\partial_y \bar{v}_x|_{i,j} \approx \left(\bar{v}_x|_{i+1,j} - \bar{v}_x|_{i,j}\right)/\Delta y \tag{2.4}$$

where $\bar{v}_x$ is an $(m-1)\times n$ matrix comprised of discreet x velocity component measurements, i is the row index from 1 to $m-1$, j is the column index from 1 to n, and Δy is the y direction length of the voxels. Since the two matrices had different dimensions from each other, they were both resized to the original $m \times n$ size using MATLAB's bicubic interpolation function in which the output pixel value is a weighted average of pixels in the nearest 4-by-4 neighborhood.

2.3 Results

2.3.1 Static Scaffold Cell Culture Results

Representative confocal micrographs of HAECs cultured in each of the four gel compositions for five days can be seen in Fig. 2.10.

Multi cellular structures formed in all four gel compositions, but variations in the size, morphology, and abundance of the structures was apparent. The ECM composition of Gel 1, which was based off of previous flow studies [27], resulted in the formation of the largest,

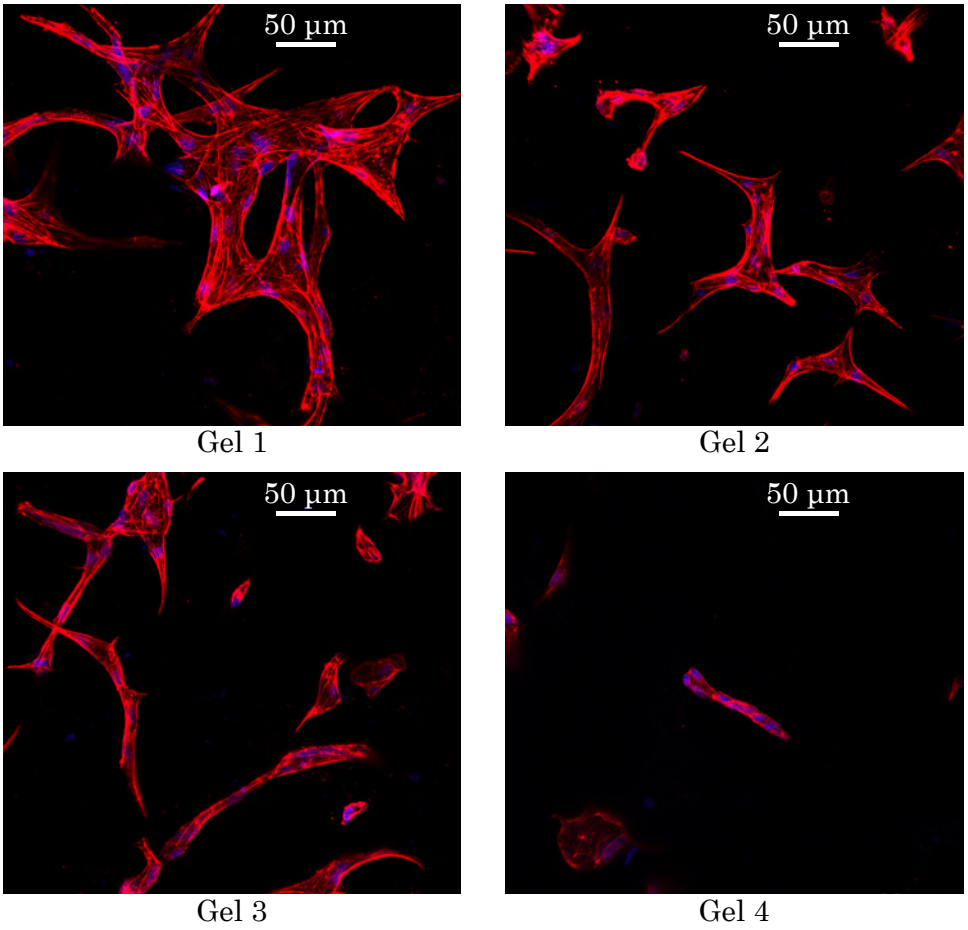

Figure 2.10: **HAEC Static Culture in Biopolymer Gels.** Representative confocal images of HAECs cultured statically in thin biopolymer hydrogel scaffolds. Cell nuclei were stained with DAPI (shown in blue) and actin was stained with Texas Red™-X Phalloidin (shown in red). (n=1)

most developed structures resembling vascular morphogenesis [128, 130]. In the confocal image of gel 1 shown in Fig. 2.10, a total of 50 nuclei were counted in two distinct structures, averaging 25 nuclei per structure. However, this gel composition was too fragile. When it was cast in the TC chamber, removal of the needles caused the channels to collapse immediately. When placed under flow, the gel rapidly disintegrated and washed out of the chamber. Cells cultured in gels 2 and 3 produced structures similar to each other in size and density. In the confocal image of Gel 2 shown in Fig. 2.10, a total of 37 nuclei were counted throughout 8 distinct structures, averaging ∼4.6 nuclei per structure. In gel 3, a

total of 38 nuclei were counted throughout 11 distinct structures, averaging ∼3.5 nuclei per structure. The multicellular structures in gels 2 and 3 were thinner in average diameter and less interconnected than the structures in gel 1. However, HAEC structures in gel 2 appeared to be more similar to those in gel 1 in their overall morphology. The degree of branching and webbing between branches was higher in gel 2 than in gel 3. The structures in gel 3 appeared more linear with less bifurcations and less webbing at bifurcated junctions. The structures in gel 4 were much sparser and smaller in size than in the other three gels. Within the structures in gel 4 the cell nuclei were more densely packed than in any of the structures seen in other gels. In the confocal image of Gel 4 shown in Fig. 2.10, a total of 11 nuclei were counted throughout 4 distinct structures, averaging ∼2.8 nuclei per structure. Gel 4 was the most mechanically stiff gel, but its poor suitability for HAEC growth made it unsuitable as a scaffold in perfusion cell culture experiments. Gels 2 and 3 were both able to withstand perfusion in the multi-inlet bioreactor for periods of up to two weeks. When cast between quartz windows they were able to maintain distinct channel geometry without collapsing. The confocal images are representative of cells cultured near the surface of the biopolymer hydrogel where nutrient and waste exchange is permitted by diffusion. These were acquired as a control to highlight the behavior of cells on the scaffold receiving adequate nutrition without experiencing shear. One sample of each gel was prepared, so further repetition is needed to ensure repeatability. At the time of acquisition, a tile scan protocol had not yet been developed to image large areas. However, the images acquired are similar in area to images in other studies of vascular morphogenesis [19, 127, 130]. Despite the potential for further optimization of the biopolymer mixture, gel 2 was chosen for additional experiments as it provided a sufficient starting point to study neovascularization within the scope of this thesis.

Representative confocal micrographs of HAECs cultured in macroporous sponges are shown in Fig. 2.11. The figure demonstrates that endothelial cells attach, proliferate, and migrate toward each other to blanket the walls and struts in collagen and gelatin sponges. Despite the fact that cells were able to attach to the alginate-RGD sponge, they did not proliferate into larger numbers, and they maintained randomly scattered positions, which

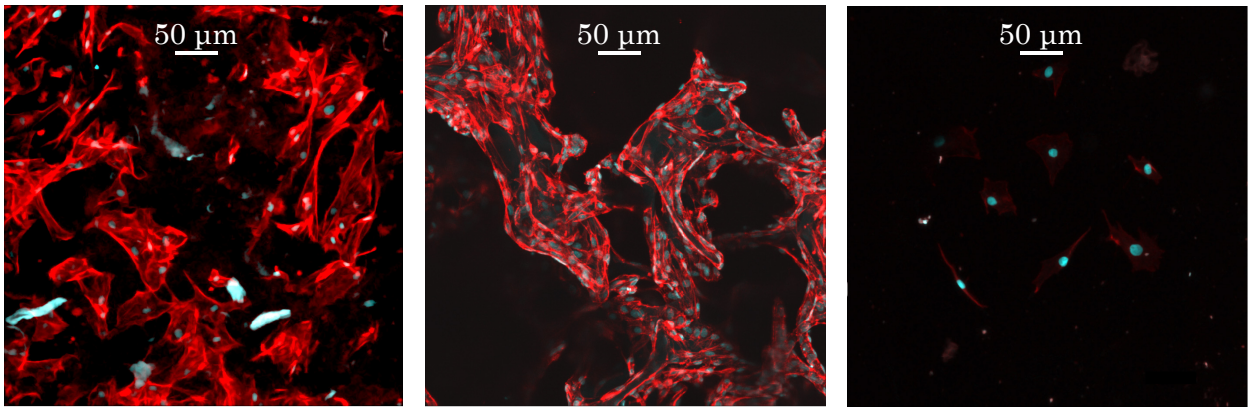

Figure 2.11: **HAEC Static Culture in Macroporous Sponges.** Representative confocal stacks of HAECs cultured statically in collagen, gelatin, and alginate-RGD sponges from left to right. Cell nuclei were stained with DAPI (shown in cyan), and actin was stained with Texas Red™-X Phalloidin (shown in red). (n=1)

indicated a lack of migration. Since the collagen and gelatin sponges promoted endothelial cell growth and were resistant to flow induced wear for up to two weeks in the bioreactor, they were both considered for 3D cell culture under flow. The confocal images are representative of cells cultured near the surface of the sponge where nutrient and waste exchange is permitted by diffusion. These were acquired as a control to highlight the behavior of cells on the scaffold receiving adequate nutrition without experiencing shear. One sample of each gel was prepared, so further repetition is needed to ensure repeatability. At the time of acquisition, a tile scan protocol had not yet been developed to image large areas. However, the images acquired are similar in area to images in other studies of vascular morphogenesis

Although the smaller and more homogenous distribution pore size of collagen sponges are preferred for generating more consistent fluid permeability properties, gelatin sponges were ultimately preferred due to their edge properties. In their commercially available form, gelatin sponges had pre-cut edges with structural pore geometry visibly consistent with the bulk interior of the scaffolds. The collagen sponges were sold with the edges formed during lyophilization still intact. These edges were less porous than the bulk interior. When cutting the commercially available sponges into thick squares using a scalpel, the gelatin sponges had consistent edge properties on all six sides, whereas the two large square faces on the

top and bottom of collagen sponges possessed distinctly different texture and pore geometry from each other and from the sides which were cut with a scalpel.

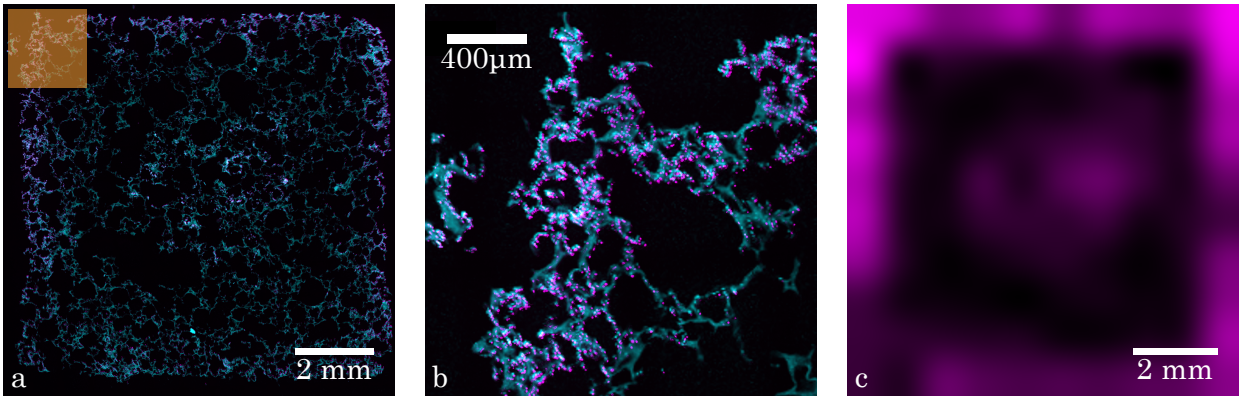

Figure 2.12: **B16-F10 Static Culture in Full-Size Macroporous Sponges.** (a) Confocal stack of 20 μm thick section of gelatin sponge cultured statically with B16-F10 cells. The gelatin sponge was cut to the size of the TC chamber and did not contain laser cut channels. Cell nuclei and gelatin sponge were stained with DAPI (shown in cyan), and mouse Ki-67 was antibody labelled with opal650 (shown in magenta). (b) Magnified view of orange highlighted region in (a). (c) Proliferating cell distribution map determined from Ki-67 confocal images of three 20 μm thick sections smoothed to a 10 by 10 grid with bicubic interpolation and averaged.

Representative confocal micrographs of B16-F10 murine melanoma cultured statically in a macroporous gelatin sponge are shown in Fig. 2.12 as a control to show the distribution of cells throughout a scaffold identical in size and material to the scaffold used in the bioreactor flow experiments. No channels were cut in this scaffold. Ki-67 was used as a marker of cell proliferation. It is shown that, across the entire scaffold, cell proliferation was localized toward the scaffold edges where nutrient availability is higher, as expected for static culture in a thick construct. The quantity of cell proliferation drops steeply about 500 μm from the scaffold edge. The average total number of proliferating cells counted in each section was $(1.55 \pm 0.03) \times 10^4$ cells.

2.3.2 Effect of flow on cell growth in 2D

The response of two dimensional (2D) surface constrained cell cultures to shear was examined using an Ibidi y-slide shown in Fig. 2.13 (a) in which a single flow path bifurcates into two symmetric paths that converge further downstream. HAECs were seeded on the bottom surface of the Ibidi y-slide channel, and pressurized endothelial cell basil media-2 (EBM™-2, Clonetics™) cell culture media was flowed through the channel at a rate of 9 mL·min^{-1}. The velocity map induced by the geometry of the channel was mapped with flow-weighted MRI. A map of wall shear calculated from the flow data is shown in Fig. 2.13 (b). Local flow induced shear at the wall of the channel was calculated from the flow rate in each voxel using the equation for fully developed pressure driven laminar flow between two infinite plates:

$$\tau_w|_{i,j} = \frac{6\mu Q_{i,j}}{W_{i,j}H^2} \tag{2.5}$$

where $Q_{i,j}$ is the total flow rate in the voxel, μ is the dynamic viscosity of cell culture media (6.92×10^{-4} kg·m^{-1}·s^{-1} [209]), $W_{i,j}$ is the projected width of the voxel perpendicular to the direction of flow in that voxel, and H is the height of the channel ($H = 400\mu$m). Volumetric flow through a voxel was determined from $Q_{i,j} = \sqrt{\bar{v}_x|_{i,j}^2 + \bar{v}_y|_{i,j}^2}W_{i,j}H$ where $W_{i,j}$ is calculated as shown in Sec. 2.4.2.2. The Ibidi slide was suspended vertically in the MRI with the device seen in Fig. 2.13 (c).

Confocal images of HAECs cultured in the bifurcation and convergence regions are shown in Fig. 2.14 (a) and (b) respectively. The specific location where confocal micrographs were taken is highlighted in these panels as well. The bifurcation region examined had a higher shear stress than the convergence region. Endothelial cells in the bifurcation region were more elongated and expressed higher quantities of NOTCH1 than cells in the convergence region. The functional dependence of NOTCH1 expression on shear was examined by measuring shear in nine adjacent ROIs along a shear gradient formed downstream of the convergence point and measuring the % of cells expressing nuclear NOTCH1 in each ROI. The results are shown in Fig. 2.14 (c). It can be seen that the dependence of nuclear NOTCH1 expression on shear stress is hyperbolic, and it can be seen that NOTCH1 expression is most sensitive to shear stresses ranging from 10 to 26 dyn·cm^{-2}. Approximately 100% of cells express nuclear

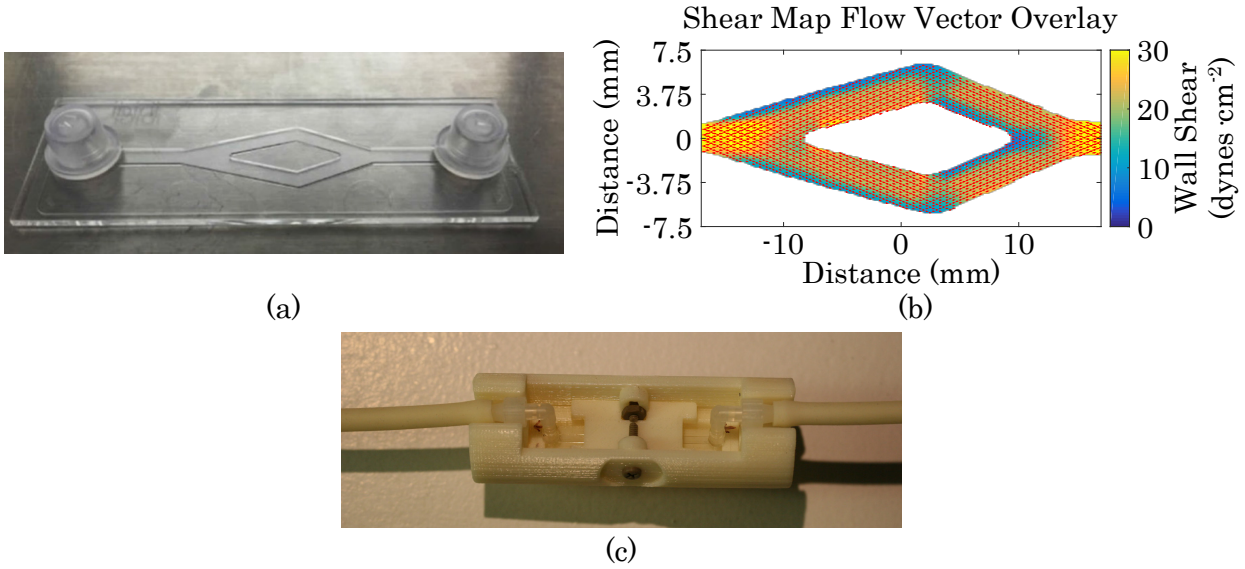

Figure 2.13: **Shear over 2D endothelial monolayer.** (a) Endothelial cells (HAECs) were plated to confluency on a y-slide (Ibidi) and subjected to laminar flow (9 mL min^{-1} applied). (b) MRI flow mapping of y-slide in the presence of flow-conditioned HAECs (48 h) generated flow vector plots across all regions of the y-slide (n = 5). (a-b) © 2017 Mack et al. Adapted from [28]; originally distributed under a Creative Commons Attribution 4.0 International License. (c) Device used to suspend y-slide in 40 mm MRI probe.

NOTCH1 above this range.

2.3.3 Effect of flow on cell growth in 3D

To explore the effect of shear distribution on parenchymal cell distribution in 3D tissue culture, B16-F10 cells were cultured for 6 days in the bioreactor with inlets 3, 4, 11, and 12 set to 0.5 mL·min^{-1}. A Gelfoam® sponge without laser cut channels was soaked in a cell suspension containing 1×10^7 cells·mL^{-1} for 30 minutes prior to placing it in the bioreactor under flow. Flow speed and fluid-induced wall shear maps corresponding to these conditions are shown in Fig. 2.15 (a) The shear distribution remained steady throughout the duration of culture. A time series of diffusion- and MT-weighted MRIs was collected according to protocols established previously for measuring B16-F10 cell density and viability [32]. Cell density and viability maps calculated from the diffusion- and MT-weighted MRIs using

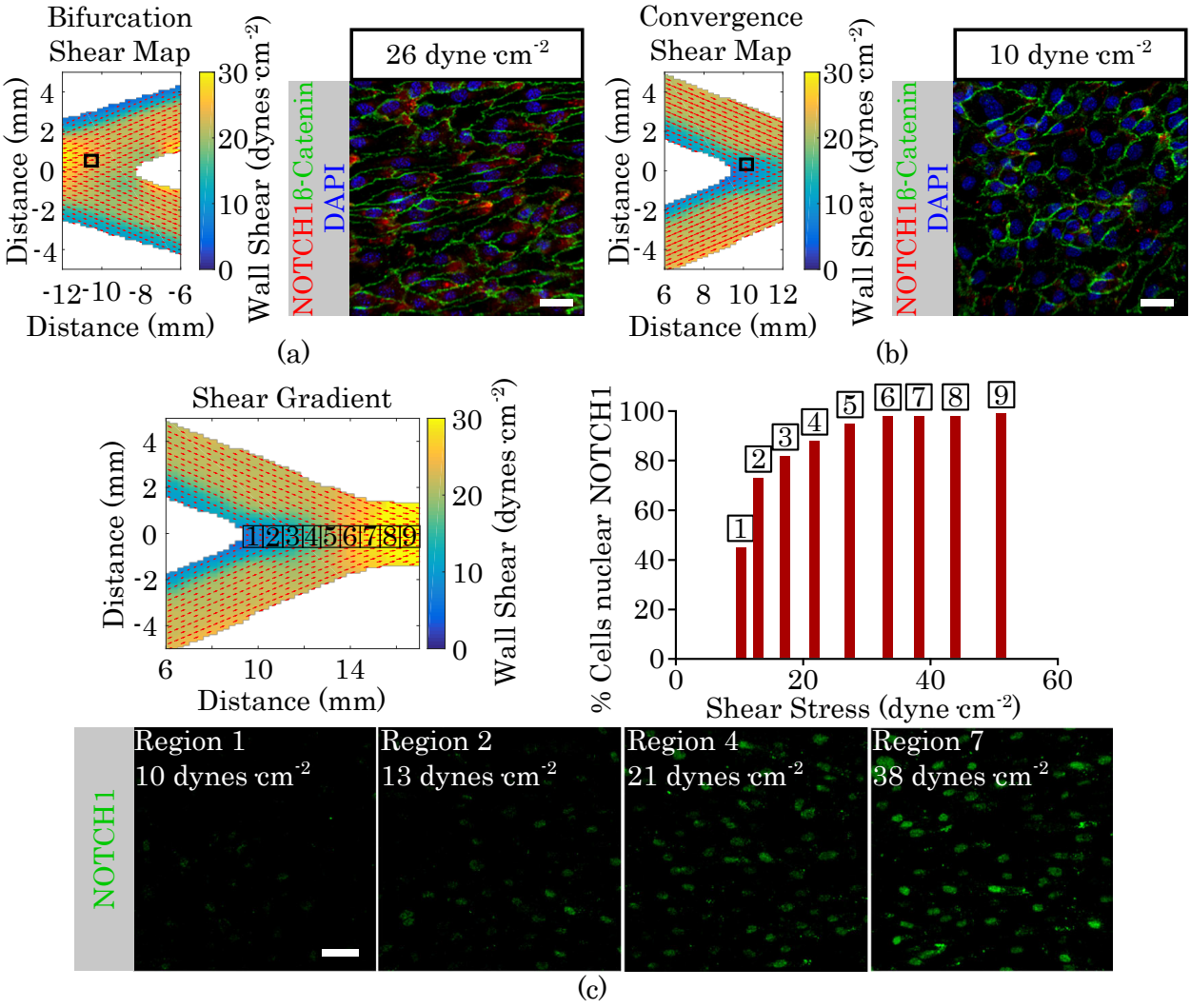

Figure 2.14: **Shear stress potentiates activation and consequent nuclear translocation of NOTCH1 protein.** (a-b) Flow vector plot of high shear stress (26 dynes cm^{-2}) (a) and low shear stress (10 dynes cm^{-2}) (b) regions and corresponding HAEC morphologies. Cell shape is defined by β-catenin expression at cell-cell borders (green). Notice polarized NOTCH1 (red) protein in high shear region. Scale bars = 20 μm. (c) Flow vector plot of the downstream region of the y-slide for nine ROIs. NOTCH1 (green) nuclear staining was quantified for each of the nine regions and plotted as a function of the measured wall shear stress. For each measurement, ~100 cells were evaluated using n = 5 biological replicates, scale bar = 20 μm.

calibrations determined previously [32] are shown in Fig. 2.15. Throughout the entire period of culture cells formed a distinct density gradient in which larger numbers of cells grew around the lower left corner flanked by channels 4 and 5, and lower numbers of cells grew near the upper right corner where channel 12 was located. The viability map was similar. The cells near channels 11 and 12 were less viable than the remainder of the scaffold. There also appeared to be a reduction in overall cell density between days 2 and 4 followed by a plateau between days 4 and 6. The overall viability numbers did not change dramatically between days.

2.3.4 General Bioreactor Performance

The bioreactor was found to be able to control all twelve flow inputs, reaching steady state flow targets within 3 minutes of starting the program with all valves completely closed as seen in Fig. 2.16. Once the correct valve inputs were found, only minor adjustments were required to maintain steady flow rates over long periods. In situations requiring large, frequent adjustments to inlet flow rates, for example, when collecting training data for a neural network based adaptive control algorithm, it was found that the valves were susceptible to long term failure in which valves jammed and required replacement parts. Valve jamming occurred at a very low frequency. It is believed to have been caused by a valve actuator overshooting the full turning range of the valve stem. It was addressed by adjusting the connection between the valve actuators and valve stems. The actuators use two grub screws to attach to the stems. One grub screw was removed. The other was tightened enough to allow the actuator to turn the valve, but not so much that the actuator would be capable of damaging the valve should it overshoot the fully closed or open positions. Images showing the bioreactor experimental setup can be seen in Fig. 2.17. Different angle images of the assembled setup are shown in Figs. 2.17 (a) and (b). A magnified view of the grub screw sockets used to connect the valve actuators to the valve stems is shown in Fig. 2.17 (d).

When porous sponges were prepared for the bioreactor, it was found that excessive application of adhesive to the TC chamber walls before inserting the sponge resulted in large

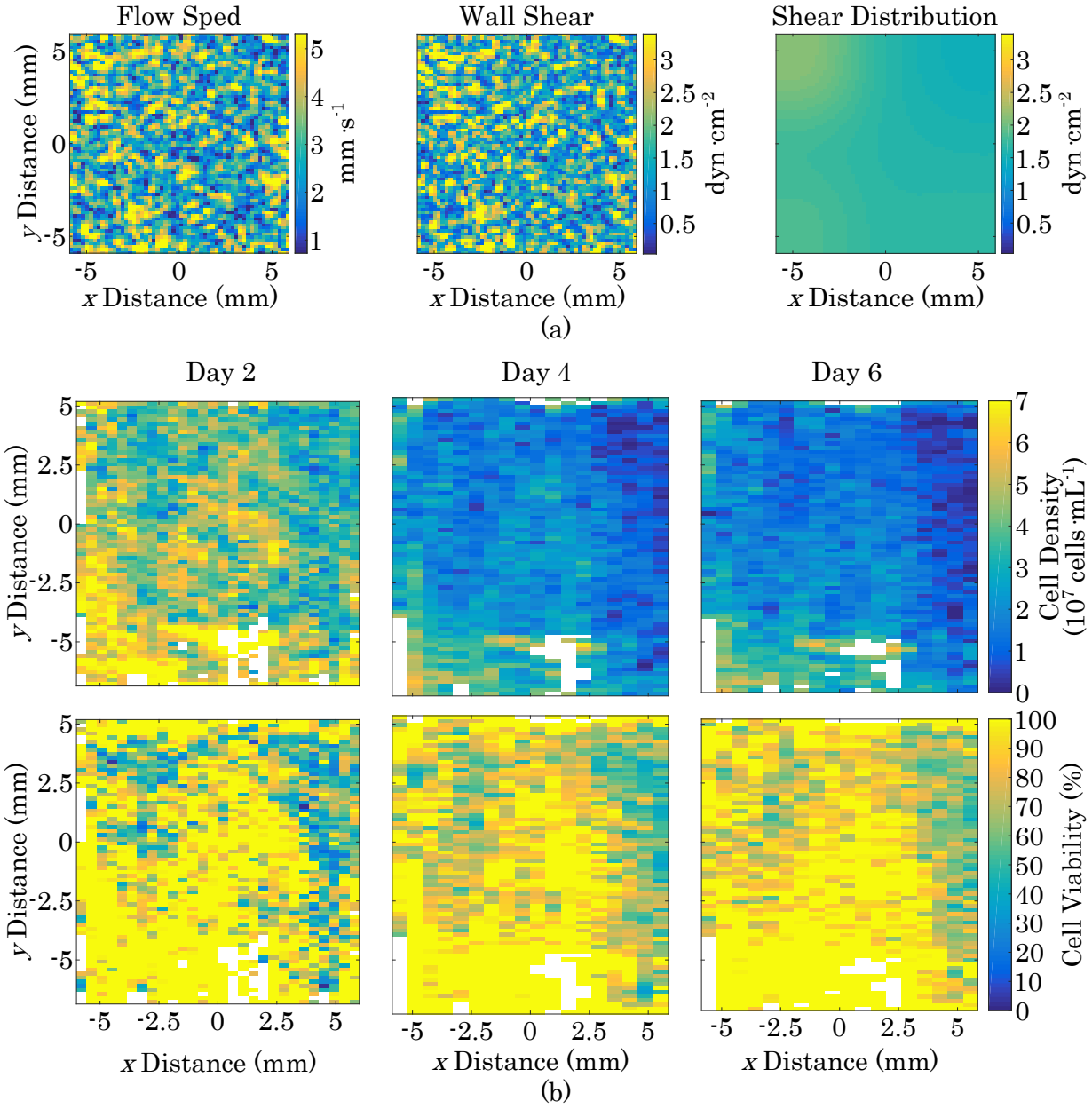

Figure 2.15: **MRI Monitoring of Bioreactor Culture.** (a) Flow speed map, pore wall shear map, and smoothed shear distribution applied to porous gelatin sponge by setting channels 3, 4, 11, and 12 to 0.5 mL·min^{-1}. (b) Time series of B16-F10 cell density (top) and viability (bottom) distributions throughout scaffold cultured under flow distribution shown in (a). Scaffolds were initially seeded with 1×10^7 cells·mL^{-1}.

burned regions in the sponge during laser cutting. When care was taken to apply only a thin coat of adhesive, the sponge did not burn in any areas other than the channel edges. When

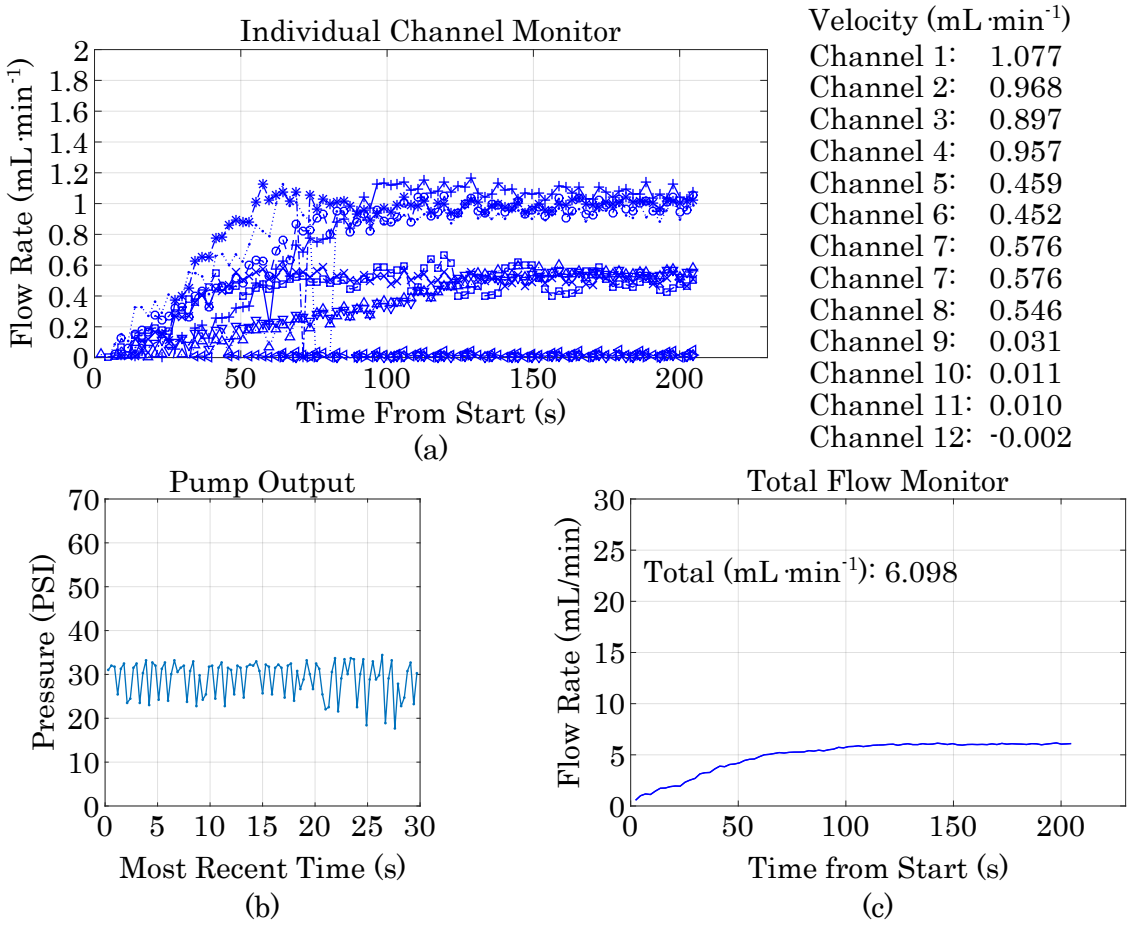

Figure 2.16: **Flow Rate Monitor.** Figure generated by MATLAB while controlling bioreactor inlet flow rates. All digitally measured parameters related to the bioreactor are plotted over time in this figure. Upper plot shows flow rates measured in each of the twelve inlets. Lower left plot shows pressure measured immediately downstream of the peristaltic pump. The Lower right plot displays the total flow rate through the bioreactor measured with an additional flowmeter. Channels 1-4 were set to 1 mL·min^{-1}, channels 5-8 were set to 0.5 mL·min^{-1}, and channels 9-12 were set to 0 mL·min^{-1}.

preparing a biopolymer hydrogel, caution was taken to avoid introducing bubbles into the mixture since bubbles generate magnetic susceptibility artifacts in the MRIs and reduce cell viability [351, 352]. To avoid bubbles, solutions with viscosity similar to water were reverse pipetted. When using positive displacement pipette tips to transfer high viscosity solutions, tips were filled and discharged while the tip was submerged twice to wet and remove air

bubbles prior to performing transfers or mixing. Despite avoiding the introduction of bubbles during mixing, bubbles nucleated from dissolved gasses during gelation as the gel was warmed to 37°C (see Fig. 2.18 (b)). To reduce the quantity of dissolved gasses, the cold component of the gel mixture was briefly placed under vacuum prior to combining it with cell suspension in fibrinogen solution.

Following glutaraldehyde sterilization of the system, care needed to be taken to thoroughly remove all traces of sterilant. This proved to be resource intensive. Despite rinsing the entire bioreactor system with copious quantities of sterile water, all additional rinse water that was flowed through the system would foam when agitated, indicating the presence of residual surfactant, which is a component of Cetylcide-G. An experiment was done to evaluate cytotoxicity of contact with the interior of the bioreactor system post sterilization. Cell culture media was circulated in the sterilized and rinsed bioreactor for a period of two weeks. Media collected at daily intervals from the reservoir was used to culture cells in 6 well plates. After eight days of contact the media was found to be cytotoxic. Cell culture media stored at room temperature and at 37°C in conical tubes for the same duration was found to promote healthy cell culture, suggesting that the cytotoxicity of media in the bioreactor was not the result of the bioreactor's long term operating temperature resulting in premature spoilage of media components. It is hypothesized that cytotoxic components of the sterilant preferentially adhere to hydrophobic surfaces and diffuse into absorbent materials such as gaskets during sterilization. It is also possible contaminants from the laboratory entered the bioreactor. This would likely be accompanied by biological contamination as well. However, since no biological contamination was observed prior to loading the TC chamber, this is less likely. If there is residual sterilant following sterilization (in rubber gaskets), it can potentially be slowly released into cell culture media flowing through the system. If this happens, the concentration of sterilant in cell culture media will initially be below the cytotoxic threshold. If cell culture media is recirculated when residual sterilant is present, the residual sterilant has time to accumulate in the cell culture media until it reaches a cytotoxic concentration. At this point the cell culture media is no longer suitable for cell culture. Two potential solutions were considered to address this problem. One potential

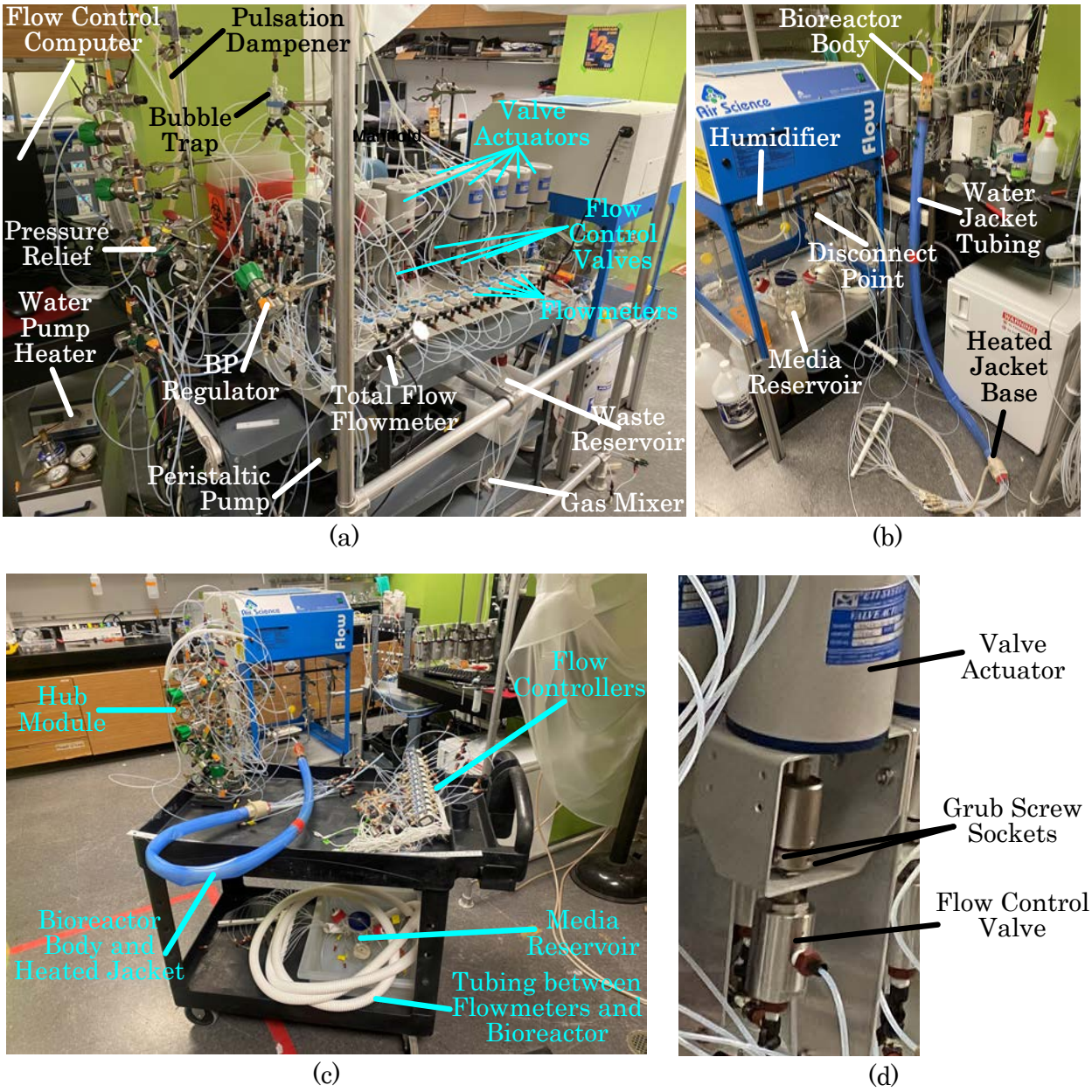

Figure 2.17: **Bioreactor Setup.** (a) Image of assembled bioreactor flow setup. Components are labelled. (b) Image of assembled bioreactor flow setup from another angle. Components are labelled. (c) Image of disassembled flow modules prepared for ethylene oxide gas sterilization. Each module corresponds to a colored region of the diagram highlighted in Fig. A.10. (d) Close up of connector between flow control metering valve and valve actuator.

solution considered was to not recirculate media in order to prevent the buildup of sterilant. The other option was to use a sterilization method that does not leave residues, in

which case cell culture media can be recirculated. The second option was selected for the multi-inlet bioreactor. The bioreactor was reconfigured for ethylene oxide gas sterilization. In order to remove all residual glutaraldehyde sterilant one time before transitioning to ethylene oxide, all bioreactor tubing and gaskets were replaced, and the valves and regulators were thoroughly washed and scrubbed. After this one-time transition, run-to-run bioreactor preparation only required rinsing and drying the system prior to sterilization (without tubing and gasket replacement). Pumping cell culture media through the bioreactor for three days following ethylene oxide sterilization validated that the sterilization was successful. However, contamination could still be introduced during bioreactor loading from microbial spores in the lab.

2.4 Addressing Partial Volume Effects when Analyzing Shear

2.4.1 Introduction to Partial Volume Effects

In clinical MRI, partial volume effects refer to the outcome of multiple tissue types occupying the space within a single voxel, in which case the intensity of that voxel is a function of the quantity of each tissue present [353]. More generally, partial volume effects can result from many types of intra-voxel heterogeneity, including fluid velocity. Partial volume effects in fluid velocity encoded MRIs are relevant when determining fluid shear forces. For example, in an MRI of a macroporous sponge, a single voxel may contain multiple whole and partial pore volumes. There are known to be large variations in fluid velocity among pores in TE scaffolds [20] Fluid velocity is encoded in the phase of nuclear spins. Two different effects occur when a population of spins moving at a uniform velocity and a population of stationary spins occupy a voxel together. First, when acquiring a phase map, each voxel contains the average phase of all spins within it, which causes an underestimate of the phase shift of the moving spins. Second, the moving spins are assumed to occupy the entire voxel, which introduces overestimation of the phase shift. These two effects can have unpredictable results, and it is advised to reduce partial volume effects as much as possible through means such as aligning flow paths with imaging planes and increasing the image resolution as

much as feasible [234]. The situation with two populations of static and moving spins is a simplification, as there can be more complicated velocity profiles. Aggregating velocity profiles into discreet voxels impacts the accuracy of shear calculations that depend on finite differences.

The impact of partial volume effects depends on the size of features and the MRI resolution. In an MRI velocimetry study of fluid convection in a bed of packed beads, theoretical predictions of flow did not match experimental measurements because of large local velocity errors in the MRI velocity maps. [354]. Another study investigated water flow in a polydimethylsiloxane (PDMS) microchannel network using MRI velocimetry. In order to remove partial volume effects at the water/PDMS interface, this study generated two threshold masks. One was based on experimentally measured voxel signal amplitudes, and the other was based on theoretical water content in each voxel. The mask based on theoretical water content was preferred because the experimental mask biased the flow rate balance [355]. Thresholding based on voxel water content is applicable to water/non-water boundaries. However, in scaffolds fully saturated with water there is little variation in water density between voxels within the scaffold volume.

In this section, fluid velocity partial volume effects, their impact on shear calculations based on finite differences, and methods to correct for these effects are examined in hydrogels with open channels and porous sponges. Particular emphasis will be placed on determining wall shear stress, or the shear stress experienced by cells growing on surfaces. This is a type of shear that has been measured and modelled because of its known impact on cells [21,354,356].

2.4.2 Flow and Shear Throughout Scaffolds

2.4.2.1 Biopolymer Matrix

Fluid velocity maps were obtained directly from flow-weighted MRI. Velocity maps corresponding to 5 mL·min^{-1} flow rates in all input channels are shown in Fig. 2.18. Total flow speed and shear rate maps calculated from the velocity maps are shown in Fig. 2.19 using equations 2.1 and 2.2, respectively.

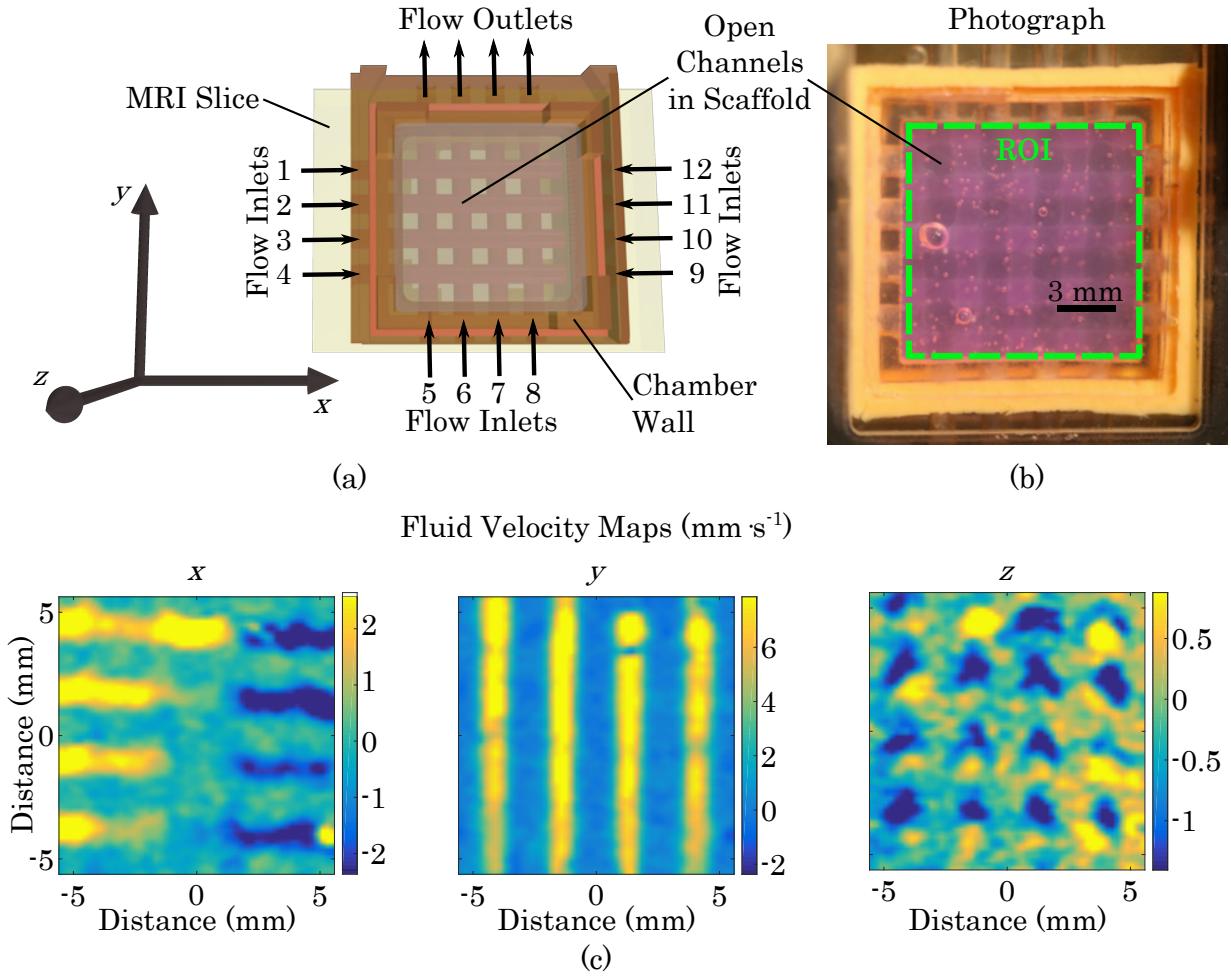

Figure 2.18: **Fluid Velocity Maps in Biopolymer Scaffold.** (a) Diagram of gel scaffold highlighting the pattern of open channels within the gel. Diagram is labelled with channel inlet numbers and the Cartesian coordinate orientation corresponding to all other fluid velocity maps presented in this work. (b) Photograph of biopolymer scaffold mounted in bioreactor. The region of interest (ROI) used when cropping and displaying flow-weighted MRIs is outlined in green. (c) Fluid velocity maps within biopolymer scaffold corresponding to input flow rates of 0.5 mL·min^{-1} in all inlet channels. Velocity maps were were cropped to include only the scaffold region of the MRI. Values in colorized scale bars are in mm·s^{-1}.

The pattern of contrast between regions of high and low flow clearly resembles the geometry of the channels in the gel with higher flow rates corresponding to channel lumen and lower flow rates corresponding to the interstitial space in the biopolymer matrix. The x

velocity component shows a relatively symmetrical pattern around $x = 0$ with flow rates exceeding 2 mm·s^{-1} in opposing directions. A negative z velocity component is visible at each intersection between the vertical and horizontal channels due to the offset of the channels from each other in the z direction (see Fig. 2.6). The shear rate map shows that shear rates at the walls of channels with high luminal flow (especially the vertically oriented channels) exceeded 6 s^{-1}, whereas shear rates in the center of these channels were close to 0 s^{-1}. The Reynolds number, Re, at the entrance of each channel where the flow rate was 0.5 mL·min^{-1} was Re=10, given a channel diameter of 1.5 mm, cell culture media density of 993.37 kg·m^{-3}, and dynamic viscosity of 6.92×10^{-4} kg·m^{-1}·s^{-1} [209, 357]. Assuming the total inlet flow was evenly split between the four outlet channels giving them each a volumetric flow rate of 1.5 mL·min^{-1}, the Reynolds number increased to Re=30 at the exits. Therefore, all flow within the channels was well within the laminar regime, even considering possible variations in the inlet flow distributions.

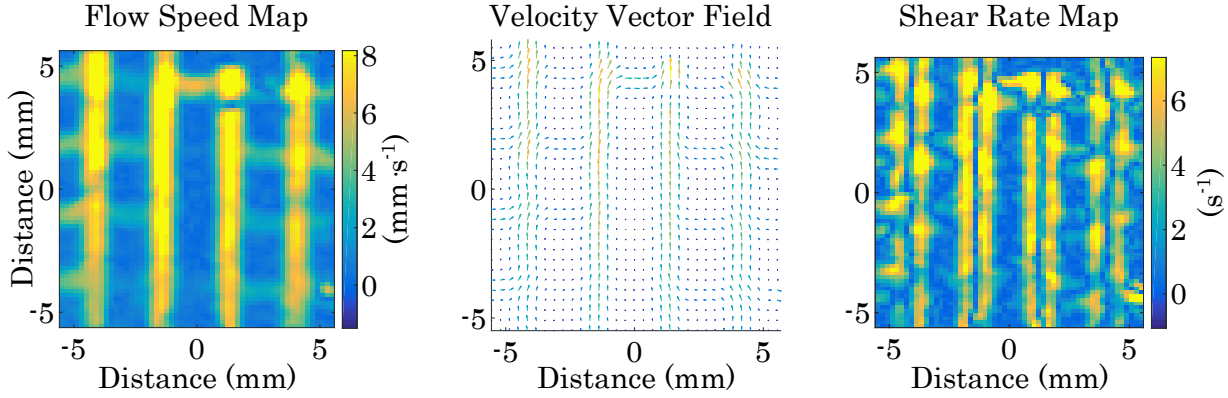

Figure 2.19: **Flow and Shear Maps.** On the left is a map of the total flow speed magnitude calculated from the directional fluid velocity maps in Fig. 2.18. The quiver plot (middle) is a vector field constructed from the x and y components of the fluid velocity. The right panel is a shear rate map calculated from the x and y fluid velocity maps.

A model flow profile in a cross-section of the gel was generated for comparison to the flow-weighted MRIs. Given the repetitive geometry of the evenly spaced channels inside the gel, the model was generated for a unit cell of a cross section of the gel. The unit cell was composed of a single channel and its surrounding matrix. The width of the cell was

equal to the distance between channels, 2.74 mm. The height of the cell was equal to the thickness of the gel, 4.32 mm. Given a channel diameter of 1.50 mm, the cross sectional area of the channel was 1.76 mm^2, and the cross sectional area of the surrounding matrix was 10.1 mm^2. The channel lumen and the interstitial space of the biopolymer matrix were considered parallel flow paths through which liquid could pass. The pressure drop, ΔP, across parallel paths is the same. According to Darcy's law, the pressure drop across a length of matrix is:

$$\Delta P = -\frac{Q_s \mu L}{kA} \tag{2.6}$$

where Q_s is the volumetric flow rate through the matrix, μ is the dynamic viscosity of the liquid, L is the length of the porous medium over which the pressure drop takes place, k is the permeability of the medium in m^2, and A is the cross sectional area of the matrix. In the channel's lumen, the pressure drop was determined by the Hagen-Poiseuille law:

$$\Delta P = -\frac{8\mu L Q_c}{\pi R^4} \tag{2.7}$$

where R is the channel radius and Q_c is the volumetric flow rate through the channel. Setting the pressure drops of the lumen and interstitial space equal to each other and solving gives:

$$-\frac{Q_s \mu L}{kA} = -\frac{8\mu L Q_c}{\pi R^4} \tag{2.8}$$

$$Q_s = \frac{8kA_s}{\pi R^4} Q_c \tag{2.9}$$

In order to estimate permeability of gel mixtures, the Happel method [358] modified for porous media comprised of a mixture of rods of varying size was used [341]. Briefly, the permeability, K_h, of a network of randomly distributed, identical rods of type h is estimated by the weighted average:

$$K_h = \frac{2}{3} K_{h,\perp} + \frac{1}{3} K_{h,\parallel}, \tag{2.10}$$

where $K_\parallel$ is the fluid permeability derived for flow through an array of unidirectional rods in which the flow is parallel to the rod cylinder axis. $K_\perp$ is the fluid permeability derived for flow through an array of unidirectional rods in which the flow is perpendicular to the rod cylinder axis. According to Happel:

$$K_{h,\perp} = \frac{b_h^2}{4}\left[\ln\frac{b_h}{a_h} - \frac{1}{2}\left(\frac{b_h^4 - a_h^4}{b_h^4 + a_h^4}\right)\right] \tag{2.11}$$

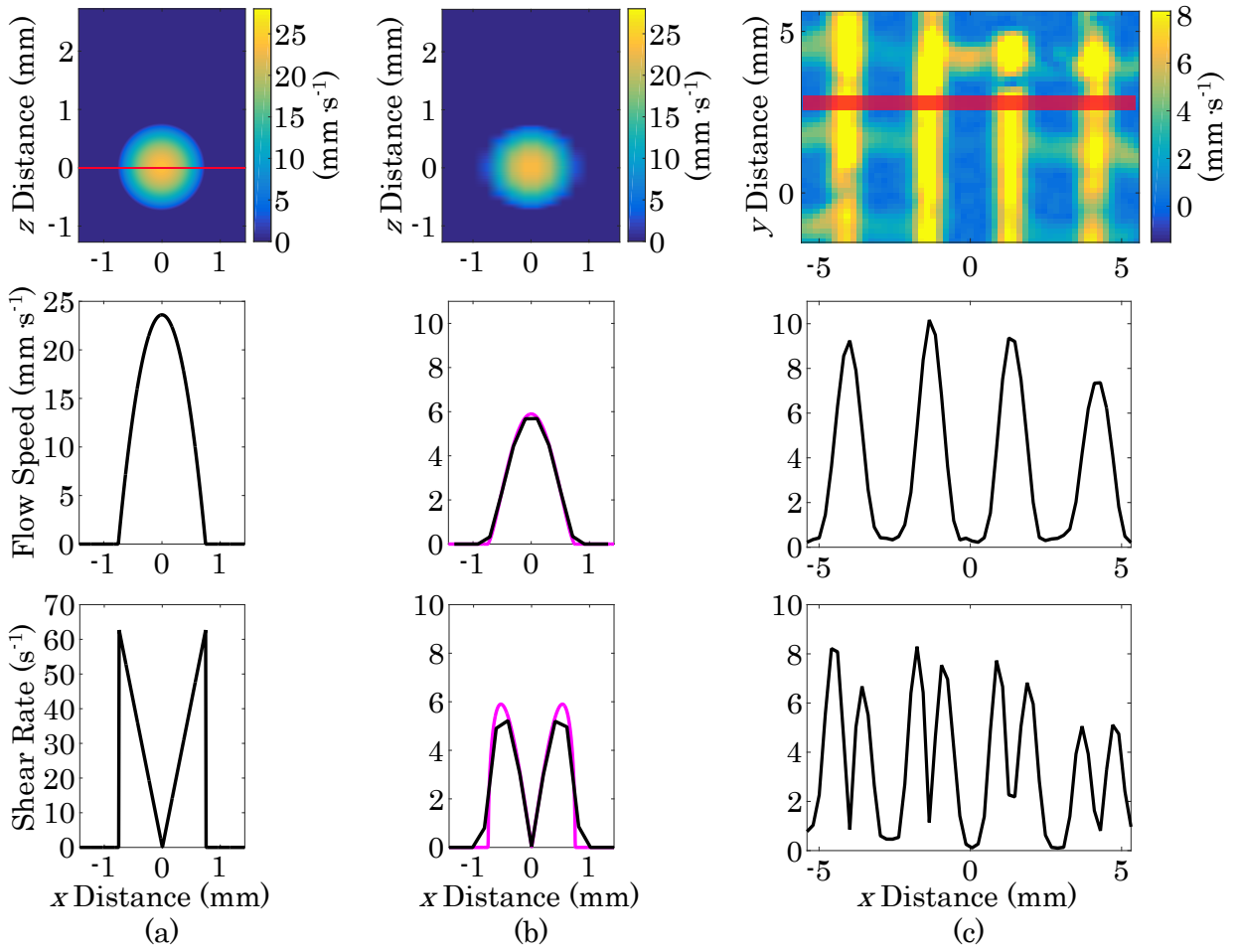

Figure 2.20: **Analysis of Flow-weighted MRI.** (a) Top: cross section view of v_y modelled in channel and surrounding matrix. Middle: plot of modelled v_y along red line. Bottom: plot of modelled $\dot{\gamma}$ in matrix and channel along red line. (b) Top: cross section view of v_y in channel and surrounding matrix segmented with the same x resolution used in the flow-weighted MRI from Fig. 2.19. Middle and Bottom: plot of modelled $\bar{v}_y$ and $\bar{\dot{\gamma}}$ profiles respectively. Black profile is segmented with same x resolution used in MRI. Magenta profile is unsegmented. (c) Top: portion of flow speed map seen in Fig. 2.19 with ROI highlighted in red. Middle: profile of average flow speed in ROI along x direction. Bottom: profile of average shear rate in ROI along x direction.

$$K_{h,\parallel} = \frac{1}{8b_h^2}\left(4a_h^2b_h^2 - a_h^4 - 3b_h^4 + 4b_h^4 \ln\frac{b_h}{a_h}\right) \tag{2.12}$$

where a_h is the radius of rod of type h and b_h is the radius of a larger, concentric cylinder

making up the unit cell of rod type h. b_h is selected such that the difference, $b_h - a_h = \lambda$, is constant for all fiber sizes and such that the average solid fraction summed over all unit cells is equal to the total solid fraction of fibers in the porous medium. The difference, λ, is found from solving the following equation:

$$\lambda^2 \left[\sum_h \frac{\phi_h}{a_h^2}\right] + 2\lambda \left[\sum_h \frac{\phi_h}{a_h}\right] + \left[\sum_h \phi_h\right] - 1 = 0 \tag{2.13}$$

where ϕ_h is the volume fraction of each polymer. Once b_h and a_h are obtained, the overall permeability of the porous medium was found from

$$K = \sum_{h=1}^{N} \left[\frac{n_h}{K_h(b_h, a_h)}\right]^{-1} \tag{2.14}$$

where n_h is the fraction of fibers with radius a_h in a random cross section found using:

$$n_h = \frac{\phi_h/\pi a_h^2}{\sum_h \left(\phi_h/\left(\pi a_h^2\right)\right)} \tag{2.15}$$

Thus we obtain a method of predicting fluid permeability by using Eq. 2.10 — the weighted averages of Eqs. 2.11 and 2.12 — together with molecular fiber radii and volume fractions reported in literature. Since this is a prediction based on a theoretical fiber matrix model, no error is reported, which is consistent with the presentation of theoretical estimates in literature that uses this model [341]. Using this method, fluid permeabilities were estimated for various gel mixtures that are shown in Table 2.4. Matrigel® was assumed to be a mixture of 60% type IV collagen, 33% laminin, and 5.4% haparan sulfate [341]. The fiber radii corresponding to type IV collagen, laminin, heparan sulfate, and type I collagen were 0.7 nm [359], 0.6 nm [360], 0.5 nm [361], and 50 nm [362,363]. The volume fractions of each fiber type were determined from $\phi_h = v_h C_h$ where v_h is the partial specific volume of a specific biopolymer and C_h is its concentration. The partial specific volumes of type IV collagen, laminin, and heparan sulfate used were 0.695 mL·g^{-1} [364–366], 0.73 mL·g^{-1} [367,368], 0.54 mL·g^{-1} [369, 370]. The partial specific volume of type I collagen was reported to be 0.70 mL·g^{-1} [371, 372], but an effective specific volume of 1.89 cm^3·g^{-1} was also reported, which takes into account intrafibrillar water content [363]. The effective specific volume of 1.89 cm^3·g^{-1} did not produce accurate predictions for K in the study in which it was reported. Instead, a more accurate effective specific volume of 1.17 was found from reported

Table 2.4: Gel Permeabilities

Gel Type	Permeability, K (m^2)
Type I Collagen (2 mg·mL^{-1})	8.56×10^{-13}
Type I Collagen (4 mg·mL^{-1})	3.68×10^{-13}
Type I Collagen (6 mg·mL^{-1})	2.21×10^{-13}
Fibrin (from 2 mg·mL^{-1} fibrinogen)	5.48×10^{-15}
Fibrin (from 4 mg·mL^{-1} fibrinogen)	2.41×10^{-15}
Matrigel (1:10 dilution)	4.29×10^{-16}
Gel 2	4.26×10^{-16}
Gel 1	4.09×10^{-16}
Matrigel, 100%	2.56×10^{-17}

volume fractions and corresponding permeabilities reported more recently [362, 373]. The volume fraction of fibrin was determined from the concentration of fibrinogen used according to: $\phi_{fibrin} = \frac{C_{Fbg}}{\rho_{Fbg}\Phi_{int}}$ where ρ_{Fbg} is the density of fibrinogen protein (1.4 g·mL^{-1}) and Φ_{int} is the internal solid fraction of a fiber found from the imperially determined relationship $\Phi_{int} = 0.015 \ln(C_{Fbg}) + 0.13$ [374].

Using the gel 2 fluid permeability estimate of 426 nm^2, the relationship between Q_s and Q_c became $Q_s = 3.46 \times 10^{-8} Q_c$, suggesting that the interstitial volumetric flow rate through the scaffold was negligible compared to luminal flow through the channels. Since flow-weighted MRIs directly measure fluid velocity, the average fluid velocity in the scaffold interstitial space, $\bar{v}_s$, was compared to the average fluid velocity in the channel lumen, $\bar{v}_c$, using the relationships $Q_c = \bar{v}_c A_c$ and $Q_s = \bar{v}_s A_s$ to give:

$$\bar{v}_s A_s = \frac{8kA_s}{\pi R^4} \bar{v}_c A_c \tag{2.16}$$

$$\bar{v}_s = \frac{8kA_c}{\pi R^4} \bar{v}_c = \frac{8k\pi R^2}{\pi R^4} \bar{v}_c = \frac{8k}{R^2} \bar{v}_c \tag{2.17}$$

The relationship between average fluid velocity in the scaffold versus average fluid velocity in the channel was $\bar{v}_s = 7.16 \times 10^{-11} \bar{v}_c$, demonstrating that any interstitial flow was well

below the range of the MRI when the imaging parameters were optimized to encompass intraluminal flow velocities.

Despite the prediction that total flow through the matrix would be significantly lower than flow through the channels, a slip boundary condition and an elevated quantity of flow penetrating the matrix immediately adjacent to the channel wall were expected [375, 376]. According to the Brinkman model, the penetration depth of fluid flow into the matrix was estimated to be on the order of $\sqrt{k}$ [375], or 20.6 nm in the case of gel 2. Since the Brinkman model relies on Darcy's law, which assumes a uniformly homogenous porous material (the length scale of the material $\gg$ the length scale of the pores), James and Davis generated a new model of flow close to the interface on the length scale of the pores. The James and Davis model found that the slip boundary term can safely be ignored in the calculation of wall shear when the solid volume fraction of the porous material is greater than 0.01, and it found that the penetration depth of elevated fluid velocity is less than what was predicted in the Brinkman model [376]. In the case of gel 2, the total fiber volume fraction was estimated to be 0.0246. This volume fraction was determined by summing up the volume fractions of each individual fiber type, which were each calculated as described previously. A volume fraction of 0.0246 is greater than 0.01, suggesting that the permeability of the gel and subsurface flow at the channel wall will have no discernable effect on endothelial cells versus an impermeable wall. In comparison to the fluid penetration depth, the height of an endothelial cell nucleus hump when cultured under flow is 1.77 μm [377]. The geometry of an endothelial cell monolayer has a greater influence on local shear stress at the channel wall than the permeability of the matrix [378, 379], and even the influence of endothelial cells on shear will be undetectable by MRI given its xy spatial resolution of roughly 100 μm.

Given the fact that bulk interstitial flow and flow penetration at the biopolymer hydrogel channel wall were negligible, flow through the unit cell cross section of the gel was modelled by considering the channel and matrix as two distinct regions. In order to validate flow-weighted MRIs, flow in the channel was modelled as flow through a pipe, and the surrounding matrix was modelled as static water. Flow in the channel was calculated using the paraboloidal function: $v_y\left(r_z, r_x\right) = 2\bar{v}_c\left(1 - \frac{r_z^2}{R^2} - \frac{r_x^2}{R^2}\right)$ where v_y is the y velocity component at a discreet

point in 3D space (not averaged over Z_{th}), r_z is the radial position in the channel along the z axis, and r_x is the radial position in the channel along the x axis. This calculation is valid for fully developed laminar flow. A map of v_y modelled in the unit cell cross section as well as corresponding velocity and shear rate profiles along a one dimensional axis intersecting the center of the channel are displayed in Fig. 2.20 (a). The shear rate profile was determined using finite differences in v_y along the x direction. The shear rate at the wall of the channel in the model determined using finite differences matched the expected wall shear (63 s^{-1}) calculated using

$$\dot{\gamma} = \frac{4Q}{\pi r^3}, \tag{2.18}$$

which is valid for flow in a pipe. $\dot{\gamma}$ is the shear rate at a point in space not averaged over Z_{th}.

In order to directly compare the modelled flow profiles across a channel to the flow profiles across channels generated by MRI, the z and x resolution of the MRI were taken into account when generating a theoretical flow profile across a channel. The flow-weighted SEMS pulse sequence had a minimum slice thickness (z resolution) of 0.75 mm. Since the channels were 1.5 mm in diameter, a 3D reconstruction of the channels was not feasible with a finely segmented z stack. It was decided to take a single 4 mm thick slice that fully encompassed both sets of channels and the surrounding matrix. The x resolution of the MRI in Fig. 2.18 was 203 μm. A map of v_y modelled in the unit cell cross section with the same x resolution as the MRI in Fig. 2.18 can be seen in Fig. 2.20 (b). Profiles of $\bar{v}_y$ averaged over the entire 4 mm thick z section and $\bar{\dot{\gamma}}$ calculated from the slice-averaged $\bar{v}_y$ values were plotted along the x direction in the same panel. In order to make the shear rate profile directly comparable to the MRI shear rate profile, the modelled shear rate was calculated using Eq. 2.2, which averages $\partial_x \bar{v}_y$ and $\partial_y \bar{v}_x$. Since the axis of the modelled channel was oriented perpendicularly to the xz plane, and since it was assumed that the flow was fully developed, $\partial_y \bar{v}_x = 0$, and therefore $\bar{\dot{\gamma}} = \partial_x \bar{v}_y/2$. $\bar{v}_y$ and $\bar{\dot{\gamma}}$ profiles segmented with the corresponding MRI x resolution were plotted in black. Continuous $\bar{v}_y$ and $\bar{\dot{\gamma}}$ profiles along the x direction were plotted in magenta for comparison. It can be seen that averaging in all liquid within the z slice thickness reduces the apparent maximum flow rate in the center of the channel by approximately a

factor of 4. In addition, the parabolic velocity profile has rounded tails near the walls when averaging the entire z slice thickness due to the fact that voxels at the edge of the channel contain more static liquid trapped in the matrix than voxels in the center of the channel. These tails cause the apparent shear rate profile to have two rounded humps rather than a simple linear relationship between radial position and shear rate.

The apparent velocity and shear rate profiles determined via MRI was also analytically solved. To find the average velocity over the entire slice thickness at any point along r_x, the function for $\bar{v}_y$ was integrated with respect to r_z while keeping r_x constant and divided by the total slice thickness since the contribution to flow in the matrix is negligible:

$$\bar{v}_y\left(r_x\right) = \frac{1}{Z_{th}} \int_{r_{z_1}}^{r_{z_2}} 2\bar{v}_c \left(1 - \frac{r_z^2}{R^2} - \frac{r_x^2}{R^2}\right) dr_z \tag{2.19}$$

where the limits r_{z_1} and r_{z_2} are the r_z values at which r_x intersects the channel wall. Solving gives:

$$\bar{v}_y(r_x) = \frac{1}{Z_{th}} \left(-\frac{2\bar{v}_c}{3R^2} r_{z_2}^3 + 2\bar{v}_c \left(1 - \frac{r_x^2}{R^2}\right) r_{z_2} + \frac{2\bar{v}_c}{3R^2} r_{z_1}^3 - 2\bar{v}_c \left(1 - \frac{r_x^2}{R^2}\right) r_{z_1}\right) \tag{2.20}$$

$$\bar{v}_y\left(r_x\right) = \frac{1}{Z_{th}} \left(\frac{2\bar{v}_c}{3R^2} \left(r_{z_1}^3 - r_{z_2}^3\right) + 2\bar{v}_c \left(1 - \frac{r_x^2}{R^2}\right) \left(r_{z_2} - r_{z_1}\right)\right) \tag{2.21}$$

Substituting $r_{z_1} = -\sqrt{R^2 - r_x^2}$ and $r_{z_2} = \sqrt{R^2 - r_x^2}$ gives:

$$\bar{v}_y\left(r_x\right) = \frac{1}{Z_{th}} \left(\frac{2\bar{v}_c}{3R^2} \left(R^2 - r_x^2\right)^{(3/2)} + 2\bar{v}_c \left(1 - \frac{r_x^2}{R^2}\right) \sqrt{R^2 - r_x^2}\right) \tag{2.22}$$

$$\bar{v}_y\left(r_x\right) = \frac{8\bar{v}_c}{3R^2 Z_{th}} \left(\left(R - r_x\right)\left(R + r_x\right)\right)^{(3/2)} \tag{2.23}$$

When plotted this gives the same z slice thickness averaged velocity profile modelled in Fig. 2.20 (b). The slice thickness averaged shear rate profile, $\bar{\dot{\gamma}}$, is analytically solved by taking the derivative of Eq. 2.23 and averaging with $\partial_y \bar{v}_x$ (in the form: $\bar{\dot{\gamma}}\left(r_x\right) = \left(\frac{d}{dx}\bar{v}_y\left(r_x\right) + \partial_y \bar{v}_x\right)/2$) to generate:

$$\bar{\dot{\gamma}}\left(r_x\right) = \frac{8\bar{v}_c r_x}{3R^2 Z_{th}} \sqrt{\left(R - r_x\right)\left(R + r_x\right)}, \tag{2.24}$$

which reflects the same z slice thickness averaged shear plot profile modelled in Fig. 2.20 (b).

In order to determine the shear rate cells experience at the wall of a channel from an MRI slice of thickness, Z_{th}, in a channel of radius, R using Eq. 2.18, Q_c needs to be determined from $Q_c = \bar{v}_c A_c$. The average velocity in the channel, $\bar{v}_c$, can be determined using the slice thickness averaged velocity at the center of the channel, $\bar{v}_y|_{r_x=0}$, which is directly measured by MRI, by setting $R = 0$ and solving Eq. 2.23 for $\bar{v}_c$ to obtain:

$$\bar{v}_c = \frac{3Z_{th}}{8R}\ \bar{v}_y|_{r_x=0} \tag{2.25}$$

Substituting this into Q_c and substituting Q_c into Eq. 2.18 gives:

$$\dot{\gamma} = \frac{4\frac{3Z_{th}}{8R}\ \bar{v}_y|_{r_x=0}\, A_c}{\pi R^3} \tag{2.26}$$

$$\dot{\gamma} = \frac{3Z_{th}A_c}{2\pi R^4}\ \bar{v}_y|_{r_x=0}\,, \tag{2.27}$$

which simplifies to

$$\dot{\gamma} = \frac{3Z_{th}}{2R^2}\ \bar{v}_y|_{r_x=0} \tag{2.28}$$

when substituting $A_c = \pi R^2$. This simple relationship enables the shear at the wall of the lumen to be calculated from the maximum measured velocity in a channel, the known channel geometry, and the MRI slice thickness.

The slice thickness averaged velocity and shear rate profiles modelled across a channel were compared to profiles generated by MRI. In order to generate flow and shear profiles from an MRI, an ROI was drawn around a portion of the image that only included vertically oriented channels and the interstitial gel space in between them. Total flow speed and calculated shear rates in the ROI were averaged along the direction of flow to make one-dimensional flow and shear rate profiles across the four channels. The ROI and corresponding flow and shear rate profiles are displayed in Fig. 2.20. It was assumed that there was no v_z or v_x contribution to the flow in this region, so $s = v_y$.

Adjusting flow inputs into each channel leads to the formation of a wide range of achievable velocity maps throughout the channel grid. Examples of several flow speed maps corresponding to different sets of inlet flowrates are shown in Fig. 2.21. These flow speed maps were selected for being easily distinguished from each other upon quick visual inspection.

They are only a small subset of the entire range of combinations available to the bioreactor. When limiting the channels to a binary on (0.5 mL·min^{-1}) or off state, there are a total of 2^{12} inlet combinations possible. With incremental adjustments to flow in each channel, the number of combinations is much greater. For example, using a range of 0 to 0.5 mL·min^{-1} with 0.1 mL·min^{-1} increments increases the number of possible combinations to 6^{12}.

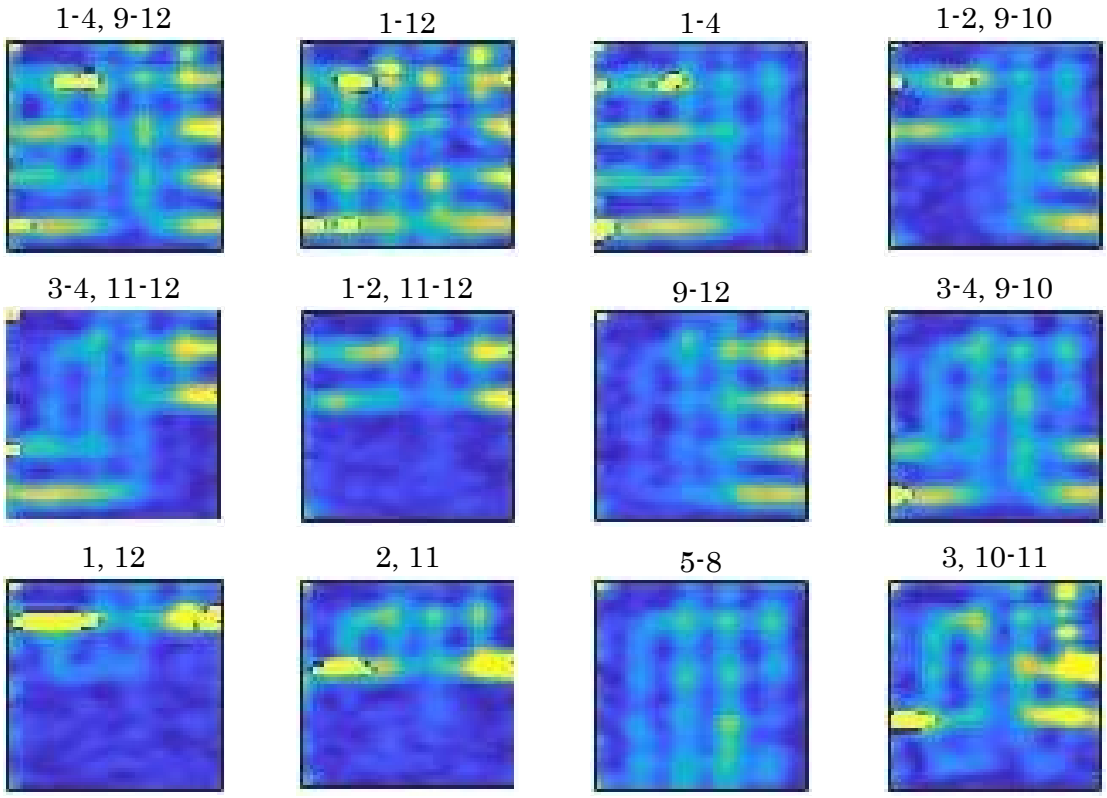

Figure 2.21: **Example Flow Speed Maps in Biopolymer Hydrogel.** Flow was allowed through different combinations of inlets into the TC chamber in order to generate multiple examples of flow speed maps in a biopolymer hydrogel containing a grid of open channels. Flow speed maps shown here were calculated from MRIs of fluid velocity using Eq. 2.1. Each flow speed map corresponds to the inlet combinations specified above it. The numbers above each image indicate the flow channels that were set to 0.5 mL·min^{-1} All other channels were not flowing. A diagram of the location of the channel inlets around the TC chamber can be seen in Fig. 2.18 (a).

2.4.2.2 Macroporous Sponges

Total flow speed and shear rate maps of flow in a porous collagen sponge are shown in Fig. 2.22. All twelve channel inputs were set to 0.5 mL·min^{-1} during flow image acquisition. Shear rate, $\bar{\dot{\gamma}}$, was calculated using Eq. 2.2. Since all channel axes in the sponge were coplanar, a thinner MRI slice of 1.6 mm was used to capture luminal flow in all channels.

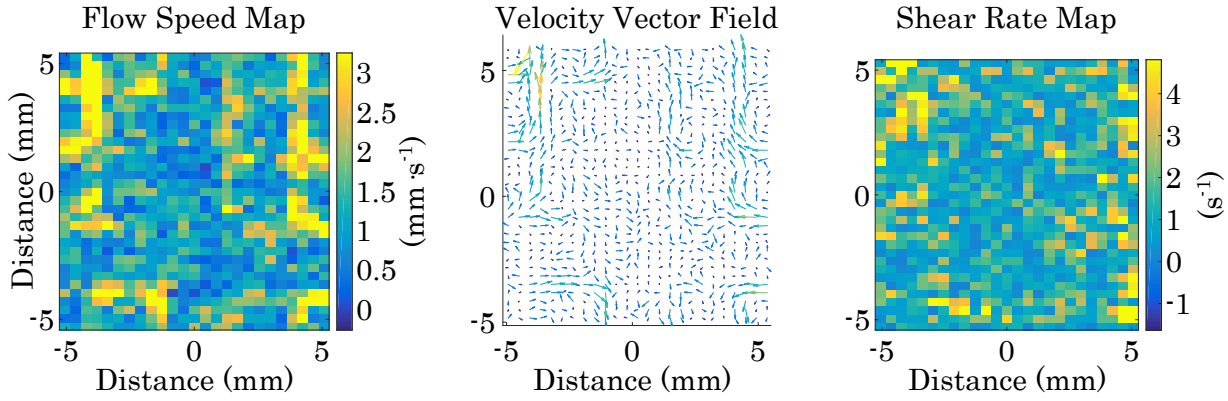

Figure 2.22: **Flow and Shear Maps in Collagen Sponge.** The left panel is a map of the total flow speed magnitude. The middle panel is a flow vector field made from the $\bar{v}_x$ and $\bar{v}_y$ maps. The right panel is a map of $\bar{\dot{\gamma}}$.

Although some luminal flow was seen in the flow speed map, the channel geometry, as indicated by regions of high flow, was much less distinct than in the biopolymer gel. The shear map showed almost no features resembling channels, and the vector plot showed greater flow in the interstitial regions with more stochastic behavior. Thicker MRI slices were not used because averaging larger volumes of interstitial flow from above and below the channels overpowered and obscured the signal from faster luminal flow. The fluid permeability of the Ultrafoam™ sponge was 2.54×10^{-12} m^2, its pores ranged from 100 to 200 μm in diameter, and its void volume was 90% [380]. Considering the unit cell of the scaffold and the relationship in Eq. 2.17, the ratio of flow in the open channels to flow in the scaffold was calculated to be $\bar{v}_s = 4.15 \times 10^{-5}\bar{v}_c$. This initially suggests that the flow through the matrix is negligible compared to luminal flow, however, the scaffold pore diameters are not small enough to consider the sponge as a homogenous material. Assuming an average pore size of 150 μm,

these pore diameters are about a tenth of the size of the channels and are on the same order of magnitude as the xy resolution of the MRI. Therefore it cannot be assumed that the porous sponge will behave like a uniform material on the observed length scale. Instead, it was assumed that the interconnected pores form a cylindrical pathway approximately twice the length of the scaffold as has been done in previous work [380, 381]. Considering all pores as parallel flow paths to the channels and to each other, the pressure drop across each individual pore is the same as the pressure drop across the channel. Therefore, flow in a single pore, Q_{p_i}, was compared to flow in the channel using the relationship:

$$\frac{8\mu L Q_c}{\pi R^4} = \frac{16\mu L Q_{p_i}}{\pi R_{p_i}^4} \tag{2.29}$$

$$Q_{p_i} = \frac{R_{p_i}^4}{2R^4} Q_c \tag{2.30}$$

where R_{p_i} is the radius of an individual pore. The total flow rate through the pores, Q_{p_t} can be found from the flow rate in a single pore using the relationship $Q_{p_i} = Q_{p_t}/n_p$ where n_p is the number of pores. The volume of an individual pore, V_{p_i} is related to the void volume in the scaffold, ϵ, and n_p by

$$V_{p_i} = \frac{\epsilon V_s}{n_p}, \tag{2.31}$$

which can be solved for n_p to obtain

$$n_p = \frac{\epsilon V_s}{V_{p_i}}. \tag{2.32}$$

Substituting this into Eq. 2.30 gives:

$$\frac{Q_{p_t} V_{p_i}}{\epsilon V_s} = \frac{R_{p_i}^4}{2R^4} Q_c \tag{2.33}$$

$$Q_{p_t} = \frac{\epsilon V_s R_{p_i}^4}{2V_{p_i} R^4} Q_c, \tag{2.34}$$

which can be further simplified by substituting the volume of a single pore, $V_{p_i} = 2L\pi R_{p_i}^2$, and the volume of the scaffold's interstitial space, $V_s = A_s L$, to obtain

$$Q_{p_t} = \frac{\epsilon A_s R_{p_i}^2}{4\pi R^4} Q_c. \tag{2.35}$$

Evaluating the expression reveals that $Q_{p_t} = 3.3 \times 10^{-3} Q_c$. This is not nearly as great a difference as seen in the gel, and it suggests that flow in the pores cannot be neglected when

modelling flow in a collagen sponge. This is consistent with the flow speed map in Fig. 2.22, which shows less flow concentrated in the channels and more diffuse flow throughout the pores. The complex flow distribution makes MRI particularly useful for measuring local flow in the macroporous environment of a sponge.

The potential to use flow-weighted MRIs to approximate the average shear rate at the walls of the pores on a voxel by voxel basis was evaluated. This was only considered for voxels entirely encompassing sponge pores that had no volume overlap with the laser cut channels. First, the total volumetric flow rate in each voxel was calculated using: $Q_{i,j} = \bar{v}_{i,j} A_v|_{i,j}$ where $Q_{i,j}$ is the volumetric flow rate through an individual voxel, $\bar{v}_{i,j}$ is the average fluid velocity measured in the voxel, and $A_v|_{i,j}$ is the area of the voxel obtained by projecting the voxel onto a plane perpendicular to the velocity vector. Since all channels were aligned in one plane, the z direction velocity component was ignored. Therefore, the equation for flow rate through a voxel became:

$$Q_{i,j} = \sqrt{\bar{v}_x|_{i,j}^2 + \bar{v}_y|_{i,j}^2} W_{i,j} Z_{th} \tag{2.36}$$

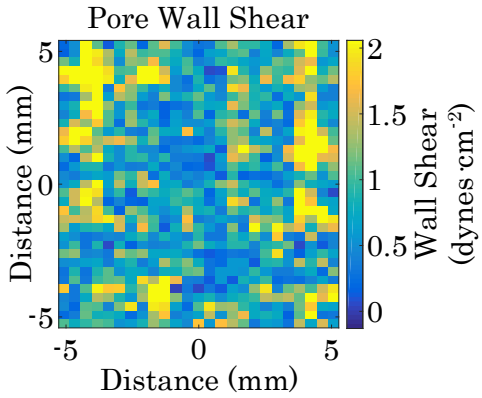

Figure 2.23: **Wall Shear in Collagen Pores.** Map of estimated shear stress at pore walls in collagen sponge plotted in dynes·cm^{-2}.

where $W_{i,j}$ is the width of the projected voxel cross section plane found from $W_{i,j} = \Delta y \cos(\theta_1|_{i,j}) + \Delta x \cos(\theta_2|_{i,j})$. $\theta_1|_{i,j}$ and $\theta_2|_{i,j}$ are the angles between the velocity vector and the x and y axes respectively. They are found using $\theta_1|_{i,j} = \arctan(\bar{v}_y|_{i,j}/\bar{v}_x|_{i,j})$ and $\theta_2|_{i,j} = \arctan(\bar{v}_x|_{i,j}/\bar{v}_y|_{i,j})$. Knowing the volumetric flow rate in each voxel and assuming

the tortuosity of the pores doubles their length relative to the length of a voxel, the average velocity in the individual pores within each voxel was estimated from:

$$v_{p_i}|_{i,j} = \frac{2L_v|_{i,j}Q_{i,j}}{\epsilon V_v} \tag{2.37}$$

where $L_v|_{i,j}$ is the length of a voxel projected in the direction of overall velocity, $L_v|_{i,j} = \Delta x \cos(\theta_1|_{i,j}) + \Delta y \cos(\theta_2|_{i,j})$ and V_v is the volume of the voxel. Applying Eq. 2.18 to wall shear in an individual pore generates $\dot{\gamma}_{p_i} = \frac{4Q_{p_i}}{\pi R_{p_i}^3}$. Substituting $v_{p_i}\pi R_{p_i}^2$ for Q_{p_i} in this equation and simplifying demonstrates that the average wall shear rate in the pores in a voxel can be approximated by:

$$\dot{\gamma}_{p_i}|_{i,j} = \frac{4v_{p_i}|_{i,j}}{R_{p_i}} \tag{2.38}$$

Using $\tau_w|_{i,j} = \mu\dot{\gamma}_{p_i}|_{i,j}$ where $\tau_w|_{i,j}$ is the approximate wall shear stress for the pores within a voxel and μ is the dynamic viscosity of cell culture media, a map of wall shear stress was plotted in Fig. 2.23.

As was the case for biopolymer hydrogels with open channels, adjusting flow inputs into each channel leads to the formation of a wide range of achievable velocity maps throughout macroporous sponges. Examples of several flow speed maps in gelatin sponges are shown in Fig. 2.24. The full MRI resolution flow speed maps are shown along side smoothed flow speed distributions, which make it easier to see the overall pattern of flow inside the scaffold.

2.5 Discussion

Multiple scaffolds, including biopolymer hydrogels and macroporous sponges were tested for their suitability as cell culture substrates in a multi-inlet bioreactor. The hydrogels materials were evaluated for their ability to promote endothelial behavior resembling vascular morphogenesis. The macroporous scaffolds were evaluated for their ability to promote cell attachment and spreading. All scaffolds were mounted in TC chambers and evaluated for their ability to withstand perfusion for extended periods without experiencing premature erosion or irreversible compression. The various scaffold materials tested in the bioreactor allow for an assortment of future tissue engineering experiments involving complex flow

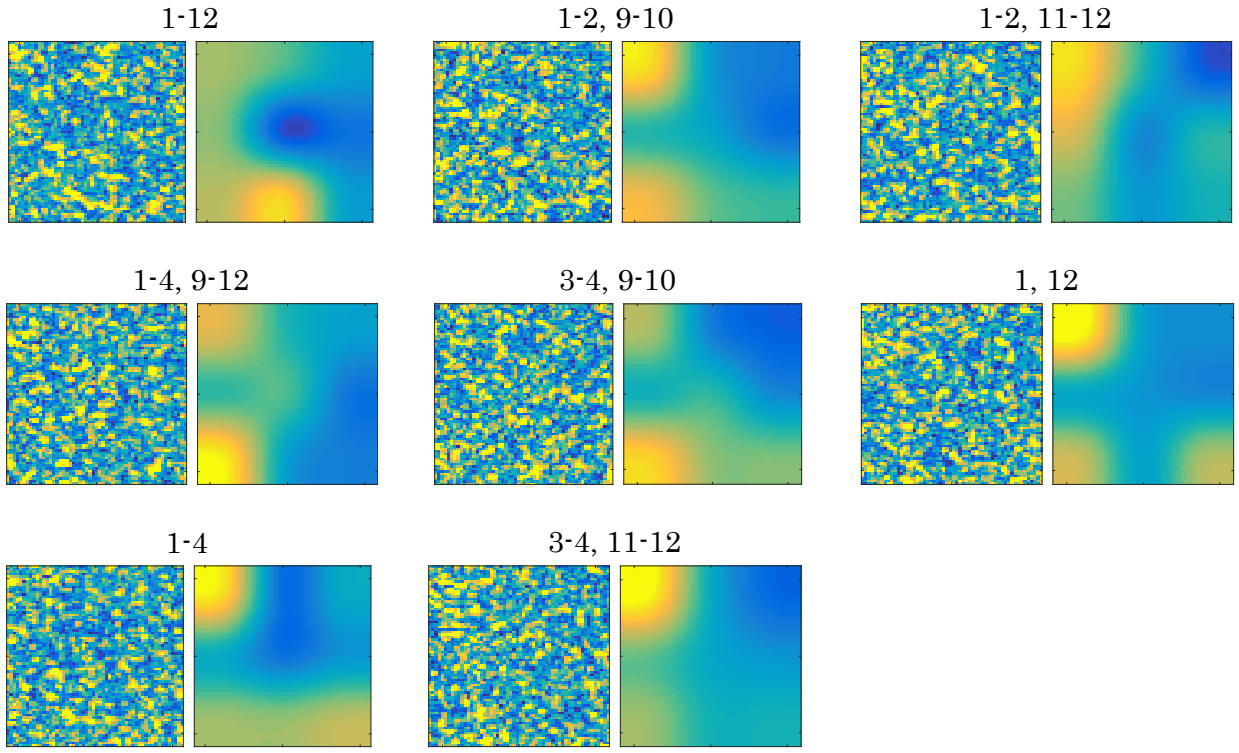

Figure 2.24: **Example Flow Speed Maps in Macroporous Sponges.** Flow was allowed through different combinations of inlets into the TC chamber in order to generate multiple examples of flow speed maps in a gelatin sponge without channels. Flow speed maps shown here were calculated from fluid velocity maps using Eq. 2.1. Each pair of images contains a MRI resolution flow speed map and the corresponding 3×3 smoothed map, which facilitates visualization of the overall flow distribution. Each pair of images corresponds to the inlet combinations specified above it. The numbers above each pair of images indicate the flow channels that were set to 0.5 mL·min^{-1}. All other channels were not flowing. A diagram of the location of the channel inlets around the TC chamber can be seen in Fig. 2.18 (a).

patterns in environments with very different fluid permeabilities and pore sizes. Biopolymer hydrogels patterned with channels provide an optimal environment to study the influence of flow on endothelial sprouting and neovascularization. Endothelial cells range in length from 22-26 μm and in width from 5-13 μm. They cover areas ranging from 70 to 245 μm^2 [382]. Compared to endothelial cells, the pores in a biopolymer hydrogel are slightly smaller than some of the cell's dimensions (such as the cell height) and much smaller than the cell in other

dimensions (length and width). This combination of dimensions allows endothelial cells to attach to and migrate across the gel surface as a monolayer, which is similar in appearance to the endothelial lining on vessel walls *in vivo*. When this occurs, a single cell blankets many matrix pores and exposed fibers at the gel surface. The dimensions of the cells also allow cells to move through the hydrogel matrix, making biopolymer gels optimal for studying endothelial sprouting in a process that resembles angiogenesis [19,127,129,214,215] and the process of *de novo* neovascularization [128,130]. In contrast, macroporous sponges are unable to support a smooth monolayer of cells due to the large pores exposed at the scaffold surface. However, macroporous sponges have found many other purposes in tissue engineering [383], and it is expected that, in the context of a bioreactor capable of controlling flow distribution, their larger permeabilities will make these sponges useful for studying the influence of large scale interstitial flow gradients on cell distribution and growth.

2.5.1 Sterilization

In the bioreactor presented in this study, the issue of residual chemical sterilant within the system that leached into cell culture media over time presented a problem for long term cell culture. One way to address this would be to configure a one way flow system in which media is not recirculated, therefore preventing the buildup of sterilant. However, the system's operating cost would increase significantly due to the large quantity of cell culture media required in one way operation. Alternatively, simply limiting culture time to under five days does not allow long term tissue culture experiments to be performed, and even on a shorter time scale sub-cytotoxic quantities of residual sterilant may influence cells in other ways and would not be optimal for sensitive cell lines. Cell culture media is needed to provide cells with nutrients and keep them hydrated. Flow of cell culture media has been used to ensure sufficient nutrient delivery deep within tissue culture constructs and to mechanically stimulate cells with shear force [13]. Without flow, the statically cultured, TC chamber-sized scaffolds only showed cell proliferation around the edges (see Fig. 2.12). The mechanical shear force introduced by flow has been shown from previous studies to impact cell behavior, and the specific effects of shear can depend on parameters such as flow direction, quantity of shear,

and chemical signals [127–129]. In this work, no cytotoxicity was observed in static cultures, which use supplies typically sterilized by irradiation. Glutaraldehyde sterilization is typically used for medical equipment, and it has been shown to cause irritation and inflammation in workers exposed to concentrations lower than 0.05 parts per million [384]

It was eventually decided to completely change the method of sterilization. Steam autoclaving is a technique that leaves no toxic residues, and residual gas from ethylene oxide sterilization was easily removed by allowing the sterilized components to degas. This sterilization method proved successful as determined by continuous flow of cell culture media through the system for three days. The downside of this method is the availability of equipment and length of time for ethylene oxide sterilization. Due to environmental regulations, there are few ethylene oxide sterilizers in use, and their use is restricted to a limited number of cycles per year. Throughout the United States, ethylene oxide emissions are regulated by the Environmental Protection Agency's (EPA's) National Emissions Standards for Hazardous Air Pollutants (NESHAPs). In addition, states and local governments may set further controls over ethylene oxide emissions. For example, in California — the location in which experiments presented in this work were conducted — ethylene oxide emissions are further governed by the airborne toxic control measure (ATCM) put forth by the California Air Resources Board (CARB). The gas sterilizer used in this work required three separate cycles due to the size of the bioreactor modules to be sterilized. The sterilization time is a major drawback because it increases the time required to prepare the bioreactor for tissue culture. Any time biological contamination occurs, cleaning and sterilization of the entire system is required. The frequency of contamination and the length of time required for gas sterilization limited the productivity of the bioreactor. Biological contamination can possibly be introduced from the lab space. Microorganism spores can travel through the air and land on surfaces which come into contact with cell culture media in the bioreactor. Although surfaces were wiped down and HEPA filtration was used, solutions of 70% alcohol solution only kills microbes in the vegetative state. Microbial spores are able to survive contact with this solution, and the entire laboratory is not HEPA filtered, only a small cabinet in which the bioreactor and media reservoir are opened for loading the TC chamber and cell culture

media.

2.5.2 Bioreactor Operation

One drawback of bioreactor system operation was its degree of complexity. The large number of steps and flow configurations required when preparing the system required extensive operator training and careful execution. One way to reduce the complexity experienced by the operator would be to replace the manually toggled stopcocks with digitally controlled solenoid valves. With these in place most aspects of priming and rinsing could be programmed to run in an automated sequence. Additionally, a simpler system could be designed with less total components to manage if one way gas pressure driven flow was implemented, since all of the components for dampening peristaltic motion would not be required. However, as noted previously, the cost of running a one way flow system would be much higher.

2.5.3 Viability and Density MRI in Bioreactor

When culturing B16-F10 cells in the bioreactor, diffusion- and MT-weighted images were used to calculate cell density and viability maps. These maps were calculated from calibrations determined from B16-F10 cells encapsulated in agarose gels in an NMR tube using different voxel dimensions [32]. Although these calibrations were able to generate initial maps of cell density and viability, the substrate was changed from an agarose gel to a gelatin sponge. The calibration parameters need to be validated and possibly corrected to account for this change using optical measurements of cell density and viability which can be achieved with histological sectioning, staining, and confocal imaging as demonstrated in Fig. 2.12. At this time the sectioning of this sample has not been completed.

2.5.4 Wall Shear and Partial Volume Effects

This work presents methods to calculate corrected wall shear from MRIs and information about the geometry of the flow environment. A method was developed to determine shear

stress at the walls of channels in biopolymer hydrogels and at the walls of pores in macroporous sponges.

A comparison of the modelled flow and shear rate profiles to those generated from the MRI showed similar profile shapes. Slight differences between the shape of the modelled profiles and the measured profiles could have resulted from the fact that there was not enough linear channel distance to achieve a fully developed, laminar flow profile. The average flow rate in these channels was determined to be 1.25 mL·min^{-1} per channel from the fact that ten of the total twelve inlet channels were located upstream of the four channel bottleneck in the ROI, and each of the inlets had a flow rate of 0.5 mL·min^{-1}. Therefore, the length of channel required to fully develop the flow profile was 2.28 mm. The length of channel in between channel intersections was only 1.14 mm. However, this did not significantly change the shape of the flow profile from what was expected according to Fig. 2.20. Instead, the biggest discrepancy between the modelled flow and measured flow was the magnitude of the fluid velocity. From Fig. 2.20, the maximum slice thickness averaged fluid velocity of the channels was measured to be 9.0 ± 1.1 mm·s^{-1}, whereas the model predicted a maximum 6.0 mm·s^{-1}. The increase in fluid velocity is likely due to an unaccounted for reduction in channel diameter. After removing the needles used for casting channels, swelling of the biopolymer matrix [385] and flow-induced deformation of soft channels [386] may induce changes to channel geometry. A biopolymer matrix bound on all sides by the TC chamber's rigid walls is restricted in the directions it can swell. One option is swelling into the open channels. The average and maximum velocity in a channel will increase by a factor of $\left(\frac{d1}{d2}\right)^2$ where $d1$ is the pre-swollen channel diameter and $d2$ is the reduced channel diameter post swelling. Therefore, a 10% decrease in diameter results in a 23% increase in velocity, and a 20% decrease in diameter results in a 56% increase in velocity. Lastly, the x resolution of the MRI was only 14% of the channel diameter. Slight changes in alignment of the voxels in the xy plane relative to the position of the channels could also affect measurements through sampling error.

In macroporous sponges, wall shear is estimated on a voxel-by-voxel bases. However, studies have shown that there is a large degree of wall shear variation among individual

pores. The pore size of macroporous sponges is on the same order of magnitude as the MRI xy resolution, making it impossible to obtain the spatially resolved velocity maps within individual pores required for directly calculating wall shear. As such, MRI is more suitable for measuring broader shear distributions in macroporous sponges, which can be highlighted by smoothing with bicubic interpolation.

2.6 Conclusion

This study presents an MRI compatible, perfusion bioreactor with multiple flow inlets capable of generating custom, steady flow patterns throughout a 3D tissue culture scaffold. The study details the design of the bioreactor, the layout of the accompanying flow system, and the protocols for sterilization and aseptic cell culture loading. Multiple types of natural ECM scaffolds including macroporous sponges and biopolymer hydrogels were demonstrated to be both suitable for endothelial cell culture and mechanically compatible with the perfused environment within the bioreactor. These scaffolds also allowed for custom flow patterns to be generated throughout the TC chamber that were unique to each type of scaffold. MRI flow maps were consistent with expected results, and they were found to be useful for determining shear stresses experienced by cells attached to surfaces in various types of 3D environments. It was demonstrated that MRIs of flow through cylindrical channels in a hydrogel with low interstitial fluid permeability could be used to calculate the shear stress experienced at the wall of the channel.

It was also shown that maps of wall shear stress in pores of a sponge could be approximated from flow-weighted MRIs. This is relevant for translating studies of the effect of shear on cell behavior from 2D to 3D environments. Most 2D studies of shear use a calculated wall shear when investigating impact of shear on cell growth, making a direct comparison of wall shear in 3D environments desirable. As demonstrated by comparing theoretical velocity and shear profiles in Fig. 2.20 (a) to measured profiles in Fig. 2.20 (c), shear rate calculated by the finite differences method does not measure wall shear accurately due to partial volume effects. The more accurate methods of determining wall shear presented here further justify

the use of MRI as a tool to investigate the impact of shear on cell behavior in thick, optically opaque environments.

Flow patterns were shown to generate patterns of parenchymal cell growth throughout the scaffold which differed from patterns of growth in static culture. Given the demonstrated compatibility of both macroporous scaffolds and biopolymer hydrogels with the multi-inlet bioreactor, it is expected that similar multi-channel perfusion bioreactors will make contributions in the study of the influence of luminal and interstitial shear gradients on the growth and development of multiple cell and tissue types. As the impact of shear distribution on cell behavior throughout large 3D volumes becomes clear, the use of shear distribution as an actuating mechanism to control cell growth may become available. Coupling this actuating mechanism with noninvasive readouts of cell viability and density distribution can potentially allow real-time control over engineered tissue development. Spatial distributions of cells throughout a construct can be directly manipulated by biomechanical signaling during culture to generate custom tissue. In addition, the potential to control cell behavior throughout a porous 3D environment using spatiotemporally varied biomechanical signals makes this bioreactor applicable to other types of biomanufacturing besides tissue engineering. For example, this bioreactor has the potential to optimize shear and nutrient distribution throughout high density cell culture in a bed of packed beads for the production of cells themselves or cell-produced proteins.

CHAPTER 3

Noninvasive Quantification of Cell Density in 3D Gels by MRI

3.1 Introduction

Tissue engineering strives to generate larger, more complex, and increasingly functional substitutes for the clinical purpose of replacing lost or damaged tissue. Additionally, there is a critical need for studying organoid systems in an *ex vivo* setting to determine cell response to controlled stimuli. These approaches typically involve a combination of scaffold, growth factors, and living cells housed in a bioreactor designed to provide suitable culture conditions for tissue growth. Recently, bioreactors have become increasingly specialized by providing dynamic and spatially controlled signals to mimic the dynamic environments present during development [387–390]. The tissues and organoids cultured *ex vivo* have increased in size and complexity, to the point where it is difficult to image them with light, such as reloaded decellularized organs and thick bioprinted tissue [391, 392]. More invasive methods such as cross-sectioning and histology are traditionally used to evaluate tissue morphology, but they are not suitable for real-time *in situ* readouts, which are necessary for adaptive control schemes [24].

Noninvasive methods for probing large masses of soft tissue include ultrasonography and magnetic resonance imaging (MRI), two methods that do not require ionizing radiation and can function without contrast agents. In this study, we investigate the utility of contrast agent-free MRI for cell density mapping. MRI provides unparalleled soft tissue contrast in clinical applications, e.g. tumor diagnosis, and has been used to measure hydrodynamic properties of biomaterials [27, 168]. Recent developments in MRI compatible incubators and

bioreactors provide additional justification for the development of MRI based, biological measurements [24, 287].

The responses of diffusion-, T_2-, and magnetization transfer (MT)-weighted nuclear magnetic resonance (NMR) parameters have been used in the past to assess cell density in the context of explanted tumors and brain abscess [271–284]. The most popular weighting for generating cell density maps has been diffusion. Correlations were found between the apparent diffusion coefficient (ADC) and cell density in neural [271–275], dermal [276], prostatic [277], renal [278], and breast [279,280] tumors in magnetic fields ranging from 1.5 T to 3 T, but one study by Yoshikawa *et al.* found no correlation between cellularity and ADC in breast cancer at 1.5 T [393]. ADC was found to be correlated to cell density in brain abscess in a 1.5 T magnetic field [281], and using a higher diffusion weighting factor in a 3 T field improved the correlation of brain abscess cell density and ADC [282]. MT signal was reported to be inversely correlated to cell density in brain abscess and brain gliomas [283,284]. T_2 was found to be inversely correlated to cell density in prostate cancer but not gliomas [273,277], and a study by Roth *et al.* noticed a decreasing trend in T_2 as cells in suspension settled and increased in cell density (significance and goodness-of-fit was not reported) [307]. One study reported a significant positive correlation between T_2-short and liver cancer cellularity [394]. In all of these previous studies (excluding Roth *et al.*), tumors or abscess were imaged *in vivo* and evaluated for cellularity via histological examination or cell counting.

Despite the large number of studies published to date investigating the MRI response to cell density *in vivo* for clinical applications, only two studies investigated immobilized cell cultures in contexts of engineered tissue. In those studies, only diffusion-weighted NMR signals were investigated [308,395]. Data by Pilatus *et al.* showed a strong correlation between cell density and fraction of intracellular volume measured with diffusion-weighted NMR (not spatially-resolved) measurements in cancer cell lines cultured on solid surfaces, including polystyrene beads and collagen sponges [395]. Anderson *et al.* found a correlation between cell volume fraction and apparent diffusion coefficient in images of hydrogel encapsulated cell pellets, but experiments were run at $\sim 20^{\circ}$C [308]. Compared to physiological conditions used for tissue culture, a lower temperature leads to lower diffusion coefficients [396] and

higher diffusion weighted signal (Stejskal-Tanner [397]). Surprisingly, whereas many studies reported a correlation between cell density and NMR signal, none of the studies reported limits of detection (LOD) or quantitation. The LOD figure-of-merit, which is a measure of the level of statistical significance, is necessary in order to correctly interpret results from cell density measurements.

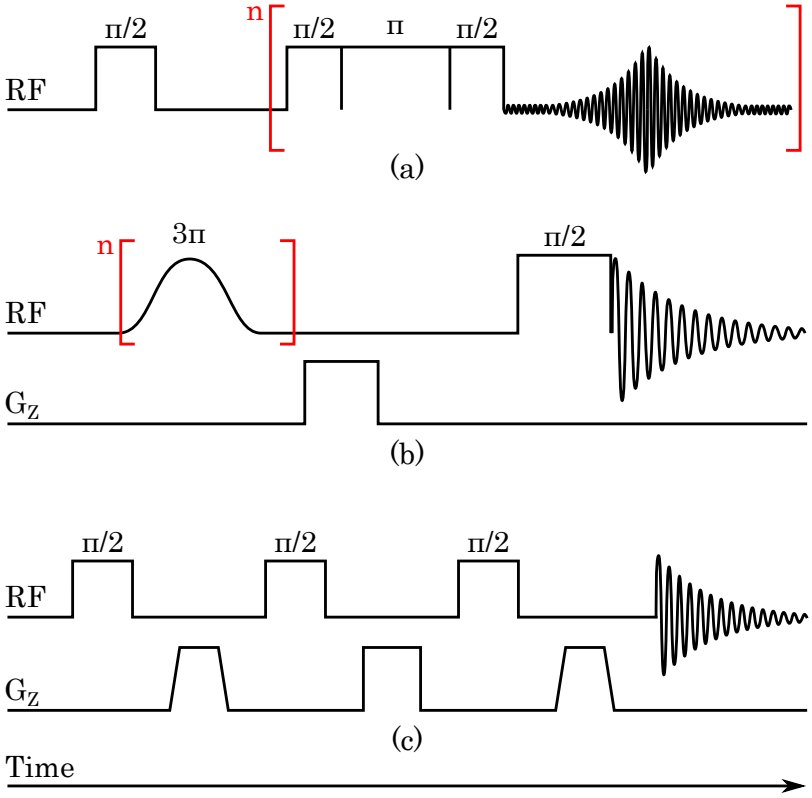

Figure 3.1: (a-c) **Timing diagrams for NMR experiments.** Diagrams of NMR pulse sequences used to calibrate ^{1}H NMR spectra or echo intensity to cell density. Portions of the sequence bracketed in red were repeated n times. (a) A Carr-Purcell-Meiboom-Gill (CPMG) sequence was used to provide T_2-weighted signals. The number of echoes collected was 2,400. (b) Pulsed, off-resonance irradiation MT sequence provides MT weighting. 400 Gauss pulses were used. (c) A PFG-STE sequence was used to provide diffusion-weighted signals.

To our knowledge, none of these NMR techniques have been applied to cells encapsulated within a hydrogel under physiological temperature conditions for tissue engineering applications. Such a method for mapping cell density in 3D scaffolds would be of paramount

Table 3.1: Phase cycling scheme for PFG-STE pulse sequence.

Pulse	Phase Cycling
1. $\pi/2$	[0, $\pi/2$, 0, $\pi/2$]
2. $\pi/2$	[0, 0, $\pi/2$, $\pi/2$]
3. $\pi/2$	[0, 0, 0, 0]
Receiver	[0, $\pi/2$, $\pi/2$, 0]

importance in tissue engineering. The extent to which MRI can be used in tissue engineering applications is presently unknown.

In this study, we examined T_2, MT, and diffusion-weighted ^{1}H NMR signals as a means to quantify cell concentration in an artificially constructed tissue sample composed of mammalian or yeast cells embedded in an agarose hydrogel. T_1 is not discussed herein because we found it to be less sensitive to cell density. Whereas each weighting (T_2, MT, diffusion) has its own unique set of influencing factors, they are all used for clinical imaging of soft tissues. For example, in living tissues, the T_2 is known to be significantly reduced for water protons that are immobilized, such as in the case of water molecules interacting with or bound to macromolecule surfaces. In MT experiments, a saturation pulse selectively eliminates net longitudinal magnetization in protons bound to macromolecules, and their depleted magnetic state is transferred to free water protons in the vicinity for readout. In T_2 and MT experiments, the signal intensity typically decreases as cell concentration, and consequently macromolecular content, increases. In excised tumor samples the apparent diffusion coefficient of water has been shown to decrease with increasing cell concentration due to reduced motion in protons that are bound to macromolecules or trapped within intracellular compartments.

Nearly all previous work on the topic has been conducted in the context of clinical imaging as a tool to study tumor composition. The situations encountered in tissue engineering represent a different regime where the cell densities are significantly lower than those of excised tissue. Hence, detection limits are very important. We investigate the efficacy of this

technology on yeast and human cell lines encapsulated in gels of varying macromolecular content. By generating quantitative analytical calibration curves for measuring cell concentration from NMR signals, this study paves the way for novel methodologies to map local cell densities in 3D bioreactors for tissue engineering applications.

3.2 Materials and methods

3.2.1 Preparation of NMR Samples

3.2.1.1 Cell Culture and Harvest

Prior to taking NMR measurements, HEK 293 cells (ATCC®, CRL-11268™) were cultured in a 37°C, 5% CO_2 incubator in Dulbecco's Modified Eagle's Medium (DMEM) supplemented with 10% FBS, L-glutamine, and penicillin/streptomycin. The temperature and CO_2 concentration were selected to match conditions used in previously established MRI compatible culture systems. [24,287]. Cells were detached from dish surfaces with trypsin and then neutralized with αDMEM containing 10% FBS. Cells were pelleted by centrifugation at 200 g for 5 min, and the remaining media was aspirated, leaving cell pellets. Quantities of pelleted cells were measured volumetrically with a positive displacement micropipette and diluted in DMEM to obtain a range of cell concentrations.

Dry yeast from *Saccharomyces cerevisiae* (Sigma, YSC2-500G) were reconstituted in phosphate buffered saline (PBS) immediately prior to use. A range of yeast concentrations was obtained by adjusting the weight % of yeast used.

3.2.1.2 Determining Cell Density in a Pellet

The concentration of HEK 293 cells in a pellet was determined by diluting volumes of cell pellet by 400, 600, or 800-fold in DMEM. The number of cells in these dilutions were counted via hemocytometer and used to determine the original cell concentration in the pellet. Yeast cell concentrations were also determined via hemocytometer counting. Average cell sizes

were measured from microscope images of suspended cells on the hemocytometer in ImageJ.

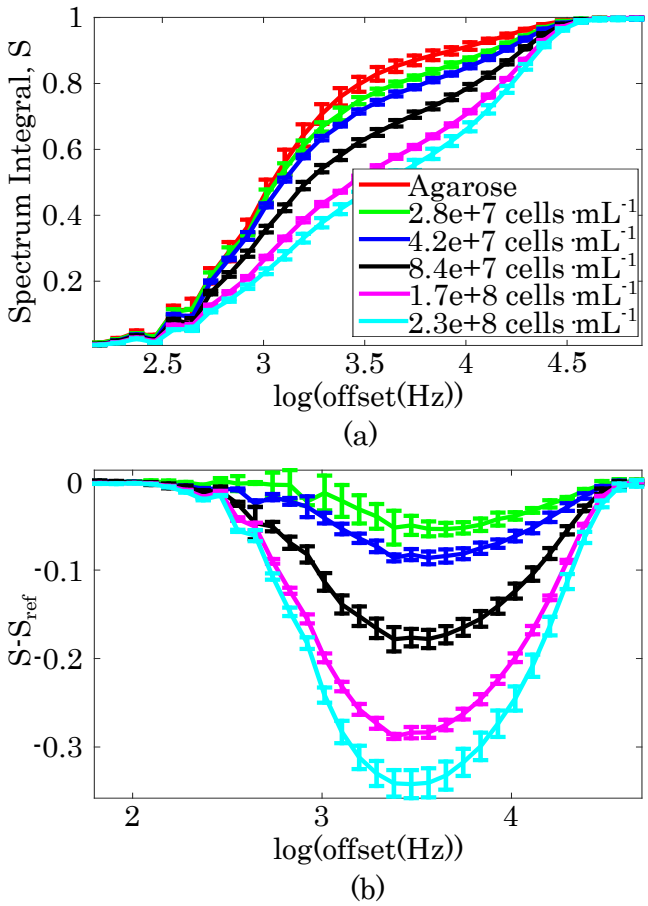

Figure 3.2: **MT Optimization.** (a) MT Z spectra of agarose samples containing range of cell concentrations. S represents the normalized intensity of the signal obtained by integrating the weighted NMR spectrum. (b) MT contrast curves obtained by subtracting an acellular agarose gel sample MT curve from curves of samples containing cells. The difference, $S - S_{\text{Ref}}$, represents the signal contrast generated by the presence of cells. (S_{Ref}) is the signal intensity of the acellular agarose sample. The frequency offset resulting in the largest signal change in response to changes in cell density was later used for imaging experiments.

3.2.1.3 Cell Encapsulation

Prior to acquiring ^{1}H spectra, HEK 293 or yeast suspensions were combined in a 1:1 ratio with a liquid solution containing 1.8% low gelling temperature agarose (Sigma, A9045-5G) in

PBS at 37°C. The mixture was immediately added to a 5 mm NMR tube and allowed to gel at room temperature. After gelation, the samples were reheated to 37°C inside the bore of a Varian 400 MHz (9.4 T) spectrometer equipped with a 10 mm broadband probe and air-flow variable temperature (VT) control. This cell encapsulation technique involving the cooling and reheating of cells during agarose gelation is an established procedure known to result in the containment of high viability cells within a gel matrix [398]. The HEK 293 cell densities used for spectroscopy calibrations were 0, 0.7, 1.4, 2.8, 4.2, 5.6, 8.4, 11.3, 16.9, and 22.2×10^7 cells·mL^{-1}, and the yeast cell densities used were 0, 0.2, 0.4, 0.8, 1.6, 2.0, 4.0, 8.0, and 10.0×10^8 cells·mL^{-1}. Each sample was repeated three times using freshly encapsulated cells.

Samples of HEK 293 and yeast cells were prepared for imaging by casting multiple layers of agarose in a 5 mm NMR tube sequentially. Each layer contained a known cell density and was allowed to anneal before the next layer was added. The four cell densities used were 1.4, 2.8, 5.6, and 11.3×10^7 cells·mL^{-1}. Pure agarose was cast above and below the cell laden layers in order to position the cells close to the center of the radio frequency (RF) coil. In the case of yeast imaging, four layers containing 0.63, 1.3, 2.5, and 5.0 $\times 10^8$ cells·mL^{-1} were cast between layers of acellular agarose. The 5 mm NMR tubes containing layered samples were suspended and imaged in a 40 mm inner diameter RF probe while the temperature was maintained at 37°C with heated airflow. A 40 mm probe was used for imaging because it has been shown to be an effective size for accommodating bioreactors and incubation systems [24, 287].

3.2.2 NMR Weighting Calibrations

The pulse sequences that were used to calibrate NMR signal to cell density are shown in Fig. 3.1a-c. T_2 values were obtained from a CPMG experiment (Fig. 3.1a) by integrating the area under the even numbered echoes, normalizing the echo integrals between 0 and 1, and fitting the resulting curve to the exponential decay in (3.1) for relaxation in the transverse plane:

$$M_{xy}(t) = M_0 e^{-t/T_2} + \beta, \tag{3.1}$$

where β is a baseline offset, M_{xy} is the transverse magnetization at time t and M_0 is the initial transverse magnetization at $t = 0$.

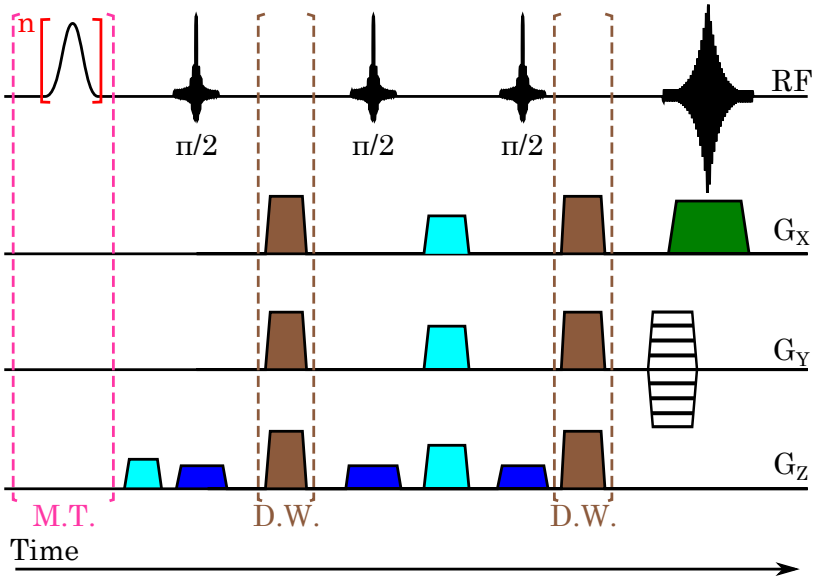

Figure 3.3: **Stimulated Echo Multi-Slice Sequence.** Diagram of a STEMS pulse sequence with optional modifications corresponding to respective weighting. Diffusion weighted (D.W.) gradients are highlighted and bracketed in brown. A pulsed, off-resonance, Gaussian saturation pulse used to generate MT weighted images is bracketed in magenta. Red brackets refer to a portion of the pulse sequence repeated n times, which in this case is the off resonance saturation pulse used for MT weighted imaging. The off resonance saturation pulse for MT was calibrated to 540° (3π). Slice select (S.S.) gradients are highlighted in blue, frequency encoding (F.E.) in green, spoiler gradients in cyan, and phase encode (P.E.) in white.

MT-weighted Z spectra were obtained by applying a train of off-resonance saturation pulses prior to a standard, on-resonance $\pi/2$ (hard) pulse (Fig. 3.1b).

Diffusion-weighted measurements were obtained using a Pulsed Field-Gradient STimulated-Echo (PFG-STE) experiment (Fig. 3.1c). The phase cycling scheme used with this sequence is shown in Table 3.1. The b-value is the diffusion weighting factor:

$$b = \gamma^2 G^2 \delta^2 (\Delta - \delta/3), \tag{3.2}$$

defined by Stejskal-Tanner [397] in their signal equation

$$\log\left(\frac{S_G}{S_0}\right) = -D\gamma^2 G^2 \delta^2 (\Delta - \delta/3), \tag{3.3}$$

where D is the diffusion coefficient of water, γ is the gyromagnetic ratio of the ^{1}H nucleus ($\gamma = 2.675 \times 10^8$ rad·s^{-1}·T^{-1}), G is the effective gradient strength of the diffusion weighted gradients measured in T·mm^{-1}, δ is the duration of a single diffusion weighted gradient in s, and Δ is the diffusion time which is defined as the time between the start of the application of the first diffusion weighting gradient and the start of the second diffusion weighting gradient. S_G stands for signal intensity acquired when using diffusion weighting gradients of effective strength, G. S_0 is the signal intensity acquired without diffusion gradients.

Pulse sequence parameters for all three weightings were chosen to maximize the contrast that results from changes in cell density. Specifically, pulse sequence parameters were arrayed over a range of values, and spectra were acquired at each value in the array. Signal intensities of cell laden gel samples (S) and acellular agarose gel (S_{Ref}) were determined by integrating ^{1}H peaks from each acquisition. Parameter values that resulted in the largest cell generated signal contrast, defined as $|S - S_{\text{Ref}}|$, per change in cell density were subsequently used for spectroscopy calibrations. The cell densities used for parameter optimization were the same that were used for spectroscopy calibrations. Prior to beginning MT weighted experiments, the frequency offset of the saturation pulse was optimized. A fifty point array of frequency offset values spaced on a log scale from 0 to 200 MHz was used for optimization (an identical optimization was performed for the range of frequency offsets from 0 to -200 MHz, but no significant difference was seen in the negative direction). Plots of frequency offset versus signal intensity and frequency offset versus cell generated contrast are displayed in Fig. 3.2 to highlight the dependence of contrast on frequency offset and show how the optimal parameter value was found. Prior to beginning T_2 weighted spectroscopy calibrations, the echo time (t_{E}) was optimized. t_{E} versus cell generated contrast ($|S - S_{\text{Ref}}|$) was plotted (not shown), and the t_{E} resulting in the largest contrast was selected for calibrations. Because a CPMG sequence was used, signal intensity, S, was found by integrating each echo rather than a full spectrum. A total of 1,500 echoes were acquired at TEs linearly spaced between 0 and 1.4

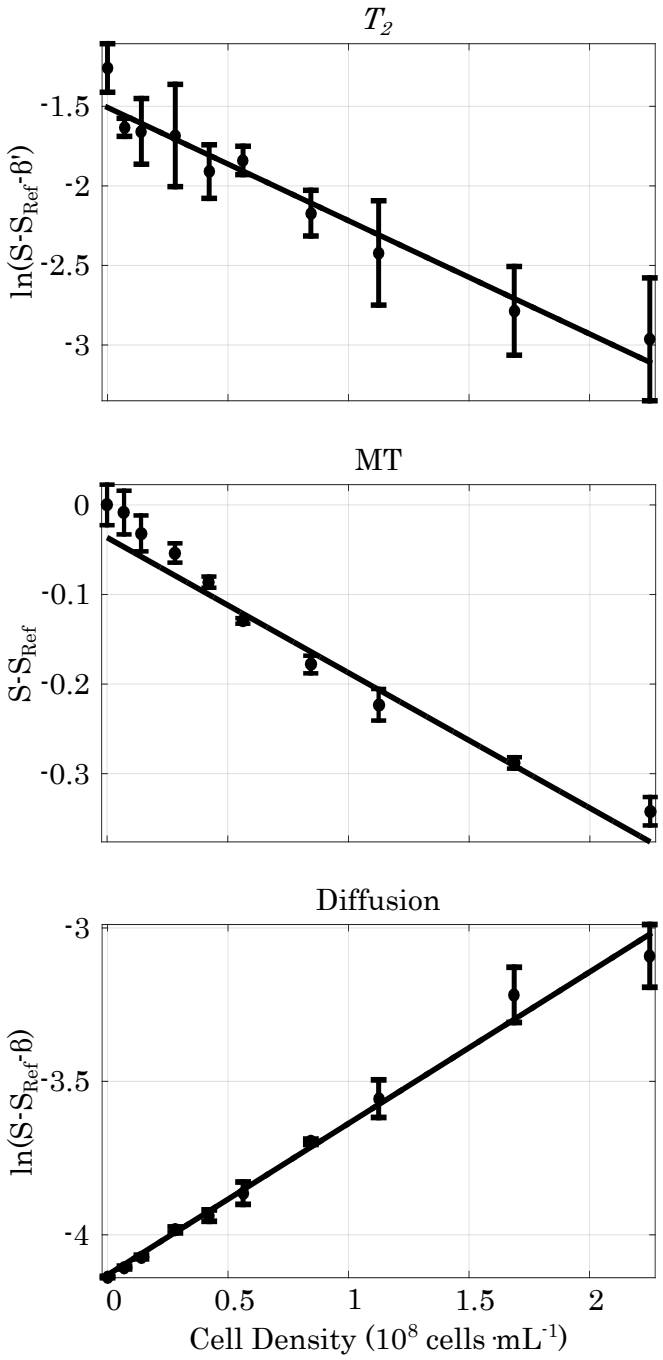

Figure 3.4: **Cell Density Calibrations.** From top to bottom: T_2-weighted, MT-weighted, and diffusion-weighted calibration curves of NMR spectra intensity to HEK 293 cell density. Each point represents the signal generated by agarose alone subtracted from S_{Ref}, the signal generated by a given cell concentration. Error bars represent one standard deviation (n=3).

seconds. Prior to diffusion weighted spectroscopy, both G and Δ were optimized to generate the best b-value. The values of Δ used were 25, 30, 50, 100, 150, and 200 ms, and at each value of Δ, G was arrayed from 0 to 50 Gauss·cm^{-1}. Spectra acquired at each combination were integrated, and the combination of parameter values resulting in the largest amount of contrast ($|S - S_{\mathrm{Ref}}|$) were used for diffusion weighted calibrations.

NMR signals weighted by T_2, MT and diffusion parameters vs cell concentration were linearly fit using a weighted least-squares regression. Relevant fitting parameters and their corresponding statistical hypothesis testing probability values (p-values) are reported [399]. The LOD corresponds to the cell concentration at which the weighted NMR signal differs from the acellular agarose NMR signal by exactly three times the average standard deviation:

$$\mathrm{LOD} = \frac{3\overline{\sigma}}{slope}, \tag{3.4}$$

where the *slope* is determined from the weighted least-squares regression linear fit and $\overline{\sigma}$ is the average standard deviation of all points used in the corresponding fit.

3.2.3 NMR Imaging Protocol

Images of cell density were obtained using a STimulated Echo Multi-Slice (STEMS) sequence modified to generate each of the three types of weightings. T_2-weighted images were obtained by setting the repetition time (TR) to a long value roughly five times T_1 and the t_{E} to the value optimized in T_2 calibrations. MT-weighted images were generated by applying a train of off-resonance saturation pulses in the beginning of the STEMS sequence, using a long TR, and a short TE. Anti-phase pulse field-gradient pairs were applied after the first and last $\pi/2$ pulses in STEMS to obtain diffusion-weighted contrast. In order to compare the quality of the three weightings over the same scale, each image was normalized between 0 and 1 by applying the following function to every voxel in the image:

$$I_{norm} = \frac{I - I_{min}}{I_{max} - I_{min}}, \tag{3.5}$$

where I_{norm} is the normalized voxel intensity, I is the pre-normalized voxel intensity, I_{min} is the value of the lowest intensity voxel in the image, and I_{max} is the value of the highest

intensity voxel in the image.

Cell density maps were generated from T_2, MT, and diffusion weighted images using calibration curves relating voxel intensity to cell density. Since images were acquired in a different NMR probe than the one used for spectroscopy measurements, new calibration curves were generated for cell density mapping (not shown). Briefly, regions of interest (ROIs) were drawn within areas of the pre-normalized images containing known cell densities. The same ROIs were used for T_2, MT, and diffusion weighted images. A calibration curve was fitted to a plot of the mean value of each ROI versus cell density using weighted least-squares regression.

All fits were generated in MATLAB. Exponential fits were generated using MATLAB's nonlinear regression function (`fitnlm`), which employs the Levenberg-Marquardt algorithm. Linear fits were generated with a nonrobust, weighted linear least squares algorithm (`fitlm`). The weight of each point was $1/\sigma^2$, where σ is the standard deviation of the measurement.

3.3 Results

3.3.1 HEK 293s

The cell concentration in a pure HEK 293 cell pellet was determined to be $(4.5 \pm 0.9) \times 10^8$ cells·mL^{-1}. The average diameter of the HEK 293 cells was 12.5 ± 2.4 μm. Calibration curves showing the response of T_2, MT, and diffusion-weighted spectral intensity to cell concentration are seen in Fig. 3.4. As expected, T_2-weighted signal decreases with increasing cell concentration. The optimal delay time for generating maximum contrast in T_2 spectroscopy experiments was found to be 140 ms. A single echo with a delay of 140 ms was integrated for each cell concentration to generate the T_2-weighted calibration curve shown in Fig. 3.4. The relationship between T_2-weighted signal and cell density appeared to take the form of an exponential decay. This type of relationship is expected when $1/T_2(C)$ (a function of concentration, C) depends linearly on cell concentration [26]:

$$\frac{1}{T_2}(C) = \frac{1}{T_{2,\mathrm{Ref}}} + const \times C, \tag{3.6}$$

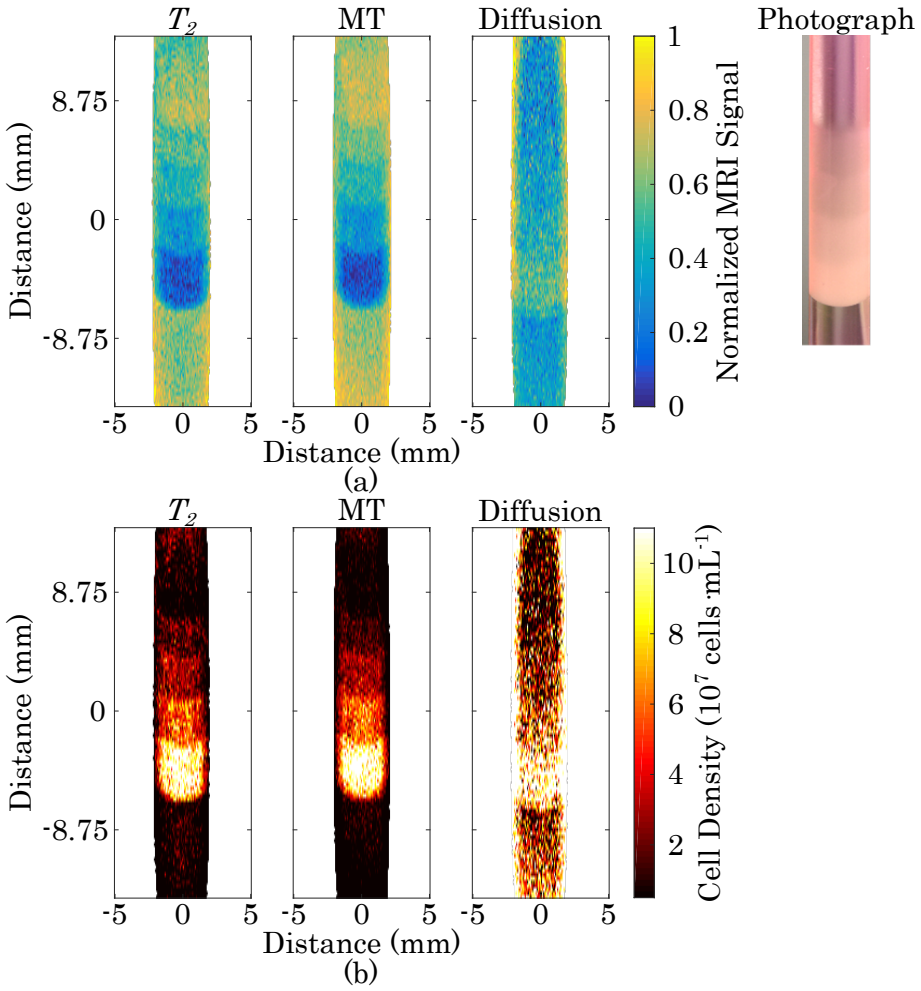

Figure 3.5: **HEK 293 Cell Density MRIs.** (a) From left to right: T_2, MT, and diffusion-weighted MRIs of an NMR tube containing stratified layers of varied HEK 293 cell densities in agarose gels. The image on the far right is a photograph showing optical opacity of the layers. Bottom and top of the tube are filled with acellular agarose gel mixed with DMEM. The phenol red in DMEM gives it a pink color. Four layers from top to bottom contain cell concentrations of 1.4, 2.8, 5.6, and 11.3×10^7 cells·mL^{-1}. The MRI signal throughout the region is normalized between 0 and 1. The curvature between layers is due to the menisci that form during the gel casting process in a 4.2 mm inner diameter NMR tube (Wilmad 513-7PP-7). Each layer was cast and annealed sequentially, allowing it to form and retain its meniscus as the agarose annealed. (b) Cell density maps calculated from T_2, MT, and diffusion-weighted MRIs using calibration curves relating voxel intensity to cell density.

where $1/T_{2,\mathrm{Ref}}$ is the transverse relaxation rate in the absence of cells and *const* is the relaxivity of the cells added to the gel solution. The NMR signal equation for the T_2-weighted signal acquired at t_E ($t = t_\mathrm{E}$) is then

$$S = S_0 e^{-t_\mathrm{E}/T_2(C)} + \beta = S_0 e^{-t_\mathrm{E}/T_{2,\mathrm{Ref}}} e^{-t_\mathrm{E} \cdot const \times C} + \beta. \tag{3.7}$$

By applying (3.1) to the reference sample:

$$S_\mathrm{Ref} = S_{0,\mathrm{Ref}} e^{-t_\mathrm{E}/T_{2,\mathrm{Ref}}} + \beta_\mathrm{Ref} \tag{3.8}$$

we can write our signal contrast as:

$$\begin{aligned} S - S_\mathrm{Ref} = S_0 e^{-t_\mathrm{E}/T_{2,\mathrm{Ref}}} e^{-t_\mathrm{E} \cdot const \times C} + \\ \beta - S_{0,\mathrm{Ref}} e^{-t_\mathrm{E}/T_{2,\mathrm{Ref}}} + \beta_\mathrm{Ref} \end{aligned} \tag{3.9}$$

where β and β_Ref are baseline offsets of cell and acellular reference samples, respectively. Because $T_{2,\mathrm{Ref}}$ is independent of cell concentration, we abbreviate $S_0' = S_0 e^{-t_\mathrm{E}/T_{2,\mathrm{Ref}}}$ and $\beta' = \beta - S_{0,\mathrm{Ref}} e^{-t_\mathrm{E}/T_{2,\mathrm{Ref}}} + \beta_\mathrm{Ref}$, so that

$$S - S_\mathrm{Ref} = S_0' e^{-t_\mathrm{E} \cdot const \times C} + \beta'. \tag{3.10}$$

Thus, there is an exponential dependence of T_2 weighted contrast on cell density. The baseline offset, β', can be found from fitting an exponential regression to the data. Correcting for this offset and taking the natural log of both sides leads to a linear relationship between $\log[S(t_\mathrm{E})]$ and C:

$$\log[S - S_\mathrm{Ref} - \beta'] = slope \times C + intercept, \tag{3.11}$$

which shows that a plot of the logarithm of baseline corrected signal vs concentration follows a straight line. None of the previous studies on the response of T_2 to cell density report this very simple relationship [273, 277, 307, 394]. After correcting for the baseline offset, β', which was determined to be 0.0864, the resulting linear fit had a coefficient of determination (R^2) of 0.95. The slope of the fit was found to be -7.1×10^{-9} (p-value, 1.3×10^{-8}). The LOD for the linearized T_2-weighted spectroscopy calibration curve was determined to be

9.0×10^7 cells·mL^{-1}. A single CPMG echo-train acquisition took 48.7 s. Thus, the LOD per root bandwidth was 1.1×10^9 cells·mL^{-1}·Hz$^{-1/2}$.

The MT-weighted results also produced an inverse correlation between signal intensity and cell concentration. An offset frequency of 3,500 Hz was found to generate the highest degree of contrast. A single spectrum at this offset was integrated to generate the MT-calibration curve. Given the equation for magnetization transfer ratio (MTR):

$$\mathrm{MTR} = 1 - \frac{S}{S_0} \tag{3.12}$$

we can express $S - S_{\mathrm{Ref}}$ as:

$$\begin{aligned} S - S_{\mathrm{Ref}} = S_0 - S_0 \times \mathrm{MTR} - \\ S_{0,\mathrm{Ref}} + S_{0,\mathrm{Ref}} \times \mathrm{MTR}_{\mathrm{Ref}}, \end{aligned} \tag{3.13}$$

where S and S_{Ref} are the signal intensities of cell laden samples and the acellular reference sample following the application of an off-resonance saturation pulse, S_0 and $S_{0,\mathrm{Ref}}$ are the signal intensities of the cell and reference samples without an off resonance pulse, and $\mathrm{MTR}_{\mathrm{Ref}}$ is the MT ratio of the reference sample at the same frequency offset used for cell samples. Combining this with the established positive linear dependence of MTR on cell concentration ($\mathrm{MTR}(C) = \mathrm{MTR}_{\mathrm{Ref}} + const \times C$) [283, 284], we can determine the dependence of $S - S_{\mathrm{Ref}}$ on C:

$$\begin{aligned} S - S_{\mathrm{Ref}} = S_0 - S_0 \times (\mathrm{MTR}_{\mathrm{Ref}} + const \times C) - \\ S_{0,\mathrm{Ref}} + S_{0,\mathrm{Ref}} \times \mathrm{MTR}_{\mathrm{Ref}}, \end{aligned} \tag{3.14}$$

which can be simplified to the linear dependence:

$$S - S_{\mathrm{Ref}} = -S_0 \cdot const \times C + S_0', \tag{3.15}$$

where *const* is a positive real number and S_0' is used to lump all terms on which there is no concentration dependence:

$$S_0' = S_0 \times (1 - \mathrm{MTR}_{\mathrm{Ref}}) - S_{0,\mathrm{Ref}} \times (1 + \mathrm{MTR}_{\mathrm{Ref}}). \tag{3.16}$$

The fitted data were linear ($R^2 = 0.97$), matching the model. The fitted slope was equal to 1.5×10^{-9} ($p = 2.7 \times 10^{-10}$). The MT weighted LOD was determined to be

2.7×10^7 cells·mL^{-1}. Given a single scan time of 28.3 s (including a delay to account for T_1 relaxation) LOD per root bandwidth is 2.5×10^8 cells·mL^{-1}·Hz$^{-1/2}$.

Diffusion-weighted signal intensity appeared to be exponentially correlated with cell density. Given the inverse linear dependence of ADC on cell density [276–278, 280–282], which can be stated as

$$D(C) = D_{\text{Ref}} - const \times C, \tag{3.17}$$

and the Stejskal-Tanner equation (3.3), the relationship between diffusion weighted signal and cell concentration becomes

$$S_G = S_0 e^{-(D_{\text{Ref}} - const \times C)b}. \tag{3.18}$$

Subtracting the reference and simplifying leads to

$$\begin{aligned} S_G - S_{G,ref} =& S_0 e^{-D_{ref} \cdot b} e^{b \cdot const \times C} - S_{0,ref} e^{-D_{ref} \cdot b} \\ =& D_0 e^{b \cdot const \times C} + \beta, \end{aligned} \tag{3.19}$$

where $D_0 = S_0 e^{-D_{\text{Ref}} b}$, $\beta = -S_{0,\text{Ref}} e^{-D_{\text{Ref}} \cdot b}$, and *const* is a positive real number. This can be linearized by correcting for the offset and taking the natural log of both sides:

$$\log[S_G - S_{G,\text{Ref}} - \beta] = slope \times C + intercept. \tag{3.20}$$

A b-value of 3,500 s·mm^{-2} and diffusion time of 0.10 s were found to generate the highest degree of contrast in diffusion-weighted NMR experiments. Prior to linearization, the offset was determined from a weighted, least-squares exponential regression to be -0.0160. The linearized diffusion data had a fitted slope of 4.9×10^{-9} ($p = 1.1 \times 10^{-11}$), ($R^2 = 0.99$). The LOD was determined to be 2.1×10^7 cells·mL^{-1}. The phase cycling scheme used in these diffusion-weighted measurements, resulted in a longer acquisition time of 104 s. The associated LOD per root bandwidth is 3.7×10^8 cells·mL^{-1}·Hz$^{-1/2}$.

Images of NMR tubes containing distinct bands of known cell densities in agarose gels are shown in Fig. 3.5. The bands contain cell densities of 1.4, 2.8, 5.6, and 11.3×10^7 cells·mL^{-1}. A t_{E} of 130 ms and TR of 25 s were used for T_2-weighted imaging due to a slight improvement

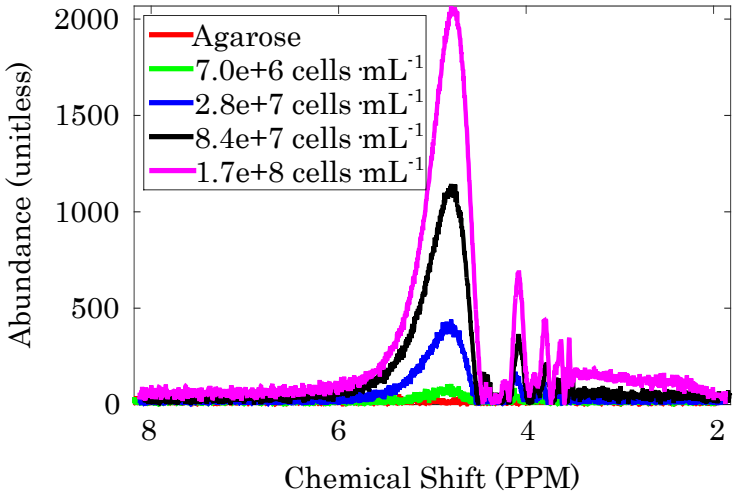

Figure 3.6: **Diffusion Weighted ^{1}H Spectra.** Several example spectra acquired with a PFG-STE spectroscopy sequence.

in image quality over the 140 ms delay that had been optimized in spectroscopy calibrations. The 3,500 Hz saturation offset value obtained from spectroscopy optimization experiments was used for MT-weighted imaging. The parameters optimized in diffusion weighted spectroscopy were found to be inadequate for diffusion-weighted imaging. The parameters did not work for imaging because the diffusion weighted signal per voxel was too weak at the given b-value. Instead, a diffusion time of 20 ms and b-value of 800 s·mm^{-2} were found to generate sufficient signal while retaining enough contrast between layers. Reducing the b-value further improved signal intensity, but lessened the degree of contrast between the layers.

T_2 and MT-weighted images were able to resolve the four different cell density gels distinctly from each other and from the background agarose signal. The diffusion-weighted images were able to resolve only the two highest cell concentrations, but the lower cell concentration layers could not be distinguished from the background. It can be seen that the diffusion-weighted spectra, especially at the lower end of the cell concentration range, have a low signal-to-noise ratio (Fig. 3.6). These spectra were generated from the entire sample volume in the RF region in the NMR probe. The HEK 293 cell density images were acquired with a resolution of 128 × 128 pixels (images shown in Fig. 3.5 are cropped) and are of

2 mm-thick slices. The total volume per voxel was only 0.043 mm^3, which does not generate enough signal to be detected at low cell concentrations.

3.3.2 Yeast

Yeast measurements show that similar correlations of signal intensity are observed for cell types across kingdoms (Fig. 3.7). It was determined that a 1% (w/w) yeast solution corresponds to $(2.0\pm0.7)\times10^8$ cells·mL^{-1}. The average diameter of the yeast cells was 5.2 ± 0.9 μm. The exponential offset was found to be 0.0247. The linearized T_2-weighted slope was found to be -7.2×10^{-10} ($p = 1.8\times10^{-9}$) ($R^2 = 0.98$), and the LOD per root bandwidth was 3.3×10^9 cells·mL^{-1}·$Hz^{-1/2}$.

The linear MT fit generated a slope of -1.8×10^{-10} ($p = 5.4\times10^{-13}$) ($R^2 = 0.997$). The corresponding MT LOD was 3.8×10^9 cells·mL^{-1}·$Hz^{-1/2}$.

The linearized diffusion fit generated a slope of 2.2×10^{-9} ($p = 5.0\times10^{-11}$) ($R^2 = 0.994$). The offset from the exponential fit was -3.6×10^{-4}. The associated diffusion LOD per root bandwidth was 2.7×10^9 cells·mL^{-1}·$Hz^{-1/2}$.

Images of low gel temperature agarose gels containing bands of various yeast concentration were acquired (Fig. 3.8). The MT weighted image produces the best results in which all four layers are distinct and distinguishable from the background. The lower cell concentrations in the T_2-weighted image blend together, but all layers are distinct from the background. In the diffusion-weighted image, the cell laden bands show an increase in signal from the background, but the signal to noise ratio is much lower than in the T_2 and MT weighted images.

3.4 Discussion

T_2 and MT weighted signals were found to decrease in response to increasing cell density whereas the diffusion weighted signal increased with increasing cell density. The decrease in T_2 and MT weighted signals with increasing cell concentration can be attributed to the in-

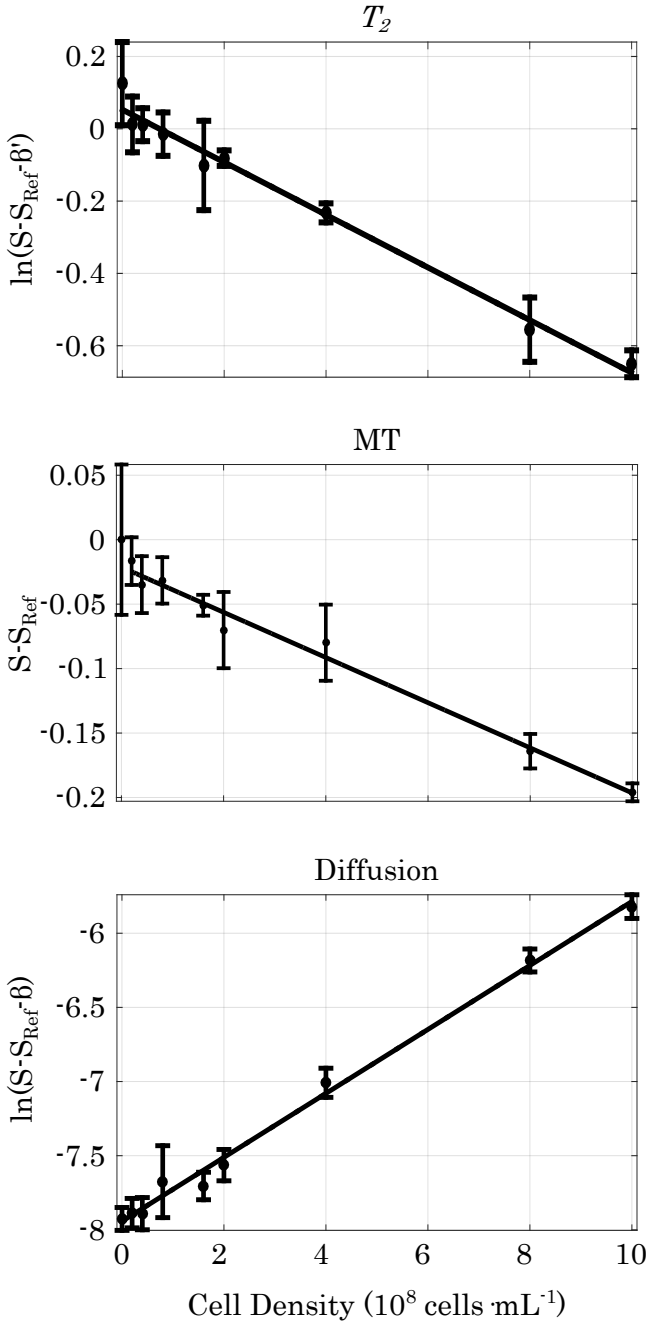

Figure 3.7: **Yeast Cell Density Calibrations.** From top to bottom: T_2, MT, and diffusion-weighted calibration curves of NMR spectra intensity to yeast cell density. Each point represents the signal generated by agarose alone subtracted from S_{Ref}, the signal generated by a given cell concentration. The T_2 and diffusion data were corrected for their respective offsets prior to linearization. Error bars represent one standard deviation (n=3).

crease in macromolecular content as cell density increases. Macromolecular content increases with increasing cell density since the intracellular environment is densely packed with macromolecules at a much higher concentration than the surrounding agarose gel environment used in this study [400].

T_2 is affected by mobility. Water molecules interacting with macromolecules are less mobile and experience reduced relaxation times. Therefore, as macromolecular concentration increases, the transverse relaxation time is reduced for an increasing fraction of water molecules in the sample. The reduced relaxation time results in less signal at t_{E} (hence, weaker T_2-weighted signal).

MT is a direct measure of macromolecular content through the selective saturation of hydrogen nuclei in water molecules interacting with macromolecules prior to a standard 90° excitation pulse. [26] Since macromolecular content increases with cell density, the fraction of water interacting with macromolecules also increases leading to more signal suppression due to higher numbers of nuclei being selectively saturated.

The slopes of the T_2 and MT fits are 9.9 and 8.3 times larger for HEK 293 cells than yeast cells, respectively. These curves are calibrated to cell number, but macromolecular content scales differently for each cell type. HEK 293 cells were measured to be 13.6 times the volume of our yeast cells using light microscopy. Given estimates of 23% and 35% macromolecular content for HEK 293 and yeast cells, respectively [401, 402], HEK 293 cells have about 8.9 times the macromolecular content per cell, which closely corresponds to the difference in slopes for both of these weightings.

Our diffusion data are consistent with many studies that have shown the diffusion-weighted signal to be linearly proportional to cell density across several tissue types. [271–282] The increase in diffusion weighted signal is due to a decrease in diffusivity according to (3.3). The decrease in water's diffusivity is a result of restriction of molecular motion. A fraction of intracellular water experiences restricted motion due to the presence of cell membranes, which act as barriers, reducing water transport. As cell density increases, the fraction of restricted water scales proportionally for a given cell type, but the fraction of restricted water

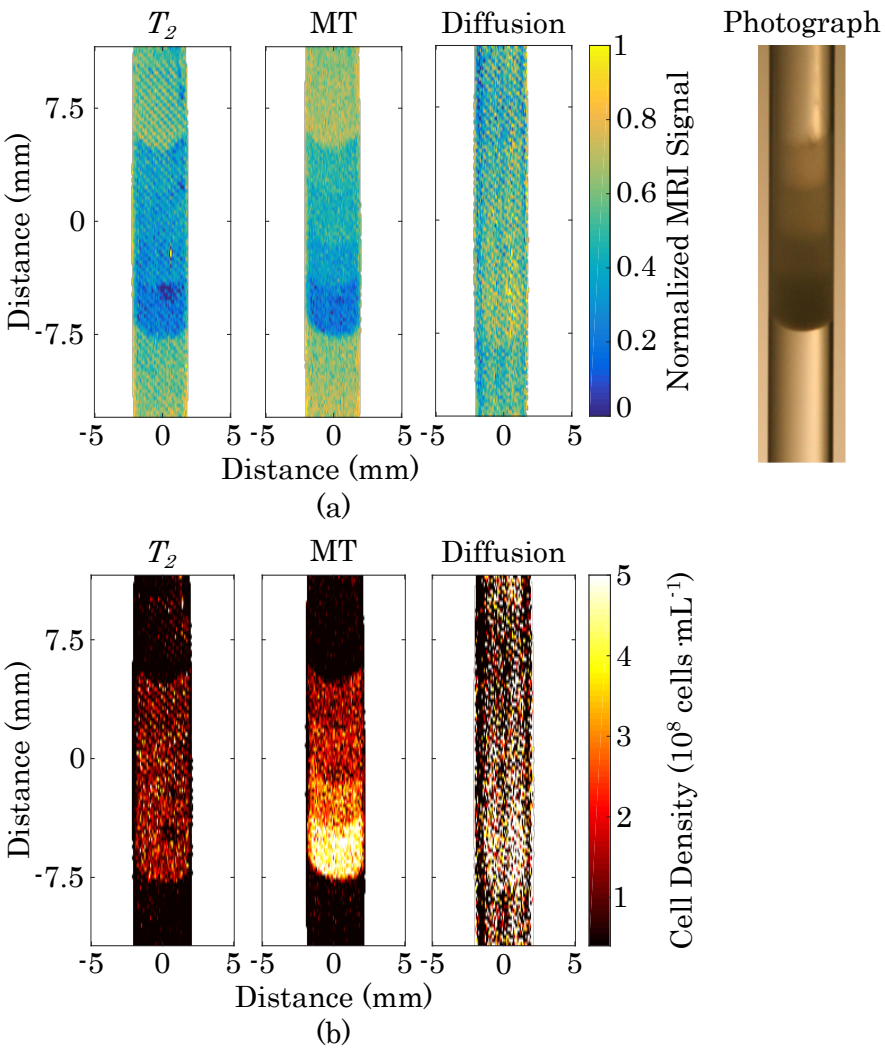

Figure 3.8: **Yeast Images.** (a) T_2, MT, and diffusion-weighted MRIs of an NMR tube containing stratified layers of various yeast cell densities in 0.6% agarose gel. A reference photograph of the tube is included. Four layers from top to bottom contain yeast cell concentrations of 0.63, 1.3, 2.5, and 5.0 $\times 10^8$ cells·mL^{-1}. (b) Cell density maps calculated from weighted images.

is not identical to the fraction of intracellular water in the total sample volume. Given their sizes and water content estimates of 77% and 65% for HEK 293 and yeast cells respectively [401, 402], HEK 293 cells have about 16 times as much total intracellular water content as yeast. However, the slope of the HEK 293 calibration plot is larger than the slope of the yeast calibration plot by a factor of two, suggesting that per cell, twice as much water experiences

restricted diffusion in HEK 293s versus yeast. This is because the restriction of intracellular water motion due to membranes only affects a fraction of intracellular water. [307] Intracellular water that is far away from membranes will have a higher diffusivity than water that is close to cell boundaries. Since the yeast diameter is about 42% of the HEK 293 diameter, a larger fraction of the intracellular water in yeast will experience restricted motion due to membrane proximity.

Compared to cell density correlations reported in previous studies, the correlations here had less variability and better coefficients of determination. [271–284, 307, 308, 395]. This can be attributed to the fact that a more controlled environment is maintained when cells are encapsulated in hydrogels for tissue engineering than when tumors and abscess are formed *in vivo* with variations in their extracellular matrix composition and cell type. In this study we used NMR tubes to contain cell laden gels, but the imaging technique can be applied to any MRI compatible bioreactor as long as perfusion is halted during acquisition.

3.5 Conclusion

In this study, we generated maps of cell density in a hydrogel scaffold using T_2, MT, and diffusion-weighted MRI. We have verified that these three weightings have a clear functional dependence on cell concentration and can be calibrated to measure exact cell densities in thick or opaque media. This is especially useful for monitoring cultures in bioreactors in which local cell density evolves over time due to proliferation and migration.

We found the three weightings to have comparable detection limits when using NMR spectroscopy pulse sequences. However, when imaging lower cell concentrations, the diffusion-weighted signal is too weak compared to T_2 and MT-weighted signals, in terms of resolving cell concentrations below 5.6×10^7 cells·mL^{-1} within a reasonable time. Our results suggest that despite the popularity of ADC mapping in clinical settings, T_2 and MT-weighted images may be more suitable for tissue engineering applications in which lower cell concentrations are present. The higher variability of T_2 measurements, both in spectroscopy and imaging experiments suggests that MT is the better option for probing small changes in cell

concentration, such as the regime of low cell concentrations.

In addition to using this cell imaging technique for studying cell growth and spatial distribution in 3D tissue culture models, the noninvasive aspect of this readout means that it can be applied to the real-time control and optimization of cell growth in bioreactor systems employing adaptive methods to control spatiotemporal patterns of mechanical and chemical stresses. T_2 and MT-weighted MRI can provide useful cell density maps when noninvasive readouts in thick tissue cultures are needed.

Acknowledgment

This research was funded by the NHLBI at NIH through grant no. 1-R01-HL114086. The authors would like to thank Amichai Goldsman, Haley Surmeian, and Eileen Lau for culturing HEK 293 cells, obtaining mammalian and yeast cell counts, and preparing yeast NMR samples for spectroscopy calibrations. The authors would like to thank J. Rachel Prado, Ph.D. for her input on analytical calibration statistical analysis and her time culturing cells. The authors are grateful for funding from Ruth L. Kirschstein National Research Service Award T32HL69766 and support by the German Academic Exchange Service (DAAD) through its Thematic Network "ACalNet" funded by the German Federal Ministry of Education and Research (BMBF).

CHAPTER 4

Quantitatively Mapping Cell Viability Independently from Cell Density in 3D Gels Noninvasively

Objective: In biomanufacturing, there is a need for quantitative methods to map cell viability and density inside 3D bioreactors to assess health and proliferation over time. Recently noninvasive MRI readouts of cell density have been achieved. Now we present an approach for measuring the viability of cells embedded in a hydrogel independently from cell density to map cell number and health. *Methods:* Independent quantification of cell viability and density was achieved calibrating the ^{1}H magnetization transfer (MT) and diffusion-weighted nuclear magnetic resonance (NMR) signals to samples of known cell density and viability using a multivariate approach. Maps of cell viability and density were generated by weighting NMR images by these parameters post-calibration. *Results:* Using this method, the limits of detection (LODs) of cell density and cell viability were found to be $\mathbf{3.88 \times 10^{8}}$ cells $\cdot$ mL$^{\mathbf{-1}}\cdot$ Hz $^{\mathbf{-1/2}}$ and $\mathbf{1.21 \times 10^{4}}\% \cdot$ Hz $^{\mathbf{-1/2}}$ respectively. *Conclusion:* This mapping technique provides a noninvasive means of visualizing cell viability and number within optically opaque bioreactors. *Significance:* We anticipate that such readouts will provide valuable feedback for monitoring and controlling cell populations in bioreactors.

4.1 Introduction

As larger and increasingly complex engineered tissues are developed for use in medicine and research, novel methods are being investigated to measure indicators of successful growth of engineered tissue products. Recently, magnetic resonance imaging (MRI) was used to spatially quantify cell density in thick, three-dimensional (3D) gels. It was found that three

nuclear magnetic resonance (NMR) weightings: T_2 relaxation, magnetization transfer (MT), and diffusion could be calibrated to measure live cell density [31]. MRI's unlimited imaging depth allows thick samples to be fully profiled without invasive physical sectioning. Recent developments in MR compatible bioreactor and incubator systems [24, 287] provide additional motivation for developing novel MRI methods for noninvasive, real-time evaluation of artificial tissue or 3D cell culture.

Spatially resolved cell density maps display growth within a tissue culture, but they do not provide a fully comprehensive profile of tissue health. Indicators of tissue health are critical for predicting the culture's outcome. Success of an artificial tissue may not be discernable until days or weeks post implantation. Measurements of viability have commercial and scientific value since they serve as early indicators of a successful product and a more immediate indicator of potential cell growth. The extent to which MRI has previously been employed to detect cellular viability is limited. In a couple studies MRI was used to track viable cell transplants [403, 404]. In these cases, cells that were transplanted *in vivo* were labelled with a viability sensitive contrast agent such as $MnCl_2$ or gadolinium liposomes (Gd-MSCs). When evaluated *in vitro*, the MR signal generated from the Gd-MSCs labelled cells could quantify cell density in suspensions containing either completely viable or completely non-viable cells. However, partially viable cell populations were not examined to determine whether the viable fraction of a cell population was quantifiable [403].

In addition to studying cells prepared in vitro, researchers have used contrast agents to target and image necrotic tissue *in vivo*. Several contrast enhanced techniques have been used to distinguish regions of viable and non-viable myocardium following infarction [405–407]. Contrast enhanced diffusion-weighted MRI was used to differentiate irradiated and non-irradiated regions of liver tumors [408]. In another study it was found that the nitroxide 4-trimethylammonium-2,2,6,6-tetramethylpiperidine-1-oxyl iodide (Cat-1) could be used as a necrosis sensitive contrast agent in muscle [409]. Røhl *et al.* found that mapping mean cerebral blood flow ratio was an effective way to differentiate regions of the penumbra around the ischemic core that will recover from those that will progress to infarction following acute stroke [410]. Lastly, Gröhn *et al.* found that exploiting the dependence of T_2 relaxation on

dissolved O_2 in the brain to identify the mismatch between oxygen delivery and metabolic consumption of O_2 following ischemic stroke was useful for distinguishing metabolically active and viable brain tissue from genuine ischemia [411].

Several contrast agent free techniques have been used to image necrosis *in vivo*. For example, T_2-weighted MRI was used to accurately identify lesions induced by ultrasound in rabbit brains [412]. Another study found a decrease in ^{39}K MRI signal correlated to necrotic cardiac tissue following infarction [413]. Neither of these techniques provided quantitative viability data. Two studies were able to quantify necrosis using contrast agent free MRI. Deng *et al.* found that diffusion-weighted PROPELLER MRI measurements quantitatively correlated with the necrotic fraction of liver tumors [414]. However, in this case the necrotic fraction was defined as the ratio of the histologically defined necrotic region to the total tumor area. In the other study using a fibrosarcoma tumor model, it was found that multispectral analysis using apparent diffusion coefficient, T_2, proton density, and a k-means clustering algorithm could identify tissue necrotic fraction (TNF) [415]. Good correlations between k-means determined- and histologically determined- TNF volume were found, but this method also relies on the binary classification of macroscopic tissue regions as either totally viable or necrotic.

Although these techniques can potentially be used as input when making clinical decisions regarding a course of treatment, they are not quantitative measurements of the viable fraction of cells within a population. Rather, they are used to distinguish distinct regions of clinically viable tissue from clinically necrotic regions. Maps of viable cell fraction distribution within a culture are relevant in the context of tissue engineering where this distribution is expected to be dependent on culture conditions such as nutrient delivery [12, 15].

In this study, we examined MT and diffusion-weighted ^{1}H NMR signals as a means to quantify viability of mammalian cells embedded in agarose hydrogels independently from cell density. This was done by exploiting key differences between how each weighting detects the presence of cells. The diffusion coefficient of water is dependent on compartmentalization of water molecules caused by the presence of intact cell membranes [416], making it sensitive to cellular events such as apoptosis, necrosis, and even volume changes [308, 417, 418]. In

contrast, MT-weighted imaging is dependent on macromolecular content [26]. It is expected that exploiting these differences to generate quantifiable maps of cell viability will provide valuable data about otherwise inaccessible thick, 3D cell cultures.

4.2 Materials and methods

4.2.1 Preparation of Viable Samples

B16-F10 cells were cultured in a 37°C, 5% CO_2 incubator in Dulbecco's Modified Eagle Medium (DMEM) supplemented with 10% FBS, L-glutamine, and penicillin/streptomycin. Cells were harvested by incubating in trypsin for 5 minutes and neutralizing trypsin with DMEM containing 10% FBS. Dead cell populations with ruptured membranes were generated by suspending cells first in 2% paraformaldehyde and later in Hank's Balanced Salt Solution containing 0.3% Triton-X and 0.05% Tween-20. Dead cells were washed twice with phosphate buffered saline (PBS) prior to use. Live and dead cell populations were counted using software developed by Arteta *et al.* [419] that was trained to recognize live and dead cells in transmission light micrographs of trypan blue stained populations suspended in disposable hemocytometers. Live and dead cell populations were combined in ratios and concentrated to generate final populations with the desired cell concentration and viable fraction.

It was noticed that every transfer step resulted in cell losses of 5-10%, and more dead cells were lost than live cells during transfers. This was likely due to cells adhering to the inner surface of serological pipettes. To account for this, cell populations were counted after the pipette that would be used to transfer them to their final tube was wetted with cell suspension. Live and dead cells were transferred to the final tube with a single transfer immediately after they were counted.

Mixed cell populations were pelleted in 50 mL conical tubes by centrifugation at 200 g for 5 min. Supernatant was aspirated down to 10 mL if applicable. The final volume of supernatant was poured off the cell pellet in one swift motion by inverting the tube to reduce cell losses caused by aspiration. Any drips remaining on the walls of the tube were aspirated

with the tube inverted. The pellet was then suspended in a 37°C liquid mixture containing a 1:1 ratio of cell culture media and 1.8% low gelling temperature agarose (Sigma, A9045-5G) dissolved in PBS. Gel cell suspensions were quickly mixed, cast in 5 mm NMR tubes, and allowed to anneal at room temperature for eight minutes. Annealed samples were reheated to 37°C and maintained at that temperature during data acquisition. All data was acquired immediately after sample preparation.

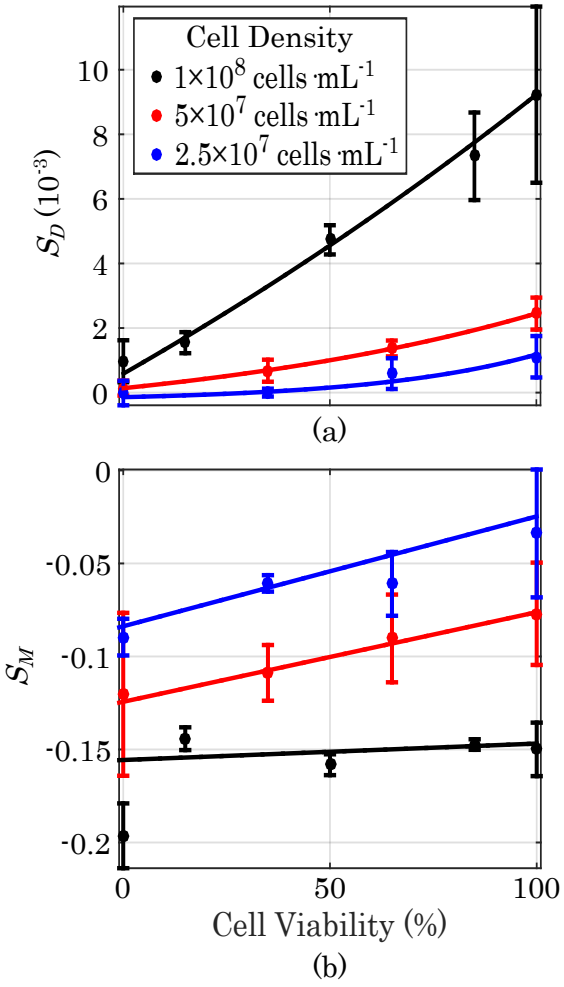

Figure 4.1: **Diffusion- and T_2-Weighted Viability Calibrations.** (a) Plots of B16-F10 cell viability versus diffusion-weighted NMR spectroscopy signal for three different cell densities. (b) Plots of B16-F10 cell viability versus MT-weighted signal for three different cell densities. Error bars represent one standard deviation. (n=3)

Samples containing layers of B16-F10 cells of various viable fractions were prepared by

casting a small quantity of agarose gel containing the desired viability and density in a 5 mm NMR tube, allowing the layer to anneal, and then casting the next layer with a different viability/density on top of the first layer. This process was repeated until all four layers were cast. The regions of the NMR tube beneath and above the RF region were filled with acellular agarose. Since imaging required a longer acquisition time, the cells used in imaging were rinsed with serum free DMEM prior to use. The gel used for imaging was a liquid mixture containing a 1:1 ratio of serum free DMEM and the 1.8% low gelling temperature agarose stock described previously. Serum was removed to slow down cell metabolism [420], preventing cells from generating CO_2 bubbles during acquisition.

4.2.2 NMR Measurements

Spectroscopy measurements and images of B16-F10 cells were acquired in a Varian 400 MHz (9.4 T) spectrometer equipped with a 10 mm broadband probe and air-flow variable temperature (VT) control. MT- and diffusion-weighted spectroscopy and imaging data were collected with pulse sequences described previously [31].

4.2.3 Data Analysis

In this study, the MT-weighted signal, represented by S_{MT}, was generated by normalizing the signal generated from an MT pulse sequence acquisition with an offset optimized for generating contrast ($S_{MT,c}$) to a reference signal obtained from an MT pulse sequence acquisition using a very large offset frequency of 200 kHz ($S_{MT,0}$), so that $S_{MT} = \frac{S_{MT,c}}{S_{MT,0}}$. Similarly, the reported diffusion-weighted signal is equivalent to $S_{Diff} = \frac{S_{Diff,c}}{S_{Diff,0}}$ where $S_{Diff,c}$ is the signal obtained from a Pulsed Field-Gradient STimulated-Echo (PFG-STE) sequence using a contrast optimized b-value, and $S_{Diff,0}$ is a reference signal obtained from the same pulse sequence without applying diffusion weighted gradients. Background diffusion and MT-weighted measurements of acellular agarose gels were obtained in the same way, such that $S_{MT,bg} = \frac{S_{MT,bg,c}}{S_{MT,bg,0}}$ and $S_{Diff,bg} = \frac{S_{Diff,bg,c}}{S_{Diff,bg,0}}$. Background signals were subtracted from all cell measurements to isolate the influence of cells alone.

To determine the cell concentration and viability limits of detection (LODs), cell concentration and viability were plotted as a function of their measured diffusion- and MT-weighted NMR signals. Surface models of the form of a second order power series ($y = b_0 + b_1x_1 + b_2x_2 + b_3x_1^2 + b_4x_1x_2 + b_5x_2^2$) were fit to the data using a weighted Levenberg-Marquardt nonlinear least squares algorithm. The LOD for the multivariate fits were calculated using the relationship, LOD $= 3 \cdot \overline{\boldsymbol{\sigma}} \cdot \boldsymbol{b}$ where $\boldsymbol{b}$ is the model coefficient vector, $\begin{pmatrix} b_1 & b_2 & b_3 & b_4 & b_5 \end{pmatrix}$, and $\overline{\boldsymbol{\sigma}}$ is the average standard deviation vector $\begin{pmatrix} \overline{\sigma}_{x_1} & \overline{\sigma}_{x_2} & \overline{\sigma}_{(x_1)^2} & \overline{\sigma}_{x_1x_2} & \overline{\sigma}_{(x_2)^2} \end{pmatrix}$. Diffusion- and MT-weighted signals (represented here by x_1 and x_2) were collected for all samples in triplicate. Using $\sigma_{x_1,n}$ to represent the standard deviation of the measured $x_{1,n}$ at a single data point, n, the average of the standard deviations of all data points from 1 to N is represented by $\overline{\sigma}_{x_1}$. Similarly, $\overline{\sigma}_{(x_1)^2}$ is the average of all the standard deviations of the value $(x_1)^2$, and the pattern continues for all other values in the average standard deviation vector. This LOD analysis is based on the International Union of Pure and Applied Chemistry (IUPAC) recommendations extended to a multivariate model [421].

Images were analyzed by manually drawing regions of interest (ROIs) around portions of the image lying entirely within discrete layers. Average voxel intensities from each ROI were compared to each other with a 1-way analysis of variance (ANOVA) for images in which only one independent variable was changed or a 2-way ANOVA when both viability and density were varied between layers. Significance for pairwise group mean comparisons was obtained using Tukey's honestly significant difference criterion.

4.3 Results

4.3.1 NMR Spectroscopy Viability and Density Calibrations

Plots of B16-F10 viability versus diffusion-weighted NMR spectrum intensity for three different cell densities are shown in Fig. 4.1 (a). A diffusion time, Δ, of 100 ms and diffusion weighting value (b-value) of 2800 s·mm^{-2} were found to be most sensitive to B16-F10 viability. The diffusion-weighted was found to have an exponential dependence on cell viability at

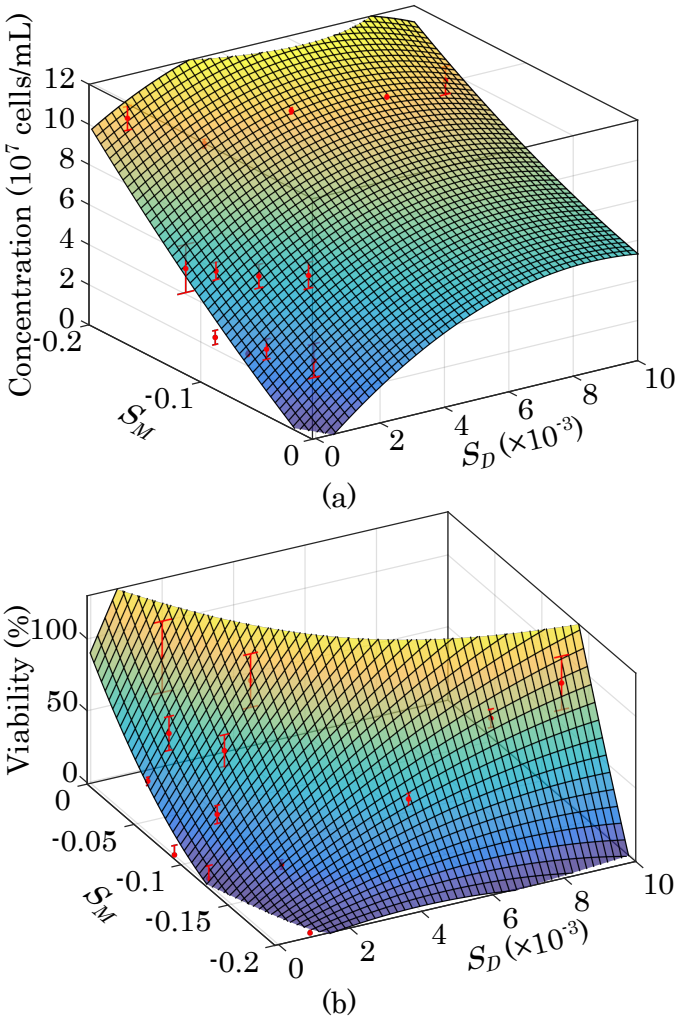

Figure 4.2: **3D Viability and Density Calibrations.** (a) Plot of calibration surface overlaid on data showing cell concentration as a function of diffusion- and MT-weighted signals. (b) Plot of calibration surface overlaid on data showing cell viability as a function of diffusion- and MT-weighted signals. (n=3)

all cell densities studied., which is similar to previously established exponential dependence of diffusion-weighted signal on cell density [31]. The response of the MT-weighted signal to cell viability at three cell densities is shown in Fig. 4.1 (b). The optimal MT-weighted saturation pulse offset was found to be 3.3 kHz. It can be seen that the MT-weighted signal is linearly dependent on cell viability, but is less dependent on viability than it is on cell density as expected. The level of dependence on viability was also seen to depend on the density at which measurements were taken.

Table 4.1: Model Parameters

Concentration	Value	Viability	Value
C_0	-1.14×10^7	V_0	66.6
C_1	1.53×10^{10}	V_1	5.27×10^4
C_2	-4.36×10^8	V_2	1.03×10^3
C_3	-8.69×10^{11}	V_3	-6.41×10^5
C_4	2.34×10^{10}	V_4	2.41×10^5
C_5	5.19×10^8	V_5	3.27×10^4

A diffusion- and MT-weighted measurement was taken for each sample with a known viability and density. Both NMR signals were dependent on both cell density and viability. In order to determine if viability and density can be measured independently from each other using a combination their respective calibration curves, cell concentration and cell viability were plotted as a function of their diffusion- and MT-weighted signals in Fig. 4.2. The points were fitted to surfaces with of the form of a second order power series of the form:

$$C = C_0 + C_1 S_D + C_2 S_M + C_3 S_D^2 + C_4 S_D S_M + C_5 S_M^2 \tag{4.1}$$

$$V = V_0 + V_1 S_D + V_2 S_M + V_3 S_D^2 + V_4 S_D S_M + V_5 S_M^2 \tag{4.2}$$

Where C and V are concentration in cells $\cdot$ mL^{-1} and viability in % respectively; C_0, C_1, $\ldots C_5$ are the coefficients of a power series expansion of second order concentration dependence; V_0, V_1, $\ldots V_5$ are the coefficients of a power series expansion of second order viability dependence; and S_D and S_M represent the background corrected, normalized diffusion- and MT-weighted signals ($S_D = S_{Diff} - S_{Diff,bg}$ and $S_M = S_{MT} - S_{MT,bg}$). The values of the fitted parameters are listed in Table 4.1. The coefficients of determination (R^2) for the concentration and viability fits are 0.952 and 0.965 respectively. Their fit p-values are 1.27×10^{-6} and 5.71×10^{-5} respectively.

Using the parameters of the fitted surfaces and the multivariate LOD formula, LOD = $3 \cdot \overline{\boldsymbol{\sigma}} \cdot \boldsymbol{b}$, the cell concentration LOD was determined to be 1.94×10^7 cells $\cdot$ mL^{-1}, which is the same order of magnitude as determined previously for HEK 293 cells all with 100%

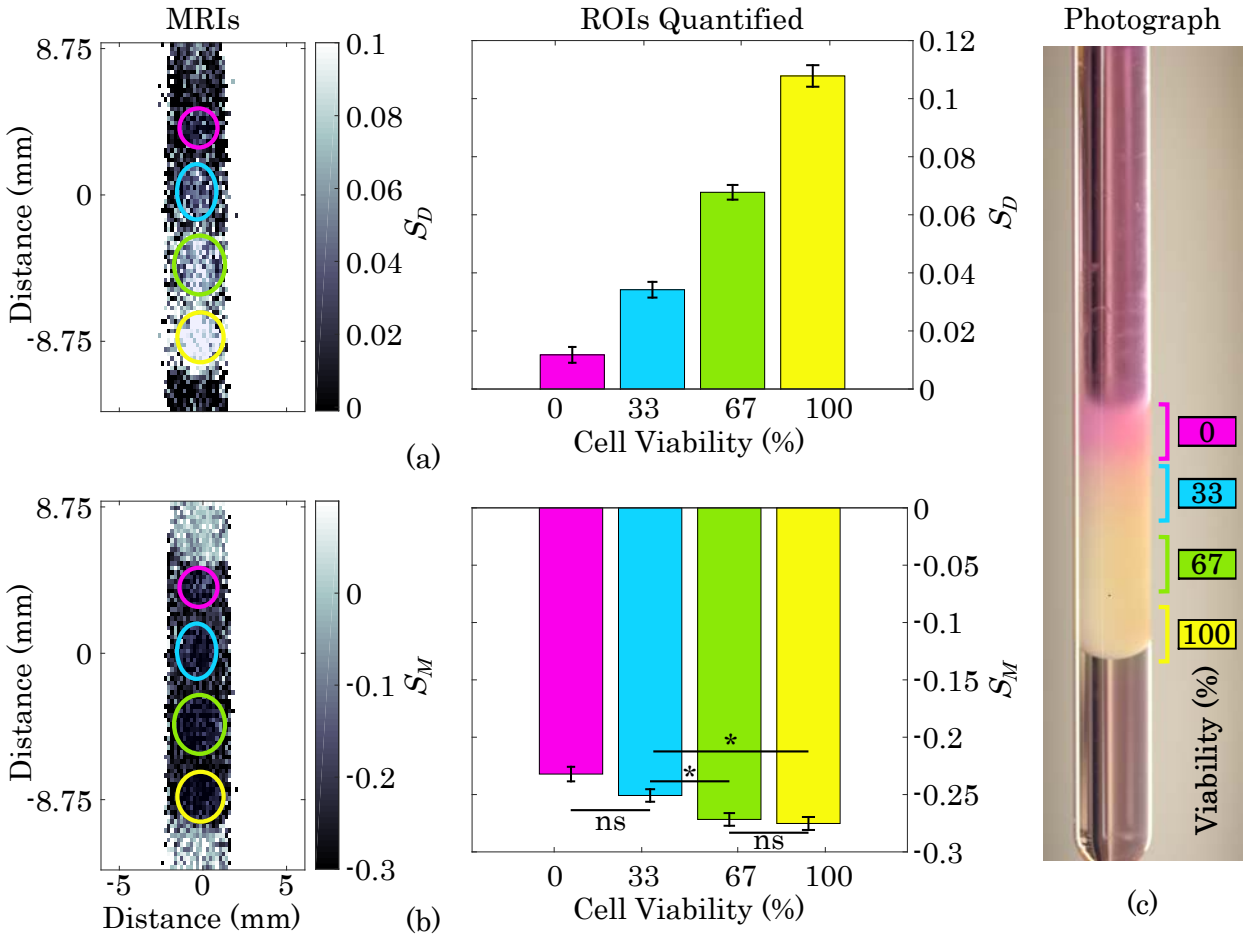

Figure 4.3: **Viability Gradient MRI.** (a) Diffusion-weighted MRI and quantification of layers of gel containing, from top to bottom, 0%, 33%, 66%, and 100% viable B16-F10 cells with a constant total cell density of 2×10^8 cells·mL^{-1} Error bars represent one standard error. All groups have a statistically significant difference from each other ($p<0.0001$). (b) MT-weighted image and quantification of viability gradient sample. ns = not significant, * indicates significant difference ($p<0.05$), and all others are significantly different ($p<0.0001$). (c) Photograph of NMR tube containing viability gradient immediately after sample prep and prior to MRI acquisition.

viability [31]. The cell viability LOD was determined to be 607%. The total combined acquisition time for a diffusion- and MT-weighted sequence was 132.3 s. Given a total of three replicates, the associated LODs per root bandwidth are 3.88×10^8 cells $\cdot$ mL$^{-1}\cdot$ Hz $^{-1/2}$ and $1.21 \times 10^4\% \cdot$ Hz $^{-1/2}$.

4.3.2 Viability Mapping

MRIs of a B16-F10 cell viability gradient are shown in Fig. 4.3. Thirty diffusion-weighted contrast acquisitions were averaged to generate the image shown in (a). A gradient amplitude of 8.12 G/cm, b-value of 800 s·mm^{-2}, and Δ of 100 ms were used to generate contrast. A reference scan, to which the contrast-optimized scan was normalized, was generated using the same pulse sequence timing, but no diffusion weighted gradients. Two scans were averaged for the diffusion-weighted reference. The frequency offset used to generate contrast for the MT-weighted image shown in (b) was 3.3 kHz. A frequency offset of 200 kHz was used for the MT reference scan to which the contrast sensitive scan was normalized. The contrast and reference scans were both averaged from two acquisitions. The same imaging settings and pulse sequences were used for all other figures in this study.

In Fig. 4.3 (a), the diffusion-weighted image shows distinct layers of increasing signal intensity corresponding to increasing viability, whereas the MT-weighted image shows much less sensitivity to the changing viability. In the diffusion-weighted image, all layers with viability greater than 0% are distinct from the baseline signal (acellular agarose above and below the layers). Despite being indistinguishable from each other, the layers in the MT-weighted image are clearly distinct from the acellular agarose region surrounding the layers, indicating that at this cell concentration, the MT weighting detects the presence of cells without being heavily impacted by viability. When the signals from each layer were quantified, all layers were found to be significantly different from each other in the diffusion-weighted image, whereas only four of the six pairwise comparisons between layers in the MT-weighted image were significantly different, and the difference was much less pronounced.

MRIs of a B16-F10 cell density gradient are shown in Fig. 4.4. It can be seen that both diffusion- and MT-weighted signals are strongly dependent on cell density with the strength of the diffusion-weighted signal positively correlated with density and the strength of the MT-weighted signal inversely correlated with density (consistent with our previous findings in HEK 293 cells [31]). The signal intensities of each layer are all significantly different from each other in both weightings.

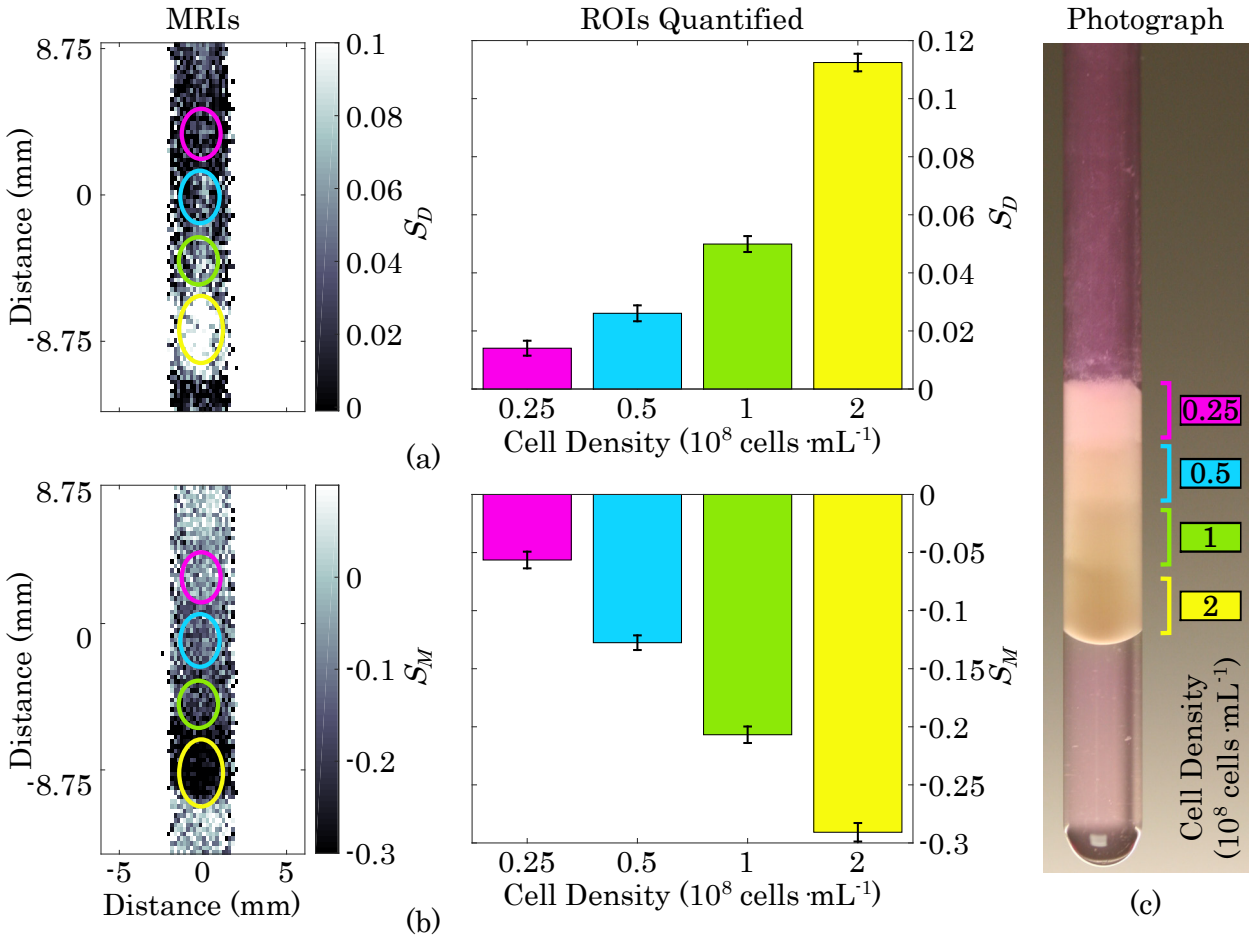

Figure 4.4: **Density Gradient MRI.** (a) Diffusion-weighted MRI and quantification of layers of gel containing, from top to bottom, 0.25, 0.5, 1, and 2 $\times 10^8$ cells · mL^{-1} B16-F10 cells with 100% viability. Error bars represent one standard error. All layers have a statistically significant difference from each other ($p<0.0001$). (b) MT-weighted image and quantification of cell density gradient. All layers have a statistically significant difference from each other ($p<0.0001$). (c) Photograph of NMR tube containing cell density gradient immediately after sample prep and prior to MRI acquisition.

Finally, MRIs of B16-F10 cells of four different combinations of viability and density are shown in Fig. 4.5. In the diffusion-weighted image, all layers were significantly different from each other except for the layer containing 2×10^8 cells·mL^{-1} at 50% viability and the layer containing 1×10^8 cells·mL^{-1} at 50% viability. Both of these layers contained the same concentration of viable cells (1×10^8 viable cells·mL^{-1}). In the MT-weighted image, all layers

were significantly different from each other, suggesting dependence on both cell density and viability.

After acquiring each image, the mean diffusion- and MT-weighted signal intensities from each ROI were fitted to viability and density calibration surfaces. The fitted equations for each image were then used to calculate the cell viability and cell density on a voxel-by-voxel basis. Images of cell density and viability are show in Fig. 4.6. With only four cell populated layers and an acellular background region, a power series with second order terms for both diffusion- and MT-weighted signal was not possible. One of the parameters needed to be restricted to first order terms in order to fit a surface. The results did not appear to depend on which parameter was restricted to first order. Fig. 4.6 shows that cell density images are clearly representative of the sample in all cases, but cell viability calibrations worked best when the layers contained a full range of viability to use in the calibration.

4.4 Discussion

4.4.1 Decoupling Cell Viability from Cell Density

Our results suggest that the viability and density of a population of cells cultured in a hydrogel can be quantifiably mapped independently of each other without contrast agents using only diffusion- and MT-weighted MRI scans. From our data it can be seen that the diffusion-weighted signal is largely dependent on the number of viable cells, as measured by intact membranes detected with trypan blue. This is supported in both our NMR spectroscopy calibrations and our images which show increasing diffusion weighted signal with increasing numbers of viable cells. However, the presence of dead cells does have some influence on the diffusion weighted measurement, likely due to partially intact membranes and remaining macromolecular content restricting water motion to a lesser degree. For example, upon close examination of Fig. 4.1 (a), the sample with 100% viable cells at 5×10^7 cells $\cdot$ mL^{-1} has a lower diffusion weighted signal than the sample containing 50% viable cells at 1×10^8 cells $\cdot$ mL^{-1} despite the fact that they both have the same number of viable cells. Additionally,

there is a pattern of increasing diffusion weighted signal with increasing cell density in the 0% viable cell samples.

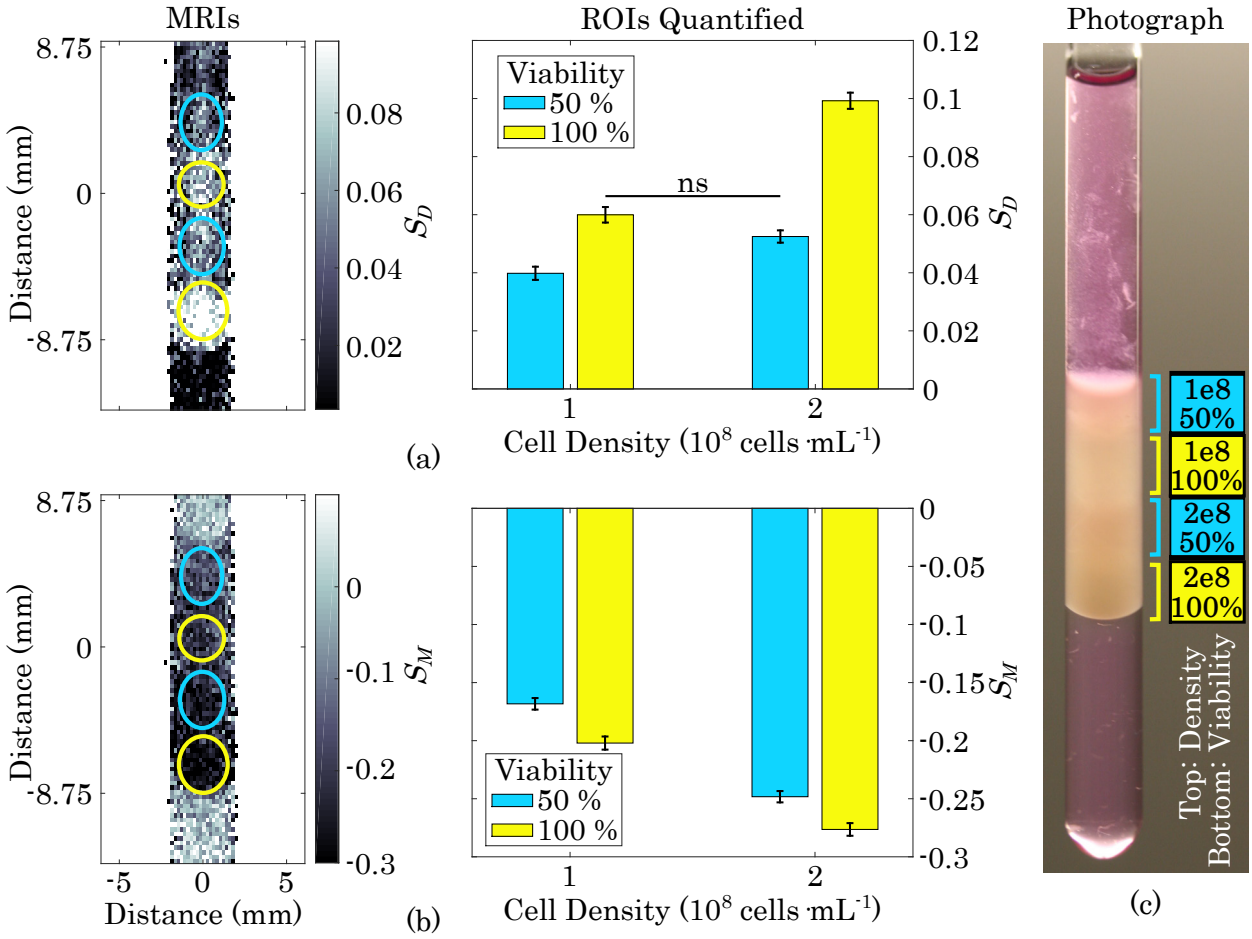

Figure 4.5: **MRI of Viability and Density Combinations.** (a) Diffusion-weighted MRI and quantification of layers of gel containing, from top to bottom, B16-F10 densities of 1, 1, 2, and 2 $\times 10^8$ cells $\cdot$ mL^{-1} and corresponding viabilities of 50, 100, 50, and 100% . Error bars represent one standard error. ns = not significant, all other layers are significantly different from each other ($p<0.0001$). (b) MT-weighted image and quantification of cell density and viability combinations. All layers are significantly different from each other ($p<0.0001$). (c) Photograph of NMR tube containing combinations of viability and density immediately after sample prep and prior to MRI acquisition.

Another notable observation is that the MT-weighted signal is mostly dependent on the total number of cells, but it is not completely independent of the viability of the cells.

Fig. 4.1 (b) shows the magnitude of MT-weighted response decrease with increasing viability at low cell concentrations, meaning the non-viable cells are contributing more to the MT-weighted signal. At the greatest cell concentration in Fig. 4.1, 1×10^8 cells $\cdot$ mL^{-1}, the MT-weighted signal has nearly zero dependence on cell viability. When imaging an even higher cell density of 2×10^8 cells $\cdot$ mL^{-1}, the magnitude of the MT-weighted response increased with increasing viability. Therefore, the type of dependence of MT-weighted signal on cell density is dependent on the density of cells at which viability is being measured, but it consistently holds that the dependence of MT-weighted signal on viability is less than its dependence on cell density over the ranges examined.

In this study, cells were fixed and permeabilized to replicate early stages of cell death in which membrane integrity is lost and the cell body is still intact. Permeabilization alone was unable to replicate this due to it completely disintegrating cells without prior fixation. Despite the fixation step keeping cells intact, this process is known to result in a 20-30% loss of mass per cell, depending on the concentrations of fixative and detergent used [422]. Since magnetization transfer is generally sensitive to macromolecular concentration, nonviable cells which have less macromolecular content should contribute less to the magnitude of the change in MT-weighted signal, which was the case at higher cell densities. At lower cell densities, the slight increase in the magnitude of the MT-weighted signal difference with decreasing viability (increasing fraction of nonviable cells) suggests another mechanism is contributing toward the MT-weighted viability dependence.

One possible explanation is the porousness of permeabilized membranes. Magnetization transfer is a process that depends on the exchange of nuclear saturation between protons interacting with macromolecules and protons in free water. Macromolecular protons are selectively saturated, but the final NMR signal is obtained by excitation of free water [25]. Therefore, factors that influence the exchange of magnetization between the two pools will influence MT-weighted signal in addition to the total quantity of macromolecular content. A factor that could influence the rate of exchange is the contact area between macromolecules and free water, which can be influenced by membrane permeabilization. Detergents form physical pores in cell membranes [416], and adding them to phospholipid bilayers increases

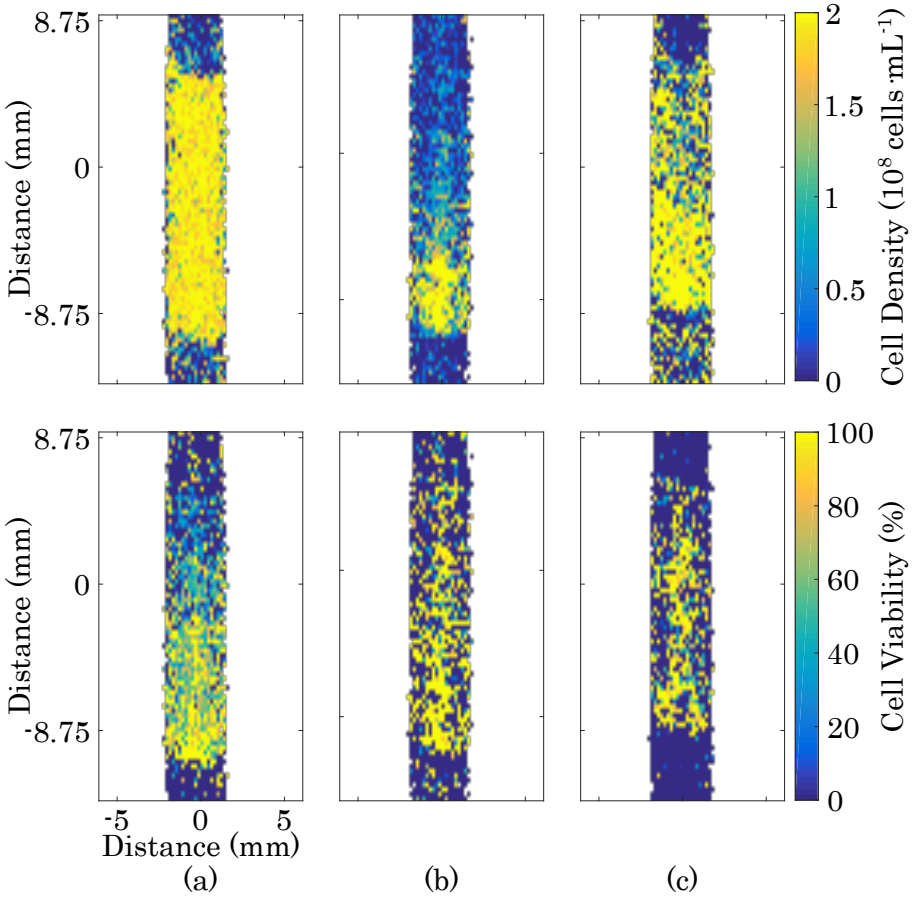

Figure 4.6: **Maps of Cell Density and Viability.** Top: cell density maps. Bottom: cell viability maps. (a) Cell viability gradient sample shown in Fig. 4.3. (b) Cell density gradient sample shown in Fig. 4.4. (c) Sample containing cell viability and density combinations shown in Fig. 4.5.

.

lipid surface area in contact with free water molecules [423, 424], which would facilitate the transfer of magnetization between macromolecules and free water, leading to an increase in the MT-weighted response with decreasing viability. At low cell densities, this process would be uninhibited by cell crowding. However, as cell density increases, crowding will cause cellular macromolecules to come in more contact with each other and less with water, negating this effect.

Despite the interdependence of diffusion- and MT-weighted signals on both total cell

number and the viable fraction of cells, measurements of cell density and viability can obtained independently of each other with only a diffusion and MT-weighted acquisition and a multivariate calibration surface. This method applies both to NMR spectroscopy bulk measurements and spatially resolved MRI maps of cell populations on a voxel by voxel basis. Compared to cell density imaging, our results suggest that mapping cell viability requires a higher numbers of scans to resolve cell viability numbers in a reasonable range. To put it in perspective, three scans corresponded to a cell density LOD of 1.94×10^7 cells $\cdot$ mL^{-1} and a cell viability LOD of 607%. The cell density LOD is in a practical range - the average physiologic hepatocellularity is $1.12{\times}10^8$ cells$\cdot$mL^{-1} (based on a reported average hepatocellularity of $1.07{\times}10^8$ cells$\cdot$g^{-1} [298] and an average hepatic density of 1.051 g$\cdot$mL^{-1} [299]) whereas engineered hepatic seeding densities have been reported with an upper range that is an order of magnitude less [300]. However, cell viability measurements need about an order of magnitude signal improvement to detect a practical viability range, meaning many more scans are needed. This is consistent with our imaging results which found that preparing a calibration standard with viability variation is more critical than cell density variation.

4.5 Conclusion

In this study, we showed that cell viability and cell density can be quantifiably mapped independently from each other in a hydrogel using diffusion and MT-weighted MRI. We showed that these two parameters have unique functional dependencies on viability and density which can be resolved with a multivariate second order power series calibration. Our findings showed that the quantity of time required to quantify viability is much greater than what is required for cell density, making it less practical for contrast-free implementation. The noninvasiveness of this technique makes it applicable for monitoring cell health and cell number in opaque 3D environments such as engineered tissues and perfusion bioreactors used for cell production.

4.6 Acknowledgment

This research was funded by the NHLBI at NIH through grant no. 1-R01-HL114086. A. W. acknowledges the National Science Foundation OISE through "IRES: Training Next Generation Researchers in Advanced Magnetic Resonance at Chemistry Interfaces" (#1658652) for financial support. The authors are grateful for funding from Ruth L. Kirschstein National Research Service Award T32HL69766 and support by the German Academic Exchange Service (DAAD) through its Thematic Network "ACalNet" funded by the German Federal Ministry of Education and Research (BMBF).

CHAPTER 5

Conclusion

5.1 Towards Controlled Tissue Growth

The long term goal of this project is to develop a feedback control loop applicable to tissue growth *in vitro*. In one possible implementation of feedback control, the distribution of viable cells is the regulated variable. Cell population dynamics will be actuated through mechanical signaling (fluid induced shear patterns) and nutrient distributions that are implemented by the bioreactor discussed in Chapter 2. Magnetic resonance has two functions in this system. MRI will be used to map cell density and viability distributions throughout the construct as described in Chapters 3 and 4. These measurements will serve as feedback for the control system. In addition, MRI velocimetry will be used to control flow and shear distributions in a separate adaptive control loop described previously [24].

In addition to the multi-inlet perfusion bioreactor and cell density and viability mapping techniques, an additional component necessary for controlling tissue growth is a control algorithm. The adaptive algorithm used to control shear patterns does so based on a given set of inlet velocities and the MRI generated shear map [24]. This algorithm can potentially be applied to controlling cell distribution in a tissue construct by defining flow/shear patterns as the adjustable input and the corresponding MRI generated maps of cell density/viability as the controlled variable. However, several intermediary steps need to be taken prior to applying this algorithm toward tissue growth.

Cell density and viability measurements need to be validated on constructs cultured under perfusion in the bioreactor, since conditions differ from cells encapsulated in agarose within an NMR tube. Each scaffold type will have a unique contribution to weighted NMR mea-

surements which must be quantified. To validate cell density and viability MRIs acquired in the bioreactor, constructs will be removed following acquisition, live/dead stained, sectioned, and imaged optically with confocal microscopy for comparison, as shown in Fig. 2.12. The scaffold cultured under flow and shown in Fig. 2.15 was in the process of being sectioned and stained at the time of writing.

Once validated readouts of the bioreactor's TC chamber can be reliably acquired, the impact of spatiotemporally controlled macrofluidic flow patterns on cell behavior throughout large volume TE constructs can be examined. Most studies of flow patterns have been performed on microfluidic scales [425] or under limited or geometrically fixed macrofluidic perfusion patterns [22, 125]. Very little is known about the impact of more complex flow fields on cell population behavior filling larger volumes approaching tissue size scales (about 1 cm^3). To investigate this, experiments will be run in which constructs are cultured under several unique static and temporally varying flow patterns. The distribution of cell density and viability will be monitored during culture.

In addition to determining the relationship between flow pattern and population distribution, flow map data generated from these experiments, examples of which are shown in Figs. 2.21 and 2.24, will be used to train the adaptive control algorithm's neural network. Training data will reduce the number of flow pattern iterations required to converge on a desired cell distribution. An alternative source of training data is a computational model of cell growth [209, 426, 427]. Simulations are inexpensive and generate data quickly compared to tissue culture experiments, but their growth predictions are based on only a few basic metabolites (oxygen, glucose, etc.) and expected flow and shear in ideal conditions.

In addition to measuring and controlling parenchymal cell distribution throughout a TE construct, magnetic resonance can potentially monitor, and thus control, vascular morphogenesis in a construct. Any tissue culture parameter that is quantifiable by magnetic resonance and predictably responsive to flow or shear has the potential to be controlled with this setup. Despite the fact that microvascular structures are smaller than MRI's spatial resolution, magnetic resonance is able to indirectly map the presence of microvasculature using techniques such as flow-weighted imaging or Dynamic contrast medium-enhanced (DCE)

imaging [428]. Since vascular morphogenesis has established relationships with flow and shear [19, 127–130, 214, 215] and can be monitored by MRI, it is a prime candidate for control using the perfusion system presented in this work.

5.2 Other Biomanufacturing Applications

In addition to tissue engineering, the response of large cell populations to flow and shear distributions has implications in cell culture bioprocesses used for biomanufacturing biopharmaceuticals, microalgae based toxins and biofuels, viruses, and large quantities of mammalian cells [429–432]. Often, a balance between nutrient delivery via convection and potential cell damage induced by shear needs to be considered when scaling up these bioprocesses [429, 432, 433]. Perfusion of cell culture media through packed beds of cell seeded microcarrier beads (which behave like porous, fluid permeable environments [434]) has previously been studied [435, 436]. The application of controlled flow and shear patterns to cell growth in a packed bed can be implemented with the system described in this work in order to optimize high density cell culture.

5.3 Concluding Remarks

This work details the development of tools for the mechanical stimulation and observation of thick cell and tissue cultures. Chapter 1 discusses the stimuli that bioreactors can use to influence cell and tissue development, and it covers the principles behind MRI that make it a promising tool for tissue culture observation. Chapter 2 describes the features and operation protocol of a bioreactor designed specifically to work in conjunction with MRI to regulate mechanical signals and monitor growth. The purpose of this bioreactor is to apply principles of fluid mechanics in porous media towards biological responses governed by mechanotransduction. It does so in an environment with a unique set of constraints specific to the confines of a narrow MRI bore and its surrounding magnetic field. These constraints add to the already challenging aspects of bioreactor design that necessitate temperature con-

trol, sterility, and biocompatibility. Few research groups have constructed MRI compatible *in vitro* cell and tissue culture systems [285–289] due to these design constraints and the prohibitive costs (in money, space, and time) required to dedicate a high field magnet for use in a biosafety rated facility. By doing so, these groups introduced new possibilities for observing conditions which are optically challenging. New developments in MRI procedures for spatially quantifying biological tissue culture parameters are described in Chapters 3 and 4. By designing a system which combines MRI's biological imaging capability with its contribution toward controlling physiological stimuli, this project has further expanded the range of offerings MRI has in 3D cell and tissue culture. As described in this chapter, further development is still required before flow induced control over cell and tissue culture is achieved. It is anticipated that this work will provide guidance for the continued development of MRI compatible bioprocess technology, and that this development will have further implications in the field of tissue engineering and other types of biomanufacturing.

APPENDIX A

Supplemental Figures

A.1 Liquid Removal Cycle

The purpose of the liquid removal cycle was to drain most liquid phase matter from the system using pressurized air. First, the peristaltic pump head was disengaged to allow fluid to flow freely through the system. All components with intricate or large internal volumes were oriented so that their outlets were positioned below their inlets in earth's gravitational field to prevent significant volumes of liquid from being trapped. These components are highlighted in Fig. A.1 and include the peristaltic pump tubing, in-line filters, pressure gauges, pressure regulators, bubble trap, pressure relief valve, pulsation dampener, and bioreactor body.

Next, all of the valves and stopcocks were opened or closed according to configuration 1 shown in Table A.1. The media reservoir was pressurized to 20 PSI with compressed air. Liquid was pushed from the media reservoir to the waste reservoir through the path highlighted in Fig. A.2.

Once the media reservoir and return line were drained, the valves were set to configuration 2 shown in Table A.2, allowing all liquid to drain from the primary bypass line. The flow path corresponding to valve configuration 2 is highlighted in Fig. A.3.

After draining the primary bypass line, the pressure relief valve was drained by setting the valves to configuration 3 specified in Table A.3. The pressure relief valve was manually opened in order to allow fluid to pass through at pressures lower than 40 PSI. Configuration 3 corresponds to the flow path highlighted in Fig. A.4. Once the pressure relief valve line was drained, the pulsation dampener was drained of liquid using valve configuration 4 specified

Table A.1: Rinse Path 1 Valve Configuration: Return Line

Valves Opened	Valves Closed
Manifold to Media Reservoir	Media Reservoir to Atmosphere
Manifold to Waste Reservoir	Media Reservoir to Pump
Compressed Air to Media Reservoir	Pressure Relief to Manifold
	Dampener to Manifold
	Bubble Trap Overflow 1 to Manifold
	Bubble Trap Overflow 2 to Manifold
	BP Regulator to Manifold
	Compressed Air to Gas Mixer
	Gas Mixer to Media Reservoir

Table A.2: Rinse Path 2 Valve Configuration: Primary Bypass

Valves Opened	Valves Closed
Media Reservoir to Pump	Media Reservoir to Atmosphere
Manifold to Waste Reservoir	Manifold to Media Reservoir
BP Regulator to Manifold	Pressure Relief to Manifold
Compressed Air to Media Reservoir	Dampener to Manifold
Bioreactor to BP Regulator	Bubble Trap Overflow 1 to Manifold
Primary Bypass	Bubble Trap Overflow 2 to Manifold
	Compressed Air to Gas Mixer
	Gas Mixer to Media Reservoir
	Primary Flow Line
	Disconnect Point

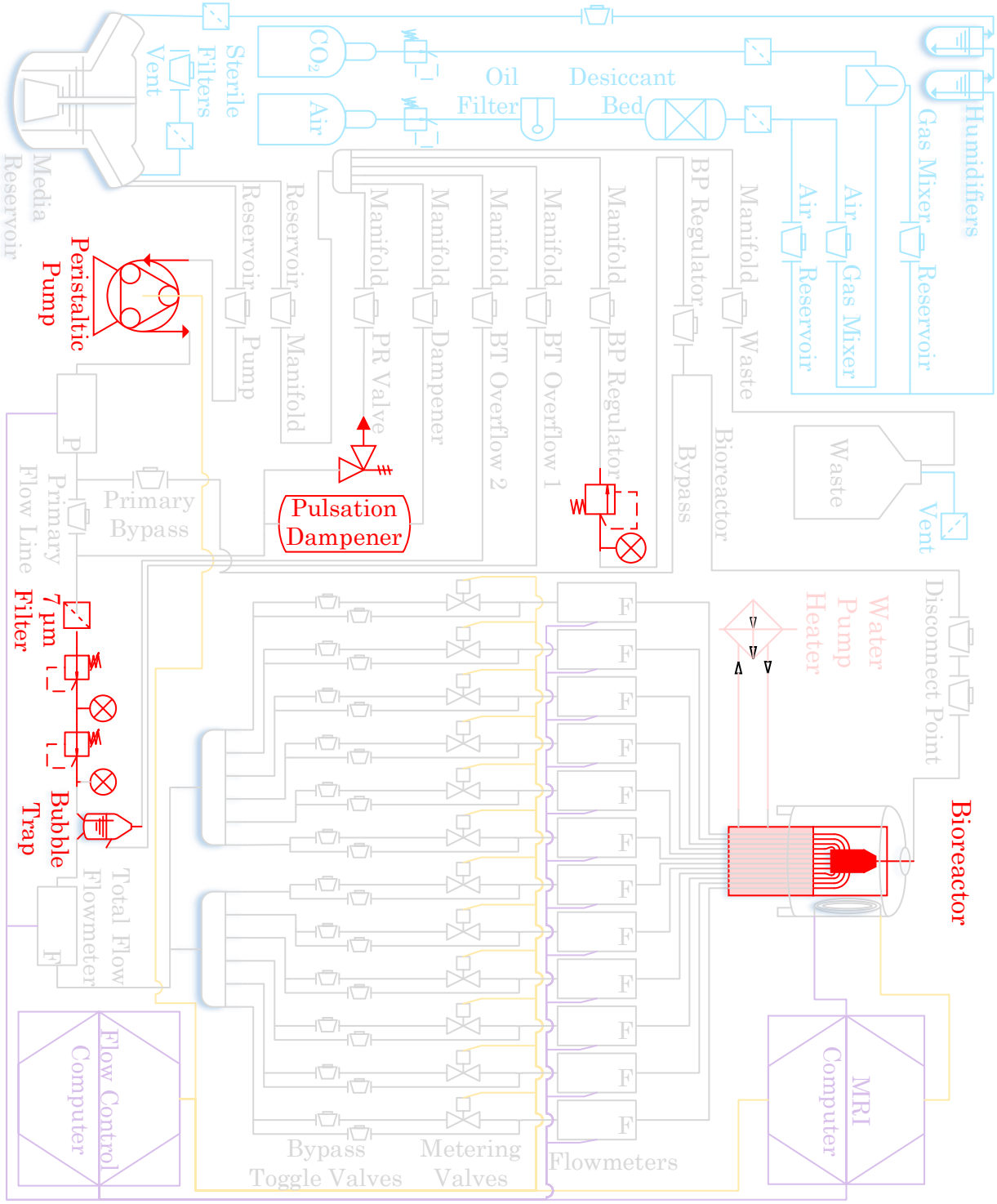

Figure A.1: **Bioreactor PFD: Traps Highlighted.** All components in the bioreactor flow setup with large or intricate internal volumes are highlighted in red. These components require correct orientation and/or agitation during the liquid removal and priming cycles.

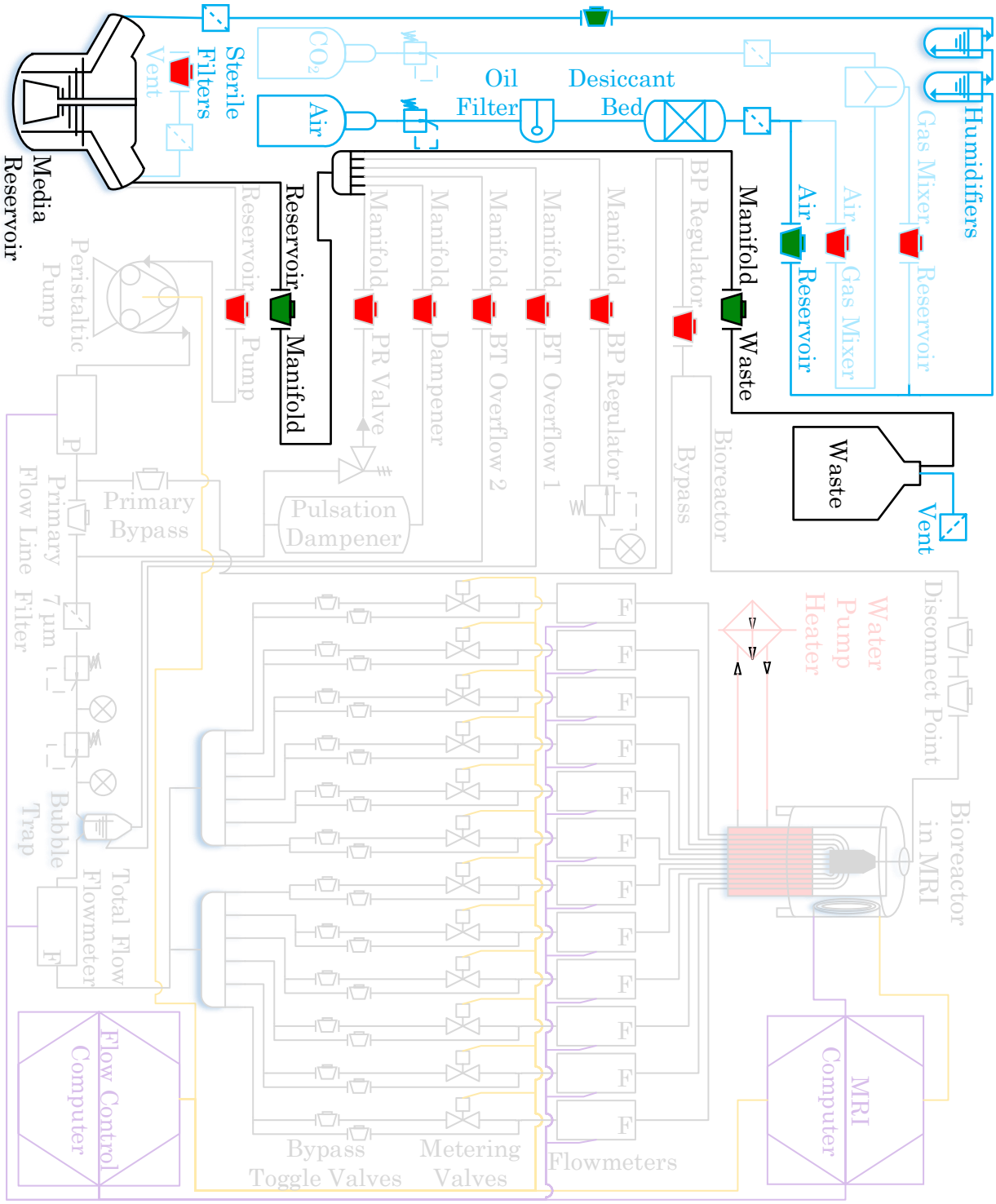

Figure A.2: **Bioreactor PFD: Rinse Path 1 - Return Line.** Bioreactor schematic highlighting the flow path corresponding to the valve configuration specified in Table A.1. Red and green colored valves correspond to closed and open valve states respectively.

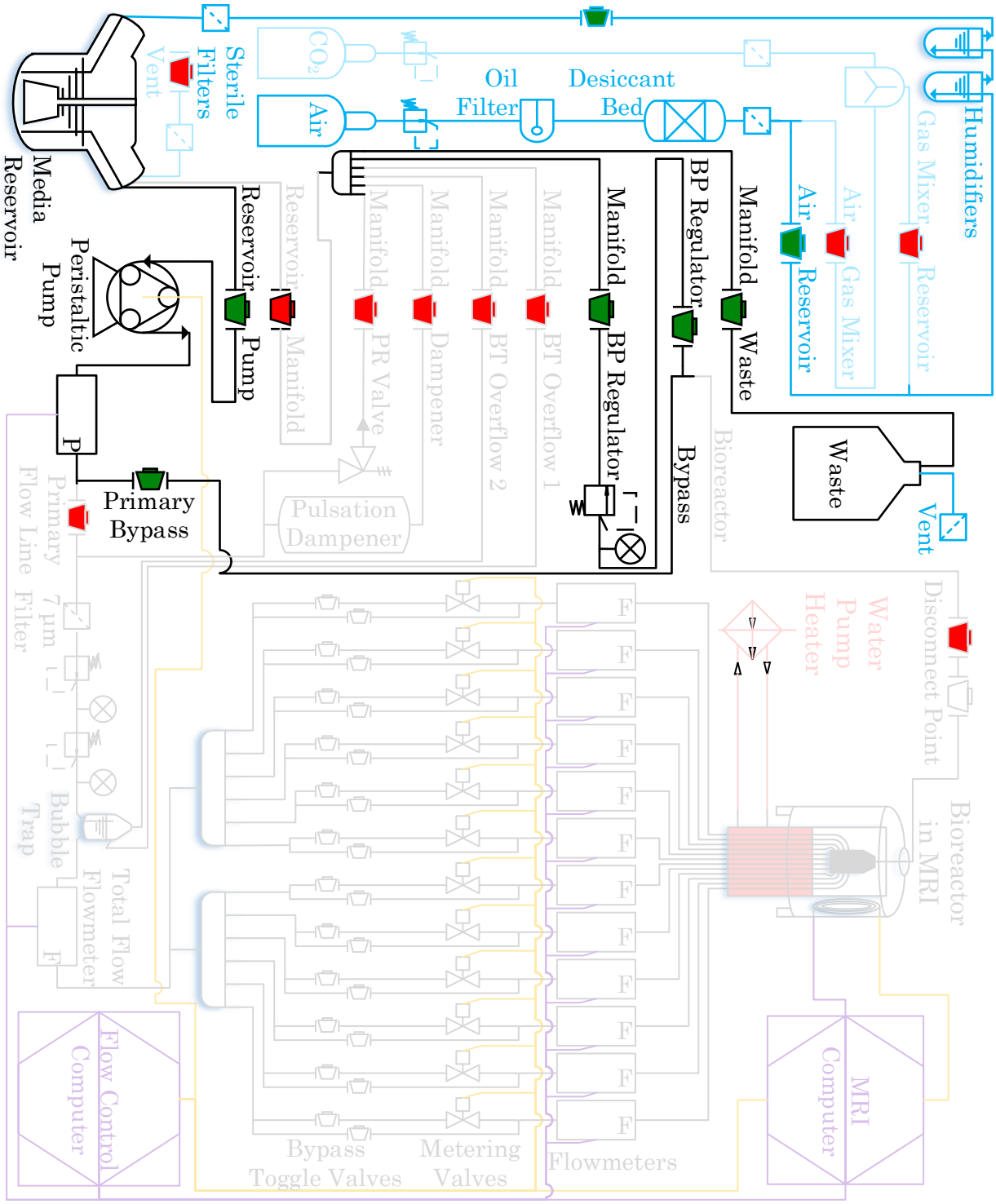

Figure A.3: **Bioreactor PFD: Rinse Path 2 - Primary Bypass.** Bioreactor schematic highlighting the flow path corresponding to the valve configuration specified in Table A.2.

Table A.3: Rinse Path 3 Valve Configuration: Pressure Relief Valve

Valves Opened	Valves Closed
Media Reservoir to Pump	Media Reservoir to Atmosphere
Pressure Relief to Manifold	Manifold to Media Reservoir
Manifold to Waste Reservoir	Manifold to Dampener
Compressed Air to Media Reservoir	Bubble Trap Overflow 1 to Manifold
Primary Flow Line	Bubble Trap Overflow 2 to Manifold
Pressure Relief Valve	Compressed Air to Gas Mixer
	Gas Mixer to Media Reservoir
	Primary Bypass
	All Bypass Toggle Valves

in Table A.5 corresponding to the flow path highlighted in Fig. A.5. Following the pulsation dampener, the bubble trap overflows were drained sequentially using valve configuration 5 seen in Table A.6 corresponding to Fig. A.6. Once all of the secondary flow paths had been drained, each of the twelve bioreactor inlet channels was drained sequentially through their flow control valve bypass channels using configuration 6 (Table A.7) corresponding to Fig. A.7. Residual liquid in the flow control valves was drained using configuration 7 (Table A.8) corresponding to Fig. A.8.

A.2 Liquid Priming Cycle

The purpose of the liquid priming cycle was to fill all tubing and components of the system with liquid and to ensure the removal of all air. First, the peristaltic pump head was disengaged to allow fluid to flow freely through the system. All components with intricate or large internal volumes (highlighted in Fig. A.1) were oriented so that their outlets were positioned above their inlets in earth's gravitational field in order to prevent air from being trapped. The media reservoir was filled with the liquid used to prime the system and pressurized to 20 PSI. The valves were sequentially cycled through configurations 1 to 7

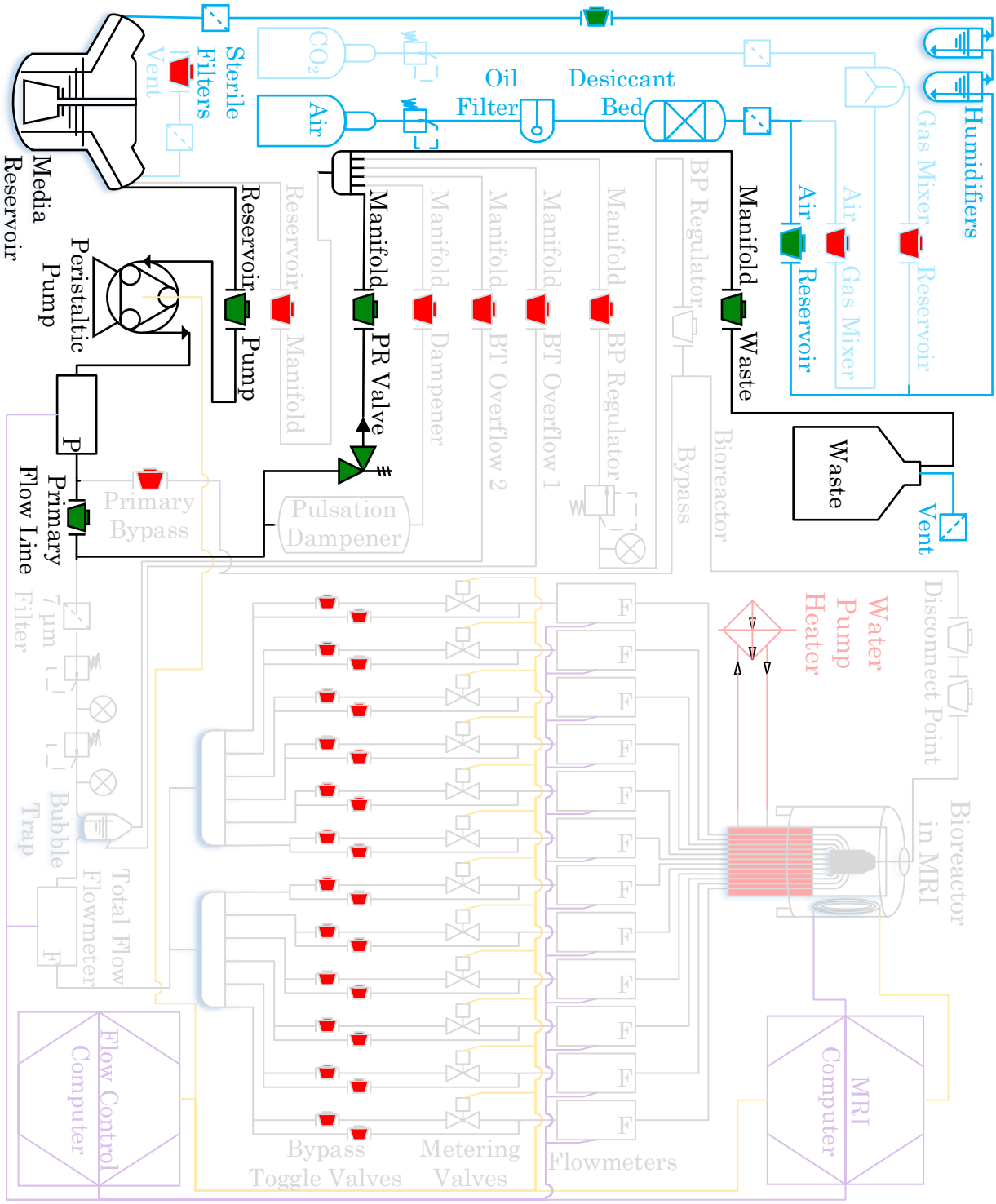

Figure A.4: **Bioreactor PFD: Rinse Path 3 - Pressure Relief.** Bioreactor schematic highlighting the flow path corresponding to the valve configuration specified in Table A.3.

Table A.4: Tubing Priming Cycle

Step	Valve Configuration	Reference Table	PDF	Primed Component
1	Configuration 1	Table A.1	Fig. A.2	Return
2	Configuration 2	Table A.2	Fig. A.3	Primary Bypass
3	Configuration 3	Table A.3	Fig. A.4	Pressure Relief Valve
4	Configuration 4	Table A.5	Fig. A.5	Pulsation Dampener
5	Configuration 5	Table A.6	Fig. A.6	Bubble Trap Overflows
6	Configuration 6	Table A.7	Fig. A.7	Flow Control Valve Bypasses
7	Configuration 7	Table A.8	Fig. A.8	Flow Control Valves

to prime each portion of the system in the order listed in Table A.4. Once one portion of the system was primed, the next valve configuration in the sequence was implemented to prime the next portion of the system until the entire system was fully primed with liquid. When priming configuration 3, the pressure relief valve was actively rotated to ensure all air bubbles were removed from the interior of the valve. When priming configuration 5, the 7 μm particle filter and pressure reducing pressure regulators were rotated and mechanically agitated to ensure all air bubbles were removed from their interior volume. In the final configuration, the BP regulator was rotated and mechanically agitated to ensure the last of the air had been removed from the system.

A.3 Cleaning Flowmeters

Any time the system was used with non-sterile aqueous solutions, biofilms grew in the flowmeters and reduced their sensitivity. To remove this type of contamination, each flow meter was individually disconnected from the line. The channel walls of the flowmeters (Fluigent XL×12, and one Sensirion SLS-1500) were cleaned by inserting a pipe cleaner through the flowmeter channel and gently scrubbing to dislodge biofilm from the inner wall. Following scrubbing, each flow meter was rinsed with copious amounts of deionized water to remove debris that may have been shed from the pipe cleaner.

Table A.5: Rinse Path 4 Valve Configuration: Pulsation Dampener

Valves Opened	Valves Closed
Media Reservoir to Pump	Media Reservoir to Atmosphere
Dampener to Manifold	Manifold to Media Reservoir
Manifold to Waste Reservoir	Pressure Relief to Manifold
Compressed Air to Media Reservoir	Bubble Trap Overflow 1 to Manifold
Pressure Relief Valve	Bubble Trap Overflow 2 to Manifold
Primary Flow Line	Compressed Air to Gas Mixer
	Gas Mixer to Media Reservoir
	Primary Bypass
	All Bypass Toggle Valves

Table A.6: Rinse Path 5 Valve Configuration: Bubble Trap Overflows

Valves Opened	Valves Closed
Media Reservoir to Pump	Media Reservoir to Atmosphere
Bubble Trap Overflows 1 and 2 to Manifold (sequentially)	Manifold to Media Reservoir
Manifold to Waste Reservoir	Pressure Relief to Manifold
Compressed Air to Media Reservoir	Dampener to Manifold
Primary Flow Line	BP Regulator to Manifold
	Compressed Air to Gas Mixer
	Gas Mixer to Media Reservoir
	Primary Bypass
	All Bypass Toggle Valves

Table A.7: Rinse Path 6 Valve Configuration: Flow Control Valve Bypasses

Valves Opened	Valves Closed
Media Reservoir to Pump	Media Reservoir to Atmosphere
Manifold to Waste Reservoir	Manifold to Media Reservoir
BP Regulator to Manifold	Pressure Relief to Manifold
Bioreactor to BP Regulator	Dampener to Manifold
Compressed Air to Media Reservoir	Bubble Trap Overflow 1 to Manifold
Primary Flow Line	Bubble Trap Overflow 2 to Manifold
Flow Control Valve Bypasses	Compressed Air to Gas Mixer
Disconnect Point	Gas Mixer to Media Reservoir
	Primary Bypass
	Flow Control Valves

Table A.8: Rinse Path 7 Valve Configuration: Flow Control Valves

Valves Opened	Valves Closed
Media Reservoir to Pump	Media Reservoir to Atmosphere
Manifold to Waste Reservoir	Manifold to Media Reservoir
BP Regulator to Manifold	Pressure Relief to Manifold
Bioreactor to BP Regulator	Dampener to Manifold
Compressed Air to Media Reservoir	Bubble Trap Overflow 1 to Manifold
Primary Flow Line	Bubble Trap Overflow 2 to Manifold
Flow Control Valves	Compressed Air to Gas Mixer
Disconnect Point	Gas Mixer to Media Reservoir
	Primary Bypass
	Flow Control Valve Bypasses

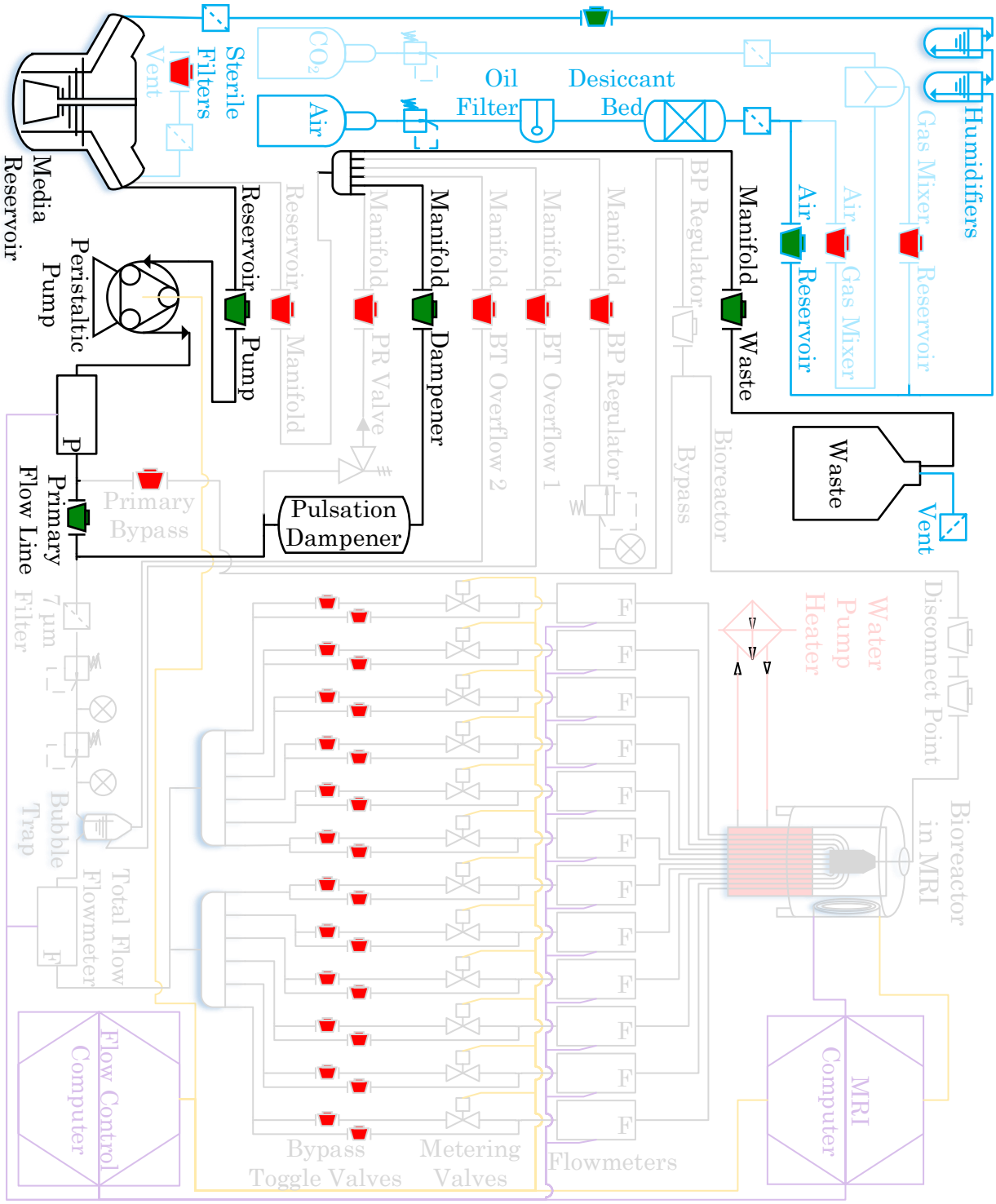

Figure A.5: **Bioreactor PFD: Rinse Path 4 - Pulsation Dampener.** Bioreactor schematic highlighting the flow path corresponding to the valve configuration specified in Table A.5.

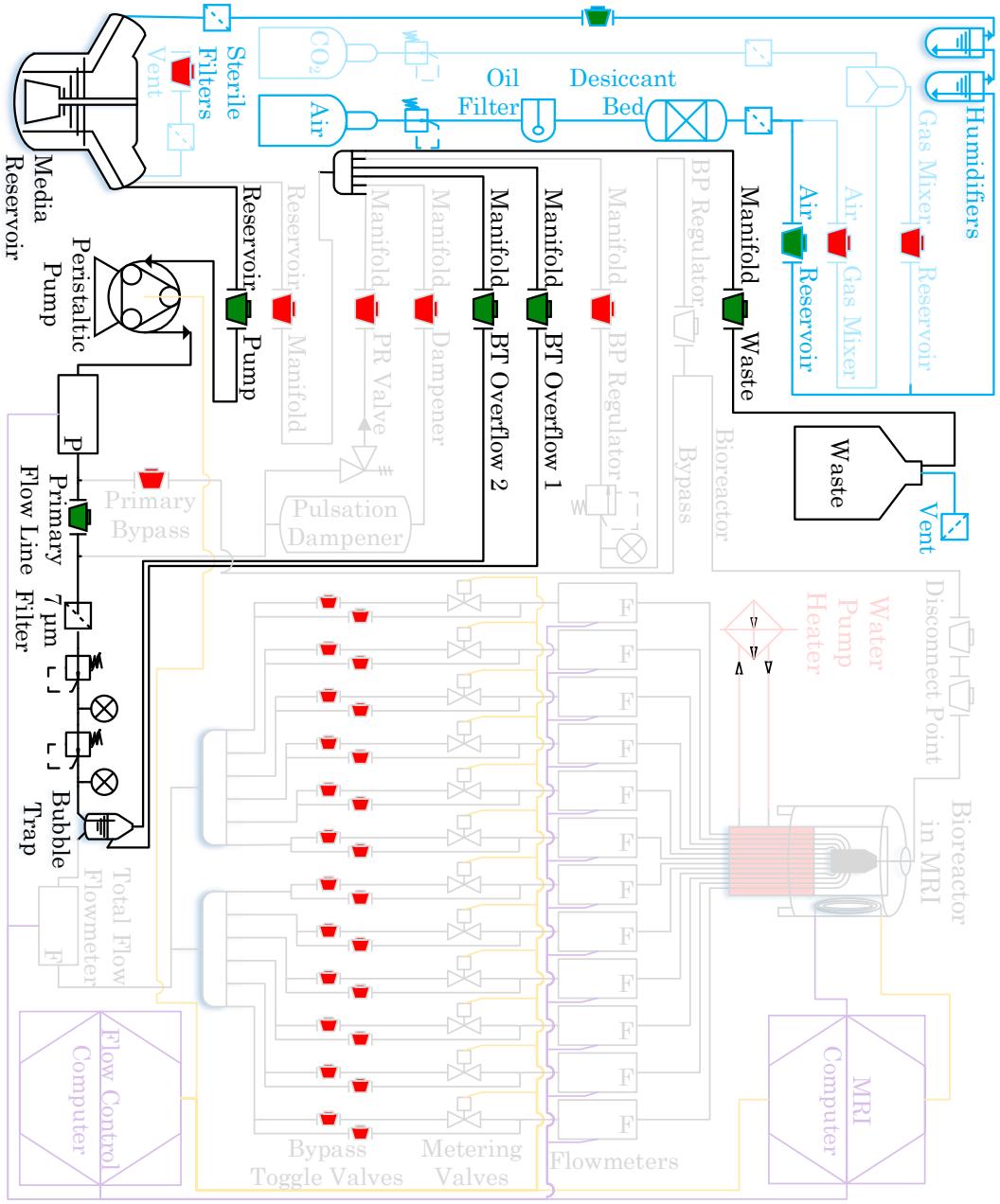

Figure A.6: **Bioreactor PFD: Rinse Path 5 - Bubble Trap Overflows.** Bioreactor schematic highlighting the flow path corresponding to the valve configuration specified in Table A.6. Bubble Trap Overflows 1 and 2 were opened sequentially.

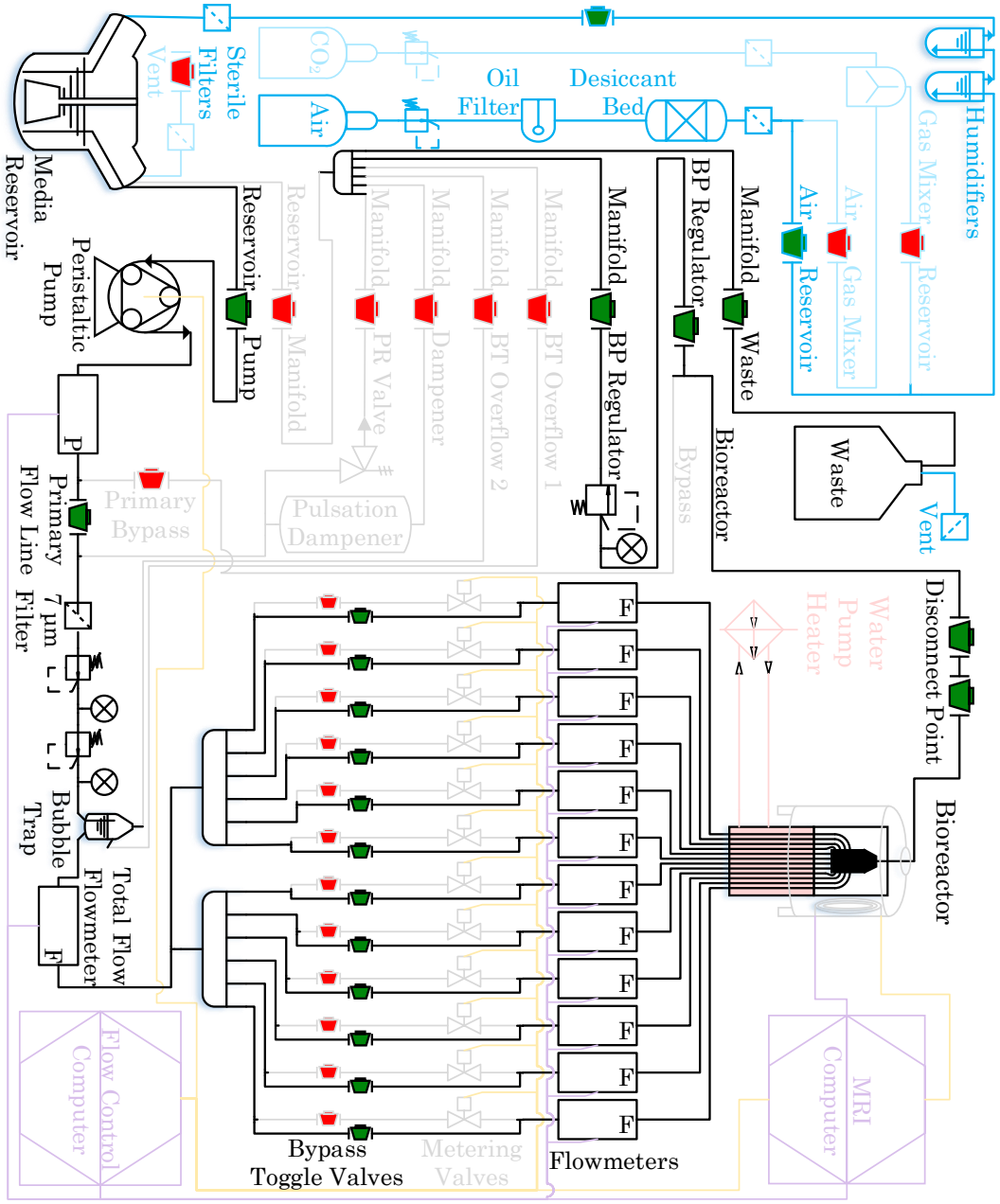

Figure A.7: **Bioreactor PFD: Rinse Path 6 - Flow Control Valve Bypasses.** Bioreactor schematic highlighting the flow path corresponding to the valve configuration specified in Table A.7.

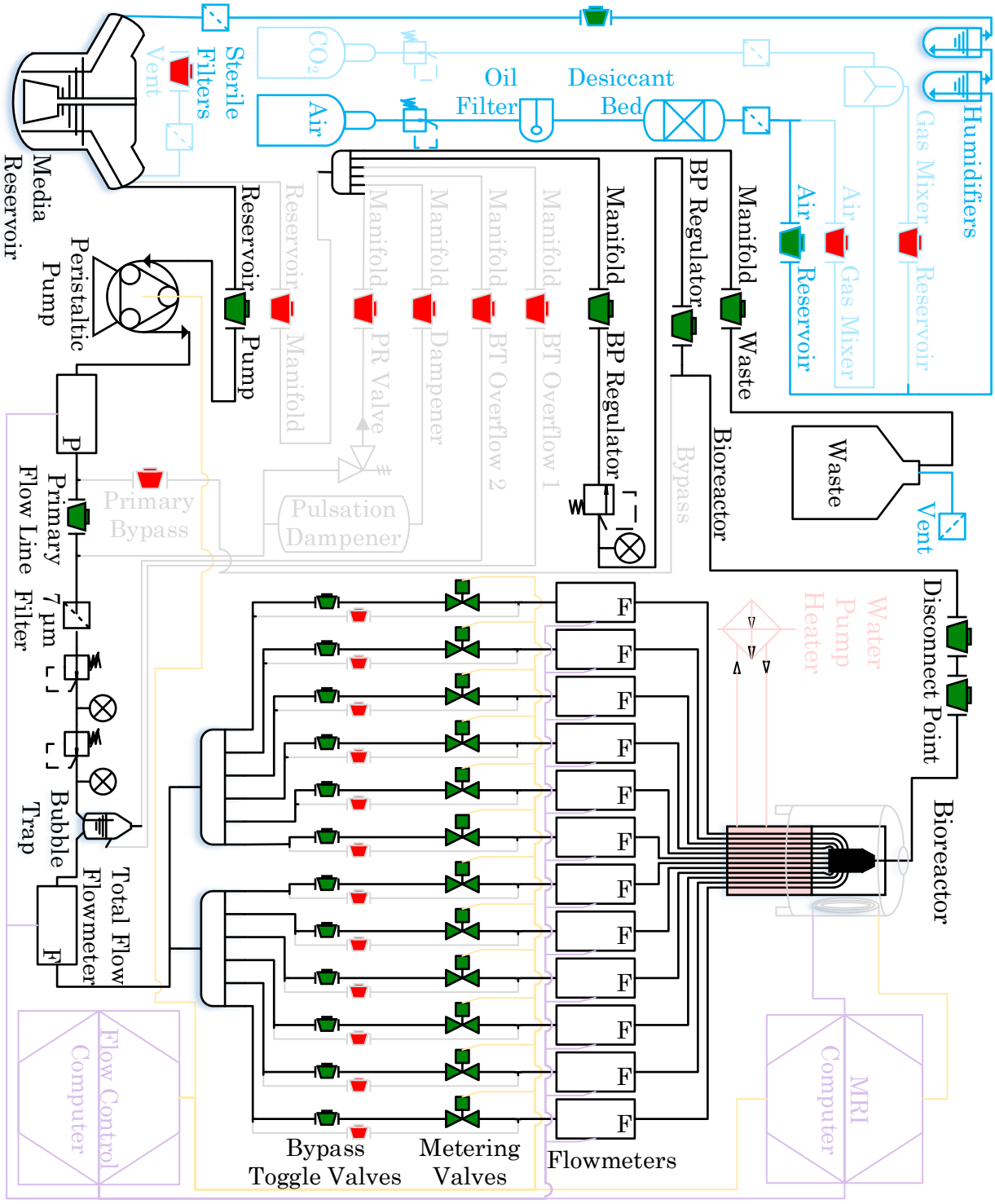

Figure A.8: **Bioreactor PFD: Rinse Path 7 - Flow Control Valves.** Bioreactor schematic highlighting the flow path corresponding to the valve configuration specified in Table A.8.

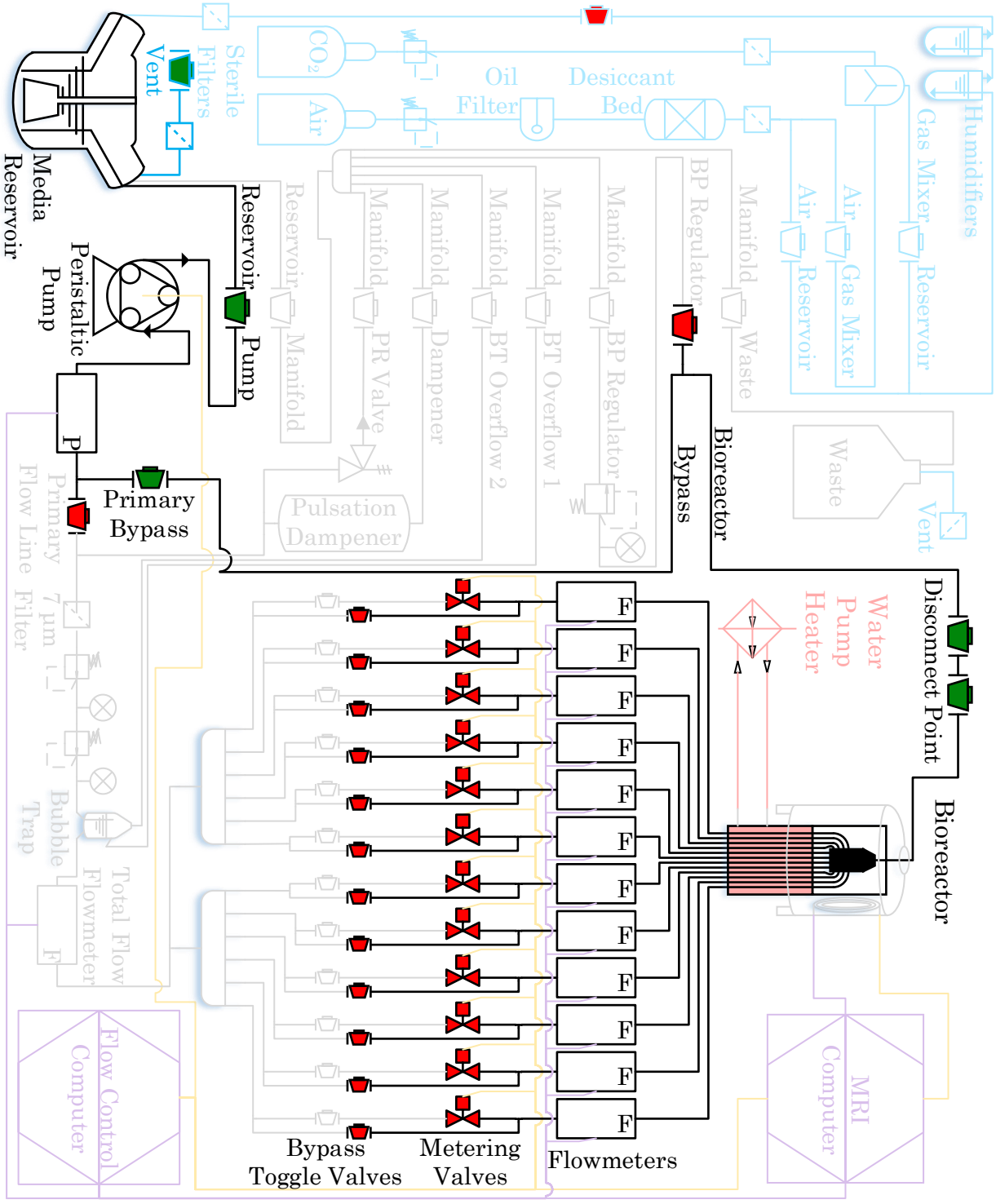

Figure A.9: **Bioreactor PFD: Configuration 8.** Bioreactor schematic highlighting the regions of negative pressure generated by reversing the direction of the peristaltic pump.

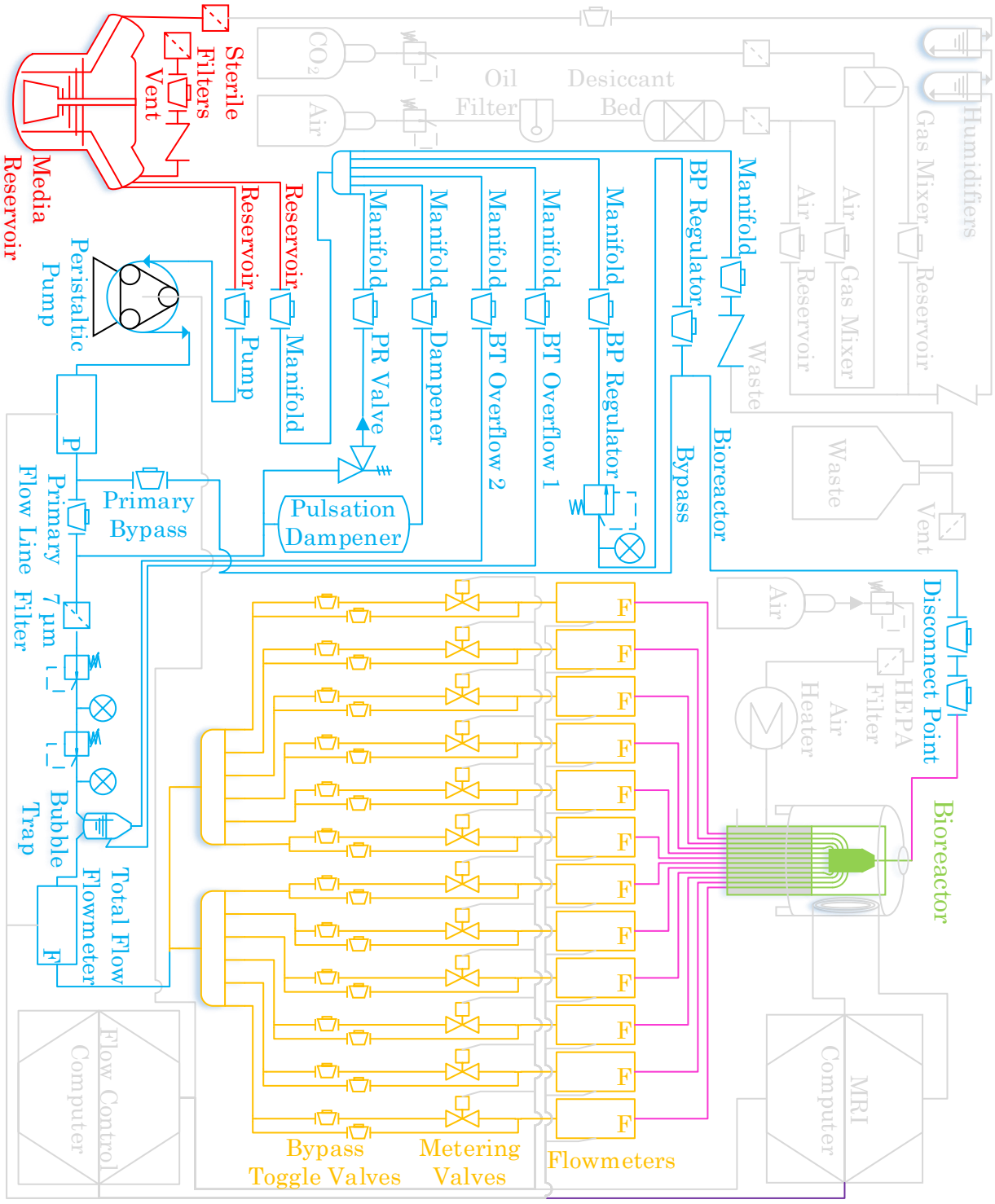

Figure A.10: **Bioreactor PFD: Configuration 8.** Bioreactor schematic highlighting separable modules to be sterilized in color. Gray regions are non-sterile. Magenta paths are steam autoclaved. All other colored regions are ethylene oxide treated.

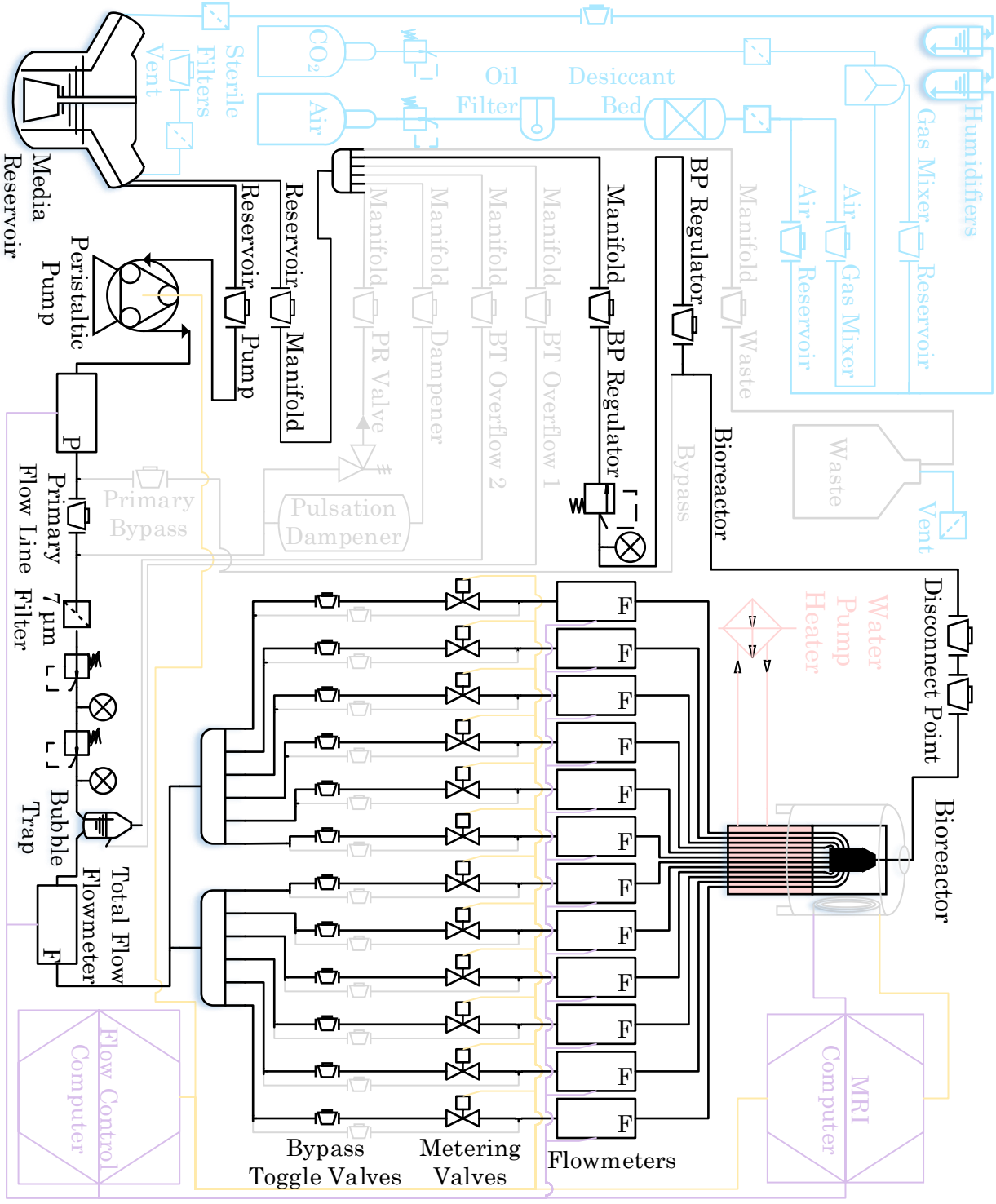

Figure A.11: **Bioreactor PFD: Primary Flow Path.** Bioreactor schematic highlighting the primary flow path in black.

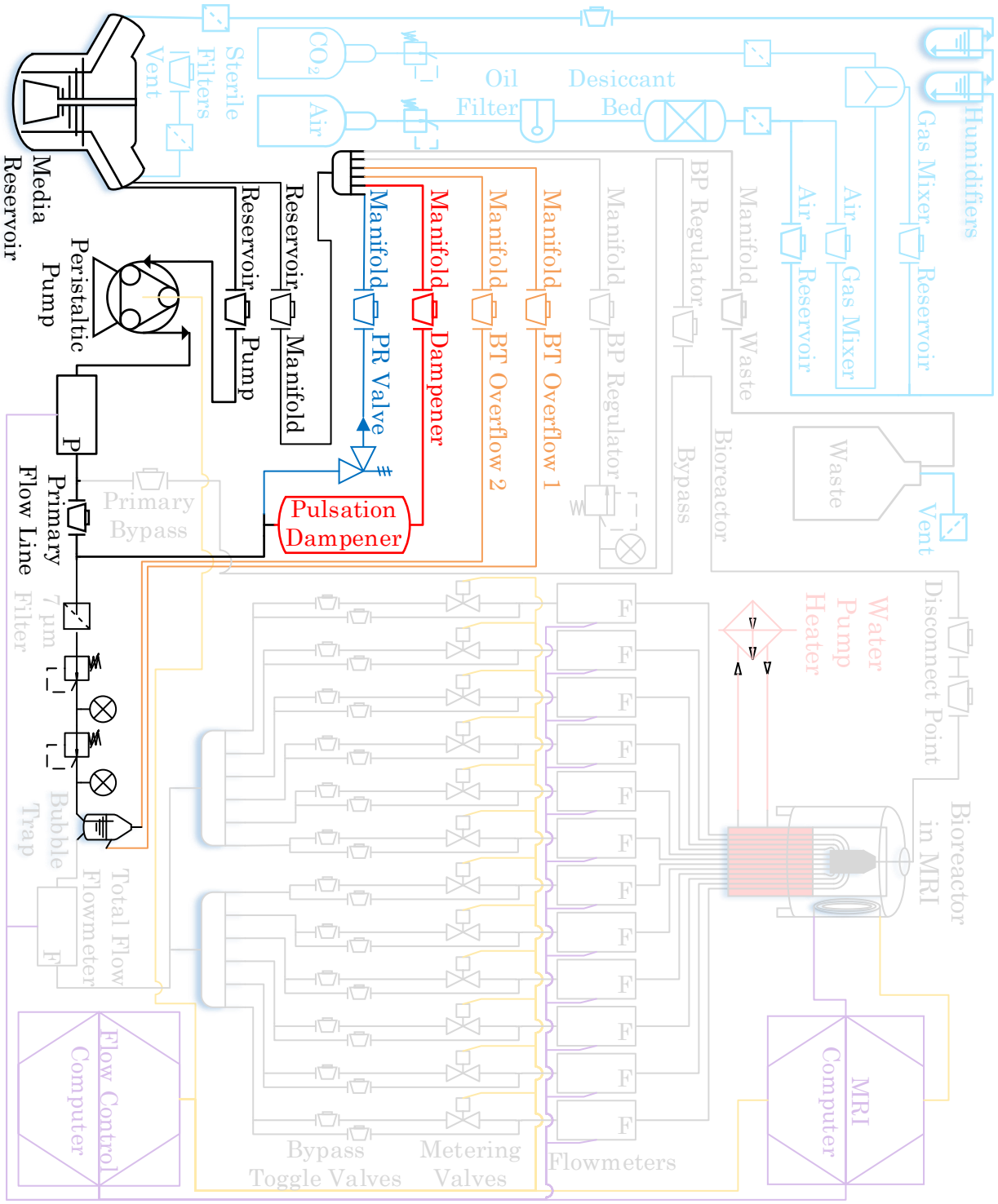

Figure A.12: **Bioreactor PFD: Secondary Flow Paths.** Bioreactor schematic highlighting the secondary flow paths. Blue: pressure relief, red: pulsation dampener, orange: bubble trap overflows.

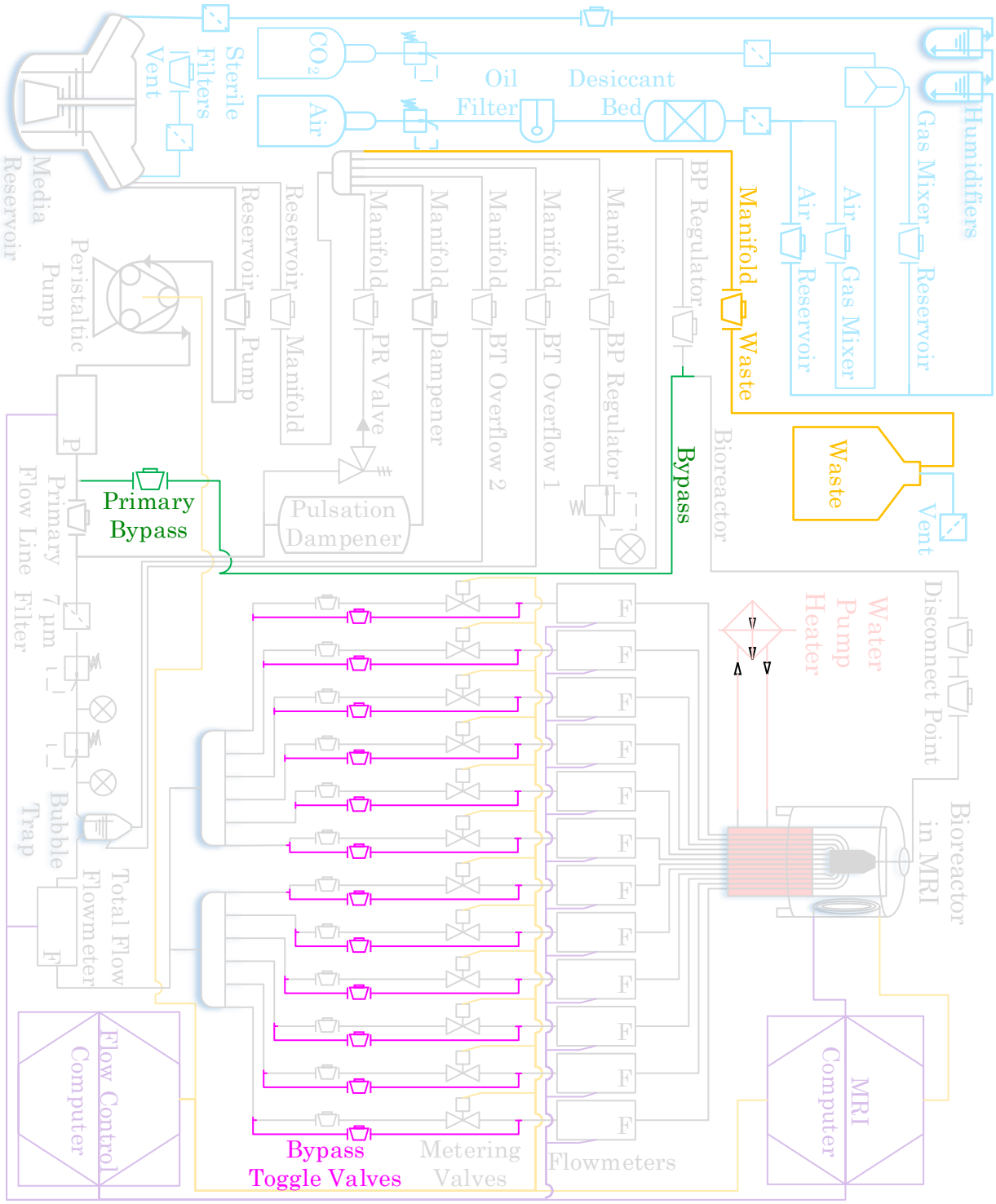

Figure A.13: **Bioreactor PFD: Other Flow Paths.** Bioreactor schematic highlighting cell culture media flow paths not included in the primary or secondary flow circuits. Green: primary bypass, orange: waste reservoir, magenta: metering valve bypasses.

APPENDIX B

Code

The code was implemented and tested using MATLAB (Mathworks, Natick, MA) version R2015a.

B.1 Twelve-Channel Flow Control Code Operator Initialization Function

This code is run by the bioreactor operator to initiate flow control.

```
function [ b11 ]=FlowControl(a,x,opclostoggle,realtime)

addpath(genpath(strcat(...
    'C:\Users\Bioreactor\Documents\MATLAB\12 Channel Flow Control\FRP ',...
    'Toolbox for MATLAB')));
direc1='C:\Users\Bioreactor\Documents\MATLAB\12 Channel Flow Control\';

if nargin < 2
    re=0;
    times=zeros(size(clock));
    save('\12 Channel Flow Control\saves.mat','re','times')
    prompt = strcat(...
        '\nSelect an option:\n\n    1.  Individual Channel Control\n  ',...
        '    2.  Total Flow Control\n    3.  Khalid Known Valve Inputs',...
        '(1x12 array 0-245)\n    4.  Passive Monitor with Pressure Mai',...
        'ntenance\n    5.  Valve Check\n    6.  Flowrate Control Calib',...
        'ration\n    7.  Priming Sequence\n    8.  Individual Channel ',...
        'Cleaning\n    9.  Controlled Push\n    10.  Liquid Change\n\n',...
        '    ');
    x = input(prompt);

    if x == 4
        prompt = '\nShould valves be open (o) or closed (c)?\n\n      ';
        opclostoggle = input(prompt,'s');
    end

    if ~exist('realtime','var') && x == 1
        prompt = strcat('Enter 1 for automated acquisition or 0 for re',...
            'gular flow\n\n');
        aa = input(prompt);
    end

end

%%
```

```
%connect to flowmeters and get number of channels connected
[handles, numchan] = FlowMeterConnect;
warning('off','all')
[handle_p, result_p, broadcast, slaveAddr, scalef ]=OpenSensirionSensor;
warning('on','all')
drawnow;

if numchan<12 %if not all channels were detected
    prognum=sprintf('x=%d;',x);
    if (exist('aa','var') && aa==1) ||...
            (exist('realtime','var') && realtime==1)
        %if there is automated acquisition
        Command([prognum...
            'realtime=1; error(''Less than twelve channels'')'],...
            handles,handle_p,a);
    elseif x ~= 4 %if no automated acquisition and the program is not
        %program 4
        Command([prognum 'error(''Less than twelve channels'')'],...
            handles,handle_p,a);
    else %if it is program 4
        Command([prognum...
            'xstr=var1; error(''Less than twelve channels'')'],...
            handles,handle_p,a,opclostoggle);
    end
end
%%
% Read flow-rate on the selected channel
[b1, b2, b3, b4, b5, b6, b7, b8, b9, b10, b11, leg, txt] = ...
    InitFlowPlot( numchan, handles );
[a1, a2, a3, a4, a5, a7]=InitPressurePlot(b6);
[c1, c2, c3, leg2, txt2] = InitTotalFlowPlot(handle_p, result_p,...
    broadcast, slaveAddr, scalef, b2, b3, b6, b7);

% if (~exist('a', 'var'))
```

```
% a=arduino('COM12')
% end

psetpoint=45;   %Input Pressure Setpoint (should be slightly less than
%tubing max rating)
pip=1.2;  %Proportional pressure control factor
pif=ones(numchan,1)*0.031;  %Proportional flow control factor individual
pift=0.031;  %Proportional flow control factor total

%Set flowrates for individual channel control(mL/min)
formatSpec = '%f';
%opens file containing setpoints
fileID = fopen('FlowSetpoints.txt','r');
%reads setpoints from file
fsetpoints = fscanf(fileID,formatSpec);
fclose(fileID); %close file

% fsetpoints=[1.2;2;2;2;2;2;2;0;2;2;0;2;2];
fsetpoint=30;  %Desired overall flowrate for overall flow control (mL/min)

pause(0.1)

%if valves are still closing from previous run
if any(b4(:,end)>0.08)
    for i=1:numchan
        a.analogWrite(i+1,0)
    end
    pause(10);
end

%%
fprintf('Start Date: %s    Time: %s\n',datestr(now,'mmmm dd, yyyy'),...
    datestr(now,'HH:MM:SS'))
t1 = datetime('now');
switch x
```

```
case 1
    if ~exist('realtime','var')
        if ~exist('aa','var') || aa~=1

            failsafe

            b11 = IndividualFlowControl(a, b1, b2, b3, b4, b5, b6,...
                b7, b8, b9,b10, leg, numchan, handles, leg2,...
                handle_p, result_p, broadcast,slaveAddr, scalef, c1,...
                c2, c3, psetpoint, fsetpoints, pip, b11,...
                pif, txt, txt2, a1, a2, a3, a4, a5, a7 );
        else
            %setup for automated aquisition
            if 7~=exist('C:\cygwin\home\Bioreactor\NewFiles','dir')
                mkdir('C:\cygwin\home\Bioreactor\NewFiles','dir')
            end

            k=dir('C:\cygwin\home\Bioreactor\NewFiles');
            N = length(k)-2;
            if N>0
                %change previous directory name containing files to a
                %new name with the date
                direct=['C:\cygwin\home\Bioreactor\'...
                    datestr(now,'yyyymmdd') '_' datestr(now,'HHMM')];
                movefile('C:\cygwin\home\Bioreactor\NewFiles',...
                    [direct 'Acquisition']);
                %make new directory with NewFiles name
                mkdir C:\cygwin\home\Bioreactor\NewFiles
                %copy noflow file into folder containing flow data  Change
                %name may be necessary

                copyfile(strcat('C:\cygwin\home\Bioreactor\2019052',...
                    '3_Sponge_Channels_Noflow.fid'),[direct...
                    strcat('Acquisition\20190523_Sponge_',...
                    'Channels_Noflow.fid')]);
```

```
        copyfile(strcat('C:\Users\Bioreactor\Documents\MAT',...
            'LAB\12 Channel Flow Control\avrgflowmeasurs.m',...
            'at'),[direct 'Acquisition']);
        copyfile(strcat('C:\Users\Bioreactor\Documents\MAT',...
            'LAB\12 Channel Flow Control\avrgfinvals.mat'),...
            [direct 'Acquisition']);
        copyfile(strcat('C:\Users\Bioreactor\Documents\MAT',...
            'LAB\12 Channel Flow Control\avrgflowstds.mat',...
            [direct 'Acquisition']));
        copyfile(strcat('C:\Users\Bioreactor\Documents\MAT',...
            'LAB\12 Channel Flow Control\flowdata.mat'),...
            [direct 'Acquisition']);
        %clear the DownloadFiles directory

    end

    cmd_rmdir('C:\cygwin\home\Bioreactor\DownloadFiles');
    pause(0.1)
    mkdir C:\cygwin\home\Bioreactor\DownloadFiles

    %start the SSH daemon
    system(strcat('C:\\cygwin\\bin\\bash --login -c /usr/s',...
        'bin/sshd && exit &'));
    pause(0.5);

    %set flag files to 0
    FLAG_FILE = 'C:\cygwin\home\Bioreactor\flag_file.txt';
%     FLAG_FILE1 = 'C:\cygwin\home\Bioreactor\flag_file1.txt';
%     FLAG_FILE2 = 'C:\cygwin\home\Bioreactor\flag_file2.txt';
    setAcqFlag(FLAG_FILE, 0);
    flag1=0;
    save([direc1 'flag1.mat'],'flag1')
    flag2=0;
    save([direc1 'flag2.mat'],'flag2')
    flag3=0;
```

```
save([direc1 'flag3.mat'],'flag3')
flag4=0;
save([direc1 'flag4.mat'],'flag4')
%               setAcqFlag(FLAG_FILE1, 0);
%               setAcqFlag(FLAG_FILE2, 0);
pause(2)

%start the au_aq.py program to watch the directory for new
%files from the NMR computer
system(sprintf(strcat('cd C:\\cygwin\\home\\Bioreactor',...
    '&& au_aq.py DownloadFiles NewFiles &')));
pause(1);

%reset matrix containing flow measurements corresponding to
%images
FlowMeasurements=zeros(numchan,1);
save(strcat('C:\Users\Bioreactor\Documents\MATLAB\12 C',...
    'hannel Flow Control\avrgflowmeasurs.mat'),...
    'FlowMeasurements');

FinVals=zeros(numchan,1);
save(strcat('C:\Users\Bioreactor\Documents\MATLAB\12 C',...
    'hannel Flow Control\avrgfinvals.mat'),'FinVals');

FlowStdDevs=zeros(numchan,1);
save(strcat('C:\Users\Bioreactor\Documents\MATLAB\12 C',...
    'hannel Flow Control\avrgflowstds.mat'),'FlowStdDevs');

%prompt user to start program in VNMRJ
fprintf(...
    '\nEnter ''start_collect'' in VnmrJ command line\n\n')
pause(20);

%start new instance of MATLAB running collectData
%note that the no flow file name must be correct
```

```
            load(...
                'C:\Users\Bioreactor\Documents\MATLAB\errorsaved.mat');
            save(strcat('C:\Users\Bioreactor\Documents\MATLAB\erro',...
                'rsaved.mat'),'numtime');
            %remove cmd from errorsaved.mat temporarily while second
            %MATLAB window opens and starts
            comd=strcat('collectData(''C:\\cygwin\\home\\Bioreacto',...
                'r\\20190523_Sponge_Channels_Noflow.fid'', ''C:\\c',...
                'ygwin\\home\\Bioreactor\\NewFiles'')');
            system(['matlab -r "' comd '"&']);
            pause(1*60)

            realtime=1;

            failsafe1 %return the failsafe file back to normal

            b11 = IndividualFlowControl(a, b1, b2, b3, b4, b5, b6,...
                b7, b8, b9,b10, leg, numchan, handles, leg2, ...
                handle_p, result_p, broadcast,slaveAddr, scalef, c1,...
                c2, c3, psetpoint, fsetpoints, pip, b11, pif, txt,...
                txt2, a1, a2, a3, a4, a5, a7,realtime );
        end
    else

        failsafe1

        b11 = IndividualFlowControl(a, b1, b2, b3, b4, b5, b6, b7,...
            b8, b9, b10, leg, numchan, handles, leg2, handle_p,...
            result_p, broadcast, slaveAddr, scalef, c1, c2, c3,...
            psetpoint, fsetpoints, pip, b11, pif, txt, txt2, a1, a2,...
            a3, a4, a5, a7, realtime );
    end
case 2
```

```
    failsafe

    b11 = OverallFlowControl(a, b1, b2, b3, b4, b5, b6, b7, b8, b9,...
        b10, leg, numchan, handles, leg2, handle_p, result_p,...
        broadcast, slaveAddr, scalef, c1, c2, c3, psetpoint, ...
        fsetpoint, pip, b11, pift, txt, txt2, a1, a2, a3, a4, a5, a7 );
case 3

    failsafe

    b11 = IndividualFlowCal(a, b1, b2, b3, b4, b5, b6, b7, b8, b9,...
        b10, leg, numchan, handles, leg2, handle_p, result_p, ...
        broadcast, slaveAddr, scalef, c1, c2, c3, psetpoint, pip,...
        txt, txt2, a1, a2, a3, a4, a5, a7 );
case 4

    failsafe2

    PassiveMonitor(a, b1, b2, b3, b4, b5, b6, b7, b8, b9,...
        b10, leg, numchan, handles, leg2, handle_p, result_p, ...
        broadcast, slaveAddr, scalef, c1, c2, c3, psetpoint, pip,...
        txt, txt2, a1, a2, a3, a4, a5, a7, opclostoggle );
case 5

    failsafe

    b11 = IndividualValveCheck(a, b1, b2, b3, b4, b5, b6, b7, b8, b9,...
        b10, leg, numchan, handles, leg2, handle_p, result_p, ...
        broadcast, slaveAddr, scalef, c1, c2, c3, psetpoint, pip,...
        txt, txt2, a1, a2, a3, a4, a5, a7 );
case 6

    failsafe

    IndividualFlowCal2(a, b1, b2, b3, b4, b5, b6, b7, b8, b9,...
```

```
        b10, leg, numchan, handles, leg2, handle_p, result_p,...
        broadcast, slaveAddr, scalef, c1, c2, c3, psetpoint, pip, ...
        b11, pif,txt, txt2, a1, a2, a3, a4, a5, a7 )
case 7

    failsafe

    PrimingSequence(a, b1, b2, b3, b4, b5, b6, b7, b8, b9,...
        b10, leg, numchan, handles, leg2, handle_p, result_p, ...
        broadcast, slaveAddr, scalef, c1, c2, c3, pif,...
        txt, txt2, a1, a2, a3, a4, a5, a7, fsetpoints )
case 8

    failsafe

    for i=1:20
        b11 = ChannelClean(a, b1, b2, b3, b4, b5, b6, b7, b8, b9,...
            b10, leg, numchan, handles, leg2, handle_p, result_p, ...
            broadcast, slaveAddr, scalef, c1, c2, c3, psetpoint, ...
            fsetpoints, pip, b11, pif, txt, txt2, a1, a2, a3, a4, ...
            a5, a7 );
    end
case 9

    failsafe

    b11 = ControlledPush(a, b1, b2, b3, b4, b5, b6, b7, b8, b9,...
        b10, leg, numchan, handles, leg2, handle_p, result_p, ...
        broadcast, slaveAddr, scalef, c1, c2, c3, psetpoint, ...
        fsetpoints, pip, b11, pif, txt, txt2, a1, a2, a3, a4, a5, a7 );
case 10

    failsafe

    LiquidChange(a, b1, b2, b3, b4, b5, b6, b7, b8, b9,...
```

```
            b10, leg, numchan, handles, leg2, handle_p, result_p, ...
            broadcast, slaveAddr, scalef, c1, c2, c3, psetpoint, pip,...
            txt, txt2, a1, a2, a3, a4, a5, a7 );
        end

pause(0.3)

%%
%Saving flow data for automated acquisition
if exist('realtime','var')
    %change previous directory name containing files to a
    %new name with the date

    [status,result] = system(strcat('tasklist /FI "imagename eq matlab',...
        '.exe" /fo table /nh'));

    if size(strfind(result,'MATLAB.exe'),2)==2
        %if there is another MATLAB window open
        %indicate to the collectData program to shut down
        flag4=1;
        save([direc1 'flag4.mat'],'flag4')

        while flag4==1
            load([direc1 'flag4.mat'])
            fprintf('\nWaiting for collectData to quit.\n\n')
            pause(4)
        end
    end

    direct=['C:\cygwin\home\Bioreactor\' datestr(now,'yyyymmdd') '_' ...
        datestr(now,'HHMM')];
    movefile('C:\cygwin\home\Bioreactor\NewFiles',[direct 'Acquisition']);
    %make new directory with NewFiles name
    mkdir C:\cygwin\home\Bioreactor\NewFiles
    %copy noflow file into folder containing flow data  Change
```

```
    %name may be necessary

    copyfile(strcat('C:\cygwin\home\Bioreactor\20190523_Sponge_Channel',...
        's_Noflow.fid'),[direct ...
        'Acquisition\20190523_Sponge_Channels_Noflow.fid']);
    copyfile(strcat('C:\Users\Bioreactor\Documents\MATLAB\12 Channel F',...
        'low Control\avrgflowmeasurs.mat'),[direct 'Acquisition']);
    copyfile(strcat('C:\Users\Bioreactor\Documents\MATLAB\12 Channel F',...
        'low Control\flowmat.mat'),[direct 'Acquisition']);
    copyfile(strcat('C:\Users\Bioreactor\Documents\MATLAB\12 Channel F',...
        'low Control\avrgfinvals.mat'),[direct 'Acquisition']);
    copyfile(strcat('C:\Users\Bioreactor\Documents\MATLAB\12 Channel F',...
        'low Control\avrgflowstds.mat'),[direct 'Acquisition']);
    copyfile(strcat('C:\Users\Bioreactor\Documents\MATLAB\12 Channel F',...
        'low Control\flowdata.mat'),[direct 'Acquisition']);
    check=1
end

%%
%Shut off all power from Arduino when quitting
a.analogWrite(44,0);
for i=2:13
    a.analogWrite(i,0);
end
% clear a
% delete(instrfind({'Port'},{'COM3'}))

set(gcf,'WindowStyle','normal');
pause(0.5)
close all;
drawnow;pause(0.5);

%clear the failsafe if program exits propoerly
numtime=0;
save('C:\Users\Bioreactor\Documents\MATLAB\errorsaved.mat','numtime')
```

```
check=2
%% Closing the Sensirion sensor and unloading the libraries.

calllib('ShdlcDriver', 'ClosePort', handle_p.Value); % Closes the port
drawnow;pause(0.03)
% Unloads both of the libraries
unloadlibrary('ShdlcDriver');drawnow;pause(0.03)
unloadlibrary('SensorCableDriver');drawnow;pause(0.03)

drawnow;pause(0.5);

%% Close the FRP session
if size(handles.HandleNumber,2)==2
    frp_close(handles.HandleNumber(1));drawnow;pause(0.03)
    frp_close(handles.HandleNumber(2),'CloseLib');drawnow;pause(0.03)
else
    frp_close(handles.HandleNumber(1),'CloseLib');drawnow;pause(0.03)
end
Str = sprintf('Session Closed\n');
fprintf('End Date: %s    Time: %s\n',datestr(now,'mmmm dd, yyyy'),...
    datestr(now,'HH:MM:SS'))
t2 = datetime('now');
fprintf('Total Duration (day:hour:min): %s\n',datestr(t2-t1,'dd:HH:MM'))
disp(Str);

load('C:\Users\Bioreactor\Documents\MATLAB\errorsaved.mat')
if exist('numtime','var')==1
    sprintf('Matlab was restarted %d time(s)',numtime)
end
if exist('strg','var')==1
    for i=1:size(strg,1)
        disp(strg{i,1})
    end
end
numtime=0;
```

```
save('C:\Users\Bioreactor\Documents\MATLAB\errorsaved.mat','numtime');
```

B.2 Initialize Flow Plot Window for Individual Channels

This function is called by the flow control function to setup the window in which all twelve flow rates are plotted over time.

```
function [ count, loop, TimeIntervalF, flowrate, plotHandle1, ...
    figureHandle1, time, meanflow, ValueArray, MarkerArray, fin, leg, ...
    txt ] = InitFlowPlot( numchan, handles )
%UNTITLED15 Summary of this function goes here
%Setup parameters for real time flow graph output (works with pressure plot
%as well)

fin=zeros(1,numchan);
TimeIntervalF=2.3;  %Frequency of flow data point collection and plotting
loop=100;%total number of points to plot on graph

time = zeros(1,1);
flowrate = zeros(numchan,1);
meanflow = zeros(numchan,1);

%% Set up the figure 1
figureHandle1 = figure('NumberTitle','off',...
    'Name','Total Flow Rate Monitor','Visible',...
    'off','Position', [450 60 1100 900],...
    'CurrentCharacter','a');

set(figureHandle1,'visible','on')

%%
% Set axes
axesHandle1 = axes('Parent',figureHandle1,...
    'YGrid','on',...
    'XGrid','on');

hold on;

%Set plot for real time flow reading and average flow reading
subplot(2,5,1:4);
plotHandle1 = plot(time,flowrate);%,time,meanflow);
drawnow;pause(0.1)
```

```
% Set axes limits and turn on grid
xlim([0 TimeIntervalF*loop]);
ylim([0 2]);
grid on

% Create title
title('Total Flow Rate Monitor','FontSize',15);

% Create xlabel
xlabel('Time (s)','FontWeight','bold','FontSize',14);

% Create ylabel
ylabel('Flow Rate (mL/min)','FontWeight','bold','FontSize',14);

% Create title
title('Total Flow Rate Monitor','FontSize',15);


%% Initializing variables
for i=1:numchan
    if i<=8
        flowrate(i,1)=double(frp_read_Q(handles.HandleNumber(1),i))/1000;
    elseif i>8 && i<=16
        flowrate(i,1)=double(frp_read_Q(handles.HandleNumber(2),i-8))/1000;
    end
    if flowrate(i,1)>6  %account for negative values
        flowrate(i,1)=flowrate(i,1)-13.107;
    end
end

time(1)=0;
count = 1;
```

```
%figure for terminating while loop on user input (hit escape key)
set(figureHandle1,'CurrentCharacter','a')
ValueArray = {'-','--',':','-.','-','--',':','-.','-','--',':','-.'}';
MarkerArray = {'+','o','.','*','x','s','^','v','<','>','d','h'};

%Generate a legend for the Fluigent flowmeter readings
leg=cell(1,numchan);  %legend command is too slow
for i=1:numchan
    leg{1,i}=['Flow Channel ' num2str(i) ', Flowrate = '...
        sprintf('%0.3f', flowrate(i,end))]; %num2str(flowrate(i,end))
end

% Add a text uicontrol to label each channel flowrate
txt = uicontrol('Style','text',...
    'Position',[850 570 180 14*numchan],...
    'String',leg);

set(figureHandle1,'toolbar','figure') %keep the figure toolbar which would
%be erased by the uicontrol
```

B.3 Initialize Flow Plot Window for Total Flow Rate

This function is called by the flow control function to setup the window in which the total flow rate is plotted over time.

```
function [ tflowrate, plotHandle3, meanflowt, leg2, txt2 ] = ...
    InitTotalFlowPlot( handle_p, result_p, broadcast, slaveAddr, ...
    scalef, loop, TimeIntervalF, figureHandle1, time )
%UNTITLED15 Summary of this function goes here
%Setup parameters for real time flow graph output (works with pressure plot
%as well)

tflowrate = zeros(1,1);
meanflowt = zeros(1,1);

% Set axes
axesHandle1 = axes('Parent',figureHandle1,...
    'YGrid','on',...
    'XGrid','on');

hold on;

%Set plot for real time flow reading and average flow reading
subplot(2,5,[8:10]);
plotHandle3 = plot(time,tflowrate,time,meanflowt);


% Set axes limits and turn on grid
xlim([0 TimeIntervalF*loop]);
ylim([0 30]);
grid on

% Create title
title('Total Flow Rate Monitor','FontSize',15);

% Create xlabel
xlabel('Time (s)','FontWeight','bold','FontSize',14);

% Create ylabel
ylabel('Flow Rate (mL/min)','FontWeight','bold','FontSize',14);
```

```
% Create title
title('Total Flow Rate Monitor','FontSize',15);


%% Initializing variables

calllib('SensorCableDriver', 'StartSingleMeasurement', handle_p.Value, ...
    broadcast, slaveAddr);
pause(0.1)
calllib('SensorCableDriver', 'GetSingleMeasurementSigned', ...
    handle_p.Value, slaveAddr, result_p);
tflowrate(1,1)=double(result_p.Value)/double(scalef);

%Create legend for total flowrate measured with Senserion flowmeter
leg2=cell(1,1);

leg2{1,1}=['Total Flowrate = ' sprintf('%0.3f', tflowrate(1,end))];

%Create text uicontrol to display Senserion reading
txt2 = uicontrol('Style','text',...
    'Position',[650 100 180 14],...
    'String',leg2);

set(figureHandle1,'toolbar','figure')  %keep the figure toolbar which
%would be erased by the uicontrol
```

B.4 Initialize Pressure Plot Window

This function is called by the flow control function to setup the window in which the peristaltic pump-generated pressure is plotted over time.

```
function [ count, loop, TimeIntervalP, pressure, plotHandle2, time ] ...
    = InitPressurePlot( figureHandle2 )
%% Initialize Pressure Plot
%Setup parameters for real time pressure graph output (works with flow plot
%as well)

TimeIntervalP=0.3;  %Frequency of pressure data point collection and plot
loop=100;%count values

time = zeros(size(loop));
pressure = zeros(size(loop));

%% Set up the figure 2
% figureHandle2 = figure('NumberTitle','off',...
%     'Name','Total Flow Rate Monitor','Visible',...
%     'off','Position', [50 80 400 300],...
%     'CurrentCharacter','a');

% Set axes
axesHandle2 = axes('Parent',figureHandle2,...
    'YGrid','on',...
    'XGrid','on');

hold on;

subplot(2,5,[6,7]);
plotHandle2 = plot(time,pressure,'Marker','.','LineWidth',1);
drawnow; pause(0.1)

% plotHandle2 = plot(axesHandle2,time,pressure,'Marker','.','LineWidth',1);

xlim([0 TimeIntervalP*loop]);
ylim([0 70]);
grid on
% xlim(axesHandle2,[0 TimeInterval*loop]);
```

```
% ylim(axesHandle2,[25 50]);

% Create xlabel
xlabel('Time (s)','FontWeight','bold','FontSize',14);

% Create ylabel
ylabel('Pressure (PSI)','FontWeight','bold','FontSize',14);

% Create title
title('Inlet Pressure Monitor','FontSize',15);

%% Initializing variables

time(1)=0;
count = 1;
end
```

B.5 Controlling Twelve Individual Channels

This function is called by the flow control function to continuously read flowrates and make adjustments to metering valves in order to control the flow rate in each channel.

```
function [ fin ]= IndividualFlowControl(a, b1, b2, b3, b4, b5, b6, b7,...
    b8, b9,b10, leg, numchan, handles, leg2, handle_p, result_p,...
    broadcast,slaveAddr, scalef, c1, c2, c3, ~, fsetpoints, ~, fin,...
    ~, txt, txt2, a1, a2, a3, a4, a5, a7, realtime )
%%
%Program controls each twelve flow channels
nwate=2*ones(1,numchan);
found=zeros(numchan,1);
finmat=zeros(numchan,1);
setpmat=zeros(numchan,1);
debugcheck=zeros(1,numchan);
formatSpec = '%f';
go=0;
tStart1 = tic;
wate=zeros(numchan,1);
tStart2=tic;
direc1='C:\Users\Bioreactor\Documents\MATLAB\12 Channel Flow Control\';

while double(get(b6,'CurrentCharacter'))~=27

    if go==0
        tStart1 = tic;
    end
    tStart=tic;
    go=go+1;
    %Pressure Reading
    if ~exist('realtime','var')
        pressure=Command('x=1;0.236*a.analogRead(1)-17.62;',...
            handles,handle_p,a); %200 PSI pressure transducer
    else
        pressure=Command(...
            'x=1;realtime=var1;0.236*a.analogRead(1)-17.62;',...
            handles,handle_p,a,realtime); %200 PSI pressure transducer
    end
```

```
%Maintain Pressure from Peristaltic Pump
if pressure <=65
    if ~exist('realtime','var')
        Command('x=1;a.analogWrite(44,245)',handles,handle_p,a);
    else
        Command('x=1;realtime=var1;a.analogWrite(44,243)',...
            handles,handle_p,a,realtime);
    end
else
    if ~exist('realtime','var')
        Command('x=1;a.analogWrite(44,220)',handles,handle_p,a);
    else
        Command('x=1;realtime=var1;a.analogWrite(44,220)',...
            handles,handle_p,a,realtime);
    end
end

%Flow Control (least efficient part of code causing most slowdown)
if toc(tStart1)>b3-a3

    %opens file containing setpoints
    %changes are made in collectData.m        WZheng
    fileID = fopen('FlowSetpoints.txt','r');
    %reads setpoints from file
    fsetpoints1=fsetpoints;
    fsetpoints = fscanf(fileID,formatSpec);
    fclose(fileID); %close file

    %if any flow setpoints are changed, reset to broader search
    found(fsetpoints1~=fsetpoints)=0;
    wate(fsetpoints1~=fsetpoints)=0;
    nwate(abs(fsetpoints1-fsetpoints)>0.5)=4;
    nwate(wate'>=nwate & nwate>2)=2;
```

```
%In case user inputs wrong number of setpoints
if ~all(size(fsetpoints)==[numchan 1])
    fsetpoints=zeros(numchan,1); %set all channels to zero
    disp('Warning: Enter 12 Flow Setpoints in Column');
    %display warning
end


%Compare current reading to setpoint
F=fsetpoints*ones(1,size(b4,2))-b4;
%note current flow reaing (b4(end)) corresponds to last flow input
%(fin)

%Change inputs by a value proportional to difference between
%each setpoint and current value
for i=1:numchan
    if fsetpoints(i)~=0 && nwate(i)==2;
        if found(i)==0
            if wate(i)==0
                if  F(i,end)>0 && ~(any(F(i,:)>0)&&any(F(i,:)<0))
                    %%|| size(Fmat,2)<3*3
                    %if we have waited enough time for the valve
                    %to finish moving, and the difference between
                    %the current reading and target (F) is greater
                    %than zero indicating the current flowrate is
                    %smaller than the setpoint, and the range has
                    %not been found (range is found when at least
                    %one point collected is above the setpoint
                    %and another point collected is below the
                    %setpoint), and the range is still not found
                    %currently:
                    if abs(F(i,end))<0.3
                        fin(i)=fin(i)+5;
                        debugcheck(i)=1;
                    elseif abs(F(i,end))>=0.3 && abs(F(i,end))<0.9
```

```
            fin(i)=fin(i)+10;
            debugcheck(i)=2;
        elseif abs(F(i,end))>=0.9
            fin(i)=fin(i)+18;
            debugcheck(i)=3;
        end
    elseif F(i,end)<0 && ~(any(F(i,:)>0)&&any(F(i,:)<0))
        %if we have waited enough time for the valve
        %to finish moving, and the difference between
        %the current reading and target (F) is less
        %than zero indicating the current flowrate is
        %larger than the setpoint, and the range has
        %not been found (range is found when at least
        %one point collected is above the setpoint
        %and another point collected is below the
        %setpoint), and the range is still not found
        %currently:
        if abs(F(i,end))<0.3
            fin(i)=fin(i)-5;
            debugcheck(i)=4;
        elseif abs(F(i,end))>=0.3 && abs(F(i,end))<0.9
            %if far, move by 10 increments
            fin(i)=fin(i)-10;
            debugcheck(i)=5;
        elseif abs(F(i,end))>=0.9
            fin(i)=fin(i)-25;
            debugcheck(i)=6;
        end
    elseif (any(F(i,:)>0)&&any(F(i,:)<0))
        %when range is found (meaning at least one
        %input was found to correspond to a flowrate
        %greater than the setpoint and another flow
        %input was found to correspond to a flowrate
        %less than the setpoint), a new flow input is
        %input which is the average of those two
```

```
                %inputs weighted for how far each of them is
                %from the setpoint, and the amount of time
                %to wait is reset
                lg=find(F(i,:)==max(F(i,F(i,:)<0)));
                %index of smallest absolute negative value
                lg=lg(1);
                sm=find(F(i,:)==min(F(i,F(i,:)>0)));
                %index of smallest positive value
                sm=sm(1);
                %weightd position
                try
                    fin(i)=round((finmat(i,lg)*abs(1/F(i,...
                        lg))+finmat(i,sm)*abs(1/F(i,sm)))/...
                        (abs(1/F(i,lg))+abs(1/F(i,sm))));
                catch
                    size(finmat)
                    size(F)
                end
                %                               debugcheck(i)=7;
                found(i)=1;
                wate(i)=1;
            end
        end

    elseif found(i)==1 %if range has been found
        if wate(i)==0 %if enough readings have been acquired to
            %make an adjustment
            if F(i,end)>0 &&...
                    abs(F(i,end))>0.15*abs(fsetpoints(i))...
                    && abs(fsetpoints(i))<0.35
                %if range has already been found and flowrate
                %difference between current and setpoint(F) is
                %greater than zero indicating the current
                %flowrate is smaller than the setpoint, and
                %(absolute flowrate difference (F) is greater
```

```
            %than 15 of the setpoint while setpoint is
            %less than 0.35 or greater than 0.85) or
            %(absolute flowrate difference (F) is greater
            %than 0.15 while setpoint is between 0.35
            %and 0.85), increment flow input by one
            fin(i)=fin(i)+1;
            %                               debugcheck(i)=8;
        elseif F(i,end)>0 &&...
                abs(F(i,end))>0.10*abs(fsetpoints(i))...
                && abs(fsetpoints(i))>=0.35
            fin(i)=fin(i)+1;
            %                               debugcheck(i)=8;
        elseif F(i,end)<0 &&...
                abs(F(i,end))>0.15*abs(fsetpoints(i)) &&...
                abs(fsetpoints(i))<0.35
            %if range has already been found and flowrate
            %difference between current and setpoint(F) is
            %less than zero indicating the current flowrate
            %is larger than the setpoint, and (absolute
            %flowrate difference (F) is greater than 15
            %of the setpoint while setpoint is less than
            %0.35 or greater than 0.85) or (absolute
            %flowrate difference (F) is greater than
            %0.15 while setpoint is between 0.35 and
            %0.85), increment flow input by one
            fin(i)=fin(i)-1;
            %                               debugcheck(i)=9;
        elseif F(i,end)<0 &&...
                abs(F(i,end))>0.10*abs(fsetpoints(i)) &&...
                abs(fsetpoints(i))>=0.35
            fin(i)=fin(i)-1;
            %                               debugcheck(i)=9;
        end
    end
end
```

```
        if wate(i)<nwate(i)
            wate(i)=wate(i)+1;
        elseif wate(i)>=nwate(i)
            wate(i)=0;
        end

    elseif nwate(i)>2 && fsetpoints(i)~=0
        wate(i)=wate(i)+1;
    elseif fsetpoints(i)==0
        fin(i)=0;  %If desired flow is 0, arduino input is
        %autimatically set to 0
    end

    fin(fin>245)=245;  %Restrict input to max value of 245
    fin(fin<0)=0;  %Restrict input to minimum value of 0

    %Input new PWM value into all flow channels
    if ~exist('realtime','var')
        Command('x=1;a.analogWrite(var2+1,var1(var2));',...
            handles,handle_p,a,fin,i);
    else
        Command(strcat('x=1;realtime=var3;a.analogWrite(var2+1',...
            ',var1(var2));'),handles,handle_p,a,fin,i,realtime);
    end

    leg{1,i}=['Flow Channel ' num2str(i) ', Flowrate = '...
        sprintf('%0.3f', b4(i,end))]; %num2str(flowrate(i,end))

end

%keep legend display updated with current setpoint)
set(txt, 'String',leg);
set(txt2, 'String',leg2);

%Plot flow data
```

```
if ~exist('realtime','var')
    [b1, b2, b3, b4, b5, b6, b7, b8, leg] =...
        FlowPlot(a, b1, b2, b3, b4, b5, b6, b7, b8, b9, b10,...
        leg, fin, numchan, handles, handle_p, 1);
    [b1, b2, b3, b4, b5, b6, b7, b8, leg2, c1, c2, c3] =...
        TotalFlowPlot(a, b1, b2, b3, b4, b5, b6, b7, b8, leg2,...
        handle_p, result_p, broadcast, slaveAddr, scalef, c1,...
        c2, c3, handles, 1);
else %case for in the middle of collecting training data
    [b1, b2, b3, b4, b5, b6, b7, b8, leg] =...
        FlowPlot(a, b1, b2, b3, b4, b5, b6, b7, b8, b9, b10,...
        leg, fin, numchan, handles, handle_p, 1, 'c', realtime);
    [b1, b2, b3, b4, b5, b6, b7, b8, leg2, c1, c2, c3] =...
        TotalFlowPlot(a, b1, b2, b3, b4, b5, b6, b7, b8, leg2,...
        handle_p, result_p, broadcast, slaveAddr, scalef, c1,...
        c2, c3, handles, 1, 'c', realtime);
end

if ~isequal(b1,b2)
    finmat(:,size(b4,2))=fin';
    setpmat(:,size(b4,2))=fsetpoints';
elseif ~isequal(size(F),size(finmat))
    finmat(:,size(F,2))=fin';
    setpmat(:,size(F,2))=fsetpoints';
else
    finmat(:,1:end-1)=finmat(:,2:end);
    finmat(:,end)=fin';
    setpmat(:,1:end-1)=setpmat(:,2:end);
    setpmat(:,end)=fsetpoints';
end



%         for i=1:numchan
%             if size(finmat,2)>2 && finmat(i,end)==finmat(i,end-1)
```

```
    %                 %if there was no change in the flow input
    %                 debugcheck(i)=0;
    %             end
    %         end

    %Uncomment to see which statements are being executed
    %debugcheck
    %         b3
    %         toc(tStart1)
    %         b3-toc(tStart1)
    drawnow; pause(b3-toc(tStart1))

    go=0;

    %         toc(tStart1)  %Uncomment to check timing of each flow
    %         point
    %         if size(finmat,2)>8
    %             finmat(:,end-6:end)
    %         end

end

%after updating matrices, check if any changes were made
try
    load([direc1 'flag3.mat'])
catch
    pause(5)
    try
        load([direc1 'flag3.mat'])
    catch
        fprintf('\nflag3 unable to be read, continuing\n\n')
        flag3=0;
    end
end
```

```
if  flag3==1 && size(setpmat,2)>21
    %if any of the setpoints changed during automated aquisition
    %due to a new desired flow pattern, save the mean values of the
    %last several data points from the last image acquired before
    %the values get changed

    load(strcat('C:\Users\Bioreactor\Documents\MATLAB\12 Channel F',...
        'low Control\avrgflowmeasurs.mat'));
    load(strcat('C:\Users\Bioreactor\Documents\MATLAB\12 Channel F',...
        'low Control\avrgfinvals.mat'));
    load(strcat('C:\Users\Bioreactor\Documents\MATLAB\12 Channel F',...
        'low Control\avrgflowstds.mat'));
    FlowMeasurements(:,end+1)=mean(b4(:,end-20:end-3),2);
    FinVals(:,end+1)=mean(finmat(:,end-20:end-3),2);
    FlowStdDevs(:,end+1)=std(b4(:,end-20:end-3),0,2);

    if all(FlowMeasurements(:,1)==zeros(numchan,1))
        %when initializing FlowMeasurements and FinVals and FlowStdDevs
        %they are set to vectors of
        %zeros as placeholders.  This removes that placeholder if
        %present
        FlowMeasurements=FlowMeasurements(:,2:end);
        FinVals=FinVals(:,2:end);
        FlowStdDevs=FlowStdDevs(:,2:end);
    end

    save(strcat('C:\Users\Bioreactor\Documents\MATLAB\12 Channel F',...
        'low Control\avrgflowmeasurs.mat'),'FlowMeasurements');
    save(strcat('C:\Users\Bioreactor\Documents\MATLAB\12 Channel F',...
        'low Control\avrgfinvals.mat'),'FinVals');
    save(strcat('C:\Users\Bioreactor\Documents\MATLAB\12 Channel F',...
        'low Control\avrgflowstds.mat'),'FlowStdDevs');

    %confirm new files saved
    flag3=0;
```

```
    pause(0.1)
    save([direc1 'flag3.mat'],'flag3')
    pause(0.1)
end

%Plot and manage pressure at faster time intervals
if ~exist('realtime','var')
    [a1, a2, a3, a4, a5, a7] = PressurePlot(a, a1, a2, a3, a4, a5, ...
        b6, a7, handles, handle_p, 1);
else
    [a1, a2, a3, a4, a5, a7] = PressurePlot(a, a1, a2, a3, a4, a5, ...
        b6, a7, handles, handle_p, 1, 'c', realtime);
end

%add small delay between pressure data point collection
if go~=0
    pause(a3-toc(tStart))
end

if toc(tStart2)>15

    for i=1:numchan
        %update legend with flowrates
        leg{1,i}=['Flow Channel ' num2str(i) ', Flowrate = '...
            sprintf('%0.3f', b4(i,end))];
        set(b5(i),'YData',b4(i,:),'XData',b7,'LineStyle',b9{i},...
            'Marker',b10{i},'LineWidth',1,'color','b');
        drawnow;pause(0.01)
        set(b6,'Visible','on');
        drawnow;pause(0.01)
    end

    %update pressure
    if size(a4,2)~=size(a7,2)
        a4=ones(size(a7))*15;
```

```
            pause(0.2)
        end
        set(a5,'YData',a4,'XData',a7);
        drawnow;pause(0.01)
        set(b6,'Visible','on');

        %Update legend with total flowrate
        leg2{1,1}=['Total Flowrate = '...
            sprintf('%0.3f', c1(end))];
        set(c2,'YData',c1(1,:),'XData',b7,'LineWidth',1,'color','b');
        set(b6,'Visible','on');

        drawnow; pause(0.05)
        tStart2=tic;

    end

    %     toc(tStart)  %Uncomment to check timing of each pressure point
    if double(get(b6,'CurrentCharacter'))==27
        disp('Escape Button Was Pressed')
    end
end
```

B.6 Connecting to Fluigent Flowmeters

This function is called by the flow control function to initialize the connection to the Fluigent flowmeters which read flowrates of every individual channel.

```
function [ handles, numchan ] = FlowMeterConnect( )
%UNTITLED Summary of this function goes here
%   Detailed explanation goes here

addpath(genpath(strcat('C:\Users\bouchard.bouchard-PC\Documents\MATLAB',...
    '\12 Channel Flow Control')));

handles.HandleNumber = 0;
serial.SerialNumber = 0;

% Detect the connected FLOWBOARD
% numb=dec2hex(frp_detect_BA);
numb=frp_detect_BA;

% Open FRP session on both FLOWBOARDs
for i=1:size(numb,1)
    HandleNumber(i) = frp_init_BA(numb(i));
    handles.HandleNumber(i) = HandleNumber(i);
end
%%
% Get the FLOWBOARD serial number
for i=1:size(numb,1)
    SerialNumber(i) = frp_get_fb_sn(handles.HandleNumber(i));
    serial.SerialNumber(i) = SerialNumber(i);

end
%%
% Get the number of connected FLOWUNITs
chk=0;
numchan=0;
for i=1:8
    ErrorCheck = calllib('frp_c','frp_data_FU',...
        HandleNumber(1),i,0,0,zeros(1,32,'uint8'),0,zeros(1,1,'uint8'),...
        zeros(1,1,'uint8'));
    if ErrorCheck~=2
```

```
        numchan=numchan+1;
    end
end

if numchan<8
    chk=1;
end
%%
if size(numb,1)>1
    for i=1:8
        ErrorCheck = calllib('frp_c','frp_data_FU',...
            HandleNumber(2),i,0,0,zeros(1,32,'uint8'),0,zeros(1,1,...
            'uint8'),zeros(1,1,'uint8'));
        if ErrorCheck~=2
            numchan=numchan+1;
        end
    end
end
%%
%set the flowboard with more flow meters to the first position
if chk==1
    handles.HandleNumber=circshift(handles.HandleNumber,[0,1]);
end

end
```

B.7 Connecting to Sensirion Flowmeter

This function is called by the flow control function to initialize the connection to the Sensirion flowmeter which reads the total flowrate passing through the bioreactor.

```
function [handle_p, result_p, broadcast, slaveAddr, scalef ] = ...
    OpenSensirionSensor()
%% Documentation for Sensirion flow sensor with Matlab.
% Created by Noam Ringach
% August 7, 2015.

%% These are the required variables that are needed for the main functions.

global  baud_p  portType resolution; % This makes a few of the needed
%variables global to other methods.

%The pointer to the port handle of the sensor. It does say 32 bit in
%the documentation, but 16 bit works.
handle_p = libpointer('uint16Ptr',uint16(0));
%Port configuration for OpenPort. Change COM4 to a different COM port
%if needed.
portConfig = 'COM4, 115200, EchoOff';
% The pointer of the baudrate
baud_p = libpointer('uint32Ptr', uint32(0));
% The pointer of the result of a single measurement
result_p = libpointer ('int16Ptr', int16(0));
% The signed pointer to the result of a continuous measurement
results_p = libpointer ('int16Ptr', int16(zeros(1,127)));
% The pointer to the length of the returned continuous measurement
length_p = libpointer ('uint8Ptr', uint8(0));
% The interval at which the sensor reads for coninuous measurements, 0
%meaning as fast as possible. Other numbers are in milliseconds, but
%are still limited by the sensor's speed.
interval = uint16(0);
% The pointer to the scale factor of the sensor.
scaleFactor_p = libpointer('uint16Ptr', uint16(0));

portType = uint8(0);     % The port type, which his serial (RS485)
slaveAddr = uint8(0);    % The address of the sensor.
broadcast = uint8(0);    % The broadcast mode, which is set to normal.
```

```
resolution = uint8(16); % The resolution of the sensor, which is set to
%16 bit, but can go as low as 9 bit.

%Adds the path to the needed library to find ShdlcDriver.dll and
%SensorCableDriver.dll
addpath('C:\Program Files\Sensirion AG\SCC1-RS485_Configurator\x86')

%% Load the needed libraries, which should be placed in the path of
%Matlab, or else it won't be able to find it.

% Loads the library that's used to connect to the sensor.
loadlibrary('ShdlcDriver.dll', 'ShdlcDriverShort.h');
% Loads the library that's used to read from the sensor.
loadlibrary('SensorCableDriver.dll', 'SensorCableDriverShort.h');



%% Setting Baudrate, opening the port, and checking sensor

%Setting Baudrate
% Opens the port to the sensor.
calllib('ShdlcDriver', 'OpenPort', portType, portConfig, handle_p);
baud_p.Value;
%Sets baud_p.Value to 115200 (hopefully).
calllib('ShdlcDriver', 'GetBaudrate', handle_p.Value, slaveAddr, baud_p);
baud_p.Value;
%Opening Port
% Opens the port to the sensor.
calllib('ShdlcDriver', 'OpenPort', portType, portConfig, handle_p);
calllib('ShdlcDriver', 'GetBaudrate', handle_p.Value, slaveAddr, baud_p);

%Starting measurement
calllib('SensorCableDriver', 'StartSingleMeasurement', handle_p.Value,...
    broadcast, slaveAddr);
```

```
%% Connect to the sensor and get the Baud Rate to make sure the connection
%is working.

% Both of these functions should return 0 when ran, which means no error.
% Opens the port to the sensor.
calllib('ShdlcDriver', 'OpenPort', portType, portConfig, handle_p);
% Gets the Baudrate of the sensor and saves it to baud_p.
calllib('ShdlcDriver', 'GetBaudrate', handle_p.Value, slaveAddr, baud_p);

% If there is an error, then you can use this to translate it:

error = uint32(0); % Change the 0 to whichever error code you recieved.
calllib('SensorCableDriver', 'TranslateErrorCode', error);

baud_p.Value; % This should return 115200 when ran.


%% Retrieving the scale factor from the sensor.
pause(0.1)
% The scale factor is saved to scaleFactor_p
calllib('SensorCableDriver', 'GetScaleFactor', handle_p.Value, ...
    slaveAddr, scaleFactor_p);
scalef=scaleFactor_p.Value;

end
```

B.8 Analyzing and Plotting Velocity, Flow, and Shear Maps

```
prompt = 'Enter name of folder containing flow data:\n\n    ';
flowfilename = input(prompt,'s');

prompt = '\nEnter name of folder containing no flow data:\n\n    ';
noflowfilename = input(prompt,'s');

%general path for all associated files
addpath(genpath('C:\Users\Brian Archer\Documents\MATLAB\Bouchard Lab'))
% addpath(genpath('C:\Users\Brian Archer\Documents\MATLAB'))
% Obtain parameters from procpar
data=fopen([flowfilename '\procpar'],'r');
parameter=struct('lpe',[],'lro',[],'ni',[],...
    'm1x',[],'m1y',[],'m1z',[],'vencx',[],'vency',[],'vencz',[],'thk',[]);
parameter=readout_procpar(parameter,data);
fclose('all');

lpe=parameter.lpe;
lro=parameter.lro;
ni=parameter.ni;
thk=parameter.thk; %thickness of slice

%first moment of bipolar gradient
m1x=parameter.m1x;
m1y=parameter.m1y;
m1z=parameter.m1z;

%maximum velocities achievable
vencx=parameter.vencx;
vency=parameter.vency;
vencz=parameter.vencz;

% Flow
[r1,~,~]=readfid([flowfilename '\fid'],-1);

gx=r1(:,1:6:end);
```

```
gmx=r1(:,2:6:end);
gy=r1(:,3:6:end);
gmy=r1(:,4:6:end);
gz=r1(:,5:6:end);
gmz=r1(:,6:6:end);

%noise smoothing parameter
ns=30;

lb1=size(gx,1); lb2=size(gx,2); ll1=-round(lb1/2);
ll2=-round(lb2/2); rr1=ll1+lb1-1; rr2=ll2+lb2-1;
[xx, yy]=meshgrid(ll1:rr1,ll2:rr2); gf=exp(-(xx.^2)/(ns^2)-(yy.^2)/(ns^2));

gx=gx.*gf'; gy=gy.*gf'; gz=gz.*gf'; gmx=gmx.*gf'; gmy=gmy.*gf';
gmz=gmz.*gf';

%M1 is set based on the flow weighted gradient strength (G) which is
%fwampy, fwampx, and fwampz
M1x1=2*m1x;
M1y1=2*m1y;
M1z1=2*m1z;

%display "anatomic" image
img=abs(fftshift(ifft2(gmx,size(gx,1),ni)));
% figure;imagesc(img); title('T2w MRI image');
% caxis([0 1.5*mean(img(:))]);colorbar;

% Vx
idiv=fftshift(ifft2(gx,size(gx,1),ni))./fftshift(ifft2(gmx,size(gx,1),ni));
prdiv=angle(idiv);
gamma=2*pi*42.2*100;
vx_flow=prdiv'/gamma/M1x1/100;

% Vy
idiv=fftshift(ifft2(gy,size(gx,1),ni))./fftshift(ifft2(gmy,size(gx,1),ni));
```

```
prdiv=angle(idiv);
gamma=2*pi*42.2*100;
vy_flow=prdiv'/gamma/M1y1/100;
% figure;imagesc(-vy_flow);title('VY - velocity values [m/s]'); colorbar;

% Vz
idiv=fftshift(ifft2(gz,size(gx,1),ni))./fftshift(ifft2(gmz,size(gx,1),ni));
prdiv=angle(idiv);
gamma=2*pi*42.2*100;
vz_flow=prdiv'/gamma/M1z1/100;
% figure;imagesc(-vz_flow);title('VZ - velocity values [m/s]'); colorbar;

%figure; quiver(vy(1:4:end,1:4:end),-vx(1:4:end,1:4:end));

ab=abs(fftshift(ifft2(gz,size(gx,1),ni)))'; %save this for later (the mask)

%%%%%%%%%%%%%%%%%%%%%%%%%%%%%%%%%%%%%%%%%%%%%%%%%%%%%%%%%%%%%%%%%%%%%%%%
% No Flow

[r1,r2,r3]=readfid([noflowfilename '\fid'],-1);

% Obtain parameters from procpar
data=fopen([noflowfilename '\procpar'],'r');
parameter=struct('m1x',[],'m1y',[],'m1z',[],'vencx',[],'vency',[],...
    'vencz',[]);
parameter=readout_procpar(parameter,data);
fclose('all');

%first moment of bipolar gradient
m1xnf=parameter.m1x;
m1ynf=parameter.m1y;
m1znf=parameter.m1z;

%maximum velocities imagable
vencxnf=parameter.vencx;
```

```
vencynf=parameter.vency;
vencznf=parameter.vencz;

gx=r1(:,1:6:end);
gmx=r1(:,2:6:end);
gy=r1(:,3:6:end);
gmy=r1(:,4:6:end);
gz=r1(:,5:6:end);
gmz=r1(:,6:6:end);

gx=gx.*gf'; gy=gy.*gf'; gz=gz.*gf'; gmx=gmx.*gf'; gmy=gmy.*gf';
gmz=gmz.*gf';

M1x1nf=2*m1xnf;
M1y1nf=2*m1ynf;
M1z1nf=2*m1znf;

img1=abs(fftshift(ifft2(gmx,size(gx,1),ni)));
% figure;imagesc(img1); title('T2w MRI image');
% caxis([0 1.5*mean(img1(:))]);colorbar;

% Vx
idiv=fftshift(ifft2(gx,size(gx,1),ni))./fftshift(ifft2(gmx,size(gx,1),ni));
prdiv=angle(idiv);
gamma=2*pi*42.2*100;
vx_noflow=prdiv'/gamma/M1x1nf/100;
% figure;imagesc(-vx_noflow);title('VX No Flow- velocity values [m/s]');
% colorbar;

% Vy
idiv=fftshift(ifft2(gy,size(gx,1),ni))./fftshift(ifft2(gmy,size(gx,1),ni));
prdiv=angle(idiv);
gamma=2*pi*42.2*100;
vy_noflow=prdiv'/gamma/M1y1nf/100;
% figure;imagesc(-vy_noflow);title('VY No Flow- velocity values [m/s]');
```

```
% colorbar;

% Vz
idiv=fftshift(ifft2(gz,size(gx,1),ni))./fftshift(ifft2(gmz,size(gx,1),ni));
prdiv=angle(idiv);
gamma=2*pi*42.2*100;
vz_noflow=prdiv'/gamma/M1z1nf/100;
% figure;imagesc(-vz_noflow);title('VZ No Flow- velocity values [m/s]');
% colorbar;

%%%%%%%%%%%%%%%%%%%%%%%%%%%%%%%%%%%%%%%%%%%%%%%%%%%%%%%%%%%
%%
%Subtract noflow from flow
res_vy=fliplr(rot90(vx_flow-vx_noflow,-1));
res_vx=fliplr(rot90(vy_flow-vy_noflow,-1)); %correct orientation for Julia
res_vz=fliplr(rot90(vz_flow-vz_noflow,-1));

% res_vx=vx_flow-vx_noflow;
% res_vy=vy_flow-vy_noflow; %correct orientation for Julia
% res_vz=vz_flow-vz_noflow;

% figure;imagesc(res_vx);colorbar;title('res-vx');
% figure;imagesc(res_vy);colorbar;title('res-vy');
% figure;imagesc(res_vz);colorbar;title('res-vz');

%Calculate total flow speed
res_speed=sqrt(res_vx.^2 + res_vy.^2 + res_vz.^2);

%Generate mask from signal intensity of flow t2 weighted image
cutoff1=0.5;   %Decreasing cutoff increases the level of noise permissible
cutoff2=2.5;     %No flow image cutoff
coff2=8;
binsize = (max(max(img))-min(min(img)))/20;
noise=zeros(size(r1(:,1:6:end)));
noise(img<=(min(min(img))+cutoff1*binsize))=1; %note where cutoff is
```

```
%included
noise(img1<=(min(min(img1))+cutoff2*binsize))=1; %note where cutoff is
%included
% noise=rot90(noise,-2)';
for i=1:2
noise(res_vx>=(mean2(res_vx(noise~=1))+coff2*std2(res_vx(noise~=1)))...
    |res_vx<=(mean2(res_vx(noise~=1))-coff2*std2(res_vx(noise~=1))))=1;
noise(res_vy>=(mean2(res_vy(noise~=1))+coff2*std2(res_vy(noise~=1)))...
    |res_vy<=(mean2(res_vy(noise~=1))-coff2*std2(res_vy(noise~=1))))=1;
noise(res_vz>=(mean2(res_vz(noise~=1))+coff2*std2(res_vz(noise~=1)))...
    |res_vz<=(mean2(res_vz(noise~=1))-coff2*std2(res_vz(noise~=1))))=1;
% figure;imshow(noise);
end

res_vx_clean=res_vx;
res_vy_clean=res_vy;
res_vz_clean=res_vz;

[u,v] = meshgrid(linspace(-lro/2*10,lro/2*10,size(gx,1)),...
    linspace(-lpe/2*10,lpe/2*10,ni));

%region of interest, slightly smaller than desired
ybottom=round(30/128*size(gx,1));
ytop=round(40/128*size(gx,1));
xright=round(43/128*ni);
xleft=round(43/128*ni);
ybottom=size(gx,1)-ybottom;
xright=ni-xright;
%%
%adjust ROI to make as large as possible without including any noisy (NaN)
%points
j=0;
while j==0
    j=1;
    if ~any(noise(ytop-1,xleft:xright))==1
```

```
        ytop=ytop-1;
        j=0;
    end
    if ~any(noise(ybottom+1,xleft:xright))==1
        ybottom=ybottom+1;
        j=0;
    end
    if ~any(noise(ytop:ybottom,xleft-1))==1
        xleft=xleft-1;
        j=0;
    end
    if ~any(noise(ytop:ybottom,xright+1))==1
        xright=xright+1;
        j=0;
    end

end

%Shave off two more pixels
ytop=ytop+2;
ybottom=ybottom-2;
xleft=xleft+2;
xright=xright-2;

%%
%Plot flow in X direction
res_vx_clean(noise==1)=NaN;
res_vx_small=res_vx_clean(ytop:ybottom,xleft:xright);

% figure('position', [500, 350, lro*500, lpe*300]);img2=imagesc(...
%     v(:,1),u(1,:),flipud(res_vx_clean));
% title('Fluid velocity in X direction (m/s)','FontSize',30);
% set(img2, 'AlphaData', ~isnan(flipud(res_vx_clean)))
% xlabel('Distance (mm)'); ylabel('Distance (mm)');
% set(gca,'YDir','normal','FontSize',24); %Fix direction of Y axis
```

```
% colorbar;caxis([nanmean(res_vx_small(:))-1.7*...
%     nanstd(res_vx_small(:)) nanstd(res_vx_small(:))+1.7*...
%     nanstd(res_vx_small(:))]);
% palate=colormap;
% colormap(palate);
% axis image

%Plot flow in X direction zoomed into region of interest
figure('position', [500, 350, lro*500, lpe*300]);img2=imagesc(v(...
    :,1)*(xright-xleft)/ni,...
    u(1,:)*(ybottom-ytop)/size(gx,1),flipud(res_vx_small));
title('Fluid velocity in X direction (m/s)','FontSize',30);
xlabel('Distance (mm)'); ylabel('Distance (mm)');
set(img2, 'AlphaData', ~isnan(flipud(res_vx_small)))
set(gca,'YDir','normal','FontSize',24); %Fix direction of Y axis
colorbar;caxis([nanmean(res_vx_small(:))-1.7*...
    nanstd(res_vx_small(:)) nanmean(res_vx_small(:))+1.7*nanstd(...
    res_vx_small(:))]);
palate=colormap;
colormap(palate);
axis image

%%
%Plot flow in Y direction
res_vy_clean(noise==1)=NaN;
res_vy_small=res_vy_clean(ytop:ybottom,xleft:xright);

% figure('position', [500, 350, lro*500, lpe*300]);img2=imagesc(...
%     v(:,1),u(1,:),flipud(res_vy_clean));
%     title('Fluid velocity in Y direction (m/s)','FontSize',30);
% xlabel('Distance (mm)'); ylabel('Distance (mm)');
% set(img2, 'AlphaData', ~isnan(flipud(res_vy_clean)))
% set(gca,'YDir','normal','FontSize',24); %Fix direction of Y axis
% colorbar;caxis([nanmean(res_vy_small(:))-1.7*...
%     nanstd(res_vy_small(:)) nanstd(res_vy_small(:))+1.7*...
```

```
%     nanstd(res_vy_small(:))]);
% palate=colormap;
% colormap(palate);
% axis image

%Plot flow in Y direction zoomed into region of interest
figure('position', [500, 350, lro*500, lpe*300]);img2=imagesc(...
    v(:,1)*(xright-xleft)/ni,...
    u(1,:)*(ybottom-ytop)/size(gx,1),flipud(res_vy_small));
title('Fluid velocity in Y direction (m/s)','FontSize',30);
xlabel('Distance (mm)'); ylabel('Distance (mm)');
set(img2, 'AlphaData', ~isnan(flipud(res_vy_small)))
set(gca,'YDir','normal','FontSize',24); %Fix direction of Y axis
colorbar;caxis([nanmean(res_vy_small(:))-1.7*...
    nanstd(res_vy_small(:)) nanmean(res_vy_small(:))+1.7*...
    nanstd(res_vy_small(:))]);
palate=colormap;
colormap(palate);
axis image

%%
%Plot flow in Z direction
res_vz_clean(noise==1)=NaN;
res_vz_small=res_vz_clean(ytop:ybottom,xleft:xright);

% figure('position', [500, 350, lro*500, lpe*300]);img2=imagesc(...
%     v(:,1),u(1,:),flipud(res_vz_clean));
% title('Fluid velocity in Y direction (m/s)','FontSize',30);
% xlabel('Distance (mm)'); ylabel('Distance (mm)');
% set(img2, 'AlphaData', ~isnan(flipud(res_vz_clean)))
% set(gca,'YDir','normal','FontSize',24); %Fix direction of Y axis
% colorbar;caxis([nanmean(res_vz_small(:))-1.7*...
%     nanstd(res_vz_small(:)) nanstd(res_vz_small(:))+1.7*...
%     nanstd(res_vz_small(:))]);
% palate=colormap;
```

```
% colormap(palate);
% axis image

%Plot flow in Z direction zoomed into region of interest
figure('position', [500, 350, lro*500, lpe*300]);img2=imagesc(...
    v(:,1)*(xright-xleft)/ni,...
    u(1,:)*(ybottom-ytop)/size(gx,1),flipud(res_vz_small));
title('Fluid velocity in Z direction (m/s)','FontSize',30);
xlabel('Distance (mm)'); ylabel('Distance (mm)');
set(img2, 'AlphaData', ~isnan(flipud(res_vz_small)))
set(gca,'YDir','normal','FontSize',24); %Fix direction of Y axis
colorbar;caxis([nanmean(res_vz_small(:))-1.7*...
    nanstd(res_vz_small(:)) nanmean(res_vz_small(:))+1.7*nanstd(...
    res_vz_small(:))]);
palate=colormap;
colormap(palate);
axis image

%%
%Plot Total Flow Speed

%Set noisy regions to a negative number which will be viewed as black
res_speed1=res_speed;
res_speed1(noise==1)=NaN;
res_speed1_small=res_speed1(ytop:ybottom,xleft:xright);

figure('position', [500, 350, lro*500, lpe*300]);img2=imagesc(...
    v(:,1),u(1,:),flipud(res_speed1));
title('Total Flow Speed (m/s)','FontSize',30);
set(img2, 'AlphaData', ~isnan(flipud(res_speed1)))
xlabel('Distance (mm)'); ylabel('Distance (mm)');
set(gca,'YDir','normal','FontSize',24); %Fix direction of Y axis
colorbar;caxis([nanmean(res_speed1_small(:))-1.7*nanstd(...
    res_speed1_small(:)) nanmean(res_speed1_small(:))+1.7*...
    nanstd(res_speed1_small(:))]);
```

```
palate=colormap;
colormap(palate);
axis image

%Plot total flow speed zoomed into region of interest
res_speed1(noise==1)=NaN;
figure('position', [500, 350, lro*500, lpe*300]);img2=imagesc(...
    v(:,1)*(xright-xleft)/ni,u(1,:)*(ybottom-ytop)/size(gx,1),...
    flipud(res_speed1_small));
title('Total Flow Speed (m/s)','FontSize',30);
xlabel('Distance (mm)'); ylabel('Distance (mm)');
set(img2, 'AlphaData', ~isnan(flipud(res_speed1_small)))
set(gca,'YDir','normal','FontSize',24); %Fix direction of Y axis
colorbar;caxis([nanmean(res_speed1_small(:))-1.7*nanstd(...
    res_speed1_small(:)) nanmean(res_speed1_small(:))+1.7*...
    nanstd(res_speed1_small(:))]);
palate=colormap;
colormap(palate);
axis image
% *(xright-xleft)/ni
% *(ybottom-ytop)/size(gx,1)
%%
%Quiver Plot

figure('position', [500, 350, lro*500, lpe*300]);
    quiver(v(xleft:xright,1),u(1,ytop:ybottom),flipud(res_vx_small),...
        flipud(res_vy_small),2.5);
xlabel('Distance (mm)'); ylabel('Distance (mm)');
title('Flow Vector Plot','FontSize',30)
set(gca,'FontSize',24);
axis image

%Thinned out quiver plot
%scale factors
sf1=0.4; %rows
```

```
sf2=0.6; %columns
res_vx_clean_thin=imresize(res_vx_small, [size(res_vx_small,1)*...
    sf1 size(res_vx_small,2)*sf2]);
res_vy_clean_thin=imresize(res_vy_small, [size(res_vx_small,1)*...
    sf1 size(res_vx_small,2)*sf2]);
refference=(res_vx_clean_thin.^2+res_vy_clean_thin.^2).^(1/2);
mn=mean2((res_vx_clean_thin.^2+res_vy_clean_thin.^2).^(1/2));
st=std2((res_vx_clean_thin.^2+res_vy_clean_thin.^2).^(1/2));
% res_vx_clean_thin(refference<mn-0.8*st)=NaN;
% res_vx_clean_thin(refference<mn-0.8*st)=NaN;

[s,t] = meshgrid(linspace(-lro/2*10*(ybottom-ytop)/size(gx,1),lro/2*10*...
    (ybottom-ytop)/size(gx,1),size(res_vx_clean_thin,2)),linspace(...
    -lpe/2*10*(xright-xleft)/ni,lpe/2*10*(xright-xleft)/ni,...
    size(res_vx_clean_thin,1)));

    ss=figure('position', [500, 350, lro*1000, lpe*600]);
    quiverc(s,t,flipud(res_vx_clean_thin),flipud(res_vy_clean_thin))%,...
   %     'LineWidth',1.5,'MaxHeadSize',0.8,'AutoScale','on',...
   %     'AutoScaleFactor',1.2,'AlignVertexCenters','on',...
   %     'ShowArrowHead','off');
xlabel('Distance (mm)'); ylabel('Distance (mm)');
title('Flow Vector Plot','FontSize',30)
set(gca,'FontSize',24);
%set(gcf, 'InvertHardCopy', 'off')
axis image
hgexport(gcf, 'Untitled.svg', hgexport('factorystyle'), 'Format', 'svg');

%% Calculate and plot shear map
r_vx=res_vx; r_vy=res_vy;
rvx=imresize(r_vx,[size(gx,1) ni]);
rvy=imresize(r_vy,[size(gx,1) ni]);
dx=((lpe/100)/ni); % x direction voxel dimension in meters
dy=((lro/100)/size(gx,1)); % y direction voxel dimension in meters
dxvy=diff(r_vy,1,2)/dx; %difference in y velocity values between
```

```
%adjacent columns (x direction differences) divided by x voxel dimension
dyvx=diff(r_vx,1,1)/dy; %difference in x velocity values between
%adjacent rows (y direction differences) divided by y voxel dimension
dxvy=imresize(dxvy,[size(gx,1) ni]);
dyvx=imresize(dyvx,[size(gx,1) ni]);
smap=(dxvy+dyvx)/2; % shear map (raw)
smap=abs(smap);
smap(noise==1)=NaN;
uvis=6.92e-4;
smap_small=smap(ytop:ybottom,xleft:xright);
%convert shear rate to shear stress
smap_small=smap_small*uvis;
smap_small_smooth=imresize(imresize(smap_small,[3,3]),[size(gx,1),ni]);

% figure('position', [500, 350, lro*500, lpe*300]);img2=imagesc(...
%     v(:,1)*(xright-xleft)/ni,u(1,:)*(ybottom-ytop)/size(gx,1),...
%     flipud(smap_small));
% title('Shear Stress','FontSize',30);
% xlabel('Distance (mm)'); ylabel('Distance (mm)');
% set(img2, 'AlphaData', ~isnan(flipud(smap_small)))
% set(gca,'YDir','normal','FontSize',24); %Fix direction of Y axis
% if nanmean(smap_small(:))-1.7*nanstd(smap_small(:))>0
% gg=colorbar;caxis([nanmean(smap_small(:))-1.7*...
%     nanstd(smap_small(:)) nanmean(smap_small(:))+1.7*...
%     nanstd(smap_small(:))]);
% else
%     gg=colorbar;caxis([0 nanmean(smap_small(:))+1.7*nanstd(...
%     smap_small(:))]);
% end
% ylabel(gg,'Shear Stress (dyn/cm^{2})');
% palate=colormap;
% colormap(palate);
% axis image
% set(colorbar,'fontsize',24);
% %%
```

```
% figure('position', [500, 350, lro*500, lpe*300]);img2=imagesc(...
%     v(:,1)*(xright-xleft)/ni, u(1,:)*(ybottom-ytop)/size(gx,1),...
%     flipud(smap_small_smooth));
% title('Smoothed Shear Stress','FontSize',30);
% xlabel('Distance (mm)'); ylabel('Distance (mm)');
% set(img2, 'AlphaData', ~isnan(flipud(smap_small_smooth)))
% set(gca,'YDir','normal','FontSize',24); %Fix direction of Y axis
% if nanmean(smap_small(:))-1.7*nanstd(smap_small(:))>0
%     gg=colorbar;caxis([nanmean(smap_small(:))-1.7*...
%     nanstd(smap_small(:)) nanmean(smap_small(:))+1.7*...
%     nanstd(smap_small(:))]);
% else
%     gg=colorbar;caxis([0 nanmean(smap_small(:))+1.7*...
%     nanstd(smap_small(:))]);
% end
% ylabel(gg,'Shear Stress (dyn/cm^{2})');
% palate=colormap;
% colormap(palate);
% axis image
% set(colorbar,'fontsize',24);


%%
%Shear estimate in pores
epsilon=0.9; %void fraction in sponge
V=dy*dx*thk; %volume of voxel
R=150e-6; %pore size in m
uvis=6.92e-4; %dynamic viscosity of cell culture media in kg/(m*s)
theta1=atand(res_vy_small./res_vx_small);
theta2=atand(res_vx_small./res_vy_small);
W=dy*cosd(theta1)+dx*cosd(theta2);
L=dx*cosd(theta1)+dy*cosd(theta2);
Q=(res_vx_small.^2+res_vy_small.^2).^(1/2).*W*thk;
v_pi=2*L.*Q/(epsilon*V);
gammapore=uvis*4*v_pi/R*10; %shear stress on walls of sponge converted
```

```
%to dyn/cm^2

figure('position', [500, 350, lro*500, lpe*300]);img2=imagesc(...
    v(:,1)*(xright-xleft)/ni, u(1,:)*(ybottom-ytop)/size(gx,1),...
    flipud(gammapore));
title('Wall Shear in Pores','FontSize',30);
xlabel('Distance (mm)'); ylabel('Distance (mm)');
set(img2, 'AlphaData', ~isnan(flipud(gammapore)))
set(gca,'YDir','normal','FontSize',24); %Fix direction of Y axis
if nanmean(nanmean(gammapore(:))-1.7*nanstd(gammapore(:)))>0
gg=colorbar;caxis([nanmean(gammapore(:))-1.7*...
    nanstd(gammapore(:)) nanmean(gammapore(:))+1.7*nanstd(gammapore(:))]);
else
    gg=colorbar;caxis([0 nanmean(gammapore(:))+1.7*nanstd(gammapore(:))]);
end
ylabel(gg,'Wall Shear (dyn/cm^{2})');
palate=colormap;
colormap(palate);
axis image

%%
gammapore_smooth=imresize(imresize(gammapore,[3,3]),size(gammapore));
figure('position', [500, 350, lro*500, lpe*300]);img2=imagesc(...
    v(:,1)*(xright-xleft)/ni, u(1,:)*(ybottom-ytop)/size(gx,1),...
    flipud(gammapore_smooth));
title('Pore Wall Shear Distribution','FontSize',30);
xlabel('Distance (mm)'); ylabel('Distance (mm)');
set(img2, 'AlphaData', ~isnan(flipud(gammapore)))
set(gca,'YDir','normal','FontSize',24); %Fix direction of Y axis
% if nanmean(nanmean(gammapore(:))-1.7*nanstd(gammapore(:)))>0
% gg=colorbar;caxis([nanmean(gammapore(:))-1.7*...
%     nanstd(gammapore(:)) nanmean(gammapore(:))+1.7*...
%     nanstd(gammapore(:))]);
% else
%     gg=colorbar;caxis([0 nanmean(gammapore(:))+1.7*...
```

```
%         nanstd(gammapore(:))]);
% end
gg=colorbar;caxis([nanmean(gammapore_smooth(:))-2.3*...
    nanstd(gammapore_smooth(:)) nanmean(gammapore_smooth(:))+2.5*...
    nanstd(gammapore_smooth(:))]);
ylabel(gg,'Wall Shear (dyn/cm^{2})');
palate=colormap;
colormap(palate);
axis image
```

B.9 Analyzing and Cell Density and Viability from Diffusion and Magnetization Transfer Data

```
%Plots STEMS image data from the pulse sequence stems_tn_pulsed which can
%be used to acquire T2-, diffusion-, T1, or MT- weighted images.  Two
%images need to be acquired.  One should be optimized for best contrast
%(using an appropriate b-value or offset frequency) and the other should be
%a reference image that generates a large signal (for example, using no
% diffusion-weighting gradients in a diffusion-weighted image or using a
% 200000 Hz saturation pulse offset difference in MT-weighted images, etc.)
% Program allows users to select regions of interest (ROIs) of areas with
% known cell density and viablity.  Pairwise comparisons are made between
% the regions of interest to determine if there is a statistically
% significant difference in the quantity of signal.

%If a diffusion- and MT-weighted image are acquired, this program can be
%used to calibrate cell density and viabiity to diffusion- and MT-weighted
%signal and generate images of cell density and viability.

% prompt = strcat('Enter name of folder containing resolved signal ',...
%     'data:\n\n    ');
% filename = input(prompt,'s');
%
% prompt = strcat('Enter name of folder containing maximum relative',...
%     'signal data:\n\n    ');
% filename2 = input(prompt,'s');
%
% prompt = strcat('Enter number corresponding to weighting:\n\n    ',...
%     '1. T1\n    2. T2\n    3. Diffusion\n    4. MT\n\n');
% wtyp = input(prompt);

filename = '20200924_DiffContrast.fid';
filename2 = '20200924_DiffMax.fid';
wtyp=3;
% filename = '20200924_MT3300Contrast.fid';
% filename2 = '20200924_MTMax.fid';
% wtyp=4;
load('optmask2_20200924.mat')
```

```
load('optmask20200924.mat')

% filename = '20201012_DiffContrast.fid';
% filename2 = '20201012_DiffMax.fid';
% wtyp=3;
% % filename = '20201012_MT3300Contrast.fid';
% % filename2 = '20201012_MTMax.fid';
% % wtyp=4;
% load('optmask2_20201012.mat')
% load('optmask20201012.mat')

% filename = '20201013_DiffContrast.fid';
% filename2 = '20201013_DiffMax.fid';
% wtyp=3;
% % filename = '20201013_MT3300Contrast.fid';
% % filename2 = '20201013_MTMax.fid';
% % wtyp=4;
% load('optmask2_20201013.mat')
% load('optmask20201013.mat')

if wtyp==1
    str='T1';
elseif wtyp==2
    str='T2';
elseif wtyp==3
    str='Diffusion';
elseif wtyp==4
    str='MT';
end

%general path for all associated files
addpath(genpath('C:\Users\Brian Archer\Documents\MATLAB\Bouchard Lab'))

%get screen size for figure positioning
scsz = get( 0, 'ScreenSize' );
```

```
data=fopen([filename '\procpar'],'r');
parameter=struct('lpe',[],'lro',[],'ppe',[],'pro',[],'ni',[],'thk',[],...
    'nv',[],'np',[],'ns',[],'ct',[]);
parameter=readout_procpar(parameter,data);
fclose('all');

lpe=parameter.lpe; %width of slide (cm)
lro=parameter.lro; %length of slide (cm)
ppe=parameter.ppe; %offset in y direction (cm)
pro=parameter.pro; %offset in x direction (cm)
ni=parameter.ni; %size of matrix in pixels
thk=parameter.thk; %thickness of slices
pep=parameter.nv; %number of pixels in phase encode direction
fep=parameter.np/2; %number of pixels in frequency encode direction
ns=parameter.ns; %number of slices
ct1=parameter.ct; %number of averages

data=fopen([filename2 '\procpar'],'r');
parameter2=struct('ct',[]);
parameter2=readout_procpar(parameter2,data);
fclose('all');

ct2=parameter2.ct; %number of averages

%Figure dimensions and position based on screen size and image size:
if lpe/lro > (scsz(4)-150)/(scsz(3)-100)
    fb3=50; %figure position from bottom of screen
    figh=scsz(4)-150; %figure height
    figw=round(figh*lro/lpe)+200; %figure width
    fb1=round(scsz(3)/2-figw/2); %distance from sides of screen
else
    fb1=50; %distance from sides of screen
    figw=scsz(3)-150; %figure width
    figh=round(figw*lpe/lro)+200; %figure height
```

```
    fb3=round(scsz(4)/2-figh/2);
end

pos=[fb1,fb3,figw,figh]; %figure positioning requirements for full image

[r1,~,~,~]=readfid([filename '\fid'],-1);
[r2,~,~,~]=readfid([filename2 '\fid'],-1);

scli=zeros(pep,fep);
scli2=zeros(pep,fep);
for i=1:pep
    scli(i,:)=r1(fep*(i-1)+1:fep*i,:);
end

for i=1:pep
    scli2(i,:,ns)=r2(fep*(i-1)+1:fep*i,:);
end


img1=rot90(abs(fftshift(ifft2(scli))));
img2=rot90(abs(fftshift(ifft2(scli2))));

%Crop Images:
%set the number of pixels to crop
%Some cropping parameters that I liked and have already determined (feel
%free to add more to the list):
if strcmp(filename(1:8),'20200924')
    vdftop=31; %vertical pixels to crop off top (minimum 0)
    vdfbottom=18; %vertical pixels to crop off bottom (minimum 1)
elseif strcmp(filename(1:8),'20201013')
    vdftop=34; %vertical pixels to crop off top (minimum 0)
    vdfbottom=15; %vertical pixels to crop off bottom (minimum 1)
elseif strcmp(filename(1:8),'20201012')
    vdftop=31; %vertical pixels to crop off top (minimum 0)
    vdfbottom=18; %vertical pixels to crop off bottom (minimum 1)
```

```
end
%%
% crop the images in vertical direction
img1crop=img1(vdfbottom:end-vdftop,:);
img2crop=img2(vdfbottom:end-vdftop,:);

%Normalize signal intensity to max signal indensity S/S_0 where S is the
%contrast signal and S_0 is the signal of maximum intensity
img3=img1crop./img2crop;
img3=(img1crop./ct1)./(img2crop./ct2);
img3a=img3;

%in case of extreme outliers
img3a(img3>mean(img3(:))+3*std(img3(:)))=NaN;
img3a(img3<mean(img3(:))-6*std(img3(:)))=NaN;
img3=img3a;
% figure;imagesc(img3a)

%%
%Filter out noisy background pixels
%initialize noise mask to be size of cropped image
noise=ones(size(img1crop));

%remove pixels which are definitely out of range of the NMR tube
%for 64 width image; adjust as needed
noise(:,end-20:end)=0;
noise(:,1:18)=0;

%for 32 width image; adjust based on actual image
% noise(:,end-8:end)=0;
% noise(:,1:10)=0;

%Normalization should cap the signal at 1, remove anything much greater
%than 1
noise(img3>1.3)=0;
```

```
%Using the max intensity image, remove pixels with a low intensity since
%they do not have any sample present
if wtyp==4
    stdfactor=0.3; %MT
elseif wtyp==3
    stdfactor=0.2; %Diff
elseif wtyp==2;
    stdfactor=0; %T2
end
noise(img2crop<nanmean(img2crop(:))-stdfactor*nanstd(img2crop(:)))=0;

img3(noise==0)=NaN;
% figure;imagesc(img3)
%%
if strcmp(filename(1:8),'20200924')
    shiftfactor=1; %more positive shifts image right, cannot be 0
elseif strcmp(filename(1:8),'20201013')
    shiftfactor=1;
elseif strcmp(filename(1:8),'20201012')
    shiftfactor=0;
end

%shift image horizontally
img4=zeros(size(img3));
if shiftfactor>0;
    img4(:,1:shiftfactor)=img3(:,end-shiftfactor+1:end);
    img4(:,shiftfactor+1:end)=img3(:,1:end-shiftfactor);
elseif shiftfactor<0;
    img4(:,1:end+shiftfactor)=img3(:,-shiftfactor+1:end);
    img4(:,end+shiftfactor+1:end)=img3(:,1:-shiftfactor);
elseif shiftfactor==0;
    img4=img3;
end
% figure;imagesc(img4)
```

```
%%
% for i=1:128
%     for j=1:128
%         if (img2(i,j)>3*img2(i+2,j)&&img2(i,j)>3*img2(i-2,j)&&...
%                 img2(i,j)>3*img2(i,j+2)&&img2(i,j)>3*img2(i,j-2))||...
%             (img2(i,j)<3*img2(i+2,j)&&img2(i,j)<3*img2(i-2,j)&&...
%                 img2(i,j)<3*img2(i,j+2)&&img2(i,j)<3*img2(i,j-2))
%             noise(i,j)=0;
%         end
%     end
% end

% %Correct for gradient in baseline/max image
% pos2=[fb1,fb3,figw*2,figh]; %figure positioning requirements for
% %editable image
% % tempcor=Adjust_Intensity(pos2,img2a);
% tempcor=0;
%
% strat=linspace(1-tempcor,1+tempcor,size(img2a,1))'*ones(1,size(img2a,2));
% img2a=img2a.*strat;
% img1a=img1a.*strat;
% img3=img2a-img1a;
%
% %normalize subtracted image to 1
% % img3=(img3-min(img3(:)))/(max(img3(:))-min(img3(:)));
% % img3=1-img3;
%
% img3(noise==0)=NaN;

% img5=img4;
%
% %number of outlier pixels to filter out of upper range:
% toprepix=40; %minimum 1
% %number of pixels to filter out of lower range:
% botrepix=10; %minimum 0
```

```
%
% % filter out outliers to enhance contrast
% [svals,idx] = sort(img5(~isnan(img5)),'descend'); % sort to vector
% img7a=(img5-svals(end-botrepix))/(svals(toprepix)-svals(end-botrepix));
% % img7a=img7;
% figure;imagesc(img7a)
%%
%Plot image to select ROIs
[u,v] = meshgrid(linspace(-lpe/2*10,lpe/2*10,pep),linspace(-lro/2*10,...
    lro/2*10,fep));
figure('position', pos);
g=imagesc(u(1,:),v(vdfbottom:end-vdftop,1),img4);hold on
set(gca,'YDir','normal'); %Fix direction of Y axis
set(g, 'AlphaData', ~isnan(img4))
xlabel('X [mm]'); ylabel('Y [mm]'); title([str ' Weighted Signal'])
set(gca,'FontSize',11)
colorbar
% caxis([0 1])
numticks('y',5,-lro/2*10,lro/2*10)
axis image
%%
%manual selection of ROIs for linear conversion
loopgo='y';
i=1;

%I saved some ROIs which can be reloaded (example: optmask20200924.mat)
if (exist('optmask', 'var')) %if a set of ROIs already exists, inquire
    %if the user would like to use it
    prompt = strcat('\nWould you like to use previous ROIs for this an',...
        'alysis (y/n)?\n\n    ');
    name = input(prompt,'s');  %first input
    if name=='n' %if user does not want to use existing ROIs
        clear optmask; %clear existing ROIs
    end
end
```

```
if (exist('optmask2', 'var')) %if a set of ROIs already exists, inquire if
    %the user would like to use it
    prompt = strcat('\nWould you like to use previous background ROI f',...
        'or this analysis (y/n)?\n\n    ');
    name = input(prompt,'s');  %first input
    if name=='n' %if user does not want to use existing ROIs
        clear optmask2; %clear existing ROIs
    end
end

if (~exist('optmask', 'var')) %run if there are no existing ROIs
    prompt = '\nEnter number of ROIs for this analysis.\n\n    ';
    %ask how many new ROIs
    numROIs = input(prompt);  %first input
    optmask=cell(1,numROIs);

    for i=1:numROIs% loopgo~='n';

        fprintf('\nSelect ROI (drag an ellipse) of concentration \n')
        ROI=imellipse;
        mask=createMask(ROI);
        optmask{i}=mask;
    end
end

if (~exist('optmask2', 'var')) %run if there are is no background ROI
    fprintf('\nDraw Freehand ROI around acellular agarose region \n')
    ROI=imfreehand;
    mask2=createMask(ROI);
    optmask2{1}=mask2;
end

maskbound=NaN(size(img4));
for i=1:size(optmask,2)
```

```
    B=bwboundaries(optmask{i});
    bb=B{1};
    for j=1:size(bb,1)
        maskbound(bb(j,1),bb(j,2))=1;
    end
end

conc_signal=zeros(1,size(optmask,2));
conc_signal2=zeros(1,size(optmask2,2));
conc_signal_std=zeros(1,size(optmask,2));
conc_signal_stderr=zeros(1,size(optmask,2));
conc_signal_weight=zeros(1,size(optmask,2));
signal_stats=cell(1,size(optmask,2));

%determine the mean value of the agarose reference region
img4a=img4;
img4a(~optmask2{1})=NaN;
conc_signal2(1)=nanmean(img4a(:));
signal_stats2{1}=img4a(~isnan(img4a)); %structure saving the pixel values
%for statistical analysis
if wtyp==3
    save(['DiffBGSignal' filename(1:8) '.mat'],'conc_signal2')
elseif wtyp==4
    save(['MTBGSignal' filename(1:8) '.mat'],'conc_signal2')
end
flag=1
%subtract acellular reference signal
img5=img4-conc_signal2(1);
% figure;imagesc(img5)

%determine mean values in ROIs of layers
for i=1:size(optmask,2)
    img5a=img5;
    img5a(~optmask{i})=NaN;
    conc_signal(i)=nanmean(img5a(:));
```

```
    signal_stats{i}=img5a(~isnan(img5a)); %structure saving the pixel
    %values for statistical analysis
    % conc_signal_std(i)=std(img7b(:),'omitnan');
    conc_signal_std(i)=std(img5a(~isnan(img5a)));
    conc_signal_stderr(i)=conc_signal_std(i)/(size(img5a(~isnan(...
        img5a)),1))^(1/2);
    conc_signal_weight(i)=1/nanvar(img5a(:));
end

%determin mean value of agarose background signal
img5a=img5;
img5a(~optmask2{1})=NaN;
conc_signal_blank=nanmean(img5a(:));
conc_signal_blank_stderr=std(img5a(~isnan(img5a)))/(size(img5a(...
    ~isnan(img5a)),1))^(1/2);

%%
if strcmp(filename(1:8),'20200924')
    cellcon=[2e8, 2e8, 1e8, 1e8];
    cellvia=[100, 50, 100, 50];
elseif strcmp(filename(1:8),'20201012')
    cellcon=[2e8, 2e8, 2e8, 2e8];
    cellvia=[100, 66.6, 33.3, 0];
elseif strcmp(filename(1:8),'20201013')
    cellcon=[2e8, 1e8, 5e7, 2.5e7];
    cellvia=[100, 100, 100, 100];
else
    prompt = strcat('\nEnter Concentrations of ROIs in order of layers',...
        'selected as [C1, C2, C3...]\n\n    ');
    cellcon = input(prompt);
    prompt = strcat('\nEnter Viabilities of ROIs in order of layers se',...
        'lected as [V1, V2, V3...]\n\n    ');
    cellvia = input(prompt);
end
%%
```

```
%ANOVA
y=signal_stats{1};
g1=ones(size(signal_stats{1}'))*cellcon(1);
g2=ones(size(signal_stats{1}'))*cellvia(1);
for i=2:size(signal_stats,2)
    y=[y; signal_stats{i};];
    g1=[g1 ones(size(signal_stats{i}'))*cellcon(i)];
    g2=[g2 ones(size(signal_stats{i}'))*cellvia(i)];
end

if range(g1) == 0
    [p,tbl,stats]=anova1(y,g2);
    multcompare(stats)
elseif range(g2) == 0
    [p,tbl,stats]=anova1(y,g1);
    multcompare(stats)
else
    %          [p,tbl,stats]=anovan(y,{g1,g2},'model','full')
    [p,tbl,stats]=anovan(y,{g1,g2});
    multcompare(stats,'Dimension',[1 2])
end

%%
%generate bar plot of viabilities in groupings of cell concentration
uniquecellcon=unique(cellcon); %determine all unique cell concentrations
%in sample layers
uniquecellvia=unique(cellvia); %determine all unique cell viabilities
%in sample layers
%pre aloquot space in matrices
labels=cell(1,size(uniquecellcon,2));
leg=cell(1,size(uniquecellvia,2));
conc=NaN(size(uniquecellcon,2),size(uniquecellvia,2));
viability=NaN(size(uniquecellcon,2),size(uniquecellvia,2));
signal=NaN(size(uniquecellcon,2),size(uniquecellvia,2));
signalstd=NaN(size(uniquecellcon,2),size(uniquecellvia,2));
```

```
signalstderr=NaN(size(uniquecellcon,2),size(uniquecellvia,2));

for i=1:size(uniquecellcon,2) %for each unique cell concentration
    for j=1:size(uniquecellvia,2) %for each unique cell viability
        %make matrix with corresponding measured signal at each cell
        %concentration/viability combo
        if ~isempty(conc_signal(cellcon==uniquecellcon(i)&cellvia==...
                uniquecellvia(j)))
            signal(i,j)=conc_signal(cellcon==uniquecellcon(i)&cellvia==...
                uniquecellvia(j));
            conc(i,j)=cellcon(cellcon==uniquecellcon(i)&cellvia==...
                uniquecellvia(j));
            viability(i,j)=cellvia(cellcon==uniquecellcon(i)&cellvia==...
                uniquecellvia(j));
            signalstd(i,j)=conc_signal_std(cellcon==uniquecellcon(i)&...
                cellvia==uniquecellvia(j));
            signalstderr(i,j)=conc_signal_stderr(cellcon==...
                uniquecellcon(i)&cellvia==uniquecellvia(j));
            if i==1;
                leg{1,j}=[num2str(uniquecellvia(j)) ' %'];
            end
        end
    end
    labels{1,i}=num2str(uniquecellcon(i)/1e8);
end

%%
% leg{1,i}=[num2str(uniquecellvia(i)) ' %'];
%make the bar plot
figure;

%if there is only one group nanpad to trick bar into thinking there are
%multiple groups
if isrow(signal);
    signal1 = vertcat(signal,nan(size(signal)));
```

```
    b = bar(signal1, 'grouped');
    xlim([0.5 1.5]) %know this to be true if no x
else
    b = bar(signal, 'grouped');
end
%%For MATLAB R2019a or earlier releases
hold on
% Find the number of groups and the number of bars in each group
ngroups = size(signal, 1);
nbars = size(signal, 2);
% Calculate the width for each bar group
groupwidth = min(0.8, nbars/(nbars + 1.5));
% Set the position of each error bar in the centre of the main bar
% Based on barweb.m by Bolu Ajiboye from MATLAB File Exchange
for i = 1:nbars
    % Calculate center of each bar
    x = (1:ngroups) - groupwidth/2 + (2*i-1) * groupwidth / (2*nbars);
    %error bars are standard deviaiton
%         errorbar(x, signal(:,i), signalstd(:,i), 'k', 'linestyle',...
%             'none','LineWidth',1.5);
    %error bars are standard error
    errorbar(x, signal(:,i), signalstderr(:,i), 'k', 'linestyle',...
        'none','LineWidth',1.5);
end
xlabel('Cell Density (108 cells.mL-1)');
ylabel(['Normalized ' str ' Weighted Signal'])
set(gca, 'XTickLabel', labels);
lgd=legend(leg);
% lgd.Title.String='Cell Viability';
% title(lgd,'Cell Viability')
hold off

%%
%allows user to make aesthetic adjustments to image.
AdjustImage( lpe, pep, lro, fep, pos, vdfbottom, vdftop, img5, str,...
```

```
    maskbound, cellcon, cellvia, optmask, wtyp )

if wtyp==3
    %for Diffusion
    Diff.V=[reshape(viability,1,size(viability,1)*size(viability,2))';0];
    Diff.C=[reshape(conc,1,size(conc,1)*size(conc,2))';0];
    Diff.S=[reshape(signal,1,size(signal,1)*size(signal,2))';...
        conc_signal_blank];
    Diff.error=[reshape(signalstderr,1,size(signalstderr,1)*...
        size(signalstderr,2))';conc_signal_blank_stderr];
    Diff.image=img5;
    save(['DiffusionData' filename(1:8) '.mat'],'Diff')
elseif wtyp==4
    %for MT
    MT.V=[reshape(viability,1,size(viability,1)*size(viability,2))';0];
    MT.C=[reshape(conc,1,size(conc,1)*size(conc,2))';0];
    MT.S=[reshape(signal,1,size(signal,1)*size(signal,2))';...
        conc_signal_blank];
    MT.error=[reshape(signalstderr,1,size(signalstderr,1)*...
        size(signalstderr,2))';conc_signal_blank_stderr];
    MT.image=img5;
    save(['MTData' filename(1:8) '.mat'],'MT')
end

%%
if exist(['MTData' filename(1:8) '.mat'],'file')==2 && ...
        exist(['DiffusionData' filename(1:8) '.mat'],'file')==2
    %%
    %This can be used to generate an image of cell viability and cell
    %density from diffusion- and MT-weighted images.  Before running this
    %program, diffusion- and MT-weighted images must have been acquired
    %of a sample containing regions with known cell density and
    %viability.  An image with parameters optimized for sensitivity
    %(contrast image) and parameters which generate maximum signal
    %(max) must have been acquired for both types of weightings.  The
```

```
%images must have been analyzed with STEMS_Viability_Density.m
%before running this.  Only one of the filenames needs to be entered
%if all filenames have the same date as the first eight characters.

% SolvingforVandC4 %use a second order fit with data from all samples
% SolvingforVandC3 %use only a 1st order fit
clear nlm1
clear nlm2
% SolvingforVandC5 %second order diffusion first order MT
SolvingforVandC6 %first order diffusion second order MT

clear Diff
clear MT
load(['MTData' filename(1:8) '.mat'])
load(['DiffusionData' filename(1:8) '.mat'])

%     %second order diffusion first order MT
%     Concplot=nlm1.Coefficients.Estimate(1)+...
%         nlm1.Coefficients.Estimate(2)* Diff.image+...
%         nlm1.Coefficients.Estimate(3)*MT.image+...
%         nlm1.Coefficients.Estimate(4)*Diff.image.^2+...
%         nlm1.Coefficients.Estimate(5)*Diff.image.*MT.image;
%     Viaplot=nlm2.Coefficients.Estimate(1)+...
%         nlm2.Coefficients.Estimate(2)*Diff.image+...
%         nlm2.Coefficients.Estimate(3)*MT.image+...
%         nlm2.Coefficients.Estimate(4)*Diff.image.^2+...
%         nlm2.Coefficients.Estimate(5)*Diff.image.*MT.image;

%first order diffusion second order MT
Concplot=nlm1.Coefficients.Estimate(1)+...
    nlm1.Coefficients.Estimate(2)*Diff.image+...
    nlm1.Coefficients.Estimate(3)*MT.image+...
    nlm1.Coefficients.Estimate(4)*...
    Diff.image.*MT.image+nlm1.Coefficients.Estimate(5).*MT.image.^2;
Viaplot=nlm2.Coefficients.Estimate(1)+...
```

```
        nlm2.Coefficients.Estimate(2)*Diff.image+...
        nlm2.Coefficients.Estimate(3)*MT.image+...
        nlm2.Coefficients.Estimate(4)*Diff.image.*MT.image+...
        nlm2.Coefficients.Estimate(5).*MT.image.^2;


    Viaplot(Concplot<0.1e8)=0;
    [u,v] = meshgrid(linspace(-lpe/2*10,lpe/2*10,pep),...
        linspace(-lro/2*10,lro/2*10,fep));
    g1=figure;
    g=imagesc(u(1,:),v(vdfbottom:end-vdftop,1),Concplot);hold on
    set(gca,'YDir','normal'); %Fix direction of Y axis
    set(g, 'AlphaData', ~isnan(Concplot))
    xlabel('X [mm]'); ylabel('Y [mm]'); title('Density (cells/mL)')
    set(gca,'FontSize',11)
    colorbar
    caxis([0 2e8])
    numticks('y',5,-lro/2*10,lro/2*10)
    axis image
    % colormap(g1,'bone')

    [u,v] = meshgrid(linspace(-lpe/2*10,lpe/2*10,pep),linspace(...
        -lro/2*10,lro/2*10,fep));
    g1=figure;
    g=imagesc(u(1,:),v(vdfbottom:end-vdftop,1),Viaplot);hold on
    set(gca,'YDir','normal'); %Fix direction of Y axis
    set(g, 'AlphaData', ~isnan(Viaplot))
    xlabel('X [mm]'); ylabel('Y [mm]'); title('Viability (%)')
    set(gca,'FontSize',11)
    colorbar
    caxis([0 100])
    numticks('y',5,-lro/2*10,lro/2*10)
    axis image
    % colormap(g1,'bone')
end
```

B.10 Mapping Cell Density and Viability from Diffusion- and Magnetization Transfer- (MT-) Weighted MRIs

```
%Plots STEMS image data from the pulse sequence stems_tn_pulsed which can
%be used to acquire T2-, diffusion-, T1, or MT- weighted images.  Two
%images need to be acquired.  One should be optimized for best contrast
%(using an appropriate b-value or offset frequency) and the other should be
%a reference image that generates a large signal (for example, using no
% diffusion-weighting gradients in a diffusion-weighted image or using a
% 200000 Hz saturation pulse offset difference in MT-weighted images, etc.)
% Program allows users to select regions of interest (ROIs) of areas with
% known cell density and viablity.  Pairwise comparisons are made between
% the regions of interest to determine if there is a statistically
% significant difference in the quantity of signal.

%If a diffusion- and MT-weighted image are acquired, this program can be
%used to calibrate cell density and viabiity to diffusion- and MT-weighted
%signal and generate images of cell density and viability.

% prompt = strcat('Enter name of folder containing resolved signal ',...
%     'data:\n\n    ');
% filename = input(prompt,'s');
%
% prompt = strcat('Enter name of folder containing maximum relative',...
%     'signal data:\n\n    ');
% filename2 = input(prompt,'s');
%
% prompt = strcat('Enter number corresponding to weighting:\n\n    ',...
%     '1. T1\n    2. T2\n    3. Diffusion\n    4. MT\n\n');
% wtyp = input(prompt);

filename = '20200924_DiffContrast.fid';
filename2 = '20200924_DiffMax.fid';
wtyp=3;
% filename = '20200924_MT3300Contrast.fid';
% filename2 = '20200924_MTMax.fid';
% wtyp=4;
load('optmask2_20200924.mat')
```

```
load('optmask20200924.mat')

% filename = '20201012_DiffContrast.fid';
% filename2 = '20201012_DiffMax.fid';
% wtyp=3;
% % filename = '20201012_MT3300Contrast.fid';
% % filename2 = '20201012_MTMax.fid';
% % wtyp=4;
% load('optmask2_20201012.mat')
% load('optmask20201012.mat')

% filename = '20201013_DiffContrast.fid';
% filename2 = '20201013_DiffMax.fid';
% wtyp=3;
% % filename = '20201013_MT3300Contrast.fid';
% % filename2 = '20201013_MTMax.fid';
% % wtyp=4;
% load('optmask2_20201013.mat')
% load('optmask20201013.mat')

if wtyp==1
    str='T1';
elseif wtyp==2
    str='T2';
elseif wtyp==3
    str='Diffusion';
elseif wtyp==4
    str='MT';
end

%general path for all associated files
addpath(genpath('C:\Users\Brian Archer\Documents\MATLAB\Bouchard Lab'))

%get screen size for figure positioning
scsz = get( 0, 'ScreenSize' );
```

```
data=fopen([filename '\procpar'],'r');
parameter=struct('lpe',[],'lro',[],'ppe',[],'pro',[],'ni',[],'thk',[],...
    'nv',[],'np',[],'ns',[],'ct',[]);
parameter=readout_procpar(parameter,data);
fclose('all');

lpe=parameter.lpe; %width of slide (cm)
lro=parameter.lro; %length of slide (cm)
ppe=parameter.ppe; %offset in y direction (cm)
pro=parameter.pro; %offset in x direction (cm)
ni=parameter.ni; %size of matrix in pixels
thk=parameter.thk; %thickness of slices
pep=parameter.nv; %number of pixels in phase encode direction
fep=parameter.np/2; %number of pixels in frequency encode direction
ns=parameter.ns; %number of slices
ct1=parameter.ct; %number of averages

data=fopen([filename2 '\procpar'],'r');
parameter2=struct('ct',[]);
parameter2=readout_procpar(parameter2,data);
fclose('all');

ct2=parameter2.ct; %number of averages

%Figure dimensions and position based on screen size and image size:
if lpe/lro > (scsz(4)-150)/(scsz(3)-100)
    fb3=50; %figure position from bottom of screen
    figh=scsz(4)-150; %figure height
    figw=round(figh*lro/lpe)+200; %figure width
    fb1=round(scsz(3)/2-figw/2); %distance from sides of screen
else
    fb1=50; %distance from sides of screen
    figw=scsz(3)-150; %figure width
    figh=round(figw*lpe/lro)+200; %figure height
```

```
    fb3=round(scsz(4)/2-figh/2);
end

pos=[fb1,fb3,figw,figh]; %figure positioning requirements for full image

[r1,~,~,~]=readfid([filename '\fid'],-1);
[r2,~,~,~]=readfid([filename2 '\fid'],-1);

scli=zeros(pep,fep);
scli2=zeros(pep,fep);
for i=1:pep
    scli(i,:)=r1(fep*(i-1)+1:fep*i,:);
end

for i=1:pep
    scli2(i,:,ns)=r2(fep*(i-1)+1:fep*i,:);
end


img1=rot90(abs(fftshift(ifft2(scli))));
img2=rot90(abs(fftshift(ifft2(scli2))));

%Crop Images:
%set the number of pixels to crop
%Some cropping parameters that I liked and have already determined (feel
%free to add more to the list):
if strcmp(filename(1:8),'20200924')
    vdftop=31; %vertical pixels to crop off top (minimum 0)
    vdfbottom=18; %vertical pixels to crop off bottom (minimum 1)
elseif strcmp(filename(1:8),'20201013')
    vdftop=34; %vertical pixels to crop off top (minimum 0)
    vdfbottom=15; %vertical pixels to crop off bottom (minimum 1)
elseif strcmp(filename(1:8),'20201012')
    vdftop=31; %vertical pixels to crop off top (minimum 0)
    vdfbottom=18; %vertical pixels to crop off bottom (minimum 1)
```

```
end
%%
% crop the images in vertical direction
img1crop=img1(vdfbottom:end-vdftop,:);
img2crop=img2(vdfbottom:end-vdftop,:);

%Normalize signal intensity to max signal indensity S/S_0 where S is the
%contrast signal and S_0 is the signal of maximum intensity
img3=img1crop./img2crop;
img3=(img1crop./ct1)./(img2crop./ct2);
img3a=img3;

%in case of extreme outliers
img3a(img3>mean(img3(:))+3*std(img3(:)))=NaN;
img3a(img3<mean(img3(:))-6*std(img3(:)))=NaN;
img3=img3a;
% figure;imagesc(img3a)

%%
%Filter out noisy background pixels
%initialize noise mask to be size of cropped image
noise=ones(size(img1crop));

%remove pixels which are definitely out of range of the NMR tube
%for 64 width image; adjust as needed
noise(:,end-20:end)=0;
noise(:,1:18)=0;

%for 32 width image; adjust based on actual image
% noise(:,end-8:end)=0;
% noise(:,1:10)=0;

%Normalization should cap the signal at 1, remove anything much greater
%than 1
noise(img3>1.3)=0;
```

```
%Using the max intensity image, remove pixels with a low intensity since
%they do not have any sample present
if wtyp==4
    stdfactor=0.3; %MT
elseif wtyp==3
    stdfactor=0.2; %Diff
elseif wtyp==2;
    stdfactor=0; %T2
end
noise(img2crop<nanmean(img2crop(:))-stdfactor*nanstd(img2crop(:)))=0;

img3(noise==0)=NaN;
% figure;imagesc(img3)
%%
if strcmp(filename(1:8),'20200924')
    shiftfactor=1; %more positive shifts image right, cannot be 0
elseif strcmp(filename(1:8),'20201013')
    shiftfactor=1;
elseif strcmp(filename(1:8),'20201012')
    shiftfactor=0;
end

%shift image horizontally
img4=zeros(size(img3));
if shiftfactor>0;
    img4(:,1:shiftfactor)=img3(:,end-shiftfactor+1:end);
    img4(:,shiftfactor+1:end)=img3(:,1:end-shiftfactor);
elseif shiftfactor<0;
    img4(:,1:end+shiftfactor)=img3(:,-shiftfactor+1:end);
    img4(:,end+shiftfactor+1:end)=img3(:,1:-shiftfactor);
elseif shiftfactor==0;
    img4=img3;
end
% figure;imagesc(img4)
```

```
%%
% for i=1:128
%     for j=1:128
%         if (img2(i,j)>3*img2(i+2,j)&&img2(i,j)>3*img2(i-2,j)&&...
%                 img2(i,j)>3*img2(i,j+2)&&img2(i,j)>3*img2(i,j-2))||...
%             (img2(i,j)<3*img2(i+2,j)&&img2(i,j)<3*img2(i-2,j)&&...
%                 img2(i,j)<3*img2(i,j+2)&&img2(i,j)<3*img2(i,j-2))
%             noise(i,j)=0;
%         end
%     end
% end

% %Correct for gradient in baseline/max image
% pos2=[fb1,fb3,figw*2,figh]; %figure positioning requirements for
% %editable image
% % tempcor=Adjust_Intensity(pos2,img2a);
% tempcor=0;
%
% strat=linspace(1-tempcor,1+tempcor,size(img2a,1))'*ones(1,size(img2a,2));
% img2a=img2a.*strat;
% img1a=img1a.*strat;
% img3=img2a-img1a;
%
% %normalize subtracted image to 1
% % img3=(img3-min(img3(:)))/(max(img3(:))-min(img3(:)));
% % img3=1-img3;
%
% img3(noise==0)=NaN;

% img5=img4;
%
% %number of outlier pixels to filter out of upper range:
% toprepix=40; %minimum 1
% %number of pixels to filter out of lower range:
% botrepix=10; %minimum 0
```

```
%
% % filter out outliers to enhance contrast
% [svals,idx] = sort(img5(~isnan(img5)),'descend'); % sort to vector
% img7a=(img5-svals(end-botrepix))/(svals(toprepix)-svals(end-botrepix));
% % img7a=img7;
% figure;imagesc(img7a)
%%
%Plot image to select ROIs
[u,v] = meshgrid(linspace(-lpe/2*10,lpe/2*10,pep),linspace(-lro/2*10,...
    lro/2*10,fep));
figure('position', pos);
g=imagesc(u(1,:),v(vdfbottom:end-vdftop,1),img4);hold on
set(gca,'YDir','normal'); %Fix direction of Y axis
set(g, 'AlphaData', ~isnan(img4))
xlabel('X [mm]'); ylabel('Y [mm]'); title([str ' Weighted Signal'])
set(gca,'FontSize',11)
colorbar
% caxis([0 1])
numticks('y',5,-lro/2*10,lro/2*10)
axis image
%%
%manual selection of ROIs for linear conversion
loopgo='y';
i=1;

%I saved some ROIs which can be reloaded (example: optmask20200924.mat)
if (exist('optmask', 'var')) %if a set of ROIs already exists, inquire
    %if the user would like to use it
    prompt = strcat('\nWould you like to use previous ROIs for this an',...
        'alysis (y/n)?\n\n    ');
    name = input(prompt,'s');  %first input
    if name=='n' %if user does not want to use existing ROIs
        clear optmask; %clear existing ROIs
    end
end
```

```
if (exist('optmask2', 'var')) %if a set of ROIs already exists, inquire if
    %the user would like to use it
    prompt = strcat('\nWould you like to use previous background ROI f',...
        'or this analysis (y/n)?\n\n    ');
    name = input(prompt,'s');  %first input
    if name=='n' %if user does not want to use existing ROIs
        clear optmask2; %clear existing ROIs
    end
end

if (~exist('optmask', 'var')) %run if there are no existing ROIs
    prompt = '\nEnter number of ROIs for this analysis.\n\n    ';
    %ask how many new ROIs
    numROIs = input(prompt);  %first input
    optmask=cell(1,numROIs);

    for i=1:numROIs% loopgo~='n';

        fprintf('\nSelect ROI (drag an ellipse) of concentration \n')
        ROI=imellipse;
        mask=createMask(ROI);
        optmask{i}=mask;
    end
end

if (~exist('optmask2', 'var')) %run if there are is no background ROI
    fprintf('\nDraw Freehand ROI around acellular agarose region \n')
    ROI=imfreehand;
    mask2=createMask(ROI);
    optmask2{1}=mask2;
end

maskbound=NaN(size(img4));
for i=1:size(optmask,2)
```

```
    B=bwboundaries(optmask{i});
    bb=B{1};
    for j=1:size(bb,1)
        maskbound(bb(j,1),bb(j,2))=1;
    end
end

conc_signal=zeros(1,size(optmask,2));
conc_signal2=zeros(1,size(optmask2,2));
conc_signal_std=zeros(1,size(optmask,2));
conc_signal_stderr=zeros(1,size(optmask,2));
conc_signal_weight=zeros(1,size(optmask,2));
signal_stats=cell(1,size(optmask,2));

%determine the mean value of the agarose reference region
img4a=img4;
img4a(~optmask2{1})=NaN;
conc_signal2(1)=nanmean(img4a(:));
signal_stats2{1}=img4a(~isnan(img4a)); %structure saving the pixel values
%for statistical analysis
if wtyp==3
    save(['DiffBGSignal' filename(1:8) '.mat'],'conc_signal2')
elseif wtyp==4
    save(['MTBGSignal' filename(1:8) '.mat'],'conc_signal2')
end
flag=1
%subtract acellular reference signal
img5=img4-conc_signal2(1);
% figure;imagesc(img5)

%determine mean values in ROIs of layers
for i=1:size(optmask,2)
    img5a=img5;
    img5a(~optmask{i})=NaN;
    conc_signal(i)=nanmean(img5a(:));
```

```
    signal_stats{i}=img5a(~isnan(img5a)); %structure saving the pixel
    %values for statistical analysis
    % conc_signal_std(i)=std(img7b(:),'omitnan');
    conc_signal_std(i)=std(img5a(~isnan(img5a)));
    conc_signal_stderr(i)=conc_signal_std(i)/(size(img5a(~isnan(...
        img5a)),1))^(1/2);
    conc_signal_weight(i)=1/nanvar(img5a(:));
end

%determin mean value of agarose background signal
img5a=img5;
img5a(~optmask2{1})=NaN;
conc_signal_blank=nanmean(img5a(:));
conc_signal_blank_stderr=std(img5a(~isnan(img5a)))/(size(img5a(...
    ~isnan(img5a)),1))^(1/2);

%%
if strcmp(filename(1:8),'20200924')
    cellcon=[2e8, 2e8, 1e8, 1e8];
    cellvia=[100, 50, 100, 50];
elseif strcmp(filename(1:8),'20201012')
    cellcon=[2e8, 2e8, 2e8, 2e8];
    cellvia=[100, 66.6, 33.3, 0];
elseif strcmp(filename(1:8),'20201013')
    cellcon=[2e8, 1e8, 5e7, 2.5e7];
    cellvia=[100, 100, 100, 100];
else
    prompt = strcat('\nEnter Concentrations of ROIs in order of layers',...
        'selected as [C1, C2, C3...]\n\n    ');
    cellcon = input(prompt);
    prompt = strcat('\nEnter Viabilities of ROIs in order of layers se',...
        'lected as [V1, V2, V3...]\n\n    ');
    cellvia = input(prompt);
end
%%
```

```
%ANOVA
y=signal_stats{1};
g1=ones(size(signal_stats{1}'))*cellcon(1);
g2=ones(size(signal_stats{1}'))*cellvia(1);
for i=2:size(signal_stats,2)
    y=[y; signal_stats{i};];
    g1=[g1 ones(size(signal_stats{i}'))*cellcon(i)];
    g2=[g2 ones(size(signal_stats{i}'))*cellvia(i)];
end

if range(g1) == 0
    [p,tbl,stats]=anova1(y,g2);
    multcompare(stats)
elseif range(g2) == 0
    [p,tbl,stats]=anova1(y,g1);
    multcompare(stats)
else
    %          [p,tbl,stats]=anovan(y,{g1,g2},'model','full')
    [p,tbl,stats]=anovan(y,{g1,g2});
    multcompare(stats,'Dimension',[1 2])
end

%%
%generate bar plot of viabilities in groupings of cell concentration
uniquecellcon=unique(cellcon); %determine all unique cell concentrations
%in sample layers
uniquecellvia=unique(cellvia); %determine all unique cell viabilities
%in sample layers
%pre aloquot space in matrices
labels=cell(1,size(uniquecellcon,2));
leg=cell(1,size(uniquecellvia,2));
conc=NaN(size(uniquecellcon,2),size(uniquecellvia,2));
viability=NaN(size(uniquecellcon,2),size(uniquecellvia,2));
signal=NaN(size(uniquecellcon,2),size(uniquecellvia,2));
signalstd=NaN(size(uniquecellcon,2),size(uniquecellvia,2));
```

```
signalstderr=NaN(size(uniquecellcon,2),size(uniquecellvia,2));

for i=1:size(uniquecellcon,2) %for each unique cell concentration
    for j=1:size(uniquecellvia,2) %for each unique cell viability
        %make matrix with corresponding measured signal at each cell
        %concentration/viability combo
        if ~isempty(conc_signal(cellcon==uniquecellcon(i)&cellvia==...
                uniquecellvia(j)))
            signal(i,j)=conc_signal(cellcon==uniquecellcon(i)&cellvia==...
                uniquecellvia(j));
            conc(i,j)=cellcon(cellcon==uniquecellcon(i)&cellvia==...
                uniquecellvia(j));
            viability(i,j)=cellvia(cellcon==uniquecellcon(i)&cellvia==...
                uniquecellvia(j));
            signalstd(i,j)=conc_signal_std(cellcon==uniquecellcon(i)&...
                cellvia==uniquecellvia(j));
            signalstderr(i,j)=conc_signal_stderr(cellcon==...
                uniquecellcon(i)&cellvia==uniquecellvia(j));
            if i==1;
                leg{1,j}=[num2str(uniquecellvia(j)) ' %'];
            end
        end
    end
    labels{1,i}=num2str(uniquecellcon(i)/1e8);
end

%%
% leg{1,i}=[num2str(uniquecellvia(i)) ' %'];
%make the bar plot
figure;

%if there is only one group nanpad to trick bar into thinking there are
%multiple groups
if isrow(signal);
    signal1 = vertcat(signal,nan(size(signal)));
```

```
    b = bar(signal1, 'grouped');
    xlim([0.5 1.5]) %know this to be true if no x
else
    b = bar(signal, 'grouped');
end
%%For MATLAB R2019a or earlier releases
hold on
% Find the number of groups and the number of bars in each group
ngroups = size(signal, 1);
nbars = size(signal, 2);
% Calculate the width for each bar group
groupwidth = min(0.8, nbars/(nbars + 1.5));
% Set the position of each error bar in the centre of the main bar
% Based on barweb.m by Bolu Ajiboye from MATLAB File Exchange
for i = 1:nbars
    % Calculate center of each bar
    x = (1:ngroups) - groupwidth/2 + (2*i-1) * groupwidth / (2*nbars);
    %error bars are standard deviaiton
%         errorbar(x, signal(:,i), signalstd(:,i), 'k', 'linestyle',...
%             'none','LineWidth',1.5);
    %error bars are standard error
    errorbar(x, signal(:,i), signalstderr(:,i), 'k', 'linestyle',...
        'none','LineWidth',1.5);
end
xlabel('Cell Density (108 cells.mL-1)');
ylabel(['Normalized ' str ' Weighted Signal'])
set(gca, 'XTickLabel', labels);
lgd=legend(leg);
% lgd.Title.String='Cell Viability';
% title(lgd,'Cell Viability')
hold off

%%
%allows user to make aesthetic adjustments to image.
AdjustImage( lpe, pep, lro, fep, pos, vdfbottom, vdftop, img5, str,...
```

```
    maskbound, cellcon, cellvia, optmask, wtyp )

if wtyp==3
    %for Diffusion
    Diff.V=[reshape(viability,1,size(viability,1)*size(viability,2))';0];
    Diff.C=[reshape(conc,1,size(conc,1)*size(conc,2))';0];
    Diff.S=[reshape(signal,1,size(signal,1)*size(signal,2))';...
        conc_signal_blank];
    Diff.error=[reshape(signalstderr,1,size(signalstderr,1)*...
        size(signalstderr,2))';conc_signal_blank_stderr];
    Diff.image=img5;
    save(['DiffusionData' filename(1:8) '.mat'],'Diff')
elseif wtyp==4
    %for MT
    MT.V=[reshape(viability,1,size(viability,1)*size(viability,2))';0];
    MT.C=[reshape(conc,1,size(conc,1)*size(conc,2))';0];
    MT.S=[reshape(signal,1,size(signal,1)*size(signal,2))';...
        conc_signal_blank];
    MT.error=[reshape(signalstderr,1,size(signalstderr,1)*...
        size(signalstderr,2))';conc_signal_blank_stderr];
    MT.image=img5;
    save(['MTData' filename(1:8) '.mat'],'MT')
end

%%
if exist(['MTData' filename(1:8) '.mat'],'file')==2 && ...
        exist(['DiffusionData' filename(1:8) '.mat'],'file')==2
    %%
    %This can be used to generate an image of cell viability and cell
    %density from diffusion- and MT-weighted images.  Before running this
    %program, diffusion- and MT-weighted images must have been acquired
    %of a sample containing regions with known cell density and
    %viability.  An image with parameters optimized for sensitivity
    %(contrast image) and parameters which generate maximum signal
    %(max) must have been acquired for both types of weightings.  The
```

```
%images must have been analyzed with STEMS_Viability_Density.m
%before running this.  Only one of the filenames needs to be entered
%if all filenames have the same date as the first eight characters.

% SolvingforVandC4 %use a second order fit with data from all samples
% SolvingforVandC3 %use only a 1st order fit
clear nlm1
clear nlm2
% SolvingforVandC5 %second order diffusion first order MT
SolvingforVandC6 %first order diffusion second order MT

clear Diff
clear MT
load(['MTData' filename(1:8) '.mat'])
load(['DiffusionData' filename(1:8) '.mat'])

%     %second order diffusion first order MT
%     Concplot=nlm1.Coefficients.Estimate(1)+...
%         nlm1.Coefficients.Estimate(2)* Diff.image+...
%         nlm1.Coefficients.Estimate(3)*MT.image+...
%         nlm1.Coefficients.Estimate(4)*Diff.image.^2+...
%         nlm1.Coefficients.Estimate(5)*Diff.image.*MT.image;
%     Viaplot=nlm2.Coefficients.Estimate(1)+...
%         nlm2.Coefficients.Estimate(2)*Diff.image+...
%         nlm2.Coefficients.Estimate(3)*MT.image+...
%         nlm2.Coefficients.Estimate(4)*Diff.image.^2+...
%         nlm2.Coefficients.Estimate(5)*Diff.image.*MT.image;

%first order diffusion second order MT
Concplot=nlm1.Coefficients.Estimate(1)+...
    nlm1.Coefficients.Estimate(2)*Diff.image+...
    nlm1.Coefficients.Estimate(3)*MT.image+...
    nlm1.Coefficients.Estimate(4)*...
    Diff.image.*MT.image+nlm1.Coefficients.Estimate(5).*MT.image.^2;
Viaplot=nlm2.Coefficients.Estimate(1)+...
```

```
        nlm2.Coefficients.Estimate(2)*Diff.image+...
        nlm2.Coefficients.Estimate(3)*MT.image+...
        nlm2.Coefficients.Estimate(4)*Diff.image.*MT.image+...
        nlm2.Coefficients.Estimate(5).*MT.image.^2;


    Viaplot(Concplot<0.1e8)=0;
    [u,v] = meshgrid(linspace(-lpe/2*10,lpe/2*10,pep),...
        linspace(-lro/2*10,lro/2*10,fep));
    g1=figure;
    g=imagesc(u(1,:),v(vdfbottom:end-vdftop,1),Concplot);hold on
    set(gca,'YDir','normal'); %Fix direction of Y axis
    set(g, 'AlphaData', ~isnan(Concplot))
    xlabel('X [mm]'); ylabel('Y [mm]'); title('Density (cells/mL)')
    set(gca,'FontSize',11)
    colorbar
    caxis([0 2e8])
    numticks('y',5,-lro/2*10,lro/2*10)
    axis image
    % colormap(g1,'bone')

    [u,v] = meshgrid(linspace(-lpe/2*10,lpe/2*10,pep),linspace(...
        -lro/2*10,lro/2*10,fep));
    g1=figure;
    g=imagesc(u(1,:),v(vdfbottom:end-vdftop,1),Viaplot);hold on
    set(gca,'YDir','normal'); %Fix direction of Y axis
    set(g, 'AlphaData', ~isnan(Viaplot))
    xlabel('X [mm]'); ylabel('Y [mm]'); title('Viability (%)')
    set(gca,'FontSize',11)
    colorbar
    caxis([0 100])
    numticks('y',5,-lro/2*10,lro/2*10)
    axis image
    % colormap(g1,'bone')
end
```

B.11 Calibrating Cell Density and Viability to Diffusion- and MT-Weighted NMR Spectroscopy Data

```
%Inverts the relationship between diffusion- and MT-weighted NMR signals,
%cell concentration, and cell viability to generate surface calibration
% plots.  The calibration surfaces allow both cell density and viability to
% be determined from a diffusion-weighted measurement and an MT-weighted
% measurement only.  The cell density calibration surface is generated by
% plotting cell concentration as a function of diffusion- and MT-weighted
% signal measurements and fitting a polynomial with second order dependence
% on each. Similarly, the cell viability calibration surface is generated
% by plotting cell viability as a function of diffusion- and MT-weighted
% signal measurments and fitting a polynomial with second order dependence
% on each.  Then limits of detection are determined for both cell viability
% and density using the multivariate LOD determination method.

load('DiffusionData.mat')
load('MTData.mat')
load('S_MTBlank.mat')
load('S_DiffBlank.mat')
%%
%plot error overlayed on concentration calibration surface (found from
%inversion of power series)

%Fit concentration to diffusion and MT signal
xData=Diff.S;
yData=MT.S;
zData=Diff.C;

%initial fit using fit function
[xData_1, yData_1, zData_1] = prepareSurfaceData( xData, yData, zData );
ft = fittype( 'poly22' );
[fitresult{1}, gof{1}] = fit( [xData_1, yData_1], zData_1, ft );

%attempt to fit with fitnlm
xy_1=[xData_1(:),yData_1(:)];
%xy(:,2) represents y and xy(:,1) represents x
modelFun = @(c,xy) (c(1) + c(2).*xy(:,1) + c(3).*xy(:,2) + c(4).*...
```

```
    xy(:,1).^2 + c(5).*xy(:,1).*xy(:,2) + c(6).*xy(:,2).^2);
startPoints = [fitresult{1}.p00 fitresult{1}.p10 fitresult{1}.p01 ...
    fitresult{1}.p20 fitresult{1}.p11 fitresult{1}.p02];
nlm1 = fitnlm(xy_1,zData_1(:),modelFun,startPoints);

%Fit viability to diffusion and MT signal
xData=Diff.S;
yData=MT.S;
zData=Diff.V;

%initial fit using fit
[xData_2, yData_2, zData_2] = prepareSurfaceData( xData, yData, zData );
ft = fittype( 'poly22' );
[fitresult{2}, gof{2}] = fit( [xData_2, yData_2], zData_2, ft );

%attempt to fit with fitnlm
xy_2=[xData_2(:),yData_2(:)];
%xy(:,2) represents y and xy(:,1) represents x
modelFun = @(v,xy) (v(1) + v(2).*xy(:,1) + v(3).*xy(:,2) + v(4).*...
    xy(:,1).^2 + v(5).*xy(:,1).*xy(:,2) + v(6).*xy(:,2).^2);
startPoints = [fitresult{2}.p00 fitresult{2}.p10 fitresult{2}.p01 ...
    fitresult{2}.p20 fitresult{2}.p11 fitresult{2}.p02];
nlm2 = fitnlm(xy_2,zData_2(:),modelFun,startPoints);

%Propagate Error
syms c0 c1 c2 c3 c4 c5 v0 v1 v2 v3 v4 v5 C V S_Diff S_MT

%Set parameters equal to numerical values from fit
c0=nlm1.Coefficients.Estimate(1); c1=nlm1.Coefficients.Estimate(2);
c2=nlm1.Coefficients.Estimate(3); c3=nlm1.Coefficients.Estimate(4);
c4=nlm1.Coefficients.Estimate(5); c5=nlm1.Coefficients.Estimate(6);
v0=nlm2.Coefficients.Estimate(1); v1=nlm2.Coefficients.Estimate(2);
v2=nlm2.Coefficients.Estimate(3); v3=nlm2.Coefficients.Estimate(4);
v4=nlm2.Coefficients.Estimate(5); v5=nlm2.Coefficients.Estimate(6);
```

```
C = c0 + c1*S_Diff + c2*S_MT + c3*S_Diff^2 + c4*S_Diff*S_MT + c5*S_MT^2;
V = v0 + v1*S_Diff + v2*S_MT + v3*S_Diff^2 + v4*S_Diff*S_MT + v5*S_MT^2;
Cerror = vpa((diff(C,S_Diff)^2).*Diff.error.^2 + ...
    vpa(diff(C,S_MT)^2).*MT.error.^2).^(1/2);
Verror = vpa((diff(V,S_Diff)^2).*Diff.error.^2 + ...
    vpa(diff(V,S_MT)^2).*MT.error.^2).^(1/2);

Cerror1=zeros(size(Cerror));
Verror1=zeros(size(Cerror));

for i=1:size(Cerror,1)
    Cerror1(i,:)=subs(Cerror(i),[S_MT, S_Diff],[MT.S(i), Diff.S(i)]);
    Verror1(i,:)=subs(Verror(i),[S_MT, S_Diff],[MT.S(i), Diff.S(i)]);
end

Cerror=Cerror1;
Verror=Verror1;
%%
viascale=1;%0.01*1e8;

%plot data points with errors where S_Diff is x, S_MT is y, and C/V are Z
figure;plot3(xData_1, yData_1, zData_1, '.','MarkerSize',10',...
    'Color','r');hold on %plot points in 3D space
title('Cell Concentration Calibration',...
    'FontSize',11, 'FontName', 'Century') ;xlabel('S_{Diff}',...
    'FontSize',11, 'FontName', 'Century');
ylabel('S_{MT}','FontSize',11, 'FontName', 'Century');
zlabel('Concentration (cells/mL)','FontSize',11, 'FontName', ...
    'Century'); set(gca,'FontSize',11, 'FontName', 'Century')
plot( fitresult{1});
errmin_1=zData_1-Cerror/2; %bottom of error bar
errmax_1=zData_1+Cerror/2; %top of error bar

errscl=1e-11; %scale the widths of the error bar brackets
for i=1:size(xData_1,1)
```

```
    plot3([xData_1(i);xData_1(i)], [yData_1(i);...
        yData_1(i)], [errmin_1(i);errmax_1(i)]','Color',...
        'r','LineWidth',1); %plot error bar
    plot3([xData_1(i)-Cerror(i)*errscl;xData_1(i)+Cerror(i)*errscl],...
        [yData_1(i);yData_1(i)], [errmax_1(i);errmax_1(i)]',...
        'Color','r','LineWidth',1);
    %place horizontal bars on top of error bars
    plot3([xData_1(i)-Cerror(i)*errscl;xData_1(i)+Cerror(i)*errscl], ...
        [yData_1(i);yData_1(i)], [errmin_1(i);errmin_1(i)]',...
        'Color','r','LineWidth',1);
    %place horizontal bars on base of error bars
end
xlim([-1e-4 10e-3]) %fix limits on x axis to be from about 0 to 100% viable
zlim([-1 1.2e8]) %fix axis on z axis to be closer to plot
caxis([0 1.2e8]) %set color axis equal to z axis

%%

%plot data points with errors where S_Diff is x, S_MT is y, and
%Viability is Z
figure;plot3(xData_2, yData_2, zData_2, '.','MarkerSize',10','Color',...
    'r');hold on %plot points in 3D space
title('Cell Viability Calibration',...
    'FontSize',11, 'FontName', 'Century') ;xlabel('S_{Diff}',...
    'FontSize',11, 'FontName', 'Century');
ylabel('S_{MT}','FontSize',11, 'FontName', 'Century');
zlabel('Viability (%)','FontSize',11, 'FontName', 'Century');
set(gca,'FontSize',11, 'FontName', 'Century')
plot( fitresult{2});

errmin_2=zData_2-Verror/2; %bottom of error bar
errmax_2=zData_2+Verror/2; %top of error bar

errsc2=5e-6/viascale; %scale the widths of the error bar brackets
for i=1:size(xData_2,1)
```

```
    plot3([xData_2(i);xData_2(i)], [yData_2(i);yData_2(i)], ...
        [errmin_2(i);errmax_2(i)]','Color',...
        'r','LineWidth',1); %plot error bar
    plot3([xData_2(i)-Verror(i)*errsc2;xData_2(i)+Verror(i)*errsc2], ...
        [yData_2(i);yData_2(i)], [errmax_2(i);errmax_2(i)]',...
        'Color','r','LineWidth',1); %place horizontal bars on top
    %of error bars
    plot3([xData_2(i)-Verror(i)*errsc2;xData_2(i)+Verror(i)*errsc2], ...
        [yData_2(i);yData_2(i)], [errmin_2(i);errmin_2(i)]',...
        'Color','r','LineWidth',1); %place horizontal bars on base of
    %error bars
end

xlim([-1e-4 10e-3]) %fix limits on x axis to be from about 0 to 100% viable
zlim([-1 130]*viascale) %fix axis on z axis to be closer to plot
caxis([-1 130]*viascale) %set color axis equal to z axis

% save('FitConcentration2OrderPoly.mat','nlm1')
% save('FitViability2OrderPoly.mat','nlm2')


%%
%Limits of detection
%params is a vector of fitted parameters
%sigma is corresponding standard deviation vector of signal measurements
clear S_Diff; clear s_MT
load('S_Diff.mat')
load('S_MT.mat')

%Concentration
S_Diffstd=zeros(1,size(S_MT,1));
S_MTstd=zeros(1,size(S_MT,1));
S_Diffstd2=zeros(1,size(S_MT,1));
S_DiffMTstd=zeros(1,size(S_MT,1));
S_MTstd2=zeros(1,size(S_MT,1));
```

```
for i=1:size(S_MT,1)
    S_Diffstd(i)=std(S_Diff{i});
    S_MTstd(i)=std(S_MT{i});
    S_Diffstd2(i)=std(S_Diff{i}.^2);
    S_DiffMTstd(i)=std(S_Diff{i}.*S_MT{i});
    S_MTstd2(i)=std(S_MT{i}.^2);
end

params_C=[nlm1.Coefficients.Estimate(2) nlm1.Coefficients.Estimate(3) ...
    nlm1.Coefficients.Estimate(4) nlm1.Coefficients.Estimate(5) ...
    nlm1.Coefficients.Estimate(6)];
params_V=[nlm2.Coefficients.Estimate(2) nlm2.Coefficients.Estimate(3) ...
    nlm2.Coefficients.Estimate(4) nlm2.Coefficients.Estimate(5) ...
    nlm2.Coefficients.Estimate(6)];
% sigma=[std(S_DiffBlank) std(S_MTBlank) std(S_DiffBlank.^2) ...
%     std(S_DiffBlank.*S_MTBlank) std(S_MTBlank.^2)];
sigma=[mean(S_Diffstd) mean(S_MTstd) mean(S_Diffstd2) ...
    mean(S_DiffMTstd) mean(S_MTstd2)];

LOD_C=3*dot(sigma,params_C);
LOD_V=3*dot(sigma,params_V);
```

B.12 Read Free Induction Decay Data from Varian .fid Files

```
function [dta,fheader,bheader,slices]=readfid(filename,n)

   %filename: vnmr fid file to read
   %n: number of points at the end of fid to use for baseline correction
   %(-1 = no correction)
   %dta: returned fid
   %fheader: returned fid file header information
   %bheader: returned fid block header information for the last block that
   %was read

   fheader=struct('nblocks',{0},'ntraces',{0},'np',{0},'ebytes',{0},...
       'tbytes',{0},'bbytes',{0},'vers_id',{0},'status',{0},...
       'nb_headers',{0});
   bheader=struct('scale',{0},'status',{0},'index',{0},'mode',{0},...
       'ctcount',{0},'lpval',{0},'rpval',{0},'lvl',{0},'tlt',{0});

   %Read vnmr file

   f=fopen(filename,'r','b');

   fheader.nblocks=fread(f,1,'long');
   fheader.ntraces=fread(f,1,'long');
   fheader.np=fread(f,1,'long');
   fheader.ebytes=fread(f,1,'long');
   fheader.tbytes=fread(f,1,'long');
   fheader.bbytes=fread(f,1,'long');
   fheader.vers_id=fread(f,1,'short');
   fheader.status=fread(f,1,'short');
   fheader.nb_headers=fread(f,1,'long');

   dta=[];

   for fv=1:fheader.nblocks
     bheader.scale=fread(f,1,'short');
     bheader.status=fread(f,1,'short');
```

```
      bheader.index=fread(f,1,'short');
      bheader.mode=fread(f,1,'short');
      bheader.ctcount=fread(f,1,'long');
      bheader.lpval=fread(f,1,'float');
      bheader.rpval=fread(f,1,'float');
      bheader.lvl=fread(f,1,'float');
      bheader.tlt=fread(f,1,'float');

%      fprintf('Reading block %d\n',fv);
      d=fread(f,fheader.np*fheader.ntraces,'float');
      slices=fheader.ntraces;

      d=transpose(reshape(d,2,size(d,1)/2));
      d=complex(d(:,1),d(:,2));
      if n>=0
         d=d-mean(d(end-n:end));
         dta=[dta,d];
      else
          dta=[dta,d];
      end
   end

fclose(f);
end
```

B.13 Read Process Parameters from Varian procpar Files

```
function parameter=readout_procpar(parameter,data)

%%This routine reads out Parameters from Varian procpar files
%%
readpar=fieldnames(parameter);
nopar=size(readpar);


while ~feof(data) % loop to read every line till the end of doc
    l = [fgetl(data) zeros(1,10)]; % read line
    for j=1:1:nopar(1) % loops every parameter
      if strcmp(l(1:sum(size(strjoin(readpar(j))))),[strjoin(...
              readpar(j)),' ']) % compares entries
        parameter1 = fgetl(data);
          if ~strcmp(parameter1,'1 "semsflow4"')
            temp2 = strread(parameter1);
            parameter = setfield(parameter,strjoin(readpar(j)),...
                temp2(2:end-1));
          else
            parameter=parameter1;
          end
       end
    end
end

end
```

REFERENCES

[1] S. Caddeo, M. Boffito, and S. Sartori, "Tissue engineering approaches in the design of healthy and pathological in vitro tissue models," *Frontiers in bioengineering and biotechnology*, vol. 5, p. 40, 2017.

[2] J. M. Zamora, "Effect of temperature-time on sterilization process for a jacketed bioreactor system: Application of a ratkowsky nonlinear model," *Revista Ingeniería*, vol. 28, no. 2, pp. 63–76, 2018.

[3] P. K. Chandra, S. Soker, and A. Atala, "Tissue engineering: Current status and future perspectives," in *Principles of Tissue Engineering*, pp. 1–35, Elsevier, 2020.

[4] S. Al-Himdani, Z. M. Jessop, A. Al-Sabah, E. Combellack, A. Ibrahim, S. H. Doak, A. M. Hart, C. W. Archer, C. A. Thornton, and I. S. Whitaker, "Tissue-engineered solutions in plastic and reconstructive surgery: principles and practice," *Frontiers in surgery*, vol. 4, p. 4, 2017.

[5] A. E. Pelling and R. J. Hickey, "Cellulose biomaterials for tissue engineering," *Frontiers in Bioengineering and Biotechnology*, vol. 7, p. 45, 2019.

[6] T. T. Lee, J. R. García, J. I. Paez, A. Singh, E. A. Phelps, S. Weis, Z. Shafiq, A. Shekaran, A. Del Campo, and A. J. García, "Light-triggered in vivo activation of adhesive peptides regulates cell adhesion, inflammation and vascularization of biomaterials," *Nature materials*, vol. 14, no. 3, pp. 352–360, 2015.

[7] J. Guo, Y. Kim, V. Xie, B. Smith, E. Watson, J. Lam, H. Pearce, P. Engel, and A. Mikos, "Modular, tissue-specific, and biodegradable hydrogel cross-linkers for tissue engineering," *Science advances*, vol. 5, no. 6, p. eaaw7396, 2019.

[8] D. C. Schoenmakers, A. E. Rowan, and P. H. Kouwer, "Crosslinking of fibrous hydrogels," *Nature communications*, vol. 9, no. 1, pp. 1–8, 2018.

[9] M. M. Zagho and A. Elzatahry, "Recent trends in electrospinning of polymer nanofibers and their applications as templates for metal oxide nanofibers preparation," *Electrospinning: Material, Techniques, and Biomedical Applications*, p. 1, 2016.

[10] J. Tan, C. Chua, and K. Leong, "Indirect fabrication of gelatin scaffolds using rapid prototyping technology," *Virtual and Physical Prototyping*, vol. 5, no. 1, pp. 45–53, 2010.

[11] S. A. Bencherif, T. M. Braschler, and P. Renaud, "Advances in the design of macroporous polymer scaffolds for potential applications in dentistry," *Journal of periodontal & implant science*, vol. 43, no. 6, pp. 251–261, 2013.

[12] M. Radisic, J. Malda, E. Epping, W. Geng, R. Langer, and G. Vunjak-Novakovic, "Oxygen gradients correlate with cell density and cell viability in engineered cardiac tissue," *Biotechnology and bioengineering*, vol. 93, no. 2, pp. 332–343, 2006.

[13] M. Sladkova and G. M. De Peppo, "Bioreactor systems for human bone tissue engineering," *Processes*, vol. 2, no. 2, pp. 494–525, 2014.

[14] L. Wang, X.-Y. Ma, Y. Zhang, Y.-F. Feng, X. Li, Y.-Y. Hu, Z. Wang, Z.-S. Ma, and W. Lei, "Repair of segmental bone defect using totally vitalized tissue engineered bone graft by a combined perfusion seeding and culture system," *PloS one*, vol. 9, no. 4, 2014.

[15] F. Galbusera, M. Cioffi, M. T. Raimondi, and R. Pietrabissa, "Computational modeling of combined cell population dynamics and oxygen transport in engineered tissue subject to interstitial perfusion," *Computer methods in biomechanics and biomedical engineering*, vol. 10, no. 4, pp. 279–287, 2007.

[16] M. Yamato and T. Okano, "Cell sheet engineering," *Materials today*, vol. 7, no. 5, pp. 42–47, 2004.

[17] H. Tekin, M. Anaya, M. D. Brigham, C. Nauman, R. Langer, and A. Khademhosseini, "Stimuli-responsive microwells for formation and retrieval of cell aggregates," *Lab on a Chip*, vol. 10, no. 18, pp. 2411–2418, 2010.

[18] R. Tiruvannamalai-Annamalai, D. R. Armant, and H. W. Matthew, "A glycosaminoglycan based, modular tissue scaffold system for rapid assembly of perfusable, high cell density, engineered tissues," *PloS one*, vol. 9, no. 1, p. e84287, 2014.

[19] P. A. Galie, D.-H. T. Nguyen, C. K. Choi, D. M. Cohen, P. A. Janmey, and C. S. Chen, "Fluid shear stress threshold regulates angiogenic sprouting," *Proceedings of the National Academy of Sciences*, vol. 111, no. 22, pp. 7968–7973, 2014.

[20] F. Maes, P. Van Ransbeeck, H. Van Oosterwyck, and P. Verdonck, "Modeling fluid flow through irregular scaffolds for perfusion bioreactors," *Biotechnology and bioengineering*, vol. 103, no. 3, pp. 621–630, 2009.

[21] C. M. Costello, M. B. Phillipsen, L. M. Hartmanis, M. A. Kwasnica, V. Chen, D. Hackam, M. W. Chang, W. E. Bentley, and J. C. March, "Microscale bioreactors for in situ characterization of gi epithelial cell physiology," *Scientific reports*, vol. 7, no. 1, pp. 1–10, 2017.

[22] B. J. Lawrence, M. Devarapalli, and S. V. Madihally, "Flow dynamics in bioreactors containing tissue engineering scaffolds," *Biotechnology and bioengineering*, vol. 102, no. 3, pp. 935–947, 2009.

[23] D. E. Conway and M. A. Schwartz, "Flow-dependent cellular mechanotransduction in atherosclerosis," *J Cell Sci*, vol. 126, no. 22, pp. 5101–5109, 2013.

[24] K. Youssef, N. N. Jarenwattananon, B. J. Archer, J. Mack, M. L. Iruela-Arispe, and L.-S. Bouchard, "4-d flow control in porous scaffolds: Toward a next generation of bioreactors," *IEEE Transactions on Biomedical Engineering*, vol. 64, no. 1, pp. 61–69, 2017.

[25] R. Henkelman, G. Stanisz, and S. Graham, "Magnetization transfer in mri: a review," *NMR in Biomedicine: An International Journal Devoted to the Development and Application of Magnetic Resonance In Vivo*, vol. 14, no. 2, pp. 57–64, 2001.

[26] R. M. Henkelman, X. Huang, Q.-S. Xiang, G. Stanisz, S. D. Swanson, and M. J. Bronskill, "Quantitative interpretation of magnetization transfer," *Magnetic resonance in medicine*, vol. 29, no. 6, pp. 759–766, 1993.

[27] J. J. Mack, K. Youssef, O. D. Noel, M. P. Lake, A. Wu, M. L. Iruela-Arispe, and L.-S. Bouchard, "Real-time maps of fluid flow fields in porous biomaterials," *Biomaterials*, vol. 34, no. 8, pp. 1980–1986, 2013.

[28] J. J. Mack, T. S. Mosqueiro, B. J. Archer, W. M. Jones, H. Sunshine, G. C. Faas, A. Briot, R. L. Aragón, T. Su, M. C. Romay, *et al.*, "Notch1 is a mechanosensor in adult arteries," *Nature communications*, vol. 8, no. 1, p. 1620, 2017.

[29] T.-M. De Witte, L. E. Fratila-Apachitei, A. A. Zadpoor, and N. A. Peppas, "Bone tissue engineering via growth factor delivery: from scaffolds to complex matrices," *Regenerative biomaterials*, vol. 5, no. 4, pp. 197–211, 2018.

[30] M. Silindir and A. Y. Özer, "Sterilization methods and the comparison of e-beam sterilization with gamma radiation sterilization," *Fabad Journal of Pharmaceutical Sciences*, vol. 34, no. 1, p. 43, 2009.

[31] B. Archer, T. Ueberrueck, J. Mack, K. Youssef, N. N. Jarenwattananon, D. Rall, D. Wypysek, M. Wiese, B. Bluemich, M. Wessling, *et al.*, "Non-invasive quantification of cell density in 3d gels by mri," 2018.

[32] B. Archer, J. Mack, S. Acosta, R. Nakasone, F. Dahoud, K. Youssef, A. Goldstein, A. Goldsman, M. C. Held, M. Wiese, *et al.*, "Mapping cell viability quantitatively and independently from cell density in 3d gels noninvasively," *IEEE Transactions on Biomedical Engineering*, 2021.

[33] R. Moscalu, A. M. Smith, and H. L. Sharma, "Diseases that can be cured only by organ donations," *Archive of Clinical Cases*, vol. 2, no. 4, 2015.

[34] P. K. Garg and V. P. Singh, "Organ failure due to systemic injury in acute pancreatitis," *Gastroenterology*, vol. 156, no. 7, pp. 2008–2023, 2019.

[35] K. K. Khush, W. S. Cherikh, D. C. Chambers, S. Goldfarb, D. Hayes, A. Y. Kucheryavaya, B. J. Levvey, B. Meiser, J. W. Rossano, and J. Stehlik, "The international thoracic organ transplant registry of the international society for heart and lung transplantation: thirty-fifth adult heart transplantation report—2018; focus theme: multiorgan transplantation," *The Journal of Heart and Lung Transplantation*, vol. 37, no. 10, pp. 1155–1168, 2018.

[36] D. C. Chambers, W. S. Cherikh, S. B. Goldfarb, D. Hayes, A. Y. Kucheryavaya, A. E. Toll, K. K. Khush, B. J. Levvey, B. Meiser, J. W. Rossano, *et al.*, "The international thoracic organ transplant registry of the international society for heart and lung

transplantation: thirty-fifth adult lung and heart-lung transplant report—2018; focus theme: multiorgan transplantation," *The Journal of Heart and Lung Transplantation*, vol. 37, no. 10, pp. 1169–1183, 2018.

[37] G. Cholankeril and A. Ahmed, "Alcoholic liver disease replaces hepatitis c virus infection as the leading indication for liver transplantation in the united states," *Clinical gastroenterology and hepatology: the official clinical practice journal of the American Gastroenterological Association*, vol. 16, no. 8, p. 1356, 2018.

[38] M. F. Chedid, "Nonalcoholic steatohepatitis: the second leading indication for liver transplantation in the usa," 2017.

[39] L. Wang, F.-S. Wang, and M. E. Gershwin, "Human autoimmune diseases: a comprehensive update," *Journal of internal medicine*, vol. 278, no. 4, pp. 369–395, 2015.

[40] R. S. Ambekar and B. Kandasubramanian, "Progress in the advancement of porous biopolymer scaffold: tissue engineering application," *Industrial & Engineering Chemistry Research*, vol. 58, no. 16, pp. 6163–6194, 2019.

[41] O. Lauthe, M. Soubeyrand, A. Babinet, V. Dumaine, P. Anract, and D. Biau, "The indications and donor-site morbidity of tibial cortical strut autografts in the management of defects in long bones," *Bone Joint J*, vol. 100, no. 5, pp. 667–674, 2018.

[42] I. Ducic, J. Yoon, and G. Buncke, "Chronic postoperative complications and donor site morbidity after sural nerve autograft harvest or biopsy," *Microsurgery*, vol. 40, no. 6, pp. 710–716, 2020.

[43] B. A. Hacken, L. K. Keyt, D. P. Leland, M. D. LaPrade, C. L. Camp, B. A. Levy, M. J. Stuart, and A. J. Krych, "A novel scoring instrument to assess donor site morbidity after anterior cruciate ligament reconstruction with a patellar tendon autograft at 2-year follow-up using contemporary graft-harvesting techniques," *Orthopaedic Journal of Sports Medicine*, vol. 8, no. 6, p. 2325967120925482, 2020.

[44] J. C. Garces, S. Giusti, C. Staffeld-Coit, H. Bohorquez, A. J. Cohen, and G. E. Loss, "Antibody-mediated rejection: a review," *Ochsner Journal*, vol. 17, no. 1, pp. 46–55, 2017.

[45] A. Loupy and C. Lefaucheur, "Antibody-mediated rejection of solid-organ allografts," *New England Journal of Medicine*, vol. 379, no. 12, pp. 1150–1160, 2018.

[46] S. L. White, W. Rawlinson, P. Boan, V. Sheppeard, G. Wong, K. Waller, H. Opdam, J. Kaldor, M. Fink, D. Verran, *et al.*, "Infectious disease transmission in solid organ transplantation: donor evaluation, recipient risk, and outcomes of transmission," *Transplantation direct*, vol. 5, no. 1, 2019.

[47] R. Saidi and S. H. Kenari, "Challenges of organ shortage for transplantation: solutions and opportunities," *International journal of organ transplantation medicine*, vol. 5, no. 3, p. 87, 2014.

[48] R. J. Ploeg, J. Niesing, M. H. Sieber-Rasch, L. Willems, K. Kranenburg, and A. Geertsma, "Shortage of donation despite an adequate number of donors: a professional attitude?," *Transplantation*, vol. 76, no. 6, pp. 948–955, 2003.

[49] C. E. Harris and S. P. Alcorn, "To solve a deadly shortage: economic incentives for human organ donation," *Issues L. & Med.*, vol. 16, p. 213, 2000.

[50] G. E. Maeng, S. D. Das, S. M. Greising, W. Gong, B. N. Singh, K. Stefan, D. Mickelson, E. Skie, O. Gafni, J. R. Sorensen, C. V. Weaver, D. J. Garry, and M. G. Garry, "Humanized skeletal muscle in myf5/myod/myf6-null pig embryos," *Nature Biomedical Engineering*, 2021.

[51] R. Lanza, R. Langer, J. P. Vacanti, and A. Atala, *Principles of tissue engineering*. Academic press, 2020.

[52] R. Lanza, R. Langer, and J. P. Vacanti, *Principles of tissue engineering*. Academic press, 2011.

[53] M. E. Scarritt, N. C. Pashos, and B. A. Bunnell, "A review of cellularization strategies for tissue engineering of whole organs," *Frontiers in bioengineering and biotechnology*, vol. 3, p. 43, 2015.

[54] X. Hu, J. Huang, Z. Ye, L. Xia, M. Li, B. Lv, X. Shen, and Z. Luo, "A novel scaffold with longitudinally oriented microchannels promotes peripheral nerve regeneration," *Tissue Engineering Part A*, vol. 15, no. 11, pp. 3297–3308, 2009.

[55] P. Fagerholm, N. S. Lagali, J. A. Ong, K. Merrett, W. B. Jackson, J. W. Polarek, E. J. Suuronen, Y. Liu, I. Brunette, and M. Griffith, "Stable corneal regeneration four years after implantation of a cell-free recombinant human collagen scaffold," *Biomaterials*, vol. 35, no. 8, pp. 2420–2427, 2014.

[56] H. Naderi, M. M. Matin, and A. R. Bahrami, "Critical issues in tissue engineering: biomaterials, cell sources, angiogenesis, and drug delivery systems," *Journal of biomaterials applications*, vol. 26, no. 4, pp. 383–417, 2011.

[57] N. Datta, H. L. Holtorf, V. I. Sikavitsas, J. A. Jansen, and A. G. Mikos, "Effect of bone extracellular matrix synthesized in vitro on the osteoblastic differentiation of marrow stromal cells," *Biomaterials*, vol. 26, no. 9, pp. 971–977, 2005.

[58] C. Z. Jin, B. H. Choi, S. R. Park, and B.-H. Min, "Cartilage engineering using cell-derived extracellular matrix scaffold in vitro," *Journal of Biomedical Materials Research Part A: An Official Journal of The Society for Biomaterials, The Japanese Society for Biomaterials, and The Australian Society for Biomaterials and the Korean Society for Biomaterials*, vol. 92, no. 4, pp. 1567–1577, 2010.

[59] S. Hinderer, N. Shen, L.-J. Ringuette, J. Hansmann, D. P. Reinhardt, S. Y. Brucker, E. C. Davis, and K. Schenke-Layland, "In vitro elastogenesis: instructing human vascular smooth muscle cells to generate an elastic fiber-containing extracellular matrix scaffold," *Biomedical Materials*, vol. 10, no. 3, p. 034102, 2015.

[60] T. Shimizu, M. Yamato, A. Kikuchi, and T. Okano, "Cell sheet engineering for myocardial tissue reconstruction," *Biomaterials*, vol. 24, no. 13, pp. 2309–2316, 2003.

[61] D. B. Joseph, J. G. Borer, R. E. De Filippo, S. J. Hodges, and G. A. McLorie, "Autologous cell seeded biodegradable scaffold for augmentation cystoplasty: phase ii study in children and adolescents with spina bifida," *The Journal of urology*, vol. 191, no. 5, pp. 1389–1395, 2014.

[62] H. Orabi, T. AbouShwareb, Y. Zhang, J. J. Yoo, and A. Atala, "Cell-seeded tubularized scaffolds for reconstruction of long urethral defects: a preclinical study," *European urology*, vol. 63, no. 3, pp. 531–538, 2013.

[63] S. Tang, J. Zhu, Y. Xu, A. P. Xiang, M. H. Jiang, and D. Quan, "The effects of gradients of nerve growth factor immobilized pcla scaffolds on neurite outgrowth in vitro and peripheral nerve regeneration in rats," *Biomaterials*, vol. 34, no. 29, pp. 7086–7096, 2013.

[64] J. S. Hammond, T. W. Gilbert, D. Howard, A. Zaitoun, G. Michalopoulos, K. M. Shakesheff, I. J. Beckingham, and S. F. Badylak, "Scaffolds containing growth factors and extracellular matrix induce hepatocyte proliferation and cell migration in normal and regenerating rat liver," *Journal of hepatology*, vol. 54, no. 2, pp. 279–287, 2011.

[65] J. Leotot, L. Coquelin, G. Bodivit, P. Bierling, P. Hernigou, H. Rouard, and N. Chevallier, "Platelet lysate coating on scaffolds directly and indirectly enhances cell migration, improving bone and blood vessel formation," *Acta biomaterialia*, vol. 9, no. 5, pp. 6630–6640, 2013.

[66] M. B. Pabbruwe, W. Kafienah, J. F. Tarlton, S. Mistry, D. J. Fox, and A. P. Hollander, "Repair of meniscal cartilage white zone tears using a stem cell/collagen-scaffold implant," *Biomaterials*, vol. 31, no. 9, pp. 2583–2591, 2010.

[67] B. Shrestha, K. Coykendall, Y. Li, A. Moon, P. Priyadarshani, and L. Yao, "Repair of injured spinal cord using biomaterial scaffolds and stem cells," *Stem cell research & therapy*, vol. 5, no. 4, p. 91, 2014.

[68] M. Hatami, N. Z. Mehrjardi, S. Kiani, K. Hemmesi, H. Azizi, A. Shahverdi, and H. Baharvand, "Human embryonic stem cell-derived neural precursor transplants in collagen scaffolds promote recovery in injured rat spinal cord," *Cytotherapy*, vol. 11, no. 5, pp. 618–630, 2009.

[69] R. Pörtner, S. Nagel-Heyer, C. Goepfert, P. Adamietz, and N. M. Meenen, "Bioreactor design for tissue engineering," *Journal of bioscience and bioengineering*, vol. 100, no. 3, pp. 235–245, 2005.

[70] A. Ratcliffe and L. E. Niklason, "Bioreactors and bioprocessing for tissue engineering," *Annals of the New York Academy of Sciences*, vol. 961, no. 1, pp. 210–215, 2002.

[71] K. Van't Riet and J. Tramper, *Basic bioreactor design*. CRC press, 1991.

[72] H. Baumert, P. Simon, M. Hekmati, G. Fromont, M. Levy, A. Balaton, V. Molinié, and B. Malavaud, "Development of a seeded scaffold in the great omentum: feasibility of an in vivo bioreactor for bladder tissue engineering," *european urology*, vol. 52, no. 3, pp. 884–892, 2007.

[73] G. E. Holt, J. L. Halpern, T. T. Dovan, D. Hamming, and H. S. Schwartz, "Evolution of an in vivo bioreactor," *Journal of orthopaedic research*, vol. 23, no. 4, pp. 916–923, 2005.

[74] C. A. Heath, "Cells for tissue engineering," *Trends in biotechnology*, vol. 18, no. 1, pp. 17–19, 2000.

[75] G. F. Muschler and R. J. Midura, "Connective tissue progenitors: practical concepts for clinical applications," *Clinical Orthopaedics and Related Research®*, vol. 395, pp. 66–80, 2002.

[76] K. Takahashi and S. Yamanaka, "Induction of pluripotent stem cells from mouse embryonic and adult fibroblast cultures by defined factors," *cell*, vol. 126, no. 4, pp. 663–676, 2006.

[77] K. Takahashi, K. Tanabe, M. Ohnuki, M. Narita, T. Ichisaka, K. Tomoda, and S. Yamanaka, "Induction of pluripotent stem cells from adult human fibroblasts by defined factors," *cell*, vol. 131, no. 5, pp. 861–872, 2007.

[78] G. F. Muschler, C. Nakamoto, and L. G. Griffith, "Engineering principles of clinical cell-based tissue engineering," *JBJS*, vol. 86, no. 7, pp. 1541–1558, 2004.

[79] J. San Choi, E. Y. Kim, M. J. Kim, M. Giegengack, F. A. Khan, G. Khang, and S. Soker, "In vitro evaluation of the interactions between human corneal endothelial cells and extracellular matrix proteins," *Biomedical materials*, vol. 8, no. 1, p. 014108, 2013.

[80] B. Loveland, T. Johns, I. Mackay, F. Vaillant, Z. Wang, and P. Hertzog, "Validation of the mtt dye assay for enumeration of cells in proliferative and antiproliferative assays.," *Biochemistry international*, vol. 27, no. 3, pp. 501–510, 1992.

[81] L. Huyck, C. Ampe, and M. Van Troys, "The xtt cell proliferation assay applied to cell layers embedded in three-dimensional matrix," *Assay and drug development technologies*, vol. 10, no. 4, pp. 382–392, 2012.

[82] E. Dirice, S. Kahraman, W. Jiang, A. El Ouaamari, D. F. De Jesus, A. K. Teo, J. Hu, D. Kawamori, J. L. Gaglia, D. Mathis, *et al.*, "Soluble factors secreted by t cells promote β-cell proliferation," *Diabetes*, vol. 63, no. 1, pp. 188–202, 2014.

[83] D. Giuffrida, I. Rogers, A. Nagy, A. Calogero, T. Brown, and R. Casper, "Human embryonic stem cells secrete soluble factors that inhibit cancer cell growth," *Cell proliferation*, vol. 42, no. 6, pp. 788–798, 2009.

[84] S.-H. Yang, M.-J. Park, I.-H. Yoon, S.-Y. Kim, S.-H. Hong, J.-Y. Shin, H.-Y. Nam, Y.-H. Kim, B. Kim, and C.-G. Park, "Soluble mediators from mesenchymal stem cells suppress t cell proliferation by inducing il-10," *Experimental & molecular medicine*, vol. 41, no. 5, pp. 315–324, 2009.

[85] T. Teshima, H. Matsumoto, and H. Koyama, "Soluble factors from adipose tissue-derived mesenchymal stem cells promote canine hepatocellular carcinoma cell proliferation and invasion," *PLoS One*, vol. 13, no. 1, p. e0191539, 2018.

[86] K. Anselme, L. Ploux, and A. Ponche, "Cell/material interfaces: influence of surface chemistry and surface topography on cell adhesion," *Journal of Adhesion Science and Technology*, vol. 24, no. 5, pp. 831–852, 2010.

[87] A. Curtis and C. Wilkinson, "Topographical control of cells," *Biomaterials*, vol. 18, no. 24, pp. 1573–1583, 1997.

[88] A. M. Ross, Z. Jiang, M. Bastmeyer, and J. Lahann, "Physical aspects of cell culture substrates: topography, roughness, and elasticity," *Small*, vol. 8, no. 3, pp. 336–355, 2012.

[89] R. G. Wells, "The role of matrix stiffness in regulating cell behavior," *Hepatology*, vol. 47, no. 4, pp. 1394–1400, 2008.

[90] J. Ando, H. Nomura, and A. Kamiya, "The effect of fluid shear stress on the migration and proliferation of cultured endothelial cells," *Microvascular research*, vol. 33, no. 1, pp. 62–70, 1987.

[91] K. Yamamoto, T. Takahashi, T. Asahara, N. Ohura, T. Sokabe, A. Kamiya, and J. Ando, "Proliferation, differentiation, and tube formation by endothelial progenitor cells in response to shear stress," *Journal of Applied Physiology*, vol. 95, no. 5, pp. 2081–2088, 2003.

[92] S. Kapur, D. J. Baylink, and K.-H. W. Lau, "Fluid flow shear stress stimulates human osteoblast proliferation and differentiation through multiple interacting and competing signal transduction pathways," *Bone*, vol. 32, no. 3, pp. 241–251, 2003.

[93] C. Dewey Jr, S. Bussolari, M. Gimbrone Jr, and P. F. Davies, "The dynamic response of vascular endothelial cells to fluid shear stress," 1981.

[94] S. Liu, R. Tao, M. Wang, J. Tian, G. M. Genin, T. J. Lu, and F. Xu, "Regulation of cell behavior by hydrostatic pressure," *Applied mechanics reviews*, vol. 71, no. 4, 2019.

[95] C. Chen, X. Bai, Y. Ding, and I.-S. Lee, "Electrical stimulation as a novel tool for regulating cell behavior in tissue engineering," *Biomaterials research*, vol. 23, no. 1, pp. 1–12, 2019.

[96] S. Samavedi, A. R. Whittington, and A. S. Goldstein, "Calcium phosphate ceramics in bone tissue engineering: a review of properties and their influence on cell behavior," *Acta biomaterialia*, vol. 9, no. 9, pp. 8037–8045, 2013.

[97] J. Kim, S. Y. Jeong, Y. M. Ju, J. J. Yoo, T. L. Smith, G. Khang, S. J. Lee, and A. Atala, "In vitro osteogenic differentiation of human amniotic fluid-derived stem cells on a poly (lactide-co-glycolide)(plga)–bladder submucosa matrix (bsm) composite scaffold for bone tissue engineering," *Biomedical Materials*, vol. 8, no. 1, p. 014107, 2013.

[98] J. A. Madri and M. Marx, "Matrix composition, organization and soluble factors: modulators of microvascular cell differentiation in vitro," *Kidney international*, vol. 41, no. 3, pp. 560–565, 1992.

[99] C. Sobacchi, E. Palagano, A. Villa, and C. Menale, "Soluble factors on stage to direct mesenchymal stem cells fate," *Frontiers in bioengineering and biotechnology*, vol. 5, p. 32, 2017.

[100] J.-F. Feng, J. Liu, X.-Z. Zhang, L. Zhang, J.-Y. Jiang, J. Nolta, and M. Zhao, "Guided migration of neural stem cells derived from human embryonic stem cells by an electric field," *Stem cells*, vol. 30, no. 2, pp. 349–355, 2012.

[101] C.-C. Liang, A. Y. Park, and J.-L. Guan, "In vitro scratch assay: a convenient and inexpensive method for analysis of cell migration in vitro," *Nature protocols*, vol. 2, no. 2, p. 329, 2007.

[102] L. Lara Rodriguez and I. C. Schneider, "Directed cell migration in multi-cue environments," *Integrative biology*, vol. 5, no. 11, pp. 1306–1323, 2013.

[103] R. J. Petrie, A. D. Doyle, and K. M. Yamada, "Random versus directionally persistent cell migration," *Nature reviews Molecular cell biology*, vol. 10, no. 8, pp. 538–549, 2009.

[104] C. D. Reyes and A. J. García, "A centrifugation cell adhesion assay for high-throughput screening of biomaterial surfaces," *Journal of Biomedical Materials Research Part A: An Official Journal of The Society for Biomaterials, The Japanese Society for Biomaterials, and The Australian Society for Biomaterials and the Korean Society for Biomaterials*, vol. 67, no. 1, pp. 328–333, 2003.

[105] T. Nagel, N. Resnick, W. J. Atkinson, C. F. Dewey, M. A. Gimbrone, *et al.*, "Shear stress selectively upregulates intercellular adhesion molecule-1 expression in cultured human vascular endothelial cells.," *The Journal of clinical investigation*, vol. 94, no. 2, pp. 885–891, 1994.

[106] Y. Ganji, Q. Li, E. S. Quabius, M. Böttner, C. Selhuber-Unkel, and M. Kasra, "Cardiomyocyte behavior on biodegradable polyurethane/gold nanocomposite scaffolds under electrical stimulation," *Materials Science and Engineering: C*, vol. 59, pp. 10–18, 2016.

[107] M. Radisic, H. Park, H. Shing, T. Consi, F. J. Schoen, R. Langer, L. E. Freed, and G. Vunjak-Novakovic, "Functional assembly of engineered myocardium by electrical stimulation of cardiac myocytes cultured on scaffolds," *Proceedings of the National Academy of Sciences*, vol. 101, no. 52, pp. 18129–18134, 2004.

[108] A.-C. Vion, M. Kheloufi, A. Hammoutene, J. Poisson, J. Lasselin, C. Devue, I. Pic, N. Dupont, J. Busse, K. Stark, *et al.*, "Autophagy is required for endothelial cell alignment and atheroprotection under physiological blood flow," *Proceedings of the National Academy of Sciences*, vol. 114, no. 41, pp. E8675–E8684, 2017.

[109] K. B. Vartanian, S. J. Kirkpatrick, S. R. Hanson, and M. T. Hinds, "Endothelial cell cytoskeletal alignment independent of fluid shear stress on micropatterned surfaces," *Biochemical and biophysical research communications*, vol. 371, no. 4, pp. 787–792, 2008.

[110] L. E. Goldfinger, E. Tzima, R. Stockton, W. B. Kiosses, K. Kinbara, E. Tkachenko, E. Gutierrez, A. Groisman, P. Nguyen, S. Chien, *et al.*, "Localized $\alpha 4$ integrin phosphorylation directs shear stress–induced endothelial cell alignment," *Circulation research*, vol. 103, no. 2, pp. 177–185, 2008.

[111] R. L. Reis, *Encyclopedia of tissue engineering and regenerative medicine*. Academic Press, 2019.

[112] S. Hashmi, *Comprehensive materials finishing*. Elsevier, 2016.

[113] S. L. Gupton and C. M. Waterman-Storer, "Spatiotemporal feedback between actomyosin and focal-adhesion systems optimizes rapid cell migration," *Cell*, vol. 125, no. 7, pp. 1361–1374, 2006.

[114] A. A. Lee, D. A. Graham, S. Dela Cruz, A. Ratcliffe, and W. J. Karlon, "Fluid shear stress-induced alignment of cultured vascular smooth muscle cells," *J. Biomech. Eng.*, vol. 124, no. 1, pp. 37–43, 2002.

[115] R. Juliano, "Cooperation between soluble factors and integrin-mediated cell anchorage in the control of cell growth and differentiation," *Bioessays*, vol. 18, no. 11, pp. 911–917, 1996.

[116] J. C. Kohn, D. W. Zhou, F. Bordeleau, A. L. Zhou, B. N. Mason, M. J. Mitchell, M. R. King, and C. A. Reinhart-King, "Cooperative effects of matrix stiffness and fluid shear stress on endothelial cell behavior," *Biophysical journal*, vol. 108, no. 3, pp. 471–478, 2015.

[117] S. Thomopoulos, R. Das, V. Birman, L. Smith, K. Ku, E. L. Elson, K. M. Pryse, J. P. Marquez, and G. M. Genin, "Fibrocartilage tissue engineering: the role of the stress environment on cell morphology and matrix expression," *Tissue Engineering Part A*, vol. 17, no. 7-8, pp. 1039–1053, 2011.

[118] M. B. Chan-Park, J. Y. Shen, Y. Cao, Y. Xiong, Y. Liu, S. Rayatpisheh, G. C.-W. Kang, and H. P. Greisler, "Biomimetic control of vascular smooth muscle cell morphology and phenotype for functional tissue-engineered small-diameter blood vessels," *Journal of Biomedical Materials Research Part A: An Official Journal of The Society for Biomaterials, The Japanese Society for Biomaterials, and The Australian Society for Biomaterials and the Korean Society for Biomaterials*, vol. 88, no. 4, pp. 1104–1121, 2009.

[119] N. F. Huang, J. Okogbaa, J. C. Lee, A. Jha, T. S. Zaitseva, M. V. Paukshto, J. S. Sun, N. Punjya, G. G. Fuller, and J. P. Cooke, "The modulation of endothelial cell morphology, function, and survival using anisotropic nanofibrillar collagen scaffolds," *Biomaterials*, vol. 34, no. 16, pp. 4038–4047, 2013.

[120] R. L. Carrier, M. Papadaki, M. Rupnick, F. J. Schoen, N. Bursac, R. Langer, L. E. Freed, G. Vunjak-Novakovic, *et al.*, "Cardiac tissue engineering: cell seeding, cultivation parameters, and tissue construct characterization," *Biotechnology and bioengineering*, vol. 64, no. 5, pp. 580–589, 1999.

[121] K. Takeno, S. Kobayashi, K. Negoro, K. Uchida, T. Miyazaki, T. Yayama, S. Shimada, and H. Baba, "Physical limitations to tissue engineering of intervertebral disc cells: effect of extracellular osmotic change on glycosaminoglycan production and cell metabolism," *Journal of Neurosurgery: Spine*, vol. 7, no. 6, pp. 637–644, 2007.

[122] H. E. Gruber, K. Leslie, J. Ingram, H. J. Norton, and E. N. Hanley Jr, "Cell-based tissue engineering for the intervertebral disc: in vitro studies of human disc cell gene expression and matrix production within selected cell carriers," *The Spine Journal*, vol. 4, no. 1, pp. 44–55, 2004.

[123] L. Liu, B. D. Ratner, E. H. Sage, and S. Jiang, "Endothelial cell migration on surface-density gradients of fibronectin, vegf, or both proteins," *Langmuir*, vol. 23, no. 22, pp. 11168–11173, 2007.

[124] R. G. Breuls, T. U. Jiya, and T. H. Smit, "Scaffold stiffness influences cell behavior: opportunities for skeletal tissue engineering," *The open orthopaedics journal*, vol. 2, p. 103, 2008.

[125] M. Y. Rotenberg, E. Ruvinov, A. Armoza, and S. Cohen, "A multi-shear perfusion bioreactor for investigating shear stress effects in endothelial cell constructs," *Lab on a Chip*, vol. 12, no. 15, pp. 2696–2703, 2012.

[126] J. W. Allen and S. N. Bhatia, "Formation of steady-state oxygen gradients in vitro: Application to liver zonation," *Biotechnology and bioengineering*, vol. 82, no. 3, pp. 253–262, 2003.

[127] H. Kang, K. J. Bayless, and R. Kaunas, "Fluid shear stress modulates endothelial cell invasion into three-dimensional collagen matrices," *American Journal of Physiology-Heart and Circulatory Physiology*, vol. 295, no. 5, pp. H2087–H2097, 2008.

[128] C.-L. E. Helm, M. E. Fleury, A. H. Zisch, F. Boschetti, and M. A. Swartz, "Synergy between interstitial flow and vegf directs capillary morphogenesis in vitro through a gradient amplification mechanism," *Proceedings of the National Academy of Sciences*, vol. 102, no. 44, pp. 15779–15784, 2005.

[129] J. W. Song and L. L. Munn, "Fluid forces control endothelial sprouting," *Proceedings of the National Academy of Sciences*, vol. 108, no. 37, pp. 15342–15347, 2011.

[130] C. P. Ng, C.-L. E. Helm, and M. A. Swartz, "Interstitial flow differentially stimulates blood and lymphatic endothelial cell morphogenesis in vitro," *Microvascular research*, vol. 68, no. 3, pp. 258–264, 2004.

[131] D. P. Noren, W. H. Chou, S. H. Lee, A. A. Qutub, A. Warmflash, D. S. Wagner, A. S. Popel, and A. Levchenko, "Endothelial cells decode vegf-mediated ca2+ signaling patterns to produce distinct functional responses," *Science signaling*, vol. 9, no. 416, pp. ra20–ra20, 2016.

[132] F. Moccia, S. Negri, M. Shekha, P. Faris, and G. Guerra, "Endothelial ca2+ signaling, angiogenesis and vasculogenesis: just what it takes to make a blood vessel," *International journal of molecular sciences*, vol. 20, no. 16, p. 3962, 2019.

[133] G. Chen, T. Ushida, and T. Tateishi, "Scaffold design for tissue engineering," *Macromolecular Bioscience*, vol. 2, no. 2, pp. 67–77, 2002.

[134] A. Eltom, G. Zhong, and A. Muhammad, "Scaffold techniques and designs in tissue engineering functions and purposes: a review," *Advances in Materials Science and Engineering*, vol. 2019, 2019.

[135] H. Zhang and J. E. Barralet, "Mimicking oxygen delivery and waste removal functions of blood," *Advanced drug delivery reviews*, vol. 122, pp. 84–104, 2017.

[136] T. S. Le, M. McCann, S. M. Azarin, and W.-S. Hu, "An introduction to mammalian cell culture," *Chem Eng Prog*, vol. 112, no. 4, pp. 34–40, 2016.

[137] H.-I. Chang and Y. Wang, "Cell responses to surface and architecture of tissue engineering scaffolds," in *Regenerative medicine and tissue engineering-cells and biomaterials*, InTechOpen, 2011.

[138] C. Chollet, C. Chanseau, M. Remy, A. Guignandon, R. Bareille, C. Labrugère, L. Bordenave, and M.-C. Durrieu, "The effect of rgd density on osteoblast and endothelial cell behavior on rgd-grafted polyethylene terephthalate surfaces," *Biomaterials*, vol. 30, no. 5, pp. 711–720, 2009.

[139] R. J. Wade, E. J. Bassin, W. M. Gramlich, and J. A. Burdick, "Nanofibrous hydrogels with spatially patterned biochemical signals to control cell behavior," *Advanced Materials*, vol. 27, no. 8, pp. 1356–1362, 2015.

[140] M. Tanaka, A. Takayama, E. Ito, H. Sunami, S. Yamamoto, and M. Shimomura, "Effect of pore size of self-organized honeycomb-patterned polymer films on spreading, focal adhesion, proliferation, and function of endothelial cells," *Journal of nanoscience and nanotechnology*, vol. 7, no. 3, pp. 763–772, 2007.

[141] J. Zeltinger, J. K. Sherwood, D. A. Graham, R. Müeller, and L. G. Griffith, "Effect of pore size and void fraction on cellular adhesion, proliferation, and matrix deposition," *Tissue engineering*, vol. 7, no. 5, pp. 557–572, 2001.

[142] C. M. Tierney, M. G. Haugh, J. Liedl, F. Mulcahy, B. Hayes, and F. J. O'Brien, "The effects of collagen concentration and crosslink density on the biological, structural and mechanical properties of collagen-gag scaffolds for bone tissue engineering," *Journal of the mechanical behavior of biomedical materials*, vol. 2, no. 2, pp. 202–209, 2009.

[143] R. J. Pelham and Y.-l. Wang, "Cell locomotion and focal adhesions are regulated by substrate flexibility," *Proceedings of the National Academy of Sciences*, vol. 94, no. 25, pp. 13661–13665, 1997.

[144] Z. Wu, T. C. Ovaert, and G. L. Niebur, "Viscoelastic properties of human cortical bone tissue depend on gender and elastic modulus," *Journal of Orthopaedic Research*, vol. 30, no. 5, pp. 693–699, 2012.

[145] M. Ahearne, "Introduction to cell–hydrogel mechanosensing," *Interface focus*, vol. 4, no. 2, p. 20130038, 2014.

[146] Z. Sun, S. S. Guo, and R. Fässler, "Integrin-mediated mechanotransduction," *Journal of Cell Biology*, vol. 215, no. 4, pp. 445–456, 2016.

[147] F. J. O'brien, "Biomaterials & scaffolds for tissue engineering," *Materials today*, vol. 14, no. 3, pp. 88–95, 2011.

[148] J. Zhu and R. E. Marchant, "Design properties of hydrogel tissue-engineering scaffolds," *Expert review of medical devices*, vol. 8, no. 5, pp. 607–626, 2011.

[149] M. Tamaddon, S. Samizadeh, L. Wang, G. Blunn, and C. Liu, "Intrinsic osteoinductivity of porous titanium scaffold for bone tissue engineering," *International journal of biomaterials*, vol. 2017, 2017.

[150] B. Dabrowski, W. Swieszkowski, D. Godlinski, and K. J. Kurzydlowski, "Highly porous titanium scaffolds for orthopaedic applications," *Journal of biomedical materials research Part B: Applied biomaterials*, vol. 95, no. 1, pp. 53–61, 2010.

[151] F. Witte, H. Ulrich, C. Palm, and E. Willbold, "Biodegradable magnesium scaffolds: Part ii: Peri-implant bone remodeling," *Journal of biomedical materials research Part A*, vol. 81, no. 3, pp. 757–765, 2007.

[152] V. K. Balla, S. Bodhak, S. Bose, and A. Bandyopadhyay, "Porous tantalum structures for bone implants: fabrication, mechanical and in vitro biological properties," *Acta biomaterialia*, vol. 6, no. 8, pp. 3349–3359, 2010.

[153] H. Tiainen, S. P. Lyngstadaas, J. E. Ellingsen, and H. J. Haugen, "Ultra-porous titanium oxide scaffold with high compressive strength," *Journal of Materials Science: Materials in Medicine*, vol. 21, no. 10, pp. 2783–2792, 2010.

[154] Q. Fu, E. Saiz, M. N. Rahaman, and A. P. Tomsia, "Bioactive glass scaffolds for bone tissue engineering: state of the art and future perspectives," *Materials Science and Engineering: C*, vol. 31, no. 7, pp. 1245–1256, 2011.

[155] H. Seitz, W. Rieder, S. Irsen, B. Leukers, and C. Tille, "Three-dimensional printing of porous ceramic scaffolds for bone tissue engineering," *Journal of Biomedical Materials Research Part B: Applied Biomaterials: An Official Journal of The Society for Biomaterials, The Japanese Society for Biomaterials, and The Australian Society for Biomaterials and the Korean Society for Biomaterials*, vol. 74, no. 2, pp. 782–788, 2005.

[156] S. Bose and S. Tarafder, "Calcium phosphate ceramic systems in growth factor and drug delivery for bone tissue engineering: a review," *Acta biomaterialia*, vol. 8, no. 4, pp. 1401–1421, 2012.

[157] S. Panseri, C. Cunha, T. D'Alessandro, M. Sandri, A. Russo, G. Giavaresi, M. Marcacci, C. T. Hung, and A. Tampieri, "Magnetic hydroxyapatite bone substitutes to enhance tissue regeneration: evaluation in vitro using osteoblast-like cells and in vivo in a bone defect," *PloS one*, vol. 7, no. 6, p. e38710, 2012.

[158] S. Jana, S. J. Florczyk, M. Leung, and M. Zhang, "High-strength pristine porous chitosan scaffolds for tissue engineering," *Journal of Materials Chemistry*, vol. 22, no. 13, pp. 6291–6299, 2012.

[159] A. M. Ferreira, P. Gentile, V. Chiono, and G. Ciardelli, "Collagen for bone tissue regeneration," *Acta biomaterialia*, vol. 8, no. 9, pp. 3191–3200, 2012.

[160] H. J. Kim, U.-J. Kim, H. S. Kim, C. Li, M. Wada, G. G. Leisk, and D. L. Kaplan, "Bone tissue engineering with premineralized silk scaffolds," *Bone*, vol. 42, no. 6, pp. 1226–1234, 2008.

[161] A. Ferrand, S. Eap, L. Richert, S. Lemoine, D. Kalaskar, S. Demoustier-Champagne, H. Atmani, Y. Mély, F. Fioretti, G. Schlatter, *et al.*, "Osteogenetic properties of electrospun nanofibrous pcl scaffolds equipped with chitosan-b ased nanoreservoirs of growth factors," *Macromolecular bioscience*, vol. 14, no. 1, pp. 45–55, 2014.

[162] T.-H. Kim, Y.-P. Yun, Y.-E. Park, S.-H. Lee, W. Yong, J. Kundu, J. W. Jung, J.-H. Shim, D.-W. Cho, S. E. Kim, *et al.*, "In vitro and in vivo evaluation of bone formation using solid freeform fabrication-based bone morphogenic protein-2 releasing pcl/plga scaffolds," *Biomedical Materials*, vol. 9, no. 2, p. 025008, 2014.

[163] D. Grafahrend, K.-H. Heffels, M. V. Beer, P. Gasteier, M. Möller, G. Boehm, P. D. Dalton, and J. Groll, "Degradable polyester scaffolds with controlled surface chemistry combining minimal protein adsorption with specific bioactivation," *Nature materials*, vol. 10, no. 1, pp. 67–73, 2011.

[164] N. Taniguchi, S. Fujibayashi, M. Takemoto, K. Sasaki, B. Otsuki, T. Nakamura, T. Matsushita, T. Kokubo, and S. Matsuda, "Effect of pore size on bone ingrowth into porous titanium implants fabricated by additive manufacturing: An in vivo experiment," *Materials Science and Engineering: C*, vol. 59, pp. 690–701, 2016.

[165] W. C. Head, D. J. Bauk, and R. H. Emerson Jr, "Titanium as the material of choice for cementless femoral components in total hip arthroplasty.," *Clinical orthopaedics and related research*, no. 311, pp. 85–90, 1995.

[166] P. Zorlutuna, Z. Rong, P. Vadgama, and V. Hasirci, "Influence of nanopatterns on endothelial cell adhesion: enhanced cell retention under shear stress," *Acta biomaterialia*, vol. 5, no. 7, pp. 2451–2459, 2009.

[167] W. A. Comisar, N. H. Kazmers, D. J. Mooney, and J. J. Linderman, "Engineering rgd nanopatterned hydrogels to control preosteoblast behavior: a combined computational and experimental approach," *Biomaterials*, vol. 28, no. 30, pp. 4409–4417, 2007.

[168] K. Youssef, J. Mack, M. Iruela-Arispe, and L.-S. Bouchard, "Macro-scale topology optimization for controlling internal shear stress in a porous scaffold bioreactor," *Biotechnology and bioengineering*, vol. 109, no. 7, pp. 1844–1854, 2012.

[169] A. Berner, M. Woodruff, C. Lam, M. Arafat, S. Saifzadeh, R. Steck, J. Ren, M. Nerlich, A. K. Ekaputra, I. Gibson, *et al.*, "Effects of scaffold architecture on cranial bone healing," *International journal of oral and maxillofacial surgery*, vol. 43, no. 4, pp. 506–513, 2014.

[170] E. Wintermantel, J. Mayer, J. Blum, K.-L. Eckert, P. Lüscher, and M. Mathey, "Tissue engineering scaffolds using superstructures," *Biomaterials*, vol. 17, no. 2, pp. 83–91, 1996.

[171] G. Raeber, M. Lutolf, and J. Hubbell, "Molecularly engineered peg hydrogels: a novel model system for proteolytically mediated cell migration," *Biophysical journal*, vol. 89, no. 2, pp. 1374–1388, 2005.

[172] J. C. Schense and J. A. Hubbell, "Three-dimensional migration of neurites is mediated by adhesion site density and affinity," *Journal of Biological Chemistry*, vol. 275, no. 10, pp. 6813–6818, 2000.

[173] Y. Tsuji, X. Li, and M. Shibayama, "Evaluation of mesh size in model polymer networks consisting of tetra-arm and linear poly (ethylene glycol) s," *Gels*, vol. 4, no. 2, p. 50, 2018.

[174] L. Moroni, J. De Wijn, and C. Van Blitterswijk, "Three-dimensional fiber-deposited peot/pbt copolymer scaffolds for tissue engineering: Influence of porosity, molecular network mesh size, and swelling in aqueous media on dynamic mechanical properties," *Journal of Biomedical Materials Research Part A: An Official Journal of The Society for Biomaterials, The Japanese Society for Biomaterials, and The Australian Society for Biomaterials and the Korean Society for Biomaterials*, vol. 75, no. 4, pp. 957–965, 2005.

[175] D. J. Munoz-Pinto, A. S. Bulick, and M. S. Hahn, "Uncoupled investigation of scaffold modulus and mesh size on smooth muscle cell behavior," *Journal of Biomedical Materials Research Part A: An Official Journal of The Society for Biomaterials, The*

Japanese Society for Biomaterials, and The Australian Society for Biomaterials and the Korean Society for Biomaterials, vol. 90, no. 1, pp. 303–316, 2009.

[176] F. Brandl, F. Sommer, and A. Goepferich, "Rational design of hydrogels for tissue engineering: impact of physical factors on cell behavior," *Biomaterials*, vol. 28, no. 2, pp. 134–146, 2007.

[177] R. J. McCoy, C. Jungreuthmayer, and F. J. O'Brien, "Influence of flow rate and scaffold pore size on cell behavior during mechanical stimulation in a flow perfusion bioreactor," *Biotechnology and bioengineering*, vol. 109, no. 6, pp. 1583–1594, 2012.

[178] S. Yunoki, T. Ikoma, A. Monkawa, K. Ohta, M. Kikuchi, S. Sotome, K. Shinomiya, and J. Tanaka, "Control of pore structure and mechanical property in hydroxyapatite/-collagen composite using unidirectional ice growth," *Materials letters*, vol. 60, no. 8, pp. 999–1002, 2006.

[179] C. M. Murphy, M. G. Haugh, and F. J. O'brien, "The effect of mean pore size on cell attachment, proliferation and migration in collagen–glycosaminoglycan scaffolds for bone tissue engineering," *Biomaterials*, vol. 31, no. 3, pp. 461–466, 2010.

[180] M. H. Zaman, L. M. Trapani, A. L. Sieminski, D. MacKellar, H. Gong, R. D. Kamm, A. Wells, D. A. Lauffenburger, and P. Matsudaira, "Migration of tumor cells in 3d matrices is governed by matrix stiffness along with cell-matrix adhesion and proteolysis," *Proceedings of the National Academy of Sciences*, vol. 103, no. 29, pp. 10889–10894, 2006.

[181] O. Lieleg, R. M. Baumgärtel, and A. R. Bausch, "Selective filtering of particles by the extracellular matrix: an electrostatic bandpass," *Biophysical journal*, vol. 97, no. 6, pp. 1569–1577, 2009.

[182] R. C. Arevalo, J. S. Urbach, and D. L. Blair, "Size-dependent rheology of type-i collagen networks," *Biophysical journal*, vol. 99, no. 8, pp. L65–L67, 2010.

[183] M. Lovett, K. Lee, A. Edwards, and D. L. Kaplan, "Vascularization strategies for tissue engineering," *Tissue Engineering Part B: Reviews*, vol. 15, no. 3, pp. 353–370, 2009.

[184] D. Y. Wong, D. R. Griffin, J. Reed, and A. M. Kasko, "Photodegradable hydrogels to generate positive and negative features over multiple length scales," *Macromolecules*, vol. 43, no. 6, pp. 2824–2831, 2010.

[185] G. Y. Huang, L. H. Zhou, Q. C. Zhang, Y. M. Chen, W. Sun, F. Xu, and T. J. Lu, "Microfluidic hydrogels for tissue engineering," *Biofabrication*, vol. 3, no. 1, p. 012001, 2011.

[186] H.-J. Sung, C. Meredith, C. Johnson, and Z. S. Galis, "The effect of scaffold degradation rate on three-dimensional cell growth and angiogenesis," *Biomaterials*, vol. 25, no. 26, pp. 5735–5742, 2004.

[187] H. Zhang, L. Zhou, and W. Zhang, "Control of scaffold degradation in tissue engineering: a review," *Tissue Engineering Part B: Reviews*, vol. 20, no. 5, pp. 492–502, 2014.

[188] C. Selden and B. Fuller, "Role of bioreactor technology in tissue engineering for clinical use and therapeutic target design," *Bioengineering*, vol. 5, no. 2, p. 32, 2018.

[189] S. Ahmed, V. M. Chauhan, A. M. Ghaemmaghami, and J. W. Aylott, "New generation of bioreactors that advance extracellular matrix modelling and tissue engineering," *Biotechnology letters*, vol. 41, no. 1, pp. 1–25, 2019.

[190] I. Martin, D. Wendt, and M. Heberer, "The role of bioreactors in tissue engineering," *TRENDS in Biotechnology*, vol. 22, no. 2, pp. 80–86, 2004.

[191] J. Rouwkema, N. C. Rivron, and C. A. van Blitterswijk, "Vascularization in tissue engineering," *Trends in biotechnology*, vol. 26, no. 8, pp. 434–441, 2008.

[192] I. S. Suh and C.-G. Lee, "Photobioreactor engineering: design and performance," *Biotechnology and Bioprocess Engineering*, vol. 8, no. 6, p. 313, 2003.

[193] M. Ebara, *Biomaterials Nanoarchitectonics*. William Andrew, 2016.

[194] C. Halberstadt and D. F. Emerich, *Cellular transplantation: from laboratory to clinic*. Elsevier, 2011.

[195] J. Sun, J. Li, C. Li, and Y. Yu, "Role of bone morphogenetic protein-2 in osteogenic differentiation of mesenchymal stem cells," *Molecular medicine reports*, vol. 12, no. 3, pp. 4230–4237, 2015.

[196] S. Javerzat, P. Auguste, and A. Bikfalvi, "The role of fibroblast growth factors in vascular development," *Trends in molecular medicine*, vol. 8, no. 10, pp. 483–489, 2002.

[197] M. Korc and R. E. Friesel, "The role of fibroblast growth factors in tumor growth," *Current cancer drug targets*, vol. 9, no. 5, pp. 639–651, 2009.

[198] M. L. Radomsky, A. Y. Thompson, R. C. Spiro, and J. W. Poser, "Potential role of fibroblast growth factor in enhancement of fracture healing," *Clinical Orthopaedics and Related Research®*, vol. 355, pp. S283–S293, 1998.

[199] M. A. van Kelle, P. J. Oomen, J. A. Bulsink, M. W. Janssen-van den Broek, R. G. Lopata, M. C. Rutten, S. Loerakker, and C. V. Bouten, "A bioreactor to identify the driving mechanical stimuli of tissue growth and remodeling," *Tissue Engineering Part C: Methods*, vol. 23, no. 6, pp. 377–387, 2017.

[200] D. Lacroix, M. Brunelli, C. Perrault, A. Baldit, M. Shariatzadeh, A. C. Marin, A. Castro, and S. Barreto, *Multiscale Mechanobiology in Tissue Engineering*. Springer, 2019.

[201] N. Salehi-Nik, G. Amoabediny, B. Pouran, H. Tabesh, M. A. Shokrgozar, N. Haghighipour, N. Khatibi, F. Anisi, K. Mottaghy, and B. Zandieh-Doulabi, "Engineering parameters in bioreactor's design: a critical aspect in tissue engineering," *BioMed research international*, vol. 2013, 2013.

[202] G. Vunjak-Novakovic, B. Obradovic, I. Martin, P. M. Bursac, R. Langer, and L. E. Freed, "Dynamic cell seeding of polymer scaffolds for cartilage tissue engineering," *Biotechnology progress*, vol. 14, no. 2, pp. 193–202, 1998.

[203] A. L. Radtke and M. M. Herbst-Kralovetz, "Culturing and applications of rotating wall vessel bioreactor derived 3d epithelial cell models," *JoVE (Journal of Visualized Experiments)*, no. 62, p. e3868, 2012.

[204] D. Pazzano, K. A. Mercier, J. M. Moran, S. S. Fong, D. D. DiBiasio, J. X. Rulfs, S. S. Kohles, and L. J. Bonassar, "Comparison of chondrogensis in static and perfused bioreactor culture," *Biotechnology progress*, vol. 16, no. 5, pp. 893–896, 2000.

[205] M. Radisic, A. Marsano, R. Maidhof, Y. Wang, and G. Vunjak-Novakovic, "Cardiac tissue engineering using perfusion bioreactor systems," *Nature protocols*, vol. 3, no. 4, p. 719, 2008.

[206] G. N. Bancroft, V. I. Sikavitsas, and A. G. Mikos, "Design of a flow perfusion bioreactor system for bone tissue-engineering applications," *Tissue engineering*, vol. 9, no. 3, pp. 549–554, 2003.

[207] J. R. Masters and G. N. Stacey, "Changing medium and passaging cell lines," *Nature protocols*, vol. 2, no. 9, p. 2276, 2007.

[208] E. C. Novosel, C. Kleinhans, and P. J. Kluger, "Vascularization is the key challenge in tissue engineering," *Advanced drug delivery reviews*, vol. 63, no. 4-5, pp. 300–311, 2011.

[209] C. Y. J. Ma, R. Kumar, X. Y. Xu, and A. Mantalaris, "A combined fluid dynamics, mass transport and cell growth model for a three-dimensional perfused biorector for tissue engineering of haematopoietic cells," *Biochemical engineering journal*, vol. 35, no. 1, pp. 1–11, 2007.

[210] C. K. Griffith, C. Miller, R. C. Sainson, J. W. Calvert, N. L. Jeon, C. C. Hughes, and S. C. George, "Diffusion limits of an in vitro thick prevascularized tissue," *Tissue engineering*, vol. 11, no. 1-2, pp. 257–266, 2005.

[211] T. Rademakers, J. M. Horvath, C. A. van Blitterswijk, and V. L. LaPointe, "Oxygen and nutrient delivery in tissue engineering: Approaches to graft vascularization," *Journal of tissue engineering and regenerative medicine*, vol. 13, no. 10, pp. 1815–1829, 2019.

[212] J. Rouwkema and A. Khademhosseini, "Vascularization and angiogenesis in tissue engineering: beyond creating static networks," *Trends in biotechnology*, vol. 34, no. 9, pp. 733–745, 2016.

[213] A. P. McGuigan and M. V. Sefton, "Vascularized organoid engineered by modular assembly enables blood perfusion," *Proceedings of the National Academy of Sciences*, vol. 103, no. 31, pp. 11461–11466, 2006.

[214] G. M. Price, K. H. Wong, J. G. Truslow, A. D. Leung, C. Acharya, and J. Tien, "Effect of mechanical factors on the function of engineered human blood microvessels in microfluidic collagen gels," *Biomaterials*, vol. 31, no. 24, pp. 6182–6189, 2010.

[215] A. Ueda, M. Koga, M. Ikeda, S. Kudo, and K. Tanishita, "Effect of shear stress on microvessel network formation of endothelial cells with in vitro three-dimensional model," *American Journal of Physiology-Heart and Circulatory Physiology*, vol. 287, no. 3, pp. H994–H1002, 2004.

[216] G. Cheng, S. Liao, H. K. Wong, D. A. Lacorre, E. di Tomaso, P. Au, D. Fukumura, R. K. Jain, and L. L. Munn, "Engineered blood vessel networks connect to host vasculature via wrapping-and-tapping anastomosis," *Blood*, vol. 118, no. 17, pp. 4740–4749, 2011.

[217] E. Silva and D. J. Mooney, "Spatiotemporal control of vascular endothelial growth factor delivery from injectable hydrogels enhances angiogenesis," *Journal of Thrombosis and Haemostasis*, vol. 5, no. 3, pp. 590–598, 2007.

[218] M. N. Nakatsu, R. C. Sainson, J. N. Aoto, K. L. Taylor, M. Aitkenhead, S. Pérez-del Pulgar, P. M. Carpenter, and C. C. Hughes, "Angiogenic sprouting and capillary lumen formation modeled by human umbilical vein endothelial cells (huvec) in fibrin gels: the role of fibroblasts and angiopoietin-1," *Microvascular research*, vol. 66, no. 2, pp. 102–112, 2003.

[219] P. Campinho, A. Vilfan, and J. Vermot, "Blood flow forces in shaping the vascular system: A focus on endothelial cell behavior.," *Front. Physiol*, vol. 11, no. 552, pp. 10–3389, 2020.

[220] S. Cai and J. Xi, "A control approach for pore size distribution in the bone scaffold based on the hexahedral mesh refinement," *Computer-Aided Design*, vol. 40, no. 10-11, pp. 1040–1050, 2008.

[221] H. Tai, M. L. Mather, D. Howard, W. Wang, L. J. White, J. A. Crowe, S. P. Morgan, A. Chandra, D. J. Williams, S. M. Howdle, *et al.*, "Control of pore size and structure of tissue engineering scaffolds produced by supercritical fluid processing," *Eur Cell Mater*, vol. 14, pp. 64–77, 2007.

[222] Y.-J. Li, M. Yu, C.-D. Xue, H.-J. Zhang, G.-Z. Wang, X.-M. Chen, and K.-R. Qin, "Modeling of endothelial calcium responses within a microfluidic generator of spatiotemporal atp and shear stress signals," *Micromachines*, vol. 12, no. 2, p. 161, 2021.

[223] G. Yang, B. Mahadik, J. Y. Choi, and J. P. Fisher, "Vascularization in tissue engineering: fundamentals and state-of-art," *Progress in Biomedical Engineering*, vol. 2, no. 1, p. 012002, 2020.

[224] K. Youssef, N. N. Jarenwattananon, B. J. Archer, J. Mack, M. L. Iruela-Arispe, and L.-S. Bouchard, "4-d flow control in porous scaffolds: Toward a next generation of bioreactors," *IEEE Transactions on Biomedical Engineering*, vol. 64, no. 1, pp. 61–69, 2016.

[225] B. Zohar, Y. Blinder, M. Epshtein, A. A. Szklanny, B. Kaplan, N. Korin, D. J. Mooney, and S. Levenberg, "Multi-flow channel bioreactor enables real-time monitoring of cellular dynamics in 3d engineered tissue," *Communications biology*, vol. 2, no. 1, pp. 1–10, 2019.

[226] O. E. Kadri, C. Williams III, V. Sikavitsas, and R. S. Voronov, "Numerical accuracy comparison of two boundary conditions commonly used to approximate shear stress distributions in tissue engineering scaffolds cultured under flow perfusion," *International journal for numerical methods in biomedical engineering*, vol. 34, no. 11, p. e3132, 2018.

[227] C. Williams, O. E. Kadri, R. S. Voronov, and V. I. Sikavitsas, "Time-dependent shear stress distributions during extended flow perfusion culture of bone tissue engineered constructs," *Fluids*, vol. 3, no. 2, p. 25, 2018.

[228] A. C. Marin, T. Grossi, E. Bianchi, G. Dubini, and D. Lacroix, "2d μ-particle image velocimetry and computational fluid dynamics study within a 3d porous scaffold," *Annals of biomedical engineering*, vol. 45, no. 5, pp. 1341–1351, 2017.

[229] Y. Guyot, F. Luyten, J. Schrooten, I. Papantoniou, and L. Geris, "A three-dimensional computational fluid dynamics model of shear stress distribution during neotissue growth in a perfusion bioreactor," *Biotechnology and bioengineering*, vol. 112, no. 12, pp. 2591–2600, 2015.

[230] I. Papantoniou, Y. Guyot, M. Sonnaert, G. Kerckhofs, F. P. Luyten, L. Geris, and J. Schrooten, "Spatial optimization in perfusion bioreactors improves bone tissue-engineered construct quality attributes," *Biotechnology and bioengineering*, vol. 111, no. 12, pp. 2560–2570, 2014.

[231] L. A. Hidalgo-Bastida, S. Thirunavukkarasu, S. Griffiths, S. H. Cartmell, and S. Naire, "Modeling and design of optimal flow perfusion bioreactors for tissue engineering applications," *Biotechnology and Bioengineering*, vol. 109, no. 4, pp. 1095–1099, 2012.

[232] J. Dubois, L. Tremblay, M. Lepage, and P. Vermette, "Flow dynamics within a bioreactor for tissue engineering by residence time distribution analysis combined with fluorescence and magnetic resonance imaging to investigate forced permeability and apparent diffusion coefficient in a perfusion cell culture chamber," *Biotechnology and bioengineering*, vol. 108, no. 10, pp. 2488–2498, 2011.

[233] W. L. Grayson, T. P. Martens, G. M. Eng, M. Radisic, and G. Vunjak-Novakovic, "Biomimetic approach to tissue engineering," in *Seminars in cell & developmental biology*, vol. 20, pp. 665–673, Elsevier, 2009.

[234] C. J. Elkins and M. T. Alley, "Magnetic resonance velocimetry: applications of magnetic resonance imaging in the measurement of fluid motion," *Experiments in Fluids*, vol. 43, no. 6, pp. 823–858, 2007.

[235] A. B. Yeatts, E. M. Geibel, F. F. Fears, and J. P. Fisher, "Human mesenchymal stem cell position within scaffolds influences cell fate during dynamic culture," *Biotechnology and Bioengineering*, vol. 109, no. 9, pp. 2381–2391, 2012.

[236] B. Porter, R. Zauel, H. Stockman, R. Guldberg, and D. Fyhrie, "3-d computational modeling of media flow through scaffolds in a perfusion bioreactor," *Journal of biomechanics*, vol. 38, no. 3, pp. 543–549, 2005.

[237] D. Katti, A. Sharma, and K. Katti, "Predictive methodologies for design of bone tissue engineering scaffolds," in *Materials for bone disorders*, pp. 453–492, Elsevier, 2017.

[238] J. A. Asenjo, *Bioreactor system design*. CRC Press, 1994.

[239] S. P. Langdon, "Cell culture contamination," in *Cancer Cell Culture*, pp. 309–317, Springer, 2004.

[240] T. F. P. de Oliveira, A. A. Fonseca Jr, M. F. Camargos, A. M. de Oliveira, A. C. P. Cottorello, A. dos Reis Souza, I. G. de Almeida, and M. B. Heinemann, "Detection of contaminants in cell cultures, sera and trypsin," *Biologicals*, vol. 41, no. 6, pp. 407–414, 2013.

[241] M. A. Suckow, S. H. Weisbroth, and C. L. Franklin, *The laboratory rat*. Elsevier, 2005.

[242] S. Rottem and M. F. Barile, "Beware of mycoplasmas," *Trends in biotechnology*, vol. 11, no. 4, pp. 143–151, 1993.

[243] A. Kappeler, C. Lutze-Wallace, T. Sapp, and M. Sidhu, "Detection of bovine polyomavirus contamination in fetal bovine sera and modified live viral vaccines using polymerase chain reaction," *Biologicals*, vol. 24, no. 2, pp. 131–135, 1996.

[244] R. W. Nims and P. J. Price, "Best practices for detecting and mitigating the risk of cell culture contaminants," *In Vitro Cellular & Developmental Biology-Animal*, vol. 53, no. 10, pp. 872–879, 2017.

[245] A. Mahmood and S. Ali, "Microbial and viral contamination of animal and stem cell cultures: Common contaminants, detection, and elimination," *J. Stem Cell Res. Ther*, vol. 2, no. 5, pp. 1–8, 2017.

[246] C. K. Lincoln and M. G. Gabridge, "Cell culture contamination: sources, consequences, prevention, and elimination," in *Methods in cell biology*, vol. 57, pp. 49–65, Elsevier, 1998.

[247] A. E. Acosta-Gío, J. L. Rueda-Patiño, and L. Sánchez-Pérez, "Sporicidal activity in liquid chemical products to sterilize or high-level disinfect medical and dental instruments," *American journal of infection control*, vol. 33, no. 5, pp. 307–309, 2005.

[248] J. Padia and P. Huntington, "Gas filtration: sterile micro-filtration for bioreactors," *Filtration & separation*, vol. 43, no. 4, pp. 28–31, 2006.

[249] B. P. Fairand, *Radiation sterilization for health care products: x-ray, gamma, and electron beam*. CRC Press, 2001.

[250] B. Ballantyne and S. L. Jordan, "Toxicological, medical and industrial hygiene aspects of glutaraldehyde with particular reference to its biocidal use in cold sterilization procedures," *Journal of Applied Toxicology: An International Journal*, vol. 21, no. 2, pp. 131–151, 2001.

[251] M. Diab-Elschahawi, A. Blacky, N. Bachhofner, and W. Koller, "Lumen claims of the sterrad 100nx sterilizer: testing performance limits when processing equipment containing long, narrow lumens," *American journal of infection control*, vol. 39, no. 9, pp. 770–774, 2011.

[252] T. L. James, "Fundamentals of nmr," *Online Textbook: Department of Pharmaceutical Chemistry, University of California, San Francisco*, pp. 1–31, 1998.

[253] J. Keeler, *Understanding NMR spectroscopy*. John Wiley & Sons, 2011.

[254] P. J. Hore, *Nuclear magnetic resonance*. Oxford University Press, USA, 2015.

[255] M. H. Levitt, *Spin dynamics: basics of nuclear magnetic resonance*. John Wiley & Sons, 2001.

[256] S. Chuppa, Y.-S. Tsai, S. Yoon, S. Shackleford, C. Rozales, R. Bhat, G. Tsay, C. Matanguihan, K. Konstantinov, and D. Naveh, "Fermentor temperature as a tool for control of high-density perfusion cultures of mammalian cells," *Biotechnology and bioengineering*, vol. 55, no. 2, pp. 328–338, 1997.

[257] P. Jorjani and S. S. Ozturk, "Effects of cell density and temperature on oxygen consumption rate for different mammalian cell lines," *Biotechnology and bioengineering*, vol. 64, no. 3, pp. 349–356, 1999.

[258] J. C. Edwards, "Principles of nmr," *Process NMR Associates LLC, 87A Sand Pit Rd, Danbury CT*, vol. 6810, 2009.

[259] M. A. Brown and R. C. Semelka, *MRI: basic principles and applications*. John Wiley & Sons, 2011.

[260] S. Meiboom and D. Gill, "Modified spin-echo method for measuring nuclear relaxation times," *Review of scientific instruments*, vol. 29, no. 8, pp. 688–691, 1958.

[261] H. Y. Carr and E. M. Purcell, "Effects of diffusion on free precession in nuclear magnetic resonance experiments," *Physical review*, vol. 94, no. 3, p. 630, 1954.

[262] E. O. Stejskal and J. E. Tanner, "Spin diffusion measurements: spin echoes in the presence of a time-dependent field gradient," *The journal of chemical physics*, vol. 42, no. 1, pp. 288–292, 1965.

[263] E. L. Hahn, "Spin echoes," *Physical review*, vol. 80, no. 4, p. 580, 1950.

[264] J. E. Tanner, "Use of the stimulated echo in nmr diffusion studies," *The Journal of Chemical Physics*, vol. 52, no. 5, pp. 2523–2526, 1970.

[265] S. D. Wolff and R. S. Balaban, "Magnetization transfer contrast (mtc) and tissue water proton relaxation in vivo," *Magnetic resonance in medicine*, vol. 10, no. 1, pp. 135–144, 1989.

[266] J. Eng, T. L. Ceckler, and R. S. Balaban, "Quantitative 1h magnetization transfer imaging in vivo," *Magnetic resonance in medicine*, vol. 17, no. 2, pp. 304–314, 1991.

[267] D. Le Bihan and E. Breton, "Imagerie de diffusion in vivo par résonance magnétique nucléaire," *Comptes rendus de l'Académie des sciences. Série 2, Mécanique, Physique, Chimie, Sciences de l'univers, Sciences de la Terre*, vol. 301, no. 15, pp. 1109–1112, 1985.

[268] J. G. Sled, "Modelling and interpretation of magnetization transfer imaging in the brain," *Neuroimage*, vol. 182, pp. 128–135, 2018.

[269] W. Wu and K. L. Miller, "Image formation in diffusion mri: a review of recent technical developments," *Journal of Magnetic Resonance Imaging*, vol. 46, no. 3, pp. 646–662, 2017.

[270] G. Katti, S. A. Ara, and A. Shireen, "Magnetic resonance imaging (mri)–a review," *Int J Dent Clin*, vol. 3, no. 1, p. 65, 2011.

[271] M. Kinoshita, N. Hashimoto, T. Goto, N. Kagawa, H. Kishima, S. Izumoto, H. Tanaka, N. Fujita, and T. Yoshimine, "Fractional anisotropy and tumor cell density of the tumor core show positive correlation in diffusion tensor magnetic resonance imaging of malignant brain tumors," *Neuroimage*, vol. 43, no. 1, pp. 29–35, 2008.

[272] T. Beppu, T. Inoue, Y. Shibata, N. Yamada, A. Kurose, K. Ogasawara, A. Ogawa, and H. Kabasawa, "Fractional anisotropy value by diffusion tensor magnetic resonance imaging as a predictor of cell density and proliferation activity of glioblastomas," *Surgical neurology*, vol. 63, no. 1, pp. 56–61, 2005.

[273] T. Sugahara, Y. Korogi, M. Kochi, I. Ikushima, Y. Shigematu, T. Hirai, T. Okuda, L. Liang, Y. Ge, Y. Komohara, *et al.*, "Usefulness of diffusion-weighted mri with echo-planar technique in the evaluation of cellularity in gliomas," *Journal of Magnetic Resonance Imaging*, vol. 9, no. 1, pp. 53–60, 1999.

[274] T. L. Chenevert, L. D. Stegman, J. M. Taylor, P. L. Robertson, H. S. Greenberg, A. Rehemtulla, and B. D. Ross, "Diffusion magnetic resonance imaging: an early surrogate marker of therapeutic efficacy in brain tumors," *JNCI: Journal of the National Cancer Institute*, vol. 92, no. 24, pp. 2029–2036, 2000.

[275] Y. Hayashida, T. Hirai, S. Morishita, M. Kitajima, R. Murakami, Y. Korogi, K. Makino, H. Nakamura, I. Ikushima, M. Yamura, *et al.*, "Diffusion-weighted imaging of metastatic brain tumors: comparison with histologic type and tumor cellularity," *American journal of neuroradiology*, vol. 27, no. 7, pp. 1419–1425, 2006.

[276] H. Lyng, O. Haraldseth, and E. K. Rofstad, "Measurement of cell density and necrotic fraction in human melanoma xenografts by diffusion weighted magnetic resonance imaging," *Magnetic resonance in medicine*, vol. 43, no. 6, pp. 828–836, 2000.

[277] P. Gibbs, G. P. Liney, M. D. Pickles, B. Zelhof, G. Rodrigues, and L. W. Turnbull, "Correlation of adc and t2 measurements with cell density in prostate cancer at 3.0 tesla," *Investigative radiology*, vol. 44, no. 9, pp. 572–576, 2009.

[278] G. Manenti, M. Di Roma, S. Mancino, D. Bartolucci, G. Palmieri, R. Mastrangeli, R. Miano, E. Squillaci, and G. Simonetti, "Malignant renal neoplasms: correlation between adc values and cellularity in diffusion weighted magnetic resonance imaging at 3 t," *La radiologia medica*, vol. 113, no. 2, pp. 199–213, 2008.

[279] Y. Guo, Y.-Q. Cai, Z.-L. Cai, Y.-G. Gao, N.-Y. An, L. Ma, S. Mahankali, and J.-H. Gao, "Differentiation of clinically benign and malignant breast lesions using diffusion-weighted imaging," *Journal of magnetic resonance imaging*, vol. 16, no. 2, pp. 172–178, 2002.

[280] M. Hatakenaka, H. Soeda, H. Yabuuchi, Y. Matsuo, T. Kamitani, Y. Oda, M. Tsuneyoshi, and H. Honda, "Apparent diffusion coefficients of breast tumors: clinical application," *Magnetic Resonance in Medical Sciences*, vol. 7, no. 1, pp. 23–29, 2008.

[281] A. M. Mishra, R. K. Gupta, S. Saksena, K. N. Prasad, C. M. Pandey, D. Rathore, A. Purwar, R. K. Rathore, N. Husain, D. K. Jha, *et al.*, "Biological correlates of diffusivity in brain abscess," *Magnetic resonance in medicine*, vol. 54, no. 4, pp. 878–885, 2005.

[282] V. Tomar, A. Yadav, R. Rathore, S. Verma, R. Awasthi, V. Bharadwaj, B. Ojha, K. Prasad, and R. Gupta, "Apparent diffusion coefficient with higher b-value correlates better with viable cell count quantified from the cavity of brain abscess," *American Journal of Neuroradiology*, vol. 32, no. 11, pp. 2120–2125, 2011.

[283] A. M. Mishra, S. J. Reddy, M. Husain, S. Behari, N. Husain, K. N. Prasad, S. Kumar, and R. K. Gupta, "Comparison of the magnetization transfer ratio and fluid-attenuated inversion recovery imaging signal intensity in differentiation of various cystic intracranial mass lesions and its correlation with biological parameters," *Journal of Magnetic Resonance Imaging*, vol. 24, no. 1, pp. 52–56, 2006.

[284] T. Kurki, N. Lundbom, H. Kalimo, and S. Valtonen, "Mr classification of brain gliomas: value of magnetization transfer and conventional imaging," *Magnetic resonance imaging*, vol. 13, no. 4, pp. 501–511, 1995.

[285] O. Kaplan, P. C. van Cohen, and J. S. Cohen, "Nmr studies of metabolism of cells and perfused organs," in *In-Vivo Magnetic Resonance Spectroscopy III: In-Vivo MR Spectroscopy: Potential and Limitations*, pp. 3–52, Springer, 1992.

[286] M. Neeman, E. Rushkin, A. Kadouri, and H. Degani, "Adaptation of culture methods for nmr studies of anchorage-dependent cells," *Magnetic resonance in medicine*, vol. 7, no. 2, pp. 236–242, 1988.

[287] V. Khalilzad-Sharghi and H. Xu, "Design and fabrication of an mri-compatible, autonomous incubation system," *Annals of biomedical engineering*, vol. 43, no. 10, pp. 2406–2415, 2015.

[288] N. F. Schwenzer, E. F. Grönewäller, E. Rodegerdts, R. Kehlbach, S. H. Duda, and C. D. Claussen, "Mri-compatible incubation chamber for cell culture experiments," *Journal of Magnetic Resonance Imaging: An Official Journal of the International Society for Magnetic Resonance in Medicine*, vol. 23, no. 1, pp. 70–76, 2006.

[289] S. F. Othman, K. Wartella, V. Khalilzad Sharghi, and H. Xu, "The e-incubator: a magnetic resonance imaging-compatible mini incubator," *Tissue Engineering Part C: Methods*, vol. 21, no. 4, pp. 347–355, 2015.

[290] N. F. Schwenzer, R. Bantleon, B. Maurer, R. Kehlbach, C. Schraml, C. D. Claussen, and E. Rodegerdts, "Detection of dna double-strand breaks using γh2ax after mri exposure at 3 tesla: An in vitro study," *Journal of Magnetic Resonance Imaging: An Official Journal of the International Society for Magnetic Resonance in Medicine*, vol. 26, no. 5, pp. 1308–1314, 2007.

[291] P.-E. Le Renard, B. Nimmervoll, F. Fellner, and P. Oppelt, "Cisplatin in-vitro activity with co-exposure to mri," in *2018 EMF-Med 1st World Conference on Biomedical Applications of Electromagnetic Fields (EMF-Med)*, pp. 1–2, IEEE, 2018.

[292] S.-I. Chun, J.-H. Cho, Y. I. Yang, J.-W. Shin, W.-J. Shin, and C.-W. Mun, "Proton (1 h) nuclear magnetic resonance spectroscopy to define metabolomic changes as a biomarker of adipogenic differentiation in human mesenchymal stem cells," *Tissue Engineering and Regenerative Medicine*, vol. 9, no. 2, pp. 101–108, 2012.

[293] H. Y. Ban, J. W. Shin, S.-I. Chun, Y. G. Kang, Y. Wu, J. E. Kim, E. J. Lee, M. J. Kim, C.-W. Mun, and J.-W. Shin, "Distinguishing tendon and ligament fibroblasts based on 1 h nuclear magnetic resonance spectroscopy," *Tissue engineering and regenerative medicine*, vol. 13, no. 6, pp. 677–683, 2016.

[294] B.-M. Kang, C.-W. Mun, S.-I. Chun, T.-h. Kim, D.-B. Son, and H.-D. Kim, "Noninvasive and repetitive measurement of cellular metabolite from human osteosarcoma cells (mg-63) using 3.0 tesla proton (1h) mr spectroscopy," *Magnetic resonance in medicine*, vol. 76, no. 6, pp. 1912–1918, 2016.

[295] H. Jaganathan, D. L. Hugar, and A. Ivanisevic, "Examining mri contrast in three-dimensional cell culture phantoms with dna-templated nanoparticle chains," *ACS applied materials & interfaces*, vol. 3, no. 4, pp. 1282–1288, 2011.

[296] S. Chun, D. Kim, J. Cho, K. Hong, J. Shin, and C. Mun, "Preliminary study on mr spectroscopy measurements for metabolomic change during adipogenic differentiation of human mesenchymal stem cell," in *Proc Intl Soc Mag Reson Med*, vol. 19, p. 1461, 2011.

[297] K. Golman, M. Thaning, *et al.*, "Real-time metabolic imaging," *Proceedings of the National Academy of Sciences*, vol. 103, no. 30, pp. 11270–11275, 2006.

[298] Z. Wilson, A. Rostami-Hodjegan, J. Burn, A. Tooley, J. Boyle, S. Ellis, and G. Tucker, "Inter-individual variability in levels of human microsomal protein and hepatocellularity per gram of liver," *British journal of clinical pharmacology*, vol. 56, no. 4, pp. 433–440, 2003.

[299] B. Overmoyer, C. McLaren, and G. Brittenham, "Uniformity of liver density and nonheme (storage) iron distribution.," *Archives of pathology & laboratory medicine*, vol. 111, no. 6, pp. 549–554, 1987.

[300] M. Dvir-Ginzberg, I. Gamlieli-Bonshtein, R. Agbaria, and S. Cohen, "Liver tissue engineering within alginate scaffolds: effects of cell-seeding density on hepatocyte viability, morphology, and function," *Tissue engineering*, vol. 9, no. 4, pp. 757–766, 2003.

[301] O. Mykhaylyk, A. Steingötter, H. Perea, J. Aigner, R. Botnar, and C. Plank, "Nucleic acid delivery to magnetically-labeled cells in a 2d array and at the luminal surface of cell culture tube and their detection by mri," *Journal of biomedical nanotechnology*, vol. 5, no. 6, pp. 692–706, 2009.

[302] A. Klasson, M. Ahren, E. Hellqvist, F. Söderlind, A. Rosen, P.-O. Käll, K. Uvdal, and M. Engström, "Positive mri contrast enhancement in thp-1 cells with gd2o3 nanoparticles," *Contrast Media & Molecular Imaging*, vol. 3, no. 3, pp. 106–111, 2008.

[303] H. Weber, N. Baxan, D. Paul, J. Maclaren, D. Schmidig, M. Mohammadzadeh, J. Hennig, and D. von Elverfeldt, "Microcoil-based mri: feasibility study and cell culture applications using a conventional animal system," *Magnetic Resonance Materials in Physics, Biology and Medicine*, vol. 24, no. 3, pp. 137–145, 2011.

[304] N. Nitin, L. LaConte, O. Zurkiya, X. Hu, and G. Bao, "Functionalization and peptide-based delivery of magnetic nanoparticles as an intracellular mri contrast agent," *JBIC Journal of Biological Inorganic Chemistry*, vol. 9, no. 6, pp. 706–712, 2004.

[305] E. Küstermann, U. Himmelreich, K. Kandal, T. Geelen, A. Ketkar, D. Wiedermann, C. Strecker, J. Esser, S. Arnhold, and M. Hoehn, "Efficient stem cell labeling for mri studies," *Contrast media & molecular imaging*, vol. 3, no. 1, pp. 27–37, 2008.

[306] C. Planchamp, M. K. Ivancevic, C. M. Pastor, J.-P. Vallée, S. Pochon, F. Terrier, J. M. Mayer, and M. Reist, "Hollow fiber bioreactor: new development for the study of contrast agent transport into hepatocytes by magnetic resonance imaging," *Biotechnology and bioengineering*, vol. 85, no. 6, pp. 656–665, 2004.

[307] Y. Roth, A. Ocherashvilli, D. Daniels, J. Ruiz-Cabello, S. E. Maier, A. Orenstein, and Y. Mardor, "Quantification of water compartmentation in cell suspensions by diffusion-weighted and t 2-weighted mri," *Magnetic resonance imaging*, vol. 26, no. 1, pp. 88–102, 2008.

[308] A. Anderson, J. Xie, J. Pizzonia, R. Bronen, D. Spencer, and J. Gore, "Effects of cell volume fraction changes on apparent diffusion in human cells," *Magnetic resonance imaging*, vol. 18, no. 6, pp. 689–695, 2000.

[309] M. Waqas, C. Vierra, D. L. Kaplan, and S. Othman, "Feasibility of low field mri and proteomics for the analysis of tissue engineered bone," *Biomedical Physics & Engineering Express*, vol. 5, no. 2, p. 025037, 2019.

[310] S. N. Williams, R. M. Callies, and K. M. Brindle, "Mapping of oxygen tension and cell distribution in a hollow-fiber bioreactor using magnetic resonance imaging," *Biotechnology and bioengineering*, vol. 56, no. 1, pp. 56–61, 1997.

[311] R. Callies, M. E. Jackson, and K. M. Brindle, "Measurements of the growth and distribution of mammalian cells in a hollow–fiber bioreactor using nuclear magnetic resonance imaging," *Bio/Technology*, vol. 12, no. 1, pp. 75–78, 1994.

[312] H.-M. Zhou, J. Wang, C. Elliott, W. Wen, D. W. Hamilton, and S. J. Conway, "Spatiotemporal expression of periostin during skin development and incisional wound healing: lessons for human fibrotic scar formation," *Journal of cell communication and signaling*, vol. 4, no. 2, pp. 99–107, 2010.

[313] L. Holmgren, A. Glaser, S. Pfeifer-Ohlsson, and R. Ohlsson, "Angiogenesis during human extraembryonic development involves the spatiotemporal control of pdgf ligand and receptor gene expression," *Development*, vol. 113, no. 3, pp. 749–754, 1991.

[314] K. Stankunas, G. K. Ma, F. J. Kuhnert, C. J. Kuo, and C.-P. Chang, "Vegf signaling has distinct spatiotemporal roles during heart valve development," *Developmental biology*, vol. 347, no. 2, pp. 325–336, 2010.

[315] S. Maxeiner, O. Krüger, K. Schilling, O. Traub, S. Urschel, and K. Willecke, "Spatiotemporal transcription of connexin45 during brain development results in neuronal expression in adult mice," *Neuroscience*, vol. 119, no. 3, pp. 689–700, 2003.

[316] M. Iwashita, N. Kataoka, K. Toida, and Y. Kosodo, "Systematic profiling of spatiotemporal tissue and cellular stiffness in the developing brain," *Development*, vol. 141, no. 19, pp. 3793–3798, 2014.

[317] T. Schwend and S. C. Ahlgren, "Zebrafish con/disp1 reveals multiple spatiotemporal requirements for hedgehog-signaling in craniofacial development," *BMC developmental biology*, vol. 9, no. 1, p. 59, 2009.

[318] F. Serwane, A. Mongera, P. Rowghanian, D. A. Kealhofer, A. A. Lucio, Z. M. Hockenbery, and O. Campàs, "In vivo quantification of spatially varying mechanical properties in developing tissues," *Nature methods*, vol. 14, no. 2, p. 181, 2017.

[319] E. E. Hui and S. N. Bhatia, "Micromechanical control of cell–cell interactions," *Proceedings of the National Academy of Sciences*, vol. 104, no. 14, pp. 5722–5726, 2007.

[320] S. Toda, L. R. Blauch, S. K. Tang, L. Morsut, and W. A. Lim, "Programming self-organizing multicellular structures with synthetic cell-cell signaling," *Science*, vol. 361, no. 6398, pp. 156–162, 2018.

[321] M. C. Moorer and J. P. Stains, "Connexin43 and the intercellular signaling network regulating skeletal remodeling," *Current osteoporosis reports*, vol. 15, no. 1, pp. 24–31, 2017.

[322] J. Davies, "Using synthetic biology to explore principles of development," *Development*, vol. 144, no. 7, pp. 1146–1158, 2017.

[323] M. J. Song, D. Dean, and M. L. K. Tate, "In situ spatiotemporal mapping of flow fields around seeded stem cells at the subcellular length scale," *PLoS one*, vol. 5, no. 9, p. e12796, 2010.

[324] X. Xu, Z. Li, L. Cai, S. Calve, and C. P. Neu, "Mapping the nonreciprocal micromechanics of individual cells and the surrounding matrix within living tissues," *Scientific reports*, vol. 6, p. 24272, 2016.

[325] D. L. Butler, S. A. Hunter, K. Chokalingam, M. J. Cordray, J. Shearn, N. Juncosa-Melvin, S. Nirmalanandhan, and A. Jain, "Using functional tissue engineering and bioreactors to mechanically stimulate tissue-engineered constructs," *Tissue Engineering Part A*, vol. 15, no. 4, pp. 741–749, 2009.

[326] S. Grad, D. Eglin, M. Alini, and M. J. Stoddart, "Physical stimulation of chondrogenic cells in vitro: a review," *Clinical Orthopaedics and Related Research®*, vol. 469, no. 10, pp. 2764–2772, 2011.

[327] T. Wang, Z. Lin, R. E. Day, B. Gardiner, E. Landao-Bassonga, J. Rubenson, T. B. Kirk, D. W. Smith, D. G. Lloyd, G. Hardisty, *et al.*, "Programmable mechanical stimulation influences tendon homeostasis in a bioreactor system," *Biotechnology and bioengineering*, vol. 110, no. 5, pp. 1495–1507, 2013.

[328] C. Meinert, K. Schrobback, D. W. Hutmacher, and T. J. Klein, "A novel bioreactor system for biaxial mechanical loading enhances the properties of tissue-engineered human cartilage," *Scientific reports*, vol. 7, no. 1, pp. 1–14, 2017.

[329] V. David, A. Guignandon, A. Martin, L. Malaval, M.-H. Lafage-Proust, A. Rattner, V. Mann, B. Noble, D. B. Jones, and L. Vico, "Ex vivo bone formation in bovine trabecular bone cultured in a dynamic 3d bioreactor is enhanced by compressive mechanical strain," *Tissue Engineering Part A*, vol. 14, no. 1, pp. 117–126, 2008.

[330] Y. Chen, M. Schellekens, S. Zhou, J. Cadman, W. Li, R. Appleyard, and Q. Li, "Design optimization of scaffold microstructures using wall shear stress criterion towards regulated flow-induced erosion," *Journal of biomechanical engineering*, vol. 133, no. 8, p. 081008, 2011.

[331] J. T. Podichetty and S. V. Madihally, "Modeling of porous scaffold deformation induced by medium perfusion," *Journal of Biomedical Materials Research Part B: Applied Biomaterials*, vol. 102, no. 4, pp. 737–748, 2014.

[332] Y. Kim, H. Ko, I. K. Kwon, and K. Shin, "Extracellular matrix revisited: roles in tissue engineering," *International neurourology journal*, vol. 20, no. Suppl 1, p. S23, 2016.

[333] S. Van Vlierberghe, P. Dubruel, and E. Schacht, "Biopolymer-based hydrogels as scaffolds for tissue engineering applications: a review," *Biomacromolecules*, vol. 12, no. 5, pp. 1387–1408, 2011.

[334] A. Rahbari, H. Montazerian, E. Davoodi, and S. Homayoonfar, "Predicting permeability of regular tissue engineering scaffolds: scaling analysis of pore architecture, scaffold length, and fluid flow rate effects," *Computer methods in biomechanics and biomedical engineering*, vol. 20, no. 3, pp. 231–241, 2017.

[335] A. A. Al-Munajjed, M. Hien, R. Kujat, J. P. Gleeson, and J. Hammer, "Influence of pore size on tensile strength, permeability and porosity of hyaluronan-collagen scaffolds," *Journal of Materials Science: Materials in Medicine*, vol. 19, no. 8, pp. 2859–2864, 2008.

[336] S. Truscello, G. Kerckhofs, S. Van Bael, G. Pyka, J. Schrooten, and H. Van Oosterwyck, "Prediction of permeability of regular scaffolds for skeletal tissue engineering: a combined computational and experimental study," *Acta biomaterialia*, vol. 8, no. 4, pp. 1648–1658, 2012.

[337] F. J. O'Brien, B. A. Harley, M. A. Waller, I. V. Yannas, L. J. Gibson, and P. J. Prendergast, "The effect of pore size on permeability and cell attachment in collagen scaffolds for tissue engineering," *Technology and Health Care*, vol. 15, no. 1, pp. 3–17, 2007.

[338] B. Starly, E. Yildirim, and W. Sun, "A tracer metric numerical model for predicting tortuosity factors in three-dimensional porous tissue scaffolds," *Computer methods and programs in biomedicine*, vol. 87, no. 1, pp. 21–27, 2007.

[339] Y. Reinwald, R. Johal, A. Ghaemmaghami, F. Rose, S. Howdle, and K. Shakesheff, "Interconnectivity and permeability of supercritical fluid-foamed scaffolds and the effect of their structural properties on cell distribution," *Polymer*, vol. 55, no. 1, pp. 435–444, 2014.

[340] J. A. Stammen, S. Williams, D. N. Ku, and R. E. Guldberg, "Mechanical properties of a novel pva hydrogel in shear and unconfined compression," *Biomaterials*, vol. 22, no. 8, pp. 799–806, 2001.

[341] W. J. McCarty and M. Johnson, "The hydraulic conductivity of matrigel™," *Biorheology*, vol. 44, no. 5-6, pp. 303–317, 2007.

[342] M. M. Caruso, D. A. Davis, Q. Shen, S. A. Odom, N. R. Sottos, S. R. White, and J. S. Moore, "Mechanically-induced chemical changes in polymeric materials," *Chemical reviews*, vol. 109, no. 11, pp. 5755–5798, 2009.

[343] A. Charles, "Preparation of collagen sponge," Nov. 17 1964. US Patent 3,157,524.

[344] H.-W. Kang, Y. Tabata, and Y. Ikada, "Fabrication of porous gelatin scaffolds for tissue engineering," *Biomaterials*, vol. 20, no. 14, pp. 1339–1344, 1999.

[345] M. Anguiano, C. Castilla, M. Maška, C. Ederra, R. Peláez, X. Morales, G. Muñoz-Arrieta, M. Mujika, M. Kozubek, A. Muñoz-Barrutia, *et al.*, "Characterization of three-dimensional cancer cell migration in mixed collagen-matrigel scaffolds using microfluidics and image analysis," *PloS one*, vol. 12, no. 2, p. e0171417, 2017.

[346] Y.-l. Yang, S. Motte, and L. J. Kaufman, "Pore size variable type i collagen gels and their interaction with glioma cells," *Biomaterials*, vol. 31, no. 21, pp. 5678–5688, 2010.

[347] R. M. Kuntz and W. M. Saltzman, "Neutrophil motility in extracellular matrix gels: mesh size and adhesion affect speed of migration," *Biophysical Journal*, vol. 72, no. 3, pp. 1472–1480, 1997.

[348] M. Wiese, S. Benders, B. Blümich, and M. Wessling, "3d mri velocimetry of non-transparent 3d-printed staggered herringbone mixers," *Chemical Engineering Journal*, vol. 343, pp. 54–60, 2018.

[349] P. M. Sundaram, K. K. Rangharajan, E. Akbari, T. J. Hadick, J. W. Song, and S. Prakash, "Direct current electric field regulates endothelial permeability under physiologically relevant fluid forces in a microfluidic vessel bifurcation model," *Lab on a Chip*, vol. 21, no. 2, pp. 319–330, 2021.

[350] M. J. Alfa, P. DeGagne, N. Olson, and R. Hizon, "Comparison of liquid chemical sterilization with peracetic acid and ethylene oxide sterilization for long narrow lumens," *American journal of infection control*, vol. 26, no. 5, pp. 469–477, 1998.

[351] S. Liu, J. Neelavalli, Y.-C. N. Cheng, J. Tang, and E. Mark Haacke, "Quantitative susceptibility mapping of small objects using volume constraints," *Magnetic resonance in medicine*, vol. 69, no. 3, pp. 716–723, 2013.

[352] C. Walsh, N. Ovenden, E. Stride, and U. Cheema, "Quantification of cell-bubble interactions in a 3d engineered tissue phantom," *Scientific reports*, vol. 7, no. 1, p. 6331, 2017.

[353] M. Á. G. Ballester, A. P. Zisserman, and M. Brady, "Estimation of the partial volume effect in mri," *Medical image analysis*, vol. 6, no. 4, pp. 389–405, 2002.

[354] M. Shattuck, R. Behringer, G. Johnson, and J. G. Georgiadis, "Convection and flow in porous media. part 1. visualization by magnetic resonance imaging," *Journal of Fluid Mechanics*, vol. 332, no. 1, pp. 215–245, 1997.

[355] L. G. Raguin, S. L. Honecker, and J. G. Georgiadis, "Mri velocimetry in microchannel networks," in *2005 3rd IEEE/EMBS Special Topic Conference on Microtechnology in Medicine and Biology*, pp. 319–322, IEEE, 2005.

[356] R. S. Reneman, T. Arts, and A. P. Hoeks, "Wall shear stress–an important determinant of endothelial cell function and structure–in the arterial system in vivo," *Journal of vascular research*, vol. 43, no. 3, pp. 251–269, 2006.

[357] R. Perry and D. Green, "Perry's chemical engineer's handbook pdf," 1984.

[358] J. Happel, "Viscous flow relative to arrays of cylinders," *AIChE Journal*, vol. 5, no. 2, pp. 174–177, 1959.

[359] C. H. Chen, D. O. Clegg, and H. G. Hansma, "Structures and dynamic motion of laminin-1 as observed by atomic force microscopy," *Biochemistry*, vol. 37, no. 22, pp. 8262–8267, 1998.

[360] C. H. Chen and H. G. Hansma, "Basement membrane macromolecules: insights from atomic force microscopy," *Journal of structural biology*, vol. 131, no. 1, pp. 44–55, 2000.

[361] C. Leblond and S. Inoue, "Structure, composition, and assembly of basement membrane," *American journal of anatomy*, vol. 185, no. 4, pp. 367–390, 1989.

[362] V. Serpooshan, M. Julien, O. Nguyen, H. Wang, A. Li, N. Muja, J. E. Henderson, and S. N. Nazhat, "Reduced hydraulic permeability of three-dimensional collagen scaffolds attenuates gel contraction and promotes the growth and differentiation of mesenchymal stem cells," *Acta biomaterialia*, vol. 6, no. 10, pp. 3978–3987, 2010.

[363] J. Levick, "Flow through interstitium and other fibrous matrices," *Quarterly Journal of Experimental Physiology: Translation and Integration*, vol. 72, no. 4, pp. 409–437, 1987.

[364] H. Sage, R. G. Woodbury, and P. Bornstein, "Structural studies on human type iv collagen.," *Journal of Biological Chemistry*, vol. 254, no. 19, pp. 9893–9900, 1979.

[365] B. Trüeb, B. Gröbli, M. Spiess, B. Odermatt, and K. Winterhalter, "Basement membrane (type iv) collagen is a heteropolymer.," *Journal of Biological Chemistry*, vol. 257, no. 9, pp. 5239–5245, 1982.

[366] R. DÖLZ, J. ENGEL, and K. KÜHN, "Folding of collagen iv," *European journal of biochemistry*, vol. 178, no. 2, pp. 357–366, 1988.

[367] P. R. Macdonald, A. Lustig, M. O. Steinmetz, and R. A. Kammerer, "Laminin chain assembly is regulated by specific coiled-coil interactions," *Journal of structural biology*, vol. 170, no. 2, pp. 398–405, 2010.

[368] P. D. Yurchenco, Y.-S. Cheng, and J. C. Schittny, "Heparin modulation of laminin polymerization.," *Journal of Biological Chemistry*, vol. 265, no. 7, pp. 3981–3991, 1990.

[369] W. D. Comper, *Heparin (and Related Polysaccharides): Structural and Functional Properties*, vol. 7. Gordon & Breach Publishing Group, 1981.

[370] A. Oldberg, L. Kjellen, and M. Höök, "Cell-surface heparan sulfate. isolation and characterization of a proteoglycan from rat liver membranes.," *Journal of Biological Chemistry*, vol. 254, no. 17, pp. 8505–8510, 1979.

[371] R. V. Rice, E. F. Casassa, R. E. Kerwin, and M. D. Maser, "On the length and molecular weight of tropocollagen from calf skin," *Archives of biochemistry and biophysics*, vol. 105, no. 2, pp. 409–423, 1964.

[372] E. G. Young and J. Lorimer, "A comparison of the acid-soluble collagens from the skin and swim bladder of the cod," *Archives of biochemistry and biophysics*, vol. 92, no. 1, pp. 183–190, 1961.

[373] V. Serpooshan, N. Muja, B. Marelli, and S. N. Nazhat, "Fibroblast contractility and growth in plastic compressed collagen gel scaffolds with microstructures correlated with hydraulic permeability," *Journal of Biomedical Materials Research Part A*, vol. 96, no. 4, pp. 609–620, 2011.

[374] A. Wufsus, N. Macera, and K. Neeves, "The hydraulic permeability of blood clots as a function of fibrin and platelet density," *Biophysical journal*, vol. 104, no. 8, pp. 1812–1823, 2013.

[375] H. Brinkman, "A calculation of the viscous force exerted by a flowing fluid on a dense swarm of particles," *Flow, Turbulence and Combustion*, vol. 1, no. 1, p. 27, 1949.

[376] D. F. James and A. M. Davis, "Flow at the interface of a model fibrous porous medium," *Journal of Fluid Mechanics*, vol. 426, pp. 47–72, 2001.

[377] K. A. Barbee, P. F. Davies, and R. Lal, "Shear stress-induced reorganization of the surface topography of living endothelial cells imaged by atomic force microscopy.," *Circulation research*, vol. 74, no. 1, pp. 163–171, 1994.

[378] K. A. Barbee, T. Mundel, R. Lal, and P. F. Davies, "Subcellular distribution of shear stress at the surface of flow-aligned and nonaligned endothelial monolayers," *American Journal of Physiology-Heart and Circulatory Physiology*, vol. 268, no. 4, pp. H1765–H1772, 1995.

[379] P. F. Davies, T. Mundel, and K. A. Barbee, "A mechanism for heterogeneous endothelial responses to flow in vivo and in vitro," *Journal of biomechanics*, vol. 28, no. 12, pp. 1553–1560, 1995.

[380] M. A. Brown, R. K. Iyer, and M. Radisic, "Pulsatile perfusion bioreactor for cardiac tissue engineering," *Biotechnology progress*, vol. 24, no. 4, pp. 907–920, 2008.

[381] W. F. Pickard, "The ascent of sap in plants," *Progress in biophysics and molecular biology*, vol. 37, pp. 181–229, 1981.

[382] B. Garipcan, S. Maenz, T. Pham, U. Settmacher, K. D. Jandt, J. Zanow, and J. Bossert, "Image analysis of endothelial microstructure and endothelial cell dimensions of human arteries–a preliminary study," *Advanced Engineering Materials*, vol. 13, no. 1-2, pp. B54–B57, 2011.

[383] B. Dhandayuthapani, Y. Yoshida, T. Maekawa, and D. S. Kumar, "Polymeric scaffolds in tissue engineering application: a review," *International journal of polymer science*, vol. 2011, 2011.

[384] T. Takigawa and Y. Endo, "Effects of glutaraldehyde exposure on human health," *Journal of occupational health*, vol. 48, no. 2, pp. 75–87, 2006.

[385] R. Van der Sman, "Biopolymer gel swelling analysed with scaling laws and flory–rehner theory," *Food Hydrocolloids*, vol. 48, pp. 94–101, 2015.

[386] T. Gervais, J. El-Ali, A. Günther, and K. F. Jensen, "Flow-induced deformation of shallow microfluidic channels," *Lab on a Chip*, vol. 6, no. 4, pp. 500–507, 2006.

[387] G. L. Converse, E. E. Buse, K. R. Neill, C. R. McFall, H. N. Lewis, M. C. VeDepo, R. W. Quinn, and R. A. Hopkins, "Design and efficacy of a single-use bioreactor for heart valve tissue engineering," *Journal of Biomedical Materials Research Part B: Applied Biomaterials*, vol. 105, no. 2, pp. 249–259, 2017.

[388] A. C. Allori, E. H. Davidson, D. D. Reformat, A. M. Sailon, J. Freeman, A. Vaughan, D. Wootton, E. Clark, J. L. Ricci, and S. M. Warren, "Design and validation of a dynamic cell-culture system for bone biology research and exogenous tissue-engineering applications," *Journal of tissue engineering and regenerative medicine*, vol. 10, no. 10, 2016.

[389] N. Dahan, U. Sarig, T. Bronshtein, L. Baruch, T. Karram, A. Hoffman, and M. Machluf, "Dynamic autologous reendothelialization of small-caliber arterial extracellular matrix: A preclinical large animal study," *Tissue Engineering Part A*, vol. 23, no. 1-2, pp. 69–79, 2017.

[390] A. J. Rogers, V. G. Fast, and P. Sethu, "Biomimetic cardiac tissue model enables the adaption of human induced pluripotent stem cell cardiomyocytes to physiological hemodynamic loads," *Analytical chemistry*, vol. 88, no. 19, pp. 9862–9868, 2016.

[391] S.-K. Goh, S. Bertera, P. Olsen, J. E. Candiello, W. Halfter, G. Uechi, M. Balasubramani, S. A. Johnson, B. M. Sicari, E. Kollar, *et al.*, "Perfusion-decellularized pancreas as a natural 3d scaffold for pancreatic tissue and whole organ engineering," *Biomaterials*, vol. 34, no. 28, pp. 6760–6772, 2013.

[392] D. B. Kolesky, K. A. Homan, M. A. Skylar-Scott, and J. A. Lewis, "Three-dimensional bioprinting of thick vascularized tissues," *Proceedings of the National Academy of Sciences*, vol. 113, no. 12, pp. 3179–3184, 2016.

[393] M. I. Yoshikawa, S. Ohsumi, S. Sugata, M. Kataoka, S. Takashima, T. Mochizuki, H. Ikura, and Y. Imai, "Relation between cancer cellularity and apparent diffusion coefficient values using diffusion-weighted magnetic resonance imaging in breast cancer," *Radiation medicine*, vol. 26, no. 4, pp. 222–226, 2008.

[394] M. E. Bernardino, W. Small, J. Goldstein, C. W. Sewell, P. J. Sones, K. Gedgaudas-McClees, J. Galambos, J. Wenger, and W. Casarella, "Multiple nmr t2 relaxation values in human liver tissue," *American Journal of Roentgenology*, vol. 141, no. 6, pp. 1203–1208, 1983.

[395] U. Pilatus, H. Shim, D. Artemov, D. Davis, P. Van Zijl, and J. D. Glickson, "Intracellular volume and apparent diffusion constants of perfused cancer cell cultures, as measured by nmr," *Magnetic resonance in medicine*, vol. 37, no. 6, pp. 825–832, 1997.

[396] C. C. Miller, "The stokes-einstein law for diffusion in solution," *Proceedings of the Royal Society of London. Series A, Containing Papers of a Mathematical and Physical Character*, vol. 106, no. 740, pp. 724–749, 1924.

[397] P. W. Kuchel, K. Nagashima, S. Velan, V. Vijayaragavan, V. Nagarajan, K. H. Chuang, *et al.*, "Stejskal–tanner equation derived in full," *Concepts in Magnetic Resonance Part A*, vol. 40, no. 5, pp. 205–214, 2012.

[398] Y. Ling, J. Rubin, Y. Deng, C. Huang, U. Demirci, J. M. Karp, and A. Khademhosseini, "A cell-laden microfluidic hydrogel," *Lab on a Chip*, vol. 7, no. 6, pp. 756–762, 2007.

[399] E. L. Lehmann and J. P. Romano, *Testing statistical hypotheses*. Springer Science & Business Media, 2006.

[400] R. J. Ellis, "Macromolecular crowding: an important but neglected aspect of the intracellular environment," *Current opinion in structural biology*, vol. 11, no. 1, pp. 114–119, 2001.

[401] G. N. Ling, "What determines the normal water content of a living cell?," *Physiological chemistry and physics and medical NMR*, vol. 36, no. 1, pp. 1–20, 2004.

[402] E. Alcázar, M. Rocha-Leão, and J. Dweck, "Yeast intracellular water determination by thermogravimetry," *Journal of Thermal Analysis and Calorimetry*, vol. 59, no. 3, pp. 643–648, 2000.

[403] J. Guenoun, A. Ruggiero, G. Doeswijk, R. C. Janssens, G. A. Koning, G. Kotek, G. P. Krestin, and M. R. Bernsen, "In vivo quantitative assessment of cell viability of gadolinium or iron-labeled cells using mri and bioluminescence imaging," *Contrast media & molecular imaging*, vol. 8, no. 2, pp. 165–174, 2013.

[404] M. Yamada, P. T. Gurney, J. Chung, P. Kundu, M. Drukker, A. K. Smith, I. L. Weissman, D. Nishimura, R. C. Robbins, and P. C. Yang, "Manganese-guided cellular mri of human embryonic stem cell and human bone marrow stromal cell viability," *Magnetic Resonance in Medicine: An Official Journal of the International Society for Magnetic Resonance in Medicine*, vol. 62, no. 4, pp. 1047–1054, 2009.

[405] M. F. Wendland, M. Saeed, G. Lund, and C. B. Higgins, "Contrast-enhanced mri for quantification of myocardial viability," *Journal of Magnetic Resonance Imaging: An Official Journal of the International Society for Magnetic Resonance in Medicine*, vol. 10, no. 5, pp. 694–702, 1999.

[406] R. Goetti, G. Feuchtner, P. Stolzmann, O. F. Donati, M. Wieser, A. Plass, T. Frauenfelder, S. Leschka, and H. Alkadhi, "Delayed enhancement imaging of myocardial viability: low-dose high-pitch ct versus mri," *European radiology*, vol. 21, no. 10, p. 2091, 2011.

[407] R. J. Kim, D. S. Fieno, T. B. Parrish, K. Harris, E.-L. Chen, O. Simonetti, J. Bundy, J. P. Finn, F. J. Klocke, and R. M. Judd, "Relationship of mri delayed contrast enhancement to irreversible injury, infarct age, and contractile function," *Circulation*, vol. 100, no. 19, pp. 1992–2002, 1999.

[408] H. J. Park, S. H. Kim, K. M. Jang, S. Lim, T. W. Kang, H. C. Park, and D. Choi, "Added value of diffusion-weighted mri for evaluating viable tumor of hepatocellular carcinomas treated with radiotherapy in patients with chronic liver disease," *American Journal of Roentgenology*, vol. 202, no. 1, pp. 92–101, 2014.

[409] B. Gallez, G. Bacic, F. Goda, J. Jiang, J. A. O' Hara, J. F. Dunn, and H. M. Swartz, "Use of nitroxides for assessing perfusion, oxygenation, and viability of tissues: in vivo epr and mri studies," *Magnetic resonance in medicine*, vol. 35, no. 1, pp. 97–106, 1996.

[410] L. Røhl, L. Østergaard, C. Z. Simonsen, P. Vestergaard-Poulsen, G. Andersen, M. Sakoh, D. Le Bihan, and C. Gyldensted, "Viability thresholds of ischemic penumbra of hyperacute stroke defined by perfusion-weighted mri and apparent diffusion coefficient," *Stroke*, vol. 32, no. 5, pp. 1140–1146, 2001.

[411] O. H. Gröhn and R. A. Kauppinen, "Assessment of brain tissue viability in acute ischemic stroke by bold mri," *NMR in Biomedicine: An International Journal Devoted to the Development and Application of Magnetic Resonance In Vivo*, vol. 14, no. 7-8, pp. 432–440, 2001.

[412] L. Chen, D. M. Bouley, B. T. Harris, and K. Butts, "Mri study of immediate cell viability in focused ultrasound lesions in the rabbit brain," *Journal of Magnetic Resonance Imaging*, vol. 13, no. 1, pp. 23–30, 2001.

[413] D. S. Fieno, R. J. Kim, W. G. Rehwald, and R. M. Judd, "Physiological basis for potassium (39k) magnetic resonance imaging of the heart," *Circulation research*, vol. 84, no. 8, pp. 913–920, 1999.

[414] J. Deng, S. Virmani, J. Young, K. Harris, G.-Y. Yang, A. Rademaker, G. Woloschak, R. A. Omary, and A. C. Larson, "Diffusion-weighted propeller mri for quantitative assessment of liver tumor necrotic fraction and viable tumor volume in vx2 rabbits," *Journal of Magnetic Resonance Imaging: An Official Journal of the International Society for Magnetic Resonance in Medicine*, vol. 27, no. 5, pp. 1069–1076, 2008.

[415] E. C. Henning, C. Azuma, C. H. Sotak, and K. G. Helmer, "Multispectral quantification of tissue types in a rif-1 tumor model with histological validation. part i," *Magnetic Resonance in Medicine: An Official Journal of the International Society for Magnetic Resonance in Medicine*, vol. 57, no. 3, pp. 501–512, 2007.

[416] A. Pizzirusso, A. De Nicola, G. A. Sevink, A. Correa, M. Cascella, T. Kawakatsu, M. Rocco, Y. Zhao, M. Celino, and G. Milano, "Biomembrane solubilization mechanism by triton x-100: a computational study of the three stage model," *Physical Chemistry Chemical Physics*, vol. 19, no. 44, pp. 29780–29794, 2017.

[417] K. R. Minard, G. R. Holtom, L. E. Kathmann, P. D. Majors, B. D. Thrall, and R. A. Wind, "Simultaneous 1h pfg-nmr and confocal microscopy of monolayer cell cultures: Effects of apoptosis and necrosis on water diffusion and compartmentalization," *Magnetic Resonance in Medicine: An Official Journal of the International Society for Magnetic Resonance in Medicine*, vol. 52, no. 3, pp. 495–505, 2004.

[418] M. D. Silva, T. Omae, K. G. Helmer, F. Li, M. Fisher, and C. H. Sotak, "Separating changes in the intra-and extracellular water apparent diffusion coefficient following focal cerebral ischemia in the rat brain," *Magnetic Resonance in Medicine: An Official Journal of the International Society for Magnetic Resonance in Medicine*, vol. 48, no. 5, pp. 826–837, 2002.

[419] C. Arteta, V. Lempitsky, J. A. Noble, and A. Zisserman, "Interactive object counting," in *European conference on computer vision*, pp. 504–518, Springer, 2014.

[420] B. Deorosan and E. A. Nauman, "The role of glucose, serum, and three-dimensional cell culture on the metabolism of bone marrow-derived mesenchymal stem cells," *Stem cells international*, vol. 2011, 2011.

[421] M. Ostra, C. Ubide, M. Vidal, and J. Zuriarrain, "Detection limit estimator for multivariate calibration by an extension of the iupac recommendations for univariate methods," *Analyst*, vol. 133, no. 4, pp. 532–539, 2008.

[422] W. Wang, Y.-W. Su, R. Cheng, F. Zhang, M. Li, and X. Wo, "Influence of fixation and permeabilization on the mass density of single cells: a surface plasmon resonance imaging study," *Frontiers in Chemistry*, vol. 7, p. 588, 2019.

[423] B. Mattei, R. B. Lira, K. R. Perez, and K. A. Riske, "Membrane permeabilization induced by triton x-100: The role of membrane phase state and edge tension," *Chemistry and physics of lipids*, vol. 202, pp. 28–37, 2017.

[424] A. Pizzirusso, A. De Nicola, and G. Milano, "Martini coarse-grained model of triton tx-100 in pure dppc monolayer and bilayer interfaces," *The Journal of Physical Chemistry B*, vol. 120, no. 16, pp. 3821–3832, 2016.

[425] J. Shemesh, I. Jalilian, A. Shi, G. H. Yeoh, M. L. K. Tate, and M. E. Warkiani, "Flow-induced stress on adherent cells in microfluidic devices," *Lab on a chip*, vol. 15, no. 21, pp. 4114–4127, 2015.

[426] C. Chung, C. Chen, C. Chen, and C. Tseng, "Enhancement of cell growth in tissue-engineering constructs under direct perfusion: Modeling and simulation," *Biotechnology and bioengineering*, vol. 97, no. 6, pp. 1603–1616, 2007.

[427] M. M. Nava, M. T. Raimondi, and R. Pietrabissa, "A multiphysics 3d model of tissue growth under interstitial perfusion in a tissue-engineering bioreactor," *Biomechanics and modeling in mechanobiology*, vol. 12, no. 6, pp. 1169–1179, 2013.

[428] R. C. Brasch, K. C. Li, J. E. Husband, M. T. Keogan, M. Neeman, A. R. Padhani, D. Shames, and K. Turetschek, "In vivo monitoring of tumor angiogenesis with mr imaging," *Academic radiology*, vol. 7, no. 10, pp. 812–823, 2000.

[429] D. Brindley, K. Moorthy, J.-H. Lee, C. Mason, H.-W. Kim, and I. Wall, "Bioprocess forces and their impact on cell behavior: implications for bone regeneration therapy," *Journal of tissue engineering*, vol. 2011, 2011.

[430] F. G. Camacho, J. G. Rodríguez, A. S. Mirón, M. C. García, E. Belarbi, and E. M. Grima, "Determination of shear stress thresholds in toxic dinoflagellates cultured in shaken flasks: implications in bioprocess engineering," *Process Biochemistry*, vol. 42, no. 11, pp. 1506–1515, 2007.

[431] H. Aizaki, S. Nagamori, M. Matsuda, H. Kawakami, O. Hashimoto, H. Ishiko, M. Kawada, T. Matsuura, S. Hasumura, Y. Matsuura, *et al.*, "Production and release of infectious hepatitis c virus from human liver cell cultures in the three-dimensional radial-flow bioreactor," *Virology*, vol. 314, no. 1, pp. 16–25, 2003.

[432] S. Abbasalizadeh, M. R. Larijani, A. Samadian, and H. Baharvand, "Bioprocess development for mass production of size-controlled human pluripotent stem cell aggregates in stirred suspension bioreactor," *Tissue Engineering Part C: Methods*, vol. 18, no. 11, pp. 831–851, 2012.

[433] T. Budzowski, C. Graham, S.-C. Jan, and R. Siegel, "Method for maintaining low shear in a bioprocessing system," May 5 2005. US Patent App. 10/980,792.

[434] F. Dullien, "Single phase flow through porous media and pore structure," *The Chemical Engineering Journal*, vol. 10, no. 1, pp. 1–34, 1975.

[435] A. Ghanem and M. Shuler, "Characterization of a perfusion reactor utilizing mammalian cells on microcarrier beads," *Biotechnology progress*, vol. 16, no. 3, pp. 471–479, 2000.

[436] G. Wang, W. Zhang, C. Jacklin, D. Freedman, L. Eppstein, and A. Kadouri, "Modified celligen-packed bed bioreactors for hybridoma cell cultures," *Cytotechnology*, vol. 9, no. 1-3, pp. 41–49, 1992.